Ph.D. Thesis

DEVELOPMENT OF TECHNIQUES FOR THE AUTOMATIC EXTRACTION AND GRADE DETECTION OF GLIOMA TUMORS FROM CONVENTIONAL BRAIN MAGNETIC RESONANT IMAGES

Submitted to the

Cochin University of Science and Technology

in partial fulfillment of the requirements for the award of the degree of

Doctor of Philosophy

under the Faculty of Technology

by

Ananda Resmi S

Under the supervision of

Dr. Tessamma Thomas

DEPARTMENT OF ELECTRONICS

COCHIN UNIVERSITY OF SCIENCE AND TECHNOLOGY

COCHIN, KERALA, INDIA 682022

August 2013

Development of Techniques for the Automatic Extraction and Grade Detection of Glioma Tumors from Conventional Brain Magnetic Resonant Images

Ph.D. Thesis in the field of Image Processing

Author

Ananda Resmi S
Research Fellow
Audio and Image Research Laboratory
Department of Electronics
Cochin University of Science and Technology
Cochin –682 022
Kerala, India.
e-mail:anandaresmi@gmail.com

Research Advisor

Dr.Tessamma Thomas
Professor
Department of Electronics
Cochin University of Science and Technology
Cochin –682 022
Kerala, India.
e-mail:tess@cusat.ac.in

August 2013

Dedicated to my beloved Parents, My Husband and Children

DEPARTMENT OF ELECTRONICS
COCHIN UNIVERSITY OF SCIENCE AND TECHNOLOGY

COCHIN-22

Certificate

This is to certify that this Thesis entitled ***Development of Techniques for the Automatic Extraction and Grade Detection of Glioma Tumors from Conventional Brain Magnetic Resonant Images*** *is a bonafide record of the research work carried out by* ***Ms. Ananda Resmi S*** *under my supervision in the Department of Electronics, Cochin University of Science and Technology. The results presented in this thesis or parts of it have not been presented for the award of any other degree.*

Cochin-22
12-08-2013

Prof.(Dr.) Tessamma Thomas
(Supervising guide)
Department of Electronics
Cochin University of Science and Technology
Cochin 682022

Declaration

I hereby declare that this Thesis entitled ***Development of Techniques for the Automatic Extraction and Grade Detection of Glioma Tumors from Conventional Brain Magnetic Resonant Images*** *is based on the original research work carried out by me under the supervision of* ***Dr. Tessamma Thomas*** *in the Department of Electronics, Cochin University of Science and Technology. The results presented in this thesis or parts of it have not been presented for the award of any other degree.*

Cochin-22
12-08-2013

Ananda Resmi S
Research Fellow
Cochin University of Science and Technology
Cochin 682022

Abstract

Cerebral glioma is the most prevalent primary brain tumor, which are classified broadly into low and high grades according to the degree of malignancy. High grade gliomas are highly malignant which possess a poor prognosis, and the patients survive less than eighteen months after diagnosis. Low grade gliomas are slow growing, least malignant and has better response to therapy. To date, histological grading is used as the standard technique for diagnosis, treatment planning and survival prediction.

The main objective of this thesis is to propose novel methods for automatic extraction of low and high grade glioma and other brain tissues, grade detection techniques for glioma using conventional magnetic resonance imaging (MRI) modalities and 3D modelling of glioma from segmented tumor slices in order to assess the growth rate of tumors. Two new methods are developed for extracting tumor regions, of which the second method, named as Adaptive Gray level Algebraic set Segmentation Algorithm (AGASA) can also extract white matter and grey matter from T1 FLAIR an T2 weighted images. The methods were validated with manual Ground truth images, which showed promising results. The developed methods were compared with widely used Fuzzy c-means clustering technique and the robustness of the algorithm with respect to noise is also checked for different noise levels. Image texture can provide significant information on the (ab)normality of tissue, and this thesis expands this idea to tumour texture grading and detection. Based on the thresholds of discriminant first order and gray level co-occurrence matrix based second order statistical features three feature sets were formulated and a decision system was developed for grade detection of glioma from conventional T2 weighted MRI modality.The quantitative performance analysis using ROC curve showed 99.03% accuracy for distinguishing between advanced (aggressive) and early stage (non-aggressive) malignant glioma. The developed brain texture analysis techniques can improve the physician's ability to detect and analyse pathologies leading to a more reliable diagnosis and treatment of disease. The segmented tumors were also used for volumetric modelling of tumors which can provide an idea of the growth rate of tumor; this can be used for assessing response to therapy and patient prognosis.

Acknowledgment

In the name of God, the Entirely Merciful, the Especially Merciful

I would like to express my heartfelt gratitude to my supervising guide Dr. Tessamma Thomas, Professor, Department of Electronics, Cochin University of Science and Technology for her valuable guidance as well as for her kind advice, constant encouragement and affectionate support.

I am greatly indebted to Dr. Bejoy Thomas, Additional Professor, Department of Imaging Sciences and Interventional Radiology, Sree Chitra Tirunal Institute of Medical Sciences and Technology (SCTMIST), Kerala, India, for his valuable suggestions in the work of segmentation and grading glioma from conventional MR images and providing me important research materials. I am thankful to the anonymous reviewers of my publications for providing valuable suggestions and motivating comments.

Let me express my sincere gratitude to Prof. C.K. Anandan, Head of the Department of Electronics, Cochin University of Science and Technology, for extending the facilities in the department for my research work. Also, I am grateful to Prof. K. Vasudevan, Professor and former Head of the Department of Electronics, Prof. P.R.S Pillai, Professor and former Head of the Department of Electronics,Prof. K. G. Balakrishnan, former Head of the Department of Electronics, Prof. Mohanan, Professor, Department of Electronics, Dr. James Kurian and Dr. Supiya M.H., Associate Professors, Department of Electronics, for their kind support and help.

I am deeply indebted to Dr. K. P.P.Pillai, former Executive secretary, Indian Society for Technical Education (ISTE) for his affectionate support throughout my career.I thankfully remember my former Principal Dr. A.V. Zachariah (late) for his inspiring words. I gratefully acknowledge Dr. Shaji senadhipan, my former Principal and Dr. Z.A. Zoya, Principal, College of Engineering Perumon, Kollam for their encouragement for completing this work. I would like to express my sincere gratitude to Dr. Deepa P. Gopinath, Department of Electronics and

Communication Engineering, College of Engineering Thiruvananthapuram and Dr.V.G. Geethamma, Department of Nanotechnology, Mahatma Gandhi University for their help and motivations provided for throughout my research. I am grateful to Prof. Bindu Prakash, Associate Professor, Department of Electrical and Electronics Engineering, College of Engineering Perumon, Kollam for her support.

I thank all my fellow researchers, especially Dr.Dinesh Kumar V.P, Dr. Deepa Sankar, Dr.Praveen N., Ms. Deepa J, Ms. Reji A.P., R. Sethunath and Nobert Thomas, for their support.

I thank all administrative staff and librarian of the Department of Electronics and Cochin University of Science and Technology for their cooperation and support.

I am greatly obliged to my husband Suresh Bhaskar and my daughters Gayathri S and Gauthami S for their constant support and motivation to complete this thesis. It is beyond words to express my gratitude to my parents and sisters for their help and encouragement. Without their help and sacrifice, I am sure I could not have accomplished this task. With great sense of gratitude I thank Mr. Ajith A., Assistant Professor, Department of Electronics and Communication Engineering, College of Engineering Perumon, Kollam for his support and encouragement for completing the thesis

Ananda Resmi S.

Contents

Chapter 1 1
Introduction..... 1
1.1 Biomedical Image Processing..... 3
1.1.1 Image formation or Image Acquisition..... 4
1.1.2 Image visualization or Image Enhancement 4
1.1.3 Image analysis..... 5
1.1.4 Image management..... 6
1.1.5 Major Challenges in Biomedical Image Processing..... 7
1.2 Glioma - Background 8
1.3 Significance of the Thesis.....10
1.4 Objective of the Thesis 12
1.5 Contributions of the Thesis.....13
1.5.1 Development of Novel techniques for Automatic Extraction of Tumor, Tumor boundary, White matter and Grey matter.....13
1.5.2 Development of Technique for Automatic Grade detection of Glioma tumors from segmented MR images using statistical methods.....13
1.5.3 3D Modeling of Glioma Tumors from Segmented 2 D slices 14
1.6 Outline of the Thesis 14
References: 16
Chapter 2 19
Introduction to Brain Anatomy, Glioma and Magnetic Resonant imaging Techniques 19
2.1 Anatomy of the brain.....21
2.2 Types of brain tumors.....24
2.2.1 Secondary (Metastatic) Malignant Brain Tumors 25
2.2.2 Primary Brain Tumors 25
2.2.3 Glioma 27
2.3 Imaging Techniques 31

2.3.1 Magnetic Resonant Imaging 33
2.3.2 Advanced MRI scans.....45
2.3.3 Noise in MR Imaging 50
2.3.4 Partial volume effect.....53
2.3.5 Intensity in-homogeneities 54
Conclusion 55
References 55
Chapter 3.....59
Biomedical Image Segmentation and Statistical Texture Classification Techniques – An Overview 59
3.1 Introduction 61
3.2 Image enhancement and Segmentation 61
3.3 Literature Review of Segmentation Methods 62
3.3.1 Intensity thresholding algorithms 62
3.3.2 Region growing and Split and Merge algorithms.....64
3.3.3 Clustering.....65
3.3.4 Artificial Neural Networks.....66
3.3.5 Markov Random Field Models.....68
3.3.6 Deformable Models 69
3.3.7 Atlas-guided Approaches.....70
3.3.8 Watershed Methods 71
3.3.9 Level Set Methods 72
3.3.10 Other Methods.....73
3.4 Validation Methods for the segmentation algorithm used in medical images- An overview.....73
3.5 An Overview of Texture based Classification/ Detection of Pathological subjects in Medical imaging 76
Conclusion 78
References 78
Chapter 4.....99
Basic Theory of Image Segmentation and Texture Quantification Techniques.....99
4.1 Mathematical Morphology 101
4.1.1 Binary Morphology 101

4.1.2 Gray –Scale Morphology 106
4.2 Spatial filtering techniques using convolution and Correlation 111
4.2.1 Correlation 112
4.3 Thresholding 113
4.3.1 Adaptive Thresholding 115
4.4 Extraction and Labeling of Connected Components 116
4.5 Validation Methods for segmentation algorithm used in medical images- A Theoretical approach 118
4.6 Representation 120
4.6.1 Boundary of a region 120
4.6.2 Texture 121
4.7 Box plot and its uses 133
4.8 An overview of decision system 134
4.9 Performance Assessment with Receiver Operating Characteristics (ROC) Curve 135
Conclusion 140
References 140
Chapter 5 143
Automatic Extraction of Glioma Tumors and other Pathological brain Tissues 143
5.1 Introduction 145
5.2 A Novel Technique for Extraction of low grade and high grade Glioma Tumor from T2-Weighted MRI (Method 1) 146
5.2.1 Method Development 146
5.2.2 Implementation of method I 150
5.2.3 Results and Discussions (Method I) 153
5.3 A Novel Automatic Extraction Technique for Pathological Subjects and other Brain Tissues from T1 FLAIR and T2-weighted MR images using Adaptive Gray level Algebraic Set Segmentation Algorithm (AGASA) .163
5.3.1 Method Development 164
5.3.2 Implementation of the Adaptive Gray level Algebraic set Segmentation Algorithm 169
5.3.3 Results and Discussion 170

5.4 A comparative study between Fuzzy C-Means clustering Technique and the two methods....183
5.4.1 Fuzzy C-Means Clustering Technique....183
Conclusion....188
References....189
Chapter 6....193
Technique for Grade Detection of Glioma Tumors from Conventional MRI using Statistical Methods....193
6.1 Introduction....195
6.2 A Novel Technique for grade Detection of Glioma....195
6.2.1 Texture Analysis and Feature Extraction....196
6.2.2 Feature Selection and Feature set Formulation....206
6.2.3 Results of Feature Selection and Feature set Formulation....206
6.2.4 Development of grade Detection system....219
6.3 Implementation of the developed system....220
6.3.1 Image Database....221
6.3.2 Implementation Steps....221
6.3.3Performance Evaluation of the glioma Detection Method....222
6.4 Results and Discussions....223
6.4.1Results of Performance evaluation of the detection system using Receiver operating characteristic curves....223
Conclusion....226
References....227
Chapter 7....231
3D Modeling of Segmented Glioma tumors from Brain MRI....231
7.1 Introduction....233
7.1.1 Back ground....233
7.2 A Novel Method for Volume Rendering of Glioma Tumor from the Segmented Axial Slices....235
7.2.1 Choice of Segmentation....237
7.2.2 Segmentation Based on Spatial Domain Filtering techniques....237
7.2.3 Volume Rendering and Visualization....238
7.2.4 Volume rendering using 3D DOCTOR....240

7.2.5 Validation....241
7.2.6 Growth rate assessment....241
7.3. Implementation of the Method....242
7.3.1 Image Database used....242
7.3.2 Implementation....242
7.3.3 Results and Discussions....242
7.4 Merits of the Method....247
Conclusion....248
References....249
Chapter 8....253
AVG Glioma-A Software System for the Visualization and Grade Detection of Glioma....253
8.1 Development of a Graphical User Interface system....255
Conclusion....268
Chapter 9....268
Conclusions and Future Work....268
9.1 Thesis Highlights....270
9.2 Extraction of Low and High Grade Glioma and other Brain Tissues using Adaptive Gray level Algebraic set Segmentation Algorithm (AGASA)..271
9.3 Grade Detection of Glioma Tumors using Statistical Texture Analysis....272
9.4 Volumetric modeling of glioma....272
9.5 Suggestions for Future research....273

List of Figures

2.1 Brain Anatomy
2.2 Primary Brain Tumors
2.3 A Brain image slice showing glioma tumor
2.4 An MRI of a patient with two separate types of brain tumor
2.5 An MRI (Magnetic resonant imaging) of the brain
2.6 Conventional MR image slices (a)T1–weighted (b) T2 – weighted (c) PD weighted (d) FLAIR
2.7 MRI views in three planes a) Axial (b) Sagittal (c) Coronal
2.8 MR images of a glioblastoma: (a) T1-weighted (b) T2-weighted (c) T2-weighted FLAIR (d) and T1-weighted contrast enhanced
2.9 Typical MRI scan of a low-grade glioma
(a) T1 sequence demonstrating T1 shortening in the right frontal lobe. (b) T2 sequence demonstrating T2 prolongation (hyper intensity) at the site of the glioma. (c) Contrast-enhanced imaging of the glioma showing no marked contrast enhancement.
2.10 An MR image sequence with 5.5 mm spacing between slices
2.11 Diffusion weighted Imaging (DWI) slices
2.12 Diffusion Tensor Imaging (DTI) slices
2.13 Perfusion weighted Imaging (PWI)
2.14 A common example of Partial volume effect
4.1 The erosion process. (a) Image A (b) Structuring element B with radius d/2 with origin at dotted point (c) Eroded image
4.2 The dilation process. Figures from left to right- A is the image, B is the structuring element with radius d/2. Dilated image $A \oplus B$
4.3 Morphological opening. a) Structuring element B rolling along inner boundary of A b) the heavy line is the outer boundary of the opening. c) Completed opening (shaded)
4.4 Morphological closing operation a) Structuring element B rolling outer boundary of set A, b) Set A after closing.
4.5 Image after Gray level dilation with a disc shaped structuring element. (a) Original Image (b) Image after gray level dilation

4.6 Image after Gray level erosion with a disc shaped structuring element. (a) Original Image (b) Image after gray level erosion
4.7 Image after Gray level opening (a) Original Image (b) Image after gray level opening with a disc shaped structuring element
4.8 Image after Gray level closing with a disc shaped structuring element. (a) Original Image (b) Image after gray level closing
4.9. A 3x3 neighborhood about a point (x ,y) in an image
4.10 Example for Correlation filtering. (a) Original Image (b) Image after correlation filtering
4.11 Gray level histograms that can be partitioned by a) A single threshold b) Multiple thresholds
4.12 Example for Thresholding. (a) Original Image (b) Image after Thresholding
4.13 Structure of a connected component. a) Pixels p and its 4-neighbours $N_4(P)$, b) Pixels p and its 8-neighbours c) The shared pixels are both 4 connected and 8 connected.
4.14 Example for connected component labeling. (a) Original Image (b) Image after connected component labeling
4.15 Boundary representation a) Original Image b)4-connected boundary
4.16 Examples of different types of Textures
4.17 An image with gray level value equal 1: entropy 0
4.18 An image with uniform noise: entropy 4.15
4.19 An image added with Gaussian noise: entropy 5.6
4.20 Direction of GLCM generation
4.21 Sample gray scale neighborhood structures having two offsets.
4.22 Construction of GLCMs.
4.23 Box plot and its properties
4.24 Illustration of decision Tree with Replication
4.25 Format of a Confusion Matrix
4.26 ROC curve: regions of a ROC graph
4.27 ROC curves: (a) an almost perfect classifier (b) a reasonable classifier (c) a poor classifier
5.1 The flow chart for Segmentation of ROI
5.2 Extraction technique for high grade tumor from T2 weighted MRI slice a)Original image b)Pre-processed image c)Complemented and dilated

image d) Filtered image e) Image after opening f) Image after closing g) Thresholded image h) Morphologically labeled image using connected component labelling i) Segmented gray level image

5.3 T2 weighted images of low grade and high grade glioma tumors a) ,b) and c) Low Grade Glioma d), ,e) and f) High Grade Glioma

5.4 Segmentation procedures for extracting low grade glioma tumor from a T2 weighted MR image a) Original Image b) Normalized and Subtracted Image c) Image after Dilation and Correlation filtering d) Image after morphological opening and closing e)Image after thresholding f)Segmented gray level tumor

5.5 Segmentation procedures for extraction of high grade glioma tumor from a T2 weighted MR image a) Original image b) Complemented and dilated and image c) Image after correlation filtering d.) Image after morphological opening e) Image after closing g) Thresholded image g) Segmented binary tumor h) Gray level tumor

5.6 Automatic extraction method applied on normal image slice a) Normal image b) Complemented and dilated image c) Filtered and subtracted image d) Image after morphological opening e) Image after morphological closing c) Final output after thresholding and labeling

5.7 Automatically labeled Tumor with respect to manual ground truth Original image b) Ground Truth image c) Automatically labelled tumor d) Labelled tumor with manual ground truth boundary superimposed.

5.8 The Tanimoto Index computed for segmentation of low and high grade glioma, The ranges of values for low and high grade glioma are 93.4-98.7 and 98.2-99.6 respectively.

5.9 Segmentation of low grade glioma tumor from a noise added image a) T2 weighted MR image b) Gaussian noise added image of PSNR 10db c) Image after dilation and correlation filtering d)Image after morphological opening and closing e) Image after thresholding f) Segmented gray level tumor

5.10 High grade glioma tumor segmented from Gaussian noise added image of PSNR 10db a) T2 weighted image b) Noise added image c) Segmented tumor from noise added image using morphological filtering technique and thresholding

5.11 Segmentation of low grade glioma tumor in speckle noise added image with PSNR of 12 db. a) Original image b) Speckle noise added image c) Image after opening d) Image after closing e) Thresholded binary image f) Segmented gray level image

5.12 High grade glioma tumor segmented from Speckle noise added image of PSNR 12db a) T2 weighted image b) Noise added image c) Segmented tumor from noise added image using morphological filtering technique and thresholding

5.13 Tanimoto Index of the segmented of low and high grade glioma with respect to SNR at different noise levels. (a) Gaussian noise added images with different noise levels ,(b) Speckle noise added images with different noise levels

5.14 Block diagram for the Method

5.15 The various steps for segmentation tumor and boundary a)T1 FLAIR b) T2 weighted c) Skull removed d) Subtracted and dilated e) Complemented image f) Intensity adjusted image g) Thresholded and labeled image h) Segmented gray level tumor i). Tumor boundary

5.16 Segmentation of grey matter with tumor removed. a) Enhanced image b) Binary mask of GM with outer layers c**)** Extracted GM with outer layers removed.

5.17 Segmentation of white matter with tumor removed a) Enhanced image b) Binary mask of white matter with tumor removed c) White matter with skull removed

5.18 Sample raw data from a patient volume used segmentation. T1-FLAIR andT2-weighted MRI slice

5.19 Example of segmented ROIs of low grade glioma tumor from MR image slices. *a)* T2 weighted b)T1 FLAIR MR image c) Segmented binary low grade glioma tumor d) Gray level tumor e) extracted tumor boundary. f*)*Binary segmented WM with tumor portion removed g) Gray level WM with outer layers removed h) Segmented binary GM i) Gray level GM with outer layers removed.

5.20 Example of segmented ROIs of high grade glioma tumor patient from MR image slices .a) T1 FLAIR image b) T2 weighted image c) Segmented binary tumor d) Gray level tumor e) Extracted tumor boundary f) Gray

level WM g) Binary segmented WM with outer layers removed h) Segmented binary GM i) Gray level GM with outer layers removed

5.21. Example for Extraction method applied on a Normal Image. a) T2-Weighted Image b) T1 FLAIR image c) Binary WM with d) Binary segmented WM with outer layers removed e) segmented gray level WM f)segmented binary GM g) Binary GM with outer layers removed h) Gray level GM i) segmented and labeled image

5.22 Segmentation problem cases, (a) Under-segmentation, (b) Over-segmentation (c) Clustering. Segmented boundaries are in yellow; red circles indicate errors.

5.23 Manually outlined Brain components on T1 FLAIR images (ground Truth) by expert Radiologist and automatically labeled brain components of high grade and low grade glioma tumors on T1-FLAIR images; *1column.* Manually segmented T1 FLAIR images containing high and low grade tumor, *2nd column*. Automatically segmented and labeled high and low grade tumors, *3rd column* Automatically segmented and labeled GM, 4th *column* Automatically segmented and labeled WM, 5th *column* Automatically segmented and labeled tumor, GM, and WM with outer layers removed.

5.24. Tanimoto index (TI) of high grade and low grade Tumor , WM, and GM of 20 patients.

5.25 The percentage match of low grade and high grade glioma tumor, GM and WM is shown using box plot.

5.26 Positive prediction (P+[%]) values of high and low grade tumors, GM, and WM respectively

5.27 Example for Fuzzy c-means algorithm (a) T2 weighted image (b) Segmented Image using fuzzy c-means algorithm

5.28 Visual validation of fuzzy c-means clustering technique. (a) Segmented using the FCM algorithm (b) Tumor boundary (c) extracted boundary super imposed on T1 weighted image (d) under segmentation detected in the rounded portions

5.29 Tanimoto index of low and high grade glioma using Fuzzy c-means clustering Algorithm.

6.1 The flow chart for decision system for grade detection of glioma

6.2 Sub image selected from the segmented tumor region
6.3 The Box plot of Average Intensity for 16x16 sub-image of segmented low and high grade glioma.
6.4 Box plot of Standard deviation for 16x16 sub-image of segmented low and high grade glioma.
6.5 Box plot of Kurtosis for 16x16 sub-image of segmented low and high grade glioma.
6.6 Box plots of Entropy for 16x16 sub-image of segmented low and high grade glioma.
6.7 Box plots of mean (Intensity) levels for forty five sets of high grade and fifty five sets of low grade glioma patients.
6.8 Box plots of standard deviation using first order statistics for forty five sets of high grade and fifty five sets of low grade glioma patients
6.9 Box plots of histogram based entropy distribution for forty five sets of high grade and fifty five low grade glioma patients
6.10 Box plots of kurtosis using first order statistics for forty five sets of high grade and fifty five low grade glioma patients.
6.11 Box plots of intensity based parameter-skewness for forty five sets of high grade and fifty five sets for low grade glioma patients
6.12 Box plots of Cluster prominence for forty five sets of high grade and fifty five sets of low grade Glioma patients .
6.13 Box plots of Cluster shade forty five sets of high grade and fifty five sets are low grade glioma patients.
6.14 Box plots of Auto correlation for forty five sets of high grade and fifty five sets of low grade glioma patients.
6.15 Box plots of Entropy forty five sets of high grade and fifty five low grade Glioma patients
6.16 Box plots of Dissimilarity for forty five sets of high grade and fifty five low grade Glioma patients
6.17 Box plots of Energy for forty five sets of high grade and fifty five low grade glioma patients
6.18 Box plots of Contrast for forty five sets of high grade and fifty five low grade glioma patients.

6.19 Box plot of Inverse difference moment for forty five sets of high grade and fifty five low grade glioma patients
6.20 Box plot of maximum probability computed using GLCM based second order statistics for forty five sets of high grade and fifty five low grade glioma patients
6.21 The flow chart of the grade detection system based on the thresholds of feature sets
6.22 Sample images from the image database a) Original T2 weighted image with low grade tumor b) Segmented gray level low grade tumor c) Original T2 weighted image with high grade tumor d)Segmented gray level tumor
6.23 The ROC curve for feature set 1. Area under the curve (AUC)-87.43%, sensitivity -94.56%, specificity-77.2%, Performance of detection-Good test
6.24 The ROC curve for feature set 2. Area under the curve (AUC)-90.083%, sensitivity -97.13%, specificity-83.04.2%, Performance of detection-Excellent test
6.25 The ROC curve for feature set 3 Area under the curve (AUC) - 97. 35%, sensitivity -99.03%, specificity-92.53%, Performance of detection-Excellent test
6.26 Performance comparison of different feature sets for detection of high and low grade Glioma tumors. TPR-True Positive Rate; AUC-Area under the curve; TNR-True Negative Rate
7.1 The flow chart for 2D Segmentation and Volumetric 3D rendering of tumor
7.2 The example for development of tumor segmentation and Boundary Extraction techniques. (a) & (b) Axial slices of T2 weighted and T1 FLAIR image in a patient image dataset. (c) Segmented binary tumor (d) Segmented Gray level tumor (e) Tumor boundary (f) Extracted boundary is superimposed T1 FLAIR image.
7.3 The basic principles behind the 3D modeling algorithm. (a) 2D Image (b) Transformed 3D points for the 2D image (c) 3D modeled tumor
7.4 Sample slices of segmented low grade glioma tumor in a dataset
7.5 Sample slices of Segmented Glioblastoma (high grade) tumor in a dataset

7.6 3D modeled images using the method. (a) 3D modeled image of low grade glioma (b) 3D modeled image of glioblastoma (high grade)
7.7 3D modeled images of low and high grade Glioblastoma tumors. (a) Low grade tumor (b) Glioblastoma
7.8 The growth rates computed from a 3D modelled tumor over a 376-day period in a 42-year-old subject.
8.1 Basic Block diagram for the entire Techniques used in the AVG glioma
8.2 Developed Graphical User Interface for 'AVG glioma'
8.3 The image selection from an image database for automatic segmentation and grade detection using browse button
8.4 T1 FLAIR image when the push button T1_FLAIR is enabled. This is for selecting one of the input image for segmentation
8.5 T2 Weighted image when the push button T2 Weighted is enabled. This is for selecting one of the input image for segmentation
8.6 The automatic extraction of Tumor region when Tumor button is activated from the selected set of images
8.7 Boundary extraction while enabling the push button Tumor _boundary.
8.8 The extraction of Grey Matter when Grey_matter push button is enabled
8.9 The extracted White matter, when the White_Matter button is activated
8.10 An example of extracted labelled image when the push button Labeled_Image is enabled
8.11 Example for grade test when push button Grade_test_ Glioma is enabled. The test result is high grade glioma
8.12 An example of Low grade glioma when activating Grade_test_Glioma push button after selecting a T2 weighted image from the database
8.13 The example of volumetric modeling of tumor using segmented tumor slices in an image database when push button Volumetric_Tumor is enabled.

List of Tables

2-1 MRI scan protocol for brain tumor patients

5.1 TP, TN, FP and TI computed values of randomly selected segmented low grade tumor for 10 images

5.2 TP, TN, FP and TI computed values of randomly selected segmented high grade tumor for 10 images

5.3 Perfomance analysis for segmented high grade tumor in MRI images

5.4 Perfomance analysis for segmented low grade tumor in MRI images

5.5 Perfomance analysis of segmented high grade WM for 10 sample images

5.6 Perfomance analysis of segmented low grade WM for 10 sample images

5.7 Perfomance analysis of segmented high grade GM for 10 sample images

5.8 Perfomance analysis of segmented low grade GM for 10 sample images

5.9 Performance Analysis of FCM method

5.10 Comparative study of proposed method I and Method II with respect to FCM method

6.1 Typical values of First order statistical features from 16x16 segmented tumor sub image of 20 high grade dataset

6.2 Typical values of First order statistical features of 16x16 segmented tumor sub image from 20 low grade glioma image dataset

6.3 Typical values of First order stastistical features of the same 0 low grade glioma patients' image dataset considering the whole tumor region.

6.4 Typical values of First order statistical features of the same set of high grade glioma considering whole tumor region

6.5 Typical values of GLCM features for randomly selected 20 images from low grade glioma patients' image dataset

6.6 The ranges of values of first order statistical features for segmented low grade and high grade glioma tumors

6.7 Ranges of values of GLCM features for the segmented ROI, with respect to low grade and high grade glioma tumors obtained using boxplot

6.8 Definition for TP, FP, FN, and TN for developed detection system

6.10 Performance evaluation of Feature set 1, Feature set 2 and Feature set 3

7.1 Performance of the 3D Model Algorithm with respect to manual method

Abbreviations

2D	-	Two Dimensional
3D	-	Three-Dimensional
ADC	-	Apparent Diffusion Coefficient
AGASA	-	Adaptive gray level Algebraic segmentation Algorithm
ANN	-	Artificial Neural Networks
ASF	-	Alternating Sequential Filter
ASM	-	Active shape model
ASM	-	Angular Second Moment
AUC	-	Area Under the Curve
AVG Glioma	-	Automatic Visualization and Grading of Glioma
AWGN	-	Additive White Gaussian Noise
BOLD	-	Blood Oxygen Level-Dependent
CBF	-	Cerebral Blood Flow
CBV	-	Cerebral Blood Volume
CCS	-	Connected Segmentation Algorithm
CI	-	Computational Intelligence
CNS	-	Central Nervous System
COLLATE	-	Consensus Level Labeler Accuracy and Truth Estimation
CSF	-	Cerebrospinal Fluid
CT	-	Computed Tomography
DICOM	-	Digital Imaging and Communications in Medicine
DSC	-	Dice Similarity Coefficient
DWI	-	Diffusion Weighted Imaging
EM	-	Expectation-Maximization
FCM	-	Fuzzy C-Means
FEA	-	Finite Element Analysis
FGM	-	Finite Gaussian Mixture
FLAIR	-	Fluid Attenuated Inversion Recovery
FMRI	-	Functional MRI
FN	-	False Negative
FP	-	False Positive

FPR	-	False Positive Rate
GBM	-	Glioblastoma Multiforme
GE	-	Gradient Echo
GHMRF	-	Gaussian hidden Markov random field
GLCM	-	Gray Level Co-occurrence Matrices
GLCP	-	Gray level co- occurrence probabilities
GM	-	Grey Matter
GT	-	Ground Truth
GUI	-	Graphical User Interface
HRCT	-	High Resolution Computed Tomography Images
IR	-	Inversion Recovery
ITAC		Intestinal-type adenocarcinoma
kNN	-	k-Nearest Neighbor
MCR	-	Misclassification Rate
MEG	-	Magneto Encephalography
MRA	-	Magnetic Resonance Angiography
MRF	-	Markov Random Field
MRI	-	Magnetic Resonant Imaging
MRS	-	Magnetic Resonance Spectroscopy
MRSI	-	MR Spectroscopic Imaging
MTT	-	Mean Transit Time
NMR	-	Nuclear Magnetic Resonance
PD	-	Proton Density
PDF	-	Probability Density Function
PET	-	Positron Emission Tomography
PM	-	Percentage Match
PNN	-	Probabilistic Neural Network
PVE	-	Partial Volume Effect
PWI	-	Perfusion-Weighted Imaging
rCBV	-	Relative Cerebral Blood Volume
RF	-	Radio Frequency
RMSE	-	Root Mean Squared Error
ROC	-	Receiver Operating Characteristics
ROI	-	Region of Interest

SAR	-	Synthetic Aperture Radar
SE	-	Spin Echo
SE	-	Structuring Element
SNR	-	Signal-to-Noise Ratio
SPECT	-	Single Photon Emission Tomography
STAPLE	-	Simultaneous Truth and Performance Level Estimation
SVM	-	Support Vector Machines
TI	-	Tanimoto Index
TN	-	True Negative
TP	-	True Positive
TPR	-	True Positive Rate
TTP	-	Time To Bolus Peak
WHO	-	World Health Organization
WM	-	White Matter

Chapter 1
Introduction

The great practical difference between the word, written or spoken, and the visual image is that we cannot read the former unless we have been initiated into the mystery of language, whereas visual images can be made intelligible to all men who have eyes.....

Human visual perception is a far more complex and selective process than that which a film records. However, unlike humans, who are limited to the visual band of electromagnetic (EM) spectrum, imaging machines cover almost the entire EM spectrum, ranging from gamma to radio waves. They can operate also on images generated by sources that humans are not accustomed to associating with images. These include ultrasound, electron microscopy, parametric imaging and computer-generated images. Thus, digital image processing encompasses a wide and varied field of applications

Digital image processing is the technology of applying computer algorithms to process digital images. The outcome of this process can be either images or set of representative characteristics or properties of original images. Digital image processing directly deals with an image, which is composed of many image points, are also namely pixels as spatial coordinates that indicate the position of points in the image, and intensity (gray level) values. A colorful image accompanies higher dimensional information than a gray image. Red, green and blue values are typically used in combinations to produce color images in real world [1].

In this chapter, we outline how a theoretical base and state-of the-art method can be integrated into prototyping environment whose objective is to provide novel methods for segmentation, grade detection and 3D modeling of glioma. This chapter starts with a brief introduction about glioma, magnetic Resonance imaging, and computer aided diagnostic systems. In addition, a general overview of the thesis is provided including the description of its structure.

1.1 Biomedical Image Processing

The commonly used term “biomedical image processing” means the provision of digital image processing for biomedical sciences. By the increasing use of the direct digital imaging systems for medical diagnostics, digital image processing becomes more and more important in health care. Based on digital

imaging techniques, the entire spectrum of digital image processing is now applicable in medicine. In general, digital image processing covers four major areas - Image formation or Image acquisition, Image visualization or Image enhancement, Image analysis and Image management.

1.1.1Image formation or Image Acquisition

Image formation or Image acquisition includes all the steps from capturing the image to forming a digital image matrix. Numerous electromagnetic and some ultrasonic sensing devices are frequently arranged in the form of a 2-D array. The response of each sensor is proportional to the light energy falling onto the surface of the sensor. Generally image acquisition stage involves preprocessing like scaling [1].

Nowadays, medical images have become a major component of diagnostics, treatment planning and procedures, and follow-up studies. Furthermore, medical images are used for education, documentation, and research describing, morphology as well as physical and biological functions in 1D, 2D, 3D, and even 4D image data. Today, a large variety of imaging modalities have been established, such as X-ray, Computed Tomography(CT), Magnetic Resonance Imaging (MRI), Fluoroscopy, Ultrasound etc. which are based on transmission, reflection or refraction of light, radiation, temperature, sound, or spin. Obviously, an algorithm for delineation of an individual that works with one imaging modality will not be applicable directly to another modality.

1.1.2Image Visualization or Image Enhancement

Image visualization or Image enhancement refers to all types of manipulation of the image matrix, resulting in an optimized output image. The goal is to process the image so that the result is more suitable than the original image for a specific application. The word specific is important because the methods for enhancing one kind of image may not be suitable for another kind, e.g. X-ray images and space craft images. Image visualization or image enhancement is low-level processing which denotes manual or automatic techniques, which can be realized without a priori knowledge on the specific content of images. These methods operate on the raw data as well as on pixel, edge, or texture levels, and thus are at a minimal level of abstraction. The Low-level methods of image

processing, i.e., procedures and algorithms, are mostly applied for pre- or post-processing of medical images [2].

1.1.3 Image analysis

Image analysis includes processing used for quantitative measurements as well as abstract interpretations of biomedical images. These steps require a priori knowledge of the nature and content of the images, which must be integrated into the algorithms at a higher level of abstraction. Thus, the process of image analysis is very specific, and developed algorithms can be transferred directly into other application domains. High-level image processing include methods at the texture, region, object, and scene levels. The required abstraction can be achieved by increased modelling of a priori knowledge. *Image analysis* techniques require extraction of certain features that aid in the identification of the object. *Image Analysis* mainly involves s*egmentation*, f*eature extraction and selection*, r*epresentation and description, classification or detection or recognition* [2, 3].

- ***Segmentation*** techniques are used to isolate the desired object from the scene so that measurements can be made on it subsequently. *Segmentation* partitions the image into its constituent connected regions or objects. The level to which the subdivision is carried depends on the problem being solved. In medical image processing, the definition accentuates the various diagnostically or therapeutically relevant image areas, namely, the discrimination between healthy anatomical structures and pathological tissue. By definition, the result of segmentation is always at the regional level of abstraction. Depending on the level of feature extraction required after segmentation, we can methodically classify the procedures into pixel, edge, and texture or region-oriented procedures. In addition, there are hybrid approaches, which result from combination of single procedures [1-3].
- ***Representation and description*** almost follow the output of a segmentation stage, which is usually raw pixel data, constituting the boundary of the region, i.e. a set of pixels separating one region from another or all the points in it. In either case, converting data to a suitable form for computer processing is necessary. Therefore, the task of feature extraction is to emphasize image information at the particular level, where subsequent algorithms operate.

Consequently, information provided on other levels must be suppressed. Thus, a data reduction to obtain the characteristic properties is executed. Feature extraction techniques according to the different levels of abstraction, that is, data level, pixel level, edge level, texture level and region level (external representation) [1-3] were used.

- ***Description*** is also called feature selection. It deals with extracting the attributes that result in some quantitative information of interest or is basic for differentiating one class of object from another [1].
- ***Recognition*** is a process that assigns a label to an object, based on its descriptors. This is usually achieved through classification or detection of objects or regions in an image. According to the general processing chain, the task of the classification/detection is to assign all connected regions which are obtained from the segmentation, to particularly specified classes of objects. Usually, region-based features that sufficiently abstract the characteristics of the objects are used to guide the classification process. These extracted features must be sufficiently discriminative and suitably adopted to the application, since they fundamentally impact the resulting quality of the classifier/detector. The classification itself reverts mostly to known numerical (statistical) and non-numerical (syntactic) procedures as well as the newer approaches of Computational Intelligence (CI), such as neural networks, evolutionary algorithms, and fuzzy logic. In general, the individual features, which are determined by different procedures, are summarized either to numerical feature vectors (also referred to as signature) or abstract strings of symbols. Statistical classification regards object identification as a problem of the statistical decision theory. A syntactic classifier can be understood as a knowledge-based classification system (*expert system*), because the classification is based on a formal heuristic, symbolic representation of expert knowledge, which is transferred into image processing systems by means of facts and rules.

1.1.4 Image management

Image management sums up all the techniques that provide efficient storage, communication, transmission, archiving, and access (retrieval) of image data. Thus,

the methods of telemedicine are also a part of the image management. *Image restoration* attempts to reconstruct or recover an image that has been degraded by using an a priori knowledge of degradation phenomenon and is based on mathematical and probabilistic models of image degradation. This includes deblurring of images degraded by the limitations of a sensor or its environment, noise filtering, and correction of geometric distortion or nonlinearities due to sensors [2].

1.1.5 Major Challenges in Biomedical Image Processing

Using medical images, it is difficult to formulate a priori knowledge such that it can be integrated directly and easily into automatic algorithms of image processing. This is referred to as the *semantic gap*, which means the discrepancy between the cognitive interpretation of a diagnostic image by the physician (high level) and the simple structure of discrete pixels, which is used in computer programs to represent an image (low level). In the medical domain, there are three main aspects hindering bridging this gap [3]

- ***Heterogeneity of images***: Medical images display living tissue, organs, or body parts. Even if captured with the same modality and following a standardized acquisition protocol, shape, size, and internal structures of these objects may vary remarkably not only from patient to patient (inter-subject variation), but also among different views of the same patient and similar views of the same patients at different times (intra-subject variation). In other words, biological structures are subject to both inter- and intra-individual alterability. Thus, universal formulation of a priori knowledge is impossible [3]
- ***Unknown delineation of objects***: Frequently, biological structures cannot be separated from the background because the diagnostically or therapeutically relevant object is represented by the entire image. Even if definable objects are observed in biomedical images, their segmentation is problematic because the shape or borderline itself is represented fuzzily or only partly. Hence, medically related items often can be abstracted most at the texture level [3].
- ***Robustness of algorithms***: In addition to these inherent properties of medical images, which complicate their high-level processing, special requirements of

reliability and robustness of medical procedures, when applied in routine, image processing algorithms are also demanded in the medical area. As a rule, automatic analysis of images in medicine should not provide wrong measurements. This means that, images which cannot be processed correctly, must be automatically, rejected and withdrawn from further processing. Consequently, all images that have not been rejected must be evaluated correctly [3].

1.2 Glioma - Background

Gliomas are the most frequent primary brain tumors that originate in glial cells. Glial cells are the building-block cells of the connective, or supportive tissue in the central nervous system (CNS) [4, 5]. Glial cells provide the structural backbone of the brain and support the function of the neurons (nerve cells), which are responsible for thought, sensation, muscle control, and coordination. According to World Health Organization (WHO), gliomas are classified into four grades that reflect the degree of malignancy. Grades I and II are considered as low-grade and grades III and IV are considered as high-grade. Grades I and II are the slowest-growing and least malignant. Grade I tumors are well circumscribed and often surgically curable, whereas grade II tumors diffuse, infiltrating lesions with a marked potential, over the time, for progression towards high grade malignant tumor [6]. Grade III tumors are considered malignant and grow at a moderate rate, and show chemo sensitivity and better prognosis. Grade IV tumors, such as glioblastoma multiforme, are fast growing and are the most malignant of primary brain tumors [4, 6]. It is also the most resistant to current standard treatment – i.e.surgery, followed by radiation and chemotherapy. Most common subtype of glioma is Astrocytoma [7]. Grade IV Astrocytoma is called Glioblastoma. Classification of glioma tumors is important for clinical understanding of tumor biology, clinical response and for assessing overall prognosis with brain tumor.

Imaging is an essential part of the decision making process for therapy and later for planning of surgical or radio therapeutic interventions. In the case of neurosurgery, neuroimaging can precisely define the location and accurately delineate the lesion and its relationship to grey and white matter structures, before intervention. In radiation therapy, imaging can define and demarcate margins for

therapy planning. Imaging is mandatory after therapeutic intervention for monitoring disease and possible side effects.

MR imaging is the standard technique for diagnosis, treatment planning, and monitoring of CNS lesions, with superior sensitivity compared to alternative modalities [8]. MR Imaging is classified broadly into two types according to the techniques and applications, i.e, conventional and advanced MR imaging. Components of a standardized protocol for conventional MR imaging include T1-weighted pre-contrast, T2-weighted, FLAIR, Diffusion Weighted Imaging (DWI), and T1-weighted contrast imaging [8]. Conventional MR imaging of the brain provides excellent soft tissue contrast and is routinely used for the noninvasive assessment of brain tumors, but its ability to define the tumor type and grade of gliomas is limited [9]. Based on the patient's conventional MRI, a radiologist cannot differentiate whether it is a low grade glioma or a high grade glioma, because both of these are almost visually similar [10]. A biopsy is usually required to establish the diagnosis and subtype of a brain tumor and to plan appropriate treatment after conventional MR imaging.

Advanced MR imaging modalities such as proton MR spectroscopic imaging (MRSI), perfusion-weighted imaging (PWI), and diffusion-weighted imaging (DWI) have been proposed as alternate methods for differential diagnosis of tumors and non tumor lesions, primary versus metastatic lesions and tumor grading [9-11]. MRSI provides metabolic signature of brain tumors and PWI measures relative cerebral blood volume (rCBV). These factors reflect variation in micro vessel density and apparent diffusion coefficient (ADC) derived from DWI and reflects changes in tissue structure [9, 10]. There are many studies in literature, for differentiating primary gliomas and metastates and glioma grading by combining conventional MRIs with PWI, MRSI and DWI [11]. PWI, MRSI and DWI are also used for Multi parametric characterization of grade 2 glioma subtypes [9]. Advanced MR imaging offers new insights into the patho physiology of brain tumors, mainly gliomas. These techniques, including MR Spectroscopy, Perfusion Weighted Imaging, and Diffusion Tensor Imaging, are increasingly incorporated into imaging protocols and complement the morphologic detail of conventional MR imaging studies, with a range of applications including assessment of

treatment response. But, advanced MR imaging facilities are not common because of high equipment and acquisition cost.

The most common conventional MRI modalities used to assess gliomas are Fluid Attenuated Inversion Recovery (FLAIR), T1 and T2-weighted modalities. T1-weighted modalities highlight fat tissues in the brain whereas T2-weighted modalities highlight tissues with higher concentration of water. FLAIR images are T2 or T1-weighted with the cerebrospinal fluid (CSF) signal suppressed. In general, edema, border definition and tumor heterogeneity are best observed on FLAIR and T2-weighted images [7].

1.3 Significance of the Thesis

The accurate segmentation of Glioma tumors, its boundary, Grey matter and White matter are essential for further analysis, treatment planning, and response to therapy and for determining prognosis. But the extraction and analysis of anatomical structures from brain MRIs are quite difficult and time consuming because of its complex structure. Usually MR images are affected by the presence of noise, intensity in-homogeneities and partial volume effect which cause accurate segmentation and boundary determination of tumor a difficult task. Most of the widely used brain tumor segmentation methods developed, such as thresholding [12], edge and region based [13] techniques. Atlas-guided methods [14], Clustering approaches [15], Region growing techniques [16], k-means clustering [17], fuzzy c means clustering techniques [18], neural network approaches, level set method [18,19], GVF snake [20] and Markov random fields have limitations, as they require too much computation time, suffer from under segmentation, over-segmentation, variation in intensity levels etc. Hence, a robust and accurate segmentation method with less complexity has to be developed for extracting the entire tumor area and other brain tissues, retaining original gray level values.

Grade detection of glioma tumors is very important for taking clinical decisions regarding the treatment and for finding survival rates without doing biopsy. The major challenges are, tumor characterization is difficult, because the neoplastic tissue is often heterogeneous with conventional MR imaging profile. The second thing is that, the external representation of tumor, which is shape, cannot be taken as a discriminant feature for detection/ classification of grade/type

of tumor because, the shape of each tumor is not consistent throughout all slices of MR image and may change quickly where the inter-slice distance is large. But, tumors are expected to have consistent textures for all slices. Texture analysis is very important in the brain tumor detection, as it is difficult to differentiate between various types of tumor tissues using shape. Several approaches are present in the literature for classification and grade detection of glioma tumors. Classification of glioma from metastatic, and grading of glioma from conventional MRI and perfusion MRI, using support vector machines (SVM) [11, 21] and artificial neural networks is cited in literature. The features used for their study were tumor shape, intensity characteristics, rotation invariant Gabor texture features, age, gender, Texture analysis using statistical quantification etc. The imaging profile used for grade detection of glioma tumors in literature are multi-parametric Images. Methods are there in literature for classification of brain tumor type and grade using advanced MRI texture and support vector machines (SVM) [22], in recent years. However, from a practical point of view perhaps the most serious problem with SVMs is the high algorithmic complexity and extensive memory required for quadratic programming in large-scale tasks and therefore binary SVMs are computationally expensive and thus run slow [23].

The diagnosis and detection of glioma currently rely on the histopathologic examination of biopsy specimens, but variations in tissue sampling for these heterogeneous tumors and restrictions on surgical accessibility make it difficult to be sure that the samples obtained are representative of the entire tumor. Hence we have to consider entire tumor texture for analysis. Usually, most of the texture analysis methods make use of only a portion of the tumor region and this may affect the accuracy of detection/classification. Hence texture based computer assisted methods have to be devised for grade detection of glioma tumors.

Volumetric change in glioma tumors over time is a critical factor in treatment decisions. Typically, the tumor volume is computed on a slice-by-slice basis using MRI scans obtained at regular intervals. The appearance of high grade MR images varies greatly, due to tissue variation inside the tumor area and the diffused growth of the tumor. Moreover, the segmented tumors should be visualized to get an opinion about the tumor's shape and location in the brain. For clinical follow-up also, the evaluation of the pre-operative tumor volume is

essential. Most of the 3D modeling techniques in literature is time consuming and much user intervention is required. Hence a method has to be devised for volumetric modeling of glioma tumors from automatically segmented tumor slices.

1.4 Objective of the Thesis

From the above described background information, it is clear that development of novel and robust techniques for accurate segmentation of low and high grade glioma, its boundary, White matter and Grey matter, which overcomes the limitations of the existing methods up to a greater extent, is a topic of relevance. The research work presented in this thesis focuses on (1) accurate segmentation of pathological tissues and other brain structures (2) texture based techniques for grade detection of glioma tumors and (3) 3D modeling of tumor region for assessing the growth rate.

Texture based feature extraction and feature set formulation are the topics of interest in this work. This research focuses on statistical texture analysis using First order statistical features and also Gray level co- occurrence matrices, for feature extraction. Texture is a measure of variation of intensity of a surface, quantifying properties such as smoothness, coarseness, and regularity. Hence a novel technique is devised for grade detection of glioma tumors from conventional brain MRIs using statistical texture quantification methods. This also emphasizes on the development of techniques which are more accurate, less time consuming and with much less human intervention, for the 3D modeling of glioma tumors for growth rate assessment, response to therapy, treatment planning etc.

The objectives of the thesis can be summarized as follows

The research work done can be classified into three phases.

1. Development of a novel automatic technique for extracting/ segmenting low and high grade glioma tumor and other brain components without any loss of tumor tissue regions, from conventional MR Image slices, for pre-operative planning and treatment.
2. To devise a concrete method to detect the grade of glioma tumors from the segmented MR images, before deciding on doing biopsy. This can be used as a second opinion to radiologists in helping glioma grade detection.

3. Devise a technique for volumetric modeling of Glioma tumors from the segmented tumor slices, in order get a better understanding of Glioma tumors, in terms of its growth rate.

1.5 Contributions of the Thesis

The contributions of the thesis are given below

1.5.1 Development of Novel Techniques for Automatic Extraction of Tumor, Tumor boundary, White matter and Grey matter.

Two methods are developed for extraction of pathological subjects and other brain components. First method extracts low and high grade glioma tumor from T2 weighted MRI. The methods involved are mathematical morphological filtering techniques such as complementation, dilation, subtraction, closing and opening, correlation filtering and thresholding. The robustness of the algorithm with respect to Gaussian noise and speckle noise is also evaluated. The second method named as Adaptive Gray level Algebraic set Segmentation Algorithm (AGASA), makes use of joint intensities of T1FLAIR and T2 weighted images to extract low and high grade Tumor, tumor boundary, White matter and Grey matter. The method is validated with respect to the manual ground truth of the images. The methods are compared with respect to the existing methods, in terms of computation time and accuracy.

1.5.2 Development of Technique for Automatic Grade detection of Glioma tumors from segmented MR images using statistical methods.

A novel method is proposed here for the grade detection of glioma using a rule based decision system. Three different feature sets are formulated from selected descriptors extracted by statistical quantification of tumor textures. This frame work consists of pre-processing and segmentation of region of interest (ROI), analysis of segmented tumor texture based on first order statistics and Gray Level Co occurrence Matrix based second order statistics for feature extraction, feature selection using box plots, feature set formulation, development of decision

system based on thresholds fixed by the features in the feature sets, and finally training and performance evaluation of results using receiver operating characteristic curve (ROC). GLCM is an effective tool for statistical quantification of textures. GLCM based statistical texture analysis of segmented tumors using conventional T2 weighted MRI has not been used before for grade detection of glioma.

1.5.3 3D Modeling of Glioma Tumors from Segmented 2D slices

Volumetric modeling of glioma tumors is devised by stacking automatically segmented 2D glioma tumor slices in the patient's image dataset by3D surface rendering method. The size and accuracy of the tumor depends upon the accuracy of segmented 2D slices. The Growth rate assessment for a tumor for different days is evaluated using this method. This method is useful for volumetric analysis and shape determination of tumors and successive assessment by doctors.

1.6 Outline of the Thesis

The Thesis is organized as follows

Chapter 1: Introduction

This chapter describes the background, challenges, basic digital image processing techniques involved, and objectives of this research. Contributions of this research work are also summarized

Chapter 2: Introduction to Brain anatomy, Glioma Tumors and Magnetic Resonance Imaging Techniques

This Chapter gives a brief introduction of brain Anatomy and characterisation of Glioma tumors. Magnetic Resonance imaging techniques are explained. Factors that affect the quality of MR images are also discussed.

Chapter 3: Biomedical Image Segmentation and Statistical Texture Classification Techniques – An Overview

A review on the biomedical image segmentation techniques used so far is presented. The state of art classification/ detection methods based on statistical texture quantification techniques are also detailed in this chapter

Chapter 4: Basic Theory of Image Segmentation and Texture Quantification Techniques

This Chapter provides a summary of the fundamental tools used in the thesis. A description about morphological filtering techniques, texture, feature extraction, feature set formulation, validation techniques and performance evaluation using Receiver Operating Characteristics curves are also explained.

Chapter 5: Automatic extraction of Glioma Tumors and other pathological brain Tissues.

This chapter provides, a novel and robust method for automatically extracting low and high grade tumors from axial slices of T2 weighted images and also a novel method for extracting Grey matter, White matter, tumor and its boundary from joint intensities of T1-FLAIR and T2-weighted MRI using spatial domain techniques. Theory and Implementation of the techniques are also provided. Robustness of the method with respect to Guassian noise and Speckle noise is also discussed. Validation of the segmentation techniques is also provided. A comparative study of the two methods with the existing methods is also discussed in this chapter.

Chapter 6: Technique for grade Detection of Glioma Tumors from Conventional MRI using Statistical Methods

This chapter discusses the development of a novel technique for grade detection of Glioma Tumors from Conventional MRI, using first order statistics and GLCM based second order statistics. It also explains feature extraction, feature selection and feature set formulation for the development of a rule based decision system, based on thresholds fixed by the feature sets. The performance of the detection system using ROC curves is also discussed

Chapter 7: Volumetric modeling of Glioma Tumors from Segmented2D Slices.

This Chapter includes development and implementation of a fully automatic volumetric modelling of Glioma tumors from segmented 2D slices. It also explains volume measurements and assessment of growth rate, from the 3D modelled Glioma tumor.

Chapter 8:'AGV glioma' A Software System for the Visualization and Grade Detection of Glioma This Chapter provides system design and Graphical user interface and its implementation for the entire method**.**

Chapter 9: Conclusion and future work

A brief summary of the research work done and the important conclusions are highlighted in this chapter. Suggestions for future research are also provided.

References:

[1] R.C. Gonzalez, R.E. Woods, "A Text Book on Digital Image Processing", 2nd Edition, Pearson Education India. (2002).

[2] R. Xu, L Luo and J Ohya, "Segmentation of brain MRI, A Text Book of Advances in brain Imaging", In Tech Publishers .pp. 143-169, (2002).

[3] R.A Lotufo, L.R Rittner. R.M. Audigier, A.V Saúde, R.C Machado, "Morphological Image processing applied in biomedicine", Thomas M. Deserno, Biomedical Image Processing, Springer, USA.pp. 107-128, (2011).

[4] E. Mandonnet, L. Capelle and U. Duffau, Extension of paralimbic low grade gliomas: toward an anatomical detection based on white matter invasion patterns, Journal of Nuero-Oncology.vol. 78(2) 179-185, (2006)

[5] D. Schiff, Low grade Astrocytomas. An article in American Brain Tumor Association, February 2007.

[6] A. Michotte, B. Neyns, C. Chaskis, et.al. Neuropathological and molecular aspects of low-grade and high grade gliomas, Acta nuerol. beig., 104, 148-153, (2004)

[7] S.cha, Update on Brain Tumor Imaging: From Anatomy to physiology, Am J Neuroradiol vol. 27, pp. 475-87, (2006)

[8] M. Essig, N. Anzalone, S. E. Combs, et.al, MR Imaging of Neoplastic Central Nervous System Lesions: Review and Recommendations for Current Practice, Am J Neuroradiol.vol. 33 pp.803-17, (2012)

[9] Wei Bian, Inas S. Khayal, Janine M. Lupo, et.al, Multiparametric Characterization of Grade 2 Glioma using magnetic Resonance

Spectroscopic, perfusion, and Diffusion Imaging, Translational Oncology. vol. 2(4) pp.271-280 , (2009)

[10] N.Bulakbasi, M. Kocaoglu, A. Farzaliyev et al. Assessment of Diagnostic Accuracy of Perfusion MR Imaging in Primary and Metastatic Solitary Malignant Brain Tumors, Am J Neuroradiol. Vol.26(9) pp.2187–2199, (2005)

[11] E. I. Zacharaki, S. Wang, S. Chawla, et.al, Classification of brain tumor type and grade using MRI texture and shape in a machine learning scheme, Magn Reson. Med.vol. 62(6) pp.1609–1618, (2009).

[12] D.L. Pharm, C. Szu, A survey of current methods in image segmentation. Technical Report JHU/ECE 99-01, Publication to Annual Medical Review of Biomedical Engineering; pp.1-27, (1998).

[13] M.M. Hossam, E.H Aboul, and M. Shoman. Brain Tumor Segmentation Scheme using K-mean Clustering and Connected Component Labeling Algorithms. 10th International Conference on Intelligent Systems Design and Applications (ISDA), pp; 320 - 324, (2010).

[14] D Selvathi and A Arulmurgan, MRI Image Segmentation Using Unsupervised Clustering Techniques, Proceedings of the Sixth International Conference on Computational Intelligence and Multimedia Applications. (ICCIMA'05):) pp. 105-110, (2005)

[15] M Kumar, M. A Kamal, Modified Method to Segment Sharp and Unsharp Edged Brain Tumors in 2D MRI Using Automatic Seeded Region Growing Method. International Journal of Soft Computing and Engineering (IJSCE);vol. 1(2) (2011)

[16] M. M. Ahmed. and D. B. Mohammad, Segmentation of Brain MR Images for Tumor Extraction by Combining Kmeans Clustering and Perona-Malik Anisotropic Diffusion Model. International Journal of Image Processing. , vol.2 (1) pp: 27-34, (2008);.

[17] Li C, Huang R., Ding Z, A Level Set Method for Image Segmentation in the Presence of Intensity In-homogeneities With Application to MRI, IEEE Transactions on Image Processing, Vol. 20, No. 7, July 2011, pp. 2007-2016.

[18] P Chandra Barman, S Miah, S Chandra. ,MRI Image Segmentation Using Level Set Method and Implement a Medical Diagnosis System, Computer Science & Engineering: An International Journal (CSEIJ), Vol.1(5), (2011)

[19] R.S. Alomari, K Suryaprakash, C Vipin, Segmentation of the Liver from Abdominal CT Using Markov Random Field model and GVF Snakes, , International Conference on Complex, Intelligent and Software Intensive Systems IEEE Computer Society, pp.293-298, (2008).

[20] S Cha, Update on Brain Tumor Imaging: From Anatomy to physiology. Am J Neuroradiol,;vol. 27: pp. 475-487,(2006)

[21] Jude HD, Kezi S, Vijila C, Fuzzy Based Experimental Verification of Significance of Skull Tissue removal in Brain Tumor Image segmentation', International Journal of Computer Applications, vol.29, pp:56-61, (2010).

[22] M Lynn, H Fletcher, O.H Lawrence, B.G Dmitry, Automatic segmentation of Non-enhancing Brain Tumors in Magnetic Resonance Images. Artificial Intelligence in Medicine, vol.21(3), pp.:43 – 63, (2001).

[23] M R Kaus, S K Warfield, A Nabavi, Automated Segmentation of MR Images of Brain Tumors., Radiology, vol. 218(2), pp.: 586–591, **(**2001).

Chapter 2

Introduction to Brain Anatomy, Glioma and Magnetic Resonance imaging Techniques

The purpose of this chapter is to introduce some basic idea about brain anatomy, different types of tumor present in the brain and different imaging techniques adopted to visualize the complex brain structures. It also discusses the different grades of glioma tumors, its causes and symptoms. It introduces types of magnetic resonance imaging techniques adopted for visualizing complex brain structures, to find out various brain disorders and for diagnosing brain tumors. Additional topic discussed in this chapter gives a brief idea about advanced magnetic resonance imaging techniques. Glioma tumors, different types of noise, partial volume effect and intensity in-homogeneities present in Magnetic Resonance Images are also presented.

2.1 Anatomy of the brain

Human brain is the most valuable, interesting and amazing part of our body. The **brain** acts as the control centre of the central nervous system and gives us the ability to learn and understand. The brain controls and coordinates most sensory systems, movement, behaviour, and homeostatic body functions such as heart rate, blood pressure, fluid balance, and body temperature. The brain is the source of cognition, emotion, memory, and motor, and other forms of learning. Much behaviour such as simple reflexes and basic locomotion, can be executed under spinal cord control alone.

The human brain is made up of four main parts: the cerebral cortex, the cerebellum, the brain stem, and the meninges as shown in Fig.2.1

The cerebral cortex is the largest part of the brain, is associated with conscious thought, movement and sensation. It contains two cerebral hemispheres each controlling the opposite side of the body. The two halves are connected by the ***corpus callosum***, a bridge of wide, flat neural fibers that act as communication relays between the two sides and is divided into four lobes such as : the frontal, temporal, parietal, and occipital lobes. The main functions of the four lobes are as follows:

Frontal Lobe is one of the four lobes of the cerebral hemisphere which extending from behind the forehead back to the parietal lobe, is the brain region that separates humans from our primate cousins. It controls attention, behavior, abstract thinking, problem solving, creative thought, emotion, intellect, initiative, judgment, coordinated movements, muscle movements, smell, physical reactions, and personality. ***Parietal Lobe*** houses the sensory cortex and motor cortex which plays an important role in controlling tactile sensation, response to internal stimuli, sensory comprehension, language reading, and some visual functions. ***Sensory cortex*** is located in the front part of the parietal lobe, or in other words, the middle area of the brain. The sensory cortex receives information from the spinal cord about the sense of touch, pressure, pain, and the perception of the position of body parts and their movements. ***Motor cortex*** is the area located in the middle, top part of the brain that helps control movement in various parts of the body.

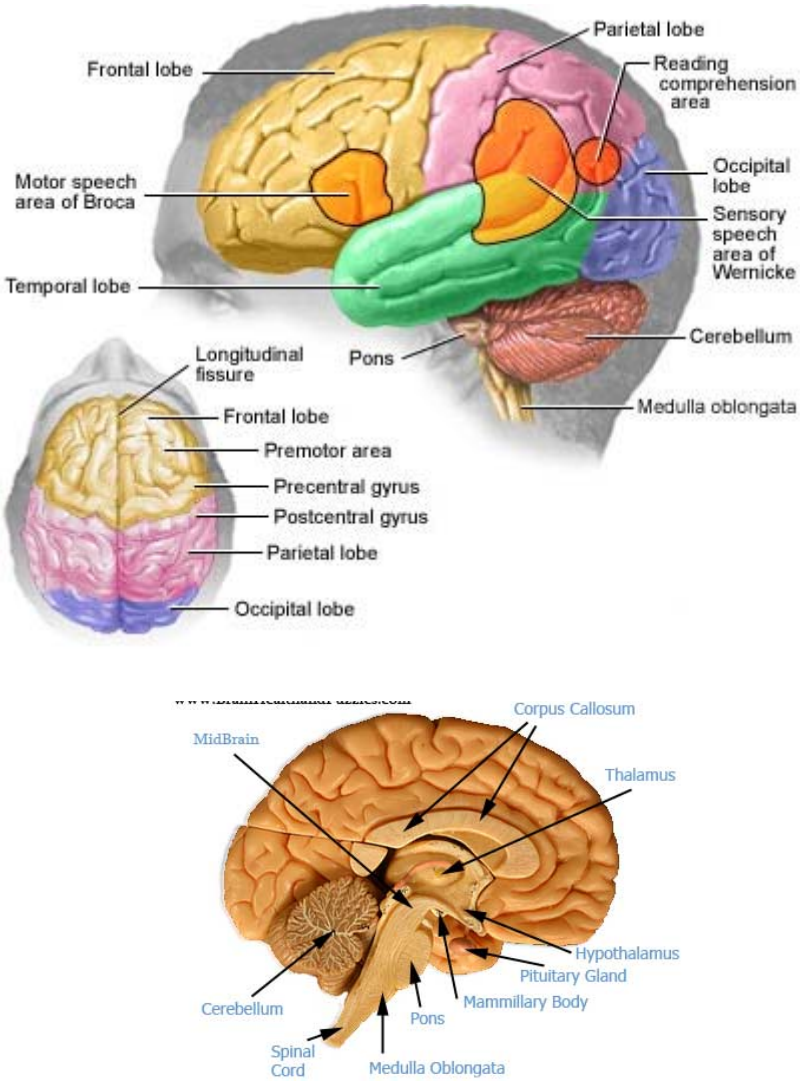

Fig.2.1 Brain Anatomy [1]

Occipital Lobe located at the back of the brain, is the seat of the primary visual cortex, the brain region responsible for processing and interpreting visual information. ***Broca's Area*** is located in the opercular and triangular sections of the inferior frontal gyrus. The function of this area is the understanding of language, speech, and the control of facial neurons.

Temporal lobe reaching from the temple back towards the occipital lobe, the temporal lobe is a major processing center for language and memory. It controls auditory and visual memories, language, some hearing and speech, language, plus some behavior. ***Wernicke's area*** is part of the temporal lobe that surrounds the auditory cortex and is thought to be essential for understanding and formulating speech. Damage in Wernicke's area causes deficits in understanding spoken language.

Cerebellum is located at the lower back of the head and is connected to the brain stem. It is the second largest structure of the brain. The cerebellum controls complex motor functions such as walking, balance, posture, and general motor coordination.

The brain stem The brain stem is involved with autonomic control of processes like breathing and heart rate as well as conduction of information to and from the peripheral nervous system, the nerves and ganglia found outside the brain and spinal cord which includes the Medulla oblongata, Pons, and Midbrain. This is located at the bottom of the brain and connects the cerebrum to the spinal cord. The brain stem controls many vitally important functions including motor and sensory pathways, cardiac and respiratory functions, and reflexes.

The meninges. These are the membranes that surround and protect the brain and spinal cord. There are three meningeal layers, called the dura mater, arachnoid, and pia mater. The cerebrospinal fluid (CSF) is produced near the center of the brain, in the lateral ventricles, and circulates around the brain and spinal cord between the arachnoid and pia layers.

Cerebrospinal Fluid, also called **CSF**, is a clear substance that circulates through the brain and spinal cord. It provides nutrients and serves to cushion the brain and therefore protect it from injury. As this fluid gets absorbed, more is produced from the choroid plexus, a structure located in the ventricles. A brain

tumor can cause a build-up or blockage of CSF. ***Ventricles*** of the brain are connected cavities within the brain, where cerebrospinal fluid is produced.

Hypothalamus is a region of the brain in partnership with the pituitary gland that controls the hormonal processes of the body as well as temperature, mood, hunger, and thirst. ***Optic Chiasm*** is located beneath the hypothalamus and is where the optic nerve crosses over to the opposite side of the brain. ***Pineal Gland*** controls the response to light and dark. The exact role of the pineal gland is not certain.

Pituitary Gland is a small, bean-sized organ that is located at the base of the brain and is connected to the hypothalamus by a stalk. The pituitary gland secretes many essential hormones for growth and sexual maturation. ***Thalamus*** is located near the center of the brain and controls input and output to and from the brain, as well as the sensation of pain and attention. [1-3]

Neurons, or brain cells, are made up of cell bodies, axons, and dendrites. The cells mainly connect to one another through synapses (small junctions between brain cells where neurotransmitters and other neuro-chemicals are passed). Synapses are often found between the axons and dendrites, which allows the cells to signal to one another. Current estimates suggest the brain has approximately 86 billion neurons [3]. The brain is made up of two types of matter: gray and white. Gray matter consists of the cell bodies and dendrites of the neurons, as well as supporting cells called astroglia and oligodendrocytes. White matter, however, is made up of mostly of axons sheathed in myelin, an insulating-type material that helps cells propagate signals more quickly. It's the myelin that gives the white matter its lighter color. For many years; neuroscientists believed white matter was simply a support resource for gray matter. However, recent studies show that white matter architecture is important in processes like learning and memory [4]

2.2 Types of brain tumors

When most normal *cells* grow old or get damaged, they die, and new cells take their place. Sometimes, this process goes wrong. New cells form when the body doesn't need them, and old or damaged cells don't die as they should. The buildup of extra cells often forms a mass of tissue called a growth or tumor. Brain

tumors are composed of cells that exhibit unrestrained growth in the brain. They can be *benign* (noncancerous, meaning that they do not spread elsewhere or invade surrounding tissue) or *malignant* (cancerous).The brain and spinal column make up the central nervous system (CNS), where all vital functions, including thought, speech, and strength of the body are controlled. When a tumor arises in the CNS, it is especially problematic because of the potential effect on a person's thought processes and movements [3].

The brain tumors are broadly classified into primary and secondary (metastatic) tumors. The terms primary and metastatic describe where the tumor has originated and brain tumors are generally classified as one or the other. Primary brain tumors arise from the brain or spinal cord while metastatic brain tumors arise from other tissue and have spread to the brain. This is the most basic form of classifying brain tumors, but yields great insight into the characteristics of these complex growths and how they might be treated.

The following section describes about primary and secondary brain tumors.

2.2.1 Secondary (Metastatic) Malignant Brain Tumors

A secondary brain tumor is a cancerous tumor that started in another part of the body (such as the breast, lung, or colon) and then spread to the brain. Secondary tumors are about three times more common than primary tumors of the brain [7,8]. Many types of cancer can spread (metastasize) to the brain, but melanoma, breast, lung, and kidney cancer are among the most common. Cancer cells are spread by blood or lymphatic vessels. Metastatic brain tumors are more common than primary brain tumors. It is believed that the commonality is not because cancer types are becoming more aggressive, it is just that people are living longer from their cancer types, and this time allows for metastasis to occur. Usually, multiple tumors develop. Solitary metastatized brain cancers may occur but are less common. Metastatic or secondary tumors of the brain will occur in 20% to 40% of patients with cancer.

2.2.2 Primary Brain Tumors

There are more than 100 types of primary brain tumors. Primary tumors start in the brain, whereas secondary tumors spread to the brain from another site

such as the breast or lung. There are many types and subtypes of primary brain tumors. They include gliomas (which in turn include astrocytomas, oligodendrogliomas, and ependydomas), meningomas, medullablastomas, pituitary adenomas, and central nervous system lymphomas [9].

Benign Brain Tumors. Benign tumors represent half of all primary brain tumors. Their cells look relatively normal, grow slowly, and do not spread (metastasize) to other sites in the body or invade brain tissue. Benign tumors can still be serious and even life-threatening if they are in vital areas of the brain where they exert pressure on sensitive nerve tissue or if they increase pressure within the brain. While some benign brain tumors may pose a health risk, including risk of disability and death, most are usually successfully treated with techniques such as surgery [4].

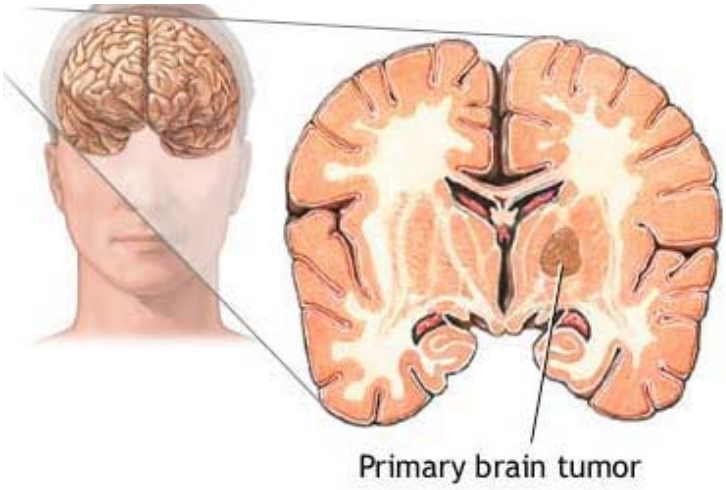

Fig 2.2. Primary Brain tumor

Malignant Brain Tumors. A primary malignant brain tumor is one that originates in the brain itself. Although primary malignant brain tumors often shed cancerous cells to other sites in the central nervous system (the brain or spine), they rarely spread to other parts of the body. Brain tumors are generally named and classified according to the type of brain cells from which they originate and the

location in which the cancer develops. Malignant brain tumors are further classified using a grade: low, intermediate, or high. More information can be found in Staging/Grading [4-6].The biologic diversity of these tumors, however, makes classification difficult.

2.2.3 Glioma

As a group, a glioma is considered the most common type of brain tumor. About 80% of malignant primary brain tumors are collectively known as *gliomas*. Glioma is not a specific type of cancer but is a term used to describe tumors that originate in glial cells. Glial cells are the building-block cells of the connective, or supportive, tissue in the central nervous system. There is two types of supportive cells: astrocytes and oligodendrocytes. A glioma is given a grade (a measure of how much the tumor appears like normal brain tissue) from I to IV based on the degree of aggressiveness.

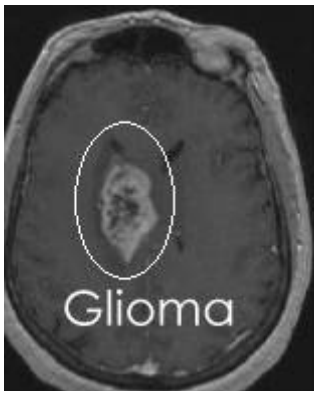

Fig. 2.3 A Brain image slice showing glioma tumor [1]

A grade I glioma is a benign tumor, while grades II through IV are tumors with an increasing degree of aggressiveness and are therefore considered increasingly cancerous in potential [10, 11]

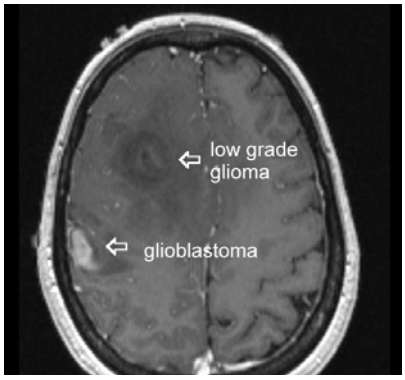

Fig. 2.4 An MRI of a patient with two separate types of brain tumor, a low grade glioma in the right frontal lobe (which is very difficult to see) and a high grade glioma (Glioblastoma) in the right parietal lobe which shows more (gray white appearance) contrast enhancement [1]

Grades I and II are considered low-grade and grades III and IV are considered high-grade. Grades I and II are the slowest-growing and least malignant; grade II tumors are generally considered borderline between benign and malignant. Grade III tumors are considered malignant and grow at a moderate rate. Grade IV tumors, such as glioblastoma multiforme, are the fastest-growing and most malignant primary brain tumor [12].High-grade gliomas are highly-vascular and have a tendency to infiltrate. Often tumor growth causes a breakdown of the blood–brain barrier in the vicinity of the tumor. As a rule, high-grade gliomas almost always grow back even after complete surgical excision, and so are commonly called recurrent cancer of the brain.

On the other hand, low-grade gliomas grow slowly, often over many years, and can be followed without treatment unless they grow and cause symptoms. Several acquired (not inherited) genetic mutations have been found in gliomas. There are several glial cell types from which gliomas form. Most common subtype of gliomas are called either astrocytoma or oligodendroglioma, or a mixture of both.

Astrocytomas are primary brain tumors derived from astrocytes, which are star-shaped glial cells. Astrocytomas account for about 60% of all malignant

primary brain tumors. It is the most common type of glioma and begins in cells called astrocytes in the cerebrum or cerebellum. There are four grades of astrocytoma[12]. Astrocytomas are the most common of the primary brain tumors. The pathologist, using a microscope, grades these tumors on a scale of I to IV based on how quickly the cells are reproducing, as well as their potential to invade nearby tissue [12].

Astrocytoma tumor types by grade include:

- Grade I. *Pilocytic astrocytoma* is one of the most common types of glioma in children.It is a slow-growing tumor that is most often benign and rarely spreads into nearby tissue. It accounts for about 2% of all brain tumors.
- Grade II. *Diffuse astrocytoma* (also called low-grade astrocytoma) is a slow-growing tumor that can often spread into nearby tissue and can become a higher grade. It accounts for about 11% of all brain tumors, typically occurring in men and women of ages 20 – 60. Grades I and II astrocytomas are the slowest growing tumors, and are also called low-grade astrocytomas.
- Grade III. *Anaplastic astrocytoma* is a malignant tumor that can quickly grow and spread to nearby tissues. It accounts for about 3% of all brain tumors. It typically occurs in adults of ages 30 - 60 and is more common among men than women.
- Grade IV. *Glioblastoma multiforme* (GBM), also called glioblastoma, accounts for about 50% of all astrocytomas and about 20% of all brain tumors.It is one of the deadliest types of brain tumors. These highly malignant, aggressive and complex tumors grow rapidly. They are most common in older adults (50s - 70s), particularly men. Only about 10% of childhood brain tumors are glioblastomas. It also is the most resistant to current standard treatment – surgery, followed by radiation and chemotherapy [3].

2.2.3.1 Statistics

It is estimated that about 52,000 people are diagnosed with a primary brain tumor (benign or malignant) each year. In 2012, an estimated 22,070 adults (12,010 men and 10,060 women) in the United States were diagnosed with primary malignant tumors of the brain and spinal cord. It is estimated that 12,920 deaths (7,330 men and 5,590 women) from this disease will occur this year. Brain tumors are the tenth most common cause of cancer death in women [13]. Primary malignant brain tumors account for about 2% of all cancers. However, brain and spinal cord tumors are the second most common type of cancer in children (after leukemia).

Survival statistics should be interpreted with caution. Estimates are based on data from thousands of cases of glioma tumors in the United States each year, but the actual risk for a particular individual may differ. It is not possible to tell a person how long he or she will live with a glioma tumor. Because the survival statistics are measured in five-year (or sometimes one-year) intervals, they may not represent advances made in the treatment or diagnosis of this cancer. In general, brain tumors are slightly more likely to occur in men than in women. Some specific types of brain tumors, such as meningiomas, are more common in women. Most brain tumors in adults occur between the ages of 65 - 79. Brain tumors also tend to occur in children younger than the ages of 8. In children, glioblastomas are the leading cause of death from solid tumors.

2.2.3.2 Prognosis and Survival rates

Recent advances in surgical and radiation treatments have significantly extended average survival rates and can also reduce the size and progression of malignant glioma [15].

The survival rates in people with brain tumors depend on many different variables:

- Type of tumor (such as astrocytoma, oligodendroglioma, or ependymoma)
- Location and size of tumor (these factors affect whether or not the tumor can be surgically removed)
- Tumor grade
- Patient's age

- Patient's ability to function
- How far the tumor has spread

Survival rates tend to be highest for younger patients and decrease with age. Five-year survival rates range from 66% for children ages 0 - 19 years, to 5% for adults of age of 75 years and older. Glioblastoma multiforme has the worst prognosis with 5-year survival rates of only 13% for people of ages 20 - 44, and 1% for patients age 55 – 64 [17, 18].

2.2.3.3 Diagnosis

Diagnosis of brain tumors involves a neurological examination and various types of imaging tests. Imaging techniques include magnetic resonance imaging (MRI), computed tomography (CT), and positron emission tomography (PET) scan. Biopsies may be performed as part of surgery to remove a tumor, or as a separate diagnostic procedure.

2.2.3.4 Treatment

The standard approach for treating brain tumors is to reduce the tumor as much as possible using surgery, radiation treatment, or chemotherapy. Such treatments are typically used in combination with each other [19].

2.3 Imaging Techniques

Among the modern medical imaging technologies, Positron Emission Tomography (PET) and Magnetic Resonance Imaging (MRI) are considered to be the most powerful diagnostic inventions. In the 1940s, modern medical imaging technology began with advancements in nuclear medicine. Advanced imaging techniques have dramatically improved the diagnosis of brain tumors.

Magnetic Resonance Imaging. Magnetic resonance imaging (MRI) is the standard crucial step for diagnosing a brain tumor. It provides pictures from various angles that can help doctors to construct a three-dimensional image of the tumor. It gives a clear picture of tumors near bones, smaller tumors, brain stem tumors, and low-grade tumors. MRI is also useful during surgery to show tumor bulk, for accurately mapping the brain, and for detecting response to therapy. Its details are given in next section 2.3.1

Computed Tomography. In the early 1970s, by combining the diagnostic properties of X-rays with computer technology, scientists were able to construct 3D images of the human body in vivo for the first time, prompting the birth of the Computed Tomography (CT). The emergence of CT was an important event that motivated scientists to invent PET and MRI [20].Computed tomography (CT) uses a sophisticated X-ray machine and a computer to create a detailed picture of the body's tissues and structures. It is not as sensitive as an MRI in detecting small tumors, brain stem tumors, and low-grade tumors. But it is useful for finding bone disorders. Often, doctors will inject the patient with a contrast material to make it easier to see abnormal tissues. A CT scan helps locate the tumor and can sometimes help determine its type. It can also help detect swelling, bleeding, and associated conditions. In addition, computed tomography is used to evaluate the effectiveness of treatments and watch for tumor recurrence [20].

Positron Emission Tomography. Positron emission tomography (PET) provides a picture of the brain's activity rather than its structure by tracking sugar that has been labeled, with a radioactive tracer. It is sometimes able to distinguish between recurrent tumor cells and dead cells or scar tissue caused by radiation therapy. PET is not routinely used for diagnosis, but it may supplement MRIs to help determine tumor grade after a diagnosis. Data from PET may also help improve the accuracy of newer radiosurgery techniques. PET scans are often done along with a CT scan.

Other Imaging Techniques. Numerous other advanced or investigational imaging techniques available include:

- Single photon emission tomography (SPECT) is similar to PET but is not as effective in distinguishing tumor cells from destroyed tissue after treatments. It may be used after CT or MRI to help distinguish between low-grade and high-grade tumors [21].
- Magnetoencephalography (MEG) scans measure the magnetic fields created by nerve cells as they produce electrical currents. It is used to evaluate functioning of various parts of the brain. However, this procedure is not widely available [21].

- MRI angiography evaluates blood flow. MRI angiography is usually limited to planning surgical removal of a tumor suspected of having a large blood supply.

Lumbar Puncture (Spinal Tap): A lumbar puncture is used to obtain a sample of cerebrospinal fluid, which is examined for the presence of tumor cells. Spinal fluid may also be examined for the presence of certain tumor markers (substances that indicate the presence of a tumor). However, most primary brain tumors do not currently have identified tumor markers. A computed tomography (CT) scan or magnetic resonance imaging (MRI) should generally be performed before a lumbar procedure to make sure that the procedure can be performed safely.

Biopsy: A biopsy is a surgical procedure in which a small sample of tissue is taken from the suspected tumor and examined under a microscope for malignancy. The results of the biopsy also provide information on the cancer cell type. Biopsies may be performed as part of surgery to remove a tumor, or as a separate diagnostic procedure. With some very slow-growing cancers, such as those that occur in the midbrain or optic nerve pathway, patients may be closely observed and not treated until the tumor shows signs of growth. The diagnosis and detection of glioma currently rely on the histopathologic examination of biopsy specimens, but variations in tissue sampling for these heterogeneous tumors and restrictions on surgical accessibility make it difficult to be sure that the samples obtained are representative of the entire tumor.

2.3.1 Magnetic Resonance Imaging

Basic Principles.

Magnetic resonance imaging (MRI) is a medical imaging technique used in radiology to visualize detailed internal structures. MRI makes use of the property of nuclear magnetic resonance (NMR) to image nuclei of atoms inside the body. MRI imaging techniques are broadly classified into two types : Conventional and advanced magnetic resonance imaging techniques. MR imaging is the preferred technique for the diagnosis, treatment planning, and monitoring of patients with neoplastic Central Nervous System lesions. Conventional MR imaging, with gadolinium-based contrast enhancement, is increasingly combined with advanced,

functional MR imaging techniques to offer morphologic, metabolic, and physiologic information [22].

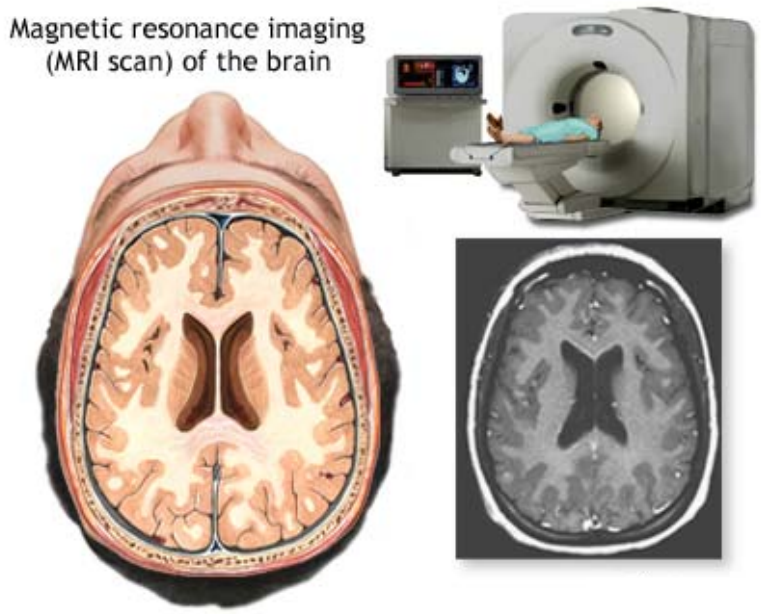

Fig. 2.5 An MRI (Magnetic resonance imaging) of the brain [3]

An MRI creates a three dimensional picture of the brain, which allows doctors to more precisely locate problems such as tumors. An MRI machine (Fig.2.5) uses a powerful magnetic field to align the magnetization of protons in the hydrogen atom present in the body, and radio frequency fields to systematically alter the alignment of this magnetization. This causes the protons to produce a rotating magnetic field of larger frequency detectable by the scanner and this information is recorded to construct an image of the scanned area of the body [23]. Strong magnetic field gradients cause hydrogen nuclei at different locations to rotate at different speeds. 3-D spatial information can be obtained by providing gradients in each direction.

MRI provides good contrast between the different soft tissues of the body, which makes it especially useful in imaging the brain, muscles, the heart, and cancers compared with other medical imaging techniques such as computed tomography (CT) or X-rays. Unlike CT scans or traditional X-rays, MRI uses no ionizing radiation.

2.3.1.1 Conventional MRIs

An MRI sequence is an ordered combination of radiofrequency (RF) and gradient pulses designed to acquire the data to form the image. The data to create an MR image is obtained in a series of steps. First the tissue magnetization is excited using an RF pulse in the presence of a slice select gradient. The other two essential elements of the sequence are phase encoding and frequency encoding (read out), which are required to spatially localize the protons in the other two dimensions. Finally, after the data has been collected, the process is repeated for a series of phase encoding steps. The MRI sequence parameters are chosen to best suit the particular clinical application.

The gradient echo (GE) sequence is the simplest type of MRI sequence. It consists of a series of excitation pulses, each separated by a repetition time TR. Data is acquired at some characteristic time after the application of the excitation pulses and this is defined as the echo time TE. The contrast in the image will vary with changes to both TR and TE. Advantages of this sequence are fast imaging, low Flip Angle and less RF power, where as the disadvantages are difficulty to generate good T2 contrast, sensitivity to in-homogeneities and sensitivity to susceptibility effects.

The spin echo (SE) sequence is similar to the GE sequence with the exception that there is an additional 180° refocusing pulse present. Inversion recovery (IR) sequence is usually a variant of a SE sequence in that it begins with a 180º inverting pulse. This inverts the longitudinal magnetization vector through 180º. When the inverting pulse is removed, the magnetization vector begins to relax back to 90º, and excitation pulse is then applied after a time from the 180º inverting pulse known as TI (time to inversion).

- The contrast of the resultant image depends primarily on the duration of the TI as well as TR and TE. The contrast in the image primarily depends on the magnitude of the longitudinal magnetization (as in spin echo) following the chosen delay time TI. Contrast is therefore based on T1 recovery curves following the 180º inversion pulse. Inversion recovery is used to produce heavily T1 weighted images to demonstrate anatomy. The 180º inverting pulse can produce a large contrast difference between fat and water because full saturation of the fat or water vectors can be achieved by utilizing the appropriate TI. In clinical practice, TE is always shorter than TR, A short TR value approximately equal to the average T1 value which is usually lower than 500 ms. A long TR is 3 times the short TR, which is normally greater than 1500 ms. A short TE is usually lower than 30 ms and a long TE = 3 times the short TE is greater than 90 ms

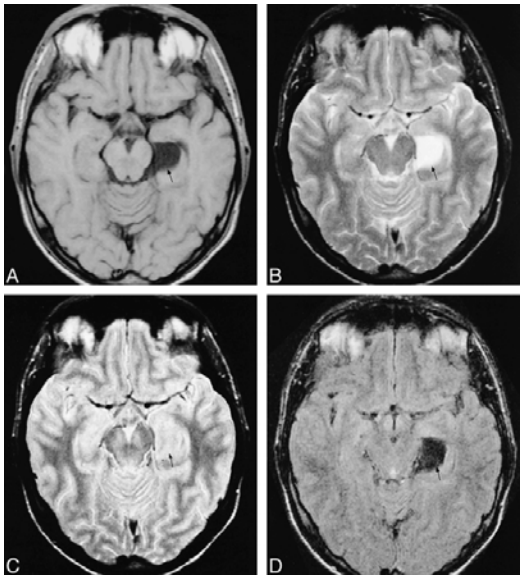

Fig.2.6 Conventional MR image slices(.a)T1–weighted (b) T2 – weighted (c) PD weighted (d) FLAIR [4]

a. Soft Tissue Contrast in MRI

Contrast is the means by which it is possible to distinguish among soft tissue types, based on the differences observed in the MRI signal intensities. For example, in musculoskeletal imaging, there is difference in intensities among cartilage, bone, and synovial fluid. In neuroimaging, there are differences between white and grey matter. The fundamental parameters that affect tissue contrast are the T1 and T2 values, proton density, tissue susceptibility and dynamics. Tissue pathology will also affect contrast, as will the static field strength, the type of sequences used, contrast media and the sequence parameters (TR, TE, TI, FA, SNR etc…)

b. T1 Weighting

To demonstrate T1, proton density and T2 contrast, specific values of TR and TE are selected for a given pulse sequence. The selection of appropriate TR and TE weights an image so that one contrast mechanism predominates over the other two. A T1 weighted image(Fig.2.6a) is one where the contrast depends predominantly on the differences in the T1 times between tissues e.g. fat and water. T1 is the longitudinal relaxation time. It indicates the time required for a substance to become magnetized after first being placed in a magnetic field or, alternatively, the time required for regaining longitudinal magnetization following an RF pulse. T1 is determined by thermal interactions between the resonating protons and other protons and other magnetic nuclei in the magnetic environment or "lattice". These interactions allow the energy absorbed by the protons during resonance to be dispersed to other nuclei in the lattice.

All molecules have natural motions due to vibration, rotation, and translation. Smaller molecules like water generally move more rapidly, thus they have higher natural frequencies. Larger molecules like proteins move more slowly. When water is held in hydration layers around a protein by hydrophilic side groups, its rapid motion slows considerably.

c. T2 -Weighting

T2 weighted image (Fig.2.6b) is one where the contrast predominantly depends on the differences in the T2 times between tissues e.g. fat and

water. T2 is the "transverse" relaxation time. It is a measure of how long transverse magnetization would last in a perfectly uniform external magnetic field. Alternatively, it is a measure of how long the resonating protons remain coherent or precess (rotate) "in phase" following a 90° RF pulse. T2 decay is due to magnetic interactions that occur between spinning protons. Unlike T1 interactions, T2 interactions do not involve a transfer of energy but only a change in phase, which leads to a loss of coherence.

T2 relaxation depends on the presence of static internal fields in the substance. These are generally due to protons on larger molecules. These stationary or slowly fluctuating magnetic fields create local regions of increased or decreased magnetic fields, depending on whether the protons align with or against the main magnetic field. Local field non-uniformities cause the protons to precess (rotate) at slightly different frequencies. Thus following the 90° pulse, the protons lose coherence and transverse magnetization is lost. This results in both T2* and T2 relaxation. The TE controls the amount of T2 decay that is allowed to occur before the signal is received. To achieve T2 weighting, the TE must be long enough to give both fat and water time to decay. If the TE is too short, neither fat nor water has had time to decay and therefore the differences in their T2 times are not demonstrated in the image.

d. Proton Density (PD) Weighting

A proton density image (Fig.2.6c) is one where the difference in the numbers of protons per unit volume in the patient is the main determining factor in forming image contrast. Proton density weighting is always present to some extent. In order to achieve proton density weighting, the effects of T1 and T2 contrast must be diminished, so that proton density weighting can dominate. A long TR allows tissues e.g. fat and water to fully recover their longitudinal magnetization and therefore diminishes T1 weighting. A short TE does not give fat or water time to decay and therefore diminishes T2 weighting. Figure 2-5 below shows a comparison of T1, T2, and PD weighting.

e. **FLAIR (Fluid Attenuate Invesion Recovery)**

It is another variation of the inversion recovery sequence. In FLAIR (Fig.2.6d), the signal from fluid (e.g. cerebrospinal fluid (CSF)) is nulled by selecting a TI corresponding to the time of recovery of CSF from 180º inversion to the transverse plane.The signal from CSF is nullified and FLAIR is used to suppress the high CSF signal in T2 and proton density weighted images so that pathology adjacent to the CSF is seen more clearly. A TI of approximately 2000 ms achieves CSF suppression at 3.0T.

f. Contrast agents (Gadolinium)

Although MRI is a very powerful imaging technique not all pathologies are clearly contrasted using only proton density or relaxation times weighting. For example, some meningiomas and small metastatic lesions do not show on normal imaging. And considering that some of these intra-cranial lesions have an abnormal vascular bed or a breakdown of the blood-brain barrier, a magnetic contrast agent that distributes throughout the extracellular space became an obvious choice to improve image contrast.

- All the common contrast agents used in MRI are Gadolinium chelates, which are not directly imaged but produce an effect, which is imaged. Gadolinium is the element of choice because of its high number of seven unpaired electrons. Each unpaired electron has a magnetic moment 657 times bigger than that of a proton, so seven unpaired electrons can induce relaxation a million times better than an isolated proton. This implies that both T1 and T2 are reduced, although the enhancement caused by the shortening of T1 is stronger than the signal loss caused by the shortening of T2; and that is why with Gadolinium contrast the images obtained are normally T1 weighted. The actual amount of T1shortening is dependent on the concentration of Gadolinium injected and the signal enhancement depends also on TE and TR.

2.3.1.2 Applications of MR Imaging in Neoplastic CNS Lesions

Conventional MR imaging is the technique of choice for differential diagnosis, tumor grading, and treatment planning of neoplastic CNS lesions. Alternative imaging modalities (CT, PET) under specific circumstances, are used as a complement to MR imaging. MR imaging represents the technique of choice

for visualizing and grading brain tumors. However, CT, with a lower resolution than MR imaging, does have applications in the emergency situations. The differential diagnosis of tumoral and pseudotumoral (mainly of inflammatory origin) lesions represents a pivotal step in patient assessment that directs subsequent management decisions. Identifying a tumoral lesion at imaging is followed typically by stereotactic biopsy or surgical resection for histologic confirmation. These represent a diagnostic challenge that may require biopsy for definitive diagnosis, which carries significant morbidity and may itself be non-diagnostic [25].

Conventional MR imaging, including T1-weighted, T2- weighted, and contrast-enhanced T1-weighted imaging, frequently provides imaging features that permit an accurate differential diagnosis between tumoral and pseudotumoral lesions in 50% of cases. It provides important information regarding contrast material enhancement, enhancement edema, distant tumor foci, hemorrhage, necrosis, mass effect, and so on, which are all helpful in characterizing tumor aggressiveness and hence tumor grade. It also readily provides evidence of contrast material enhancement, signifying blood-brain barrier breakdown, which is often associated with higher tumor grade. However, contrast material enhancement alone is not always accurate in predicting tumor [26].

Based on the patient's conventional MRI, a radiologist cannot differentiate whether it is a low grade glioma or a high grade glioma, because both of these are almost visually similar [26]. A biopsy is usually required to establish the diagnosis and subtype of a brain tumor and to plan appropriate treatment after conventional MR imaging. The most common conventional MRI modalities used to assess gliomas are Fluid Attenuated Inversion Recovery (FLAIR), T1 and T2-weighted modalities. T1-weighted modalities highlight fat tissues in the brain whereas T2-weighted modalities highlight tissues with higher concentration of water. FLAIR images are T2 or T1-weighted with the cerebrospinal fluid (CSF) signal suppressed. In general, edema, border definition and tumor heterogeneity are best observed on FLAIR and T2-weighted images [34].

Grade detection of glioma tumors is very important for taking clinical decisions regarding the treatment and for finding survival rates without doing biopsy. The major challenges are, tumor characterization is difficult, because the

neoplastic tissue is often heterogeneous with conventional MR imaging profile. The second thing is that, the external representation of tumor, which is shape, could not be taken as a discriminant feature for detection/ classification of grade/type of tumor because, the shape of each tumor is not consistent throughout all slices of MR image and may change quickly where the inter-slice distance is large. Advanced MR imaging modalities such as proton MR spectroscopic imaging (MRSI), perfusion-weighted imaging (PWI), and diffusion-weighted imaging (DWI) have been proposed as alternate methods for differential diagnosis of tumors and non tumor lesions, primary versus metastatic lesions and tumor grading [26-28].

2.3.1.3 Clinical Practice of Brain Tumor Imaging

The clinical practice of imaging patients with a suspected brain tumor is a standardized MRI protocol. MRI images are commonly viewed in three planes: axial, coronal, and sagittal as shown Fig. 2.7. Seven different MR sequences are performed to provide a complete MRI data set for one patient. The different sequence properties are shown in Table 2-1.

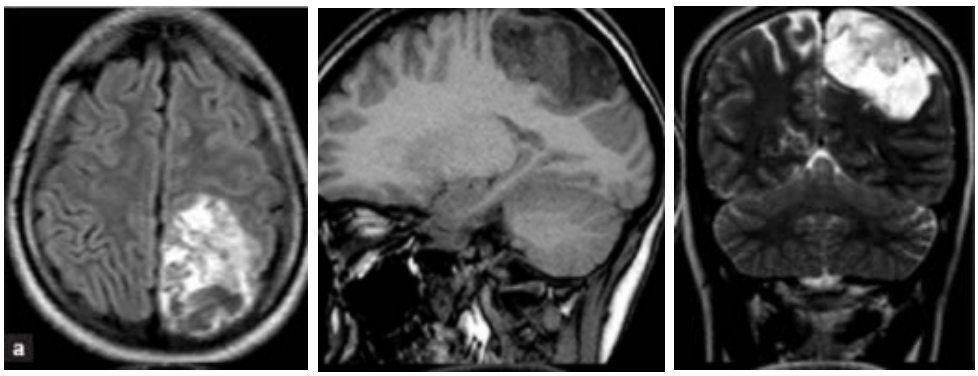

(a) (b) (c)

Fig.2.7 shows MRI views in three planes a) Axial (b) Sagittal (c) Coronal

Table 2-1: MRI scan protocol for brain tumor patients [35]

Anatomical plane	Weighting	Contrast	Slice thickness / Spacing between slices
Sagittal -	T1-weighted	Nil	5 mm / 6 mm
Axial	T1-weighted	Nil	4 mm / 4 mm
Axial	T2-weighted	Nil	5 mm / 6 mm
Axial-	T2-weighted FLAIR	Nil	5 mm / 6 mm
Axial	T1-weighted	Gadolinium	4 mm / 4 mm
Coronal	T1-weighted	Gadolinium	4 mm / 4 mm
Sagittal	T1-weighted	Gadolinium	5 mm / 6 mm

Twenty slices were acquired for each anatomical plane with TR/TE 2000/45 ms, matrix size 128×128, pixel spacing 1.5×1.5 mm, slice thickness 5.0mm. T1-weighted images are first taken without and then with contrast agent (gadolinium). These images show hyperintense and irregular tumor margins. Surrounding low-signal components correspond to the surrounding brain tissue that is often diffusely infiltrated by tumor cells. Hyperintense tissue that appears in both image types is related to recent bleeding and the tissue that appears hyperintense in T1-weighted contrast enhanced images only, is considered to be malignant tumor [3, 21].

On T2-weighted images the solid part shows hyper intense characteristics [20, 21]. Edema around the tumor shows less hyper-intense signal than the solid tumor part but more intense signal than healthy brain tissue. Both T2-weighted with and without FLAIR can be used to identify edema.

To separate CSF from edema, T2-weighted FLAIR sequences are preferred since the CSF shows no signal. Tumor necrosis is often located in the tumor center. On T2- and T1-weighted images necrosis appears hyper-intense and hyper-iso or hypo-intense, respectively [22-24].

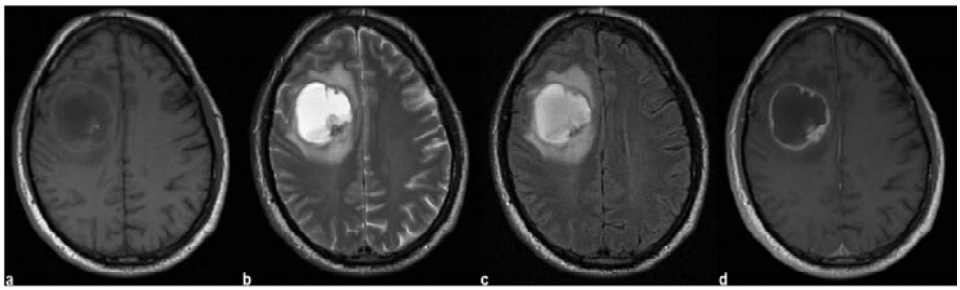

Fig. 2.8 MR images of a glioblastoma: (a) T1-weighted (b) T2-weighted (c) T2-weighted FLAIR (d) and T1-weighted contrast enhanced [35]

Fig. 2.8 shows a glioblastoma in the left temporal lobe acquired in a 1.5 T MRI scanner. A solid mass lesion with edema around the tumor is distinguishable. Fig. 2.8(a) and (b) are T1-weighted and T2-weighted, respectively. A large tumor area consists of necrosis (hypo- and hyper-intense regions on T1- and T2-weighted images, respectively). The edema around the tumor can be identified on the T2-weighted or T2-weighted FLAIR (2.8(c)) images, where it appears hypointense in relation to the bright necrosis. In comparison to the T2-weighted, the CSF on the T2-weighted FLAIR has no hyperintense characteristics. Fig. 2.8d shows the tumor after gadolinium contrast medium application. The tumor borders are well enhanced and the necrosis inside the bright borders is noticeable [23].

Fig.2.9 shows the MR images of low grade glioma. Fig.2.9 (a) shows T1 pre-contrast image and contrast enhanced low grade glioma is shown in Fig.2.9(c). From the pre and post contrast images, it can be observed that there is no significant intensity variations for tumor necrosis. Usually low grade gliomas are non-enhancing tumors and high grade gliomas are enhancing type. But some low grade more edema will be enhanced by applying contrast agent. Hence this factor alone cannot be taken as a factor for grade detection. Although these images are considered 'typical', numerous studies have questioned the reliability and accuracy of these imaging characteristics for the diagnosis of low-grade glioma.

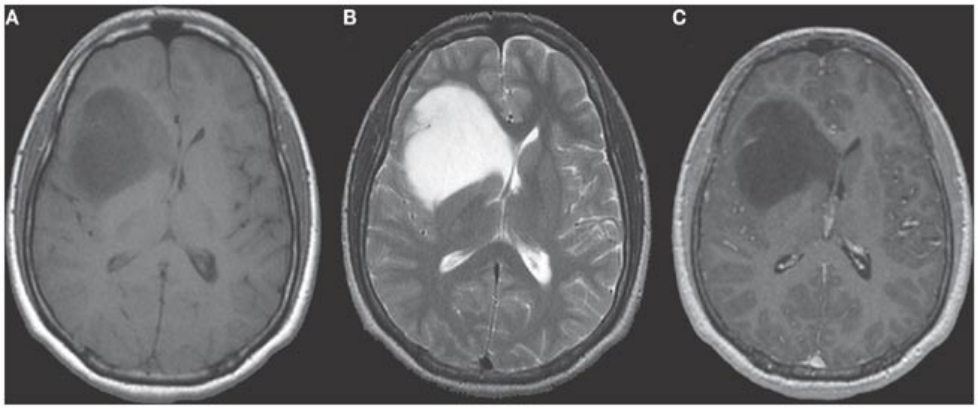

Fig. 2.9 Typical MRI scan of a low-grade glioma [4]
(**a**) T1 sequence demonstrating T1 shortening in the right frontal lobe. (**b**) T2 sequence demonstrating T2 prolongation (hyper intensity) at the site of the glioma. (**c**) Contrast-enhanced imaging of the glioma showing no marked contrast enhancement.

2.3.1.4 MR Image Representation

MR images are grids of pixels with ***M*** rows and ***N*** columns. Every pixel of an MR image corresponds to a voxel, a volume element, whose values represents v(x,y,z). The volume of a voxel depends on MR scan parameters, i.e. slice thickness and pixel spacing. MR images are usually delivered in DICOM (Digital Imaging and Communications in Medicine) format. Besides the MR image, DICOM-files contain information about the MR scan and patient. Normally an MR scan acquires more than one slice, which leads to an image sequence ***MxNxK*** with ***K*** slices as shown in Fig. 2.10. The size of the shown image sequence is ***512 x 512 x 9.*** The spacing between slices is 5.5 mm [34].

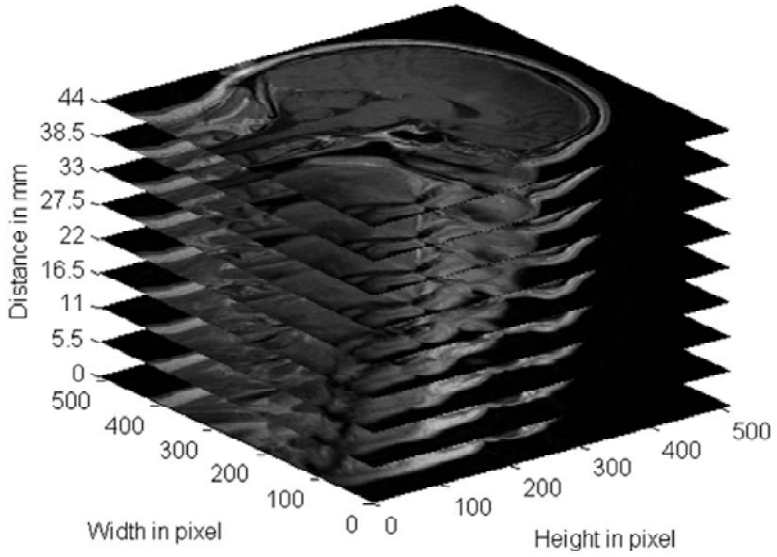

Fig. 2.10 An MR image sequence with 5.5 mm spacing between slices [4]

2.3.2Advanced MRI scans

Advanced MR imaging techniques provide s new methods for the assessment of brain tumors. Various advanced imaging techniques are summarised below.

2.3.2.1 Magnetic resonance spectroscopy

Magnetic resonance spectroscopy (MRS), also known as MRSI (MRS Imaging) and Volume Selective Nuclear Magnetic Resonance (NMR) Spectroscopy, is a technique which combines the spatially-addressable nature of MRI with the spectroscopically-rich information obtainable from nuclear magnetic resonance (NMR). That is to say, MRI allows one to study a particular region within an organism or sample, but gives relatively little information about the chemical or physical nature of that region--its chief value is in being able to distinguish the properties of that region relative to those of surrounding regions.

MR spectroscopy, however, provides a wealth of chemical information about that region, as would an NMR spectrum of that region [25,26].

2.3.2.2 Functional MRI

Functional MRI (fMRI) measures signal changes in the brain that are due to changing neural activity. The brain is scanned at low resolution but at a rapid rate (typically once every 2-3 seconds). Increase in neural activity cause changes in the MR signal via a mechanism called the BOLD (blood oxygen level-dependent) effect. Increased neural activity causes an increased demand for oxygen, and the vascular system actually overcompensates for this, increasing the amount of oxygenated hemoglobin ("haemoglobin" in British English) relative to deoxygenated hemoglobin. Because deoxygenated hemoglobin reduces MR signal, the vascular response leads to a signal growth that is related to the neural activity. The precise nature of the relationship between neural activity and the BOLD signal is a subject of current research. The BOLD effect also allows for the generation of high resolution 3D maps of the venous vasculature within neural tissue. Likewise, MRI can—within minutes— noninvasively acquire functional images in any plane or volume at comparatively high resolution. Functional MRI (fMRI) can image the hemodynamic and metabolic changes that are associated with human brain functions, such as vision, motor skills, language, memory, and mental processes. These techniques have also revolutionized detection of a wide variety of disease states, such as stroke, multiple sclerosis, and tumors [27].

2.3.2.3 Diffusion MRI

Diffusion MRI measures the diffusion of water molecules in biological tissues. Following an ischemic stroke, brain cells die, trapping water molecules inside them (cellular pumps are no longer functioning). The resultant areas of *restricted diffusion* are detectable by diffusion weighted imaging (DWI). This finding is identifiable much earlier after a stroke than findings on CT or on conventional MRI, making DWI one of the most sensitive methods for the detection of early stroke [28].

Diffusion MRI (Fig.2.11) is also a tool to study connections in the brain. In an isotropic medium (inside a glass of water for example) water

molecules naturally move according to Brownian motion. In biological tissues however the diffusion is very often anisotropic.

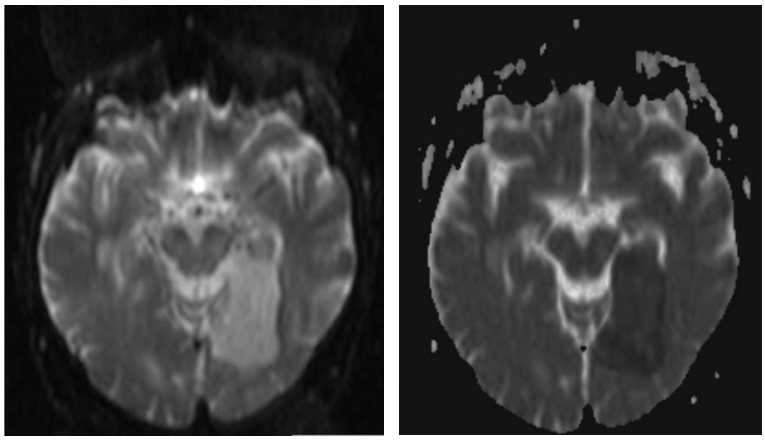

Fig. 2.11 Diffusion weighted Imaging (DWI) slices [23]

For example a molecule inside the axon of a neuron has a low probability to cross a myelin membrane. Therefore the molecule will move principally along the axis of the neural fiber. Conversely, if we know that molecules locally diffuse principally in one direction we can make the assumption that this corresponds to a set of fibers. Diffusion MRI for this application is still at the research stage. Identifying fibers on diffusion MRI is called tractography [29].

DWI is sensitive to motion on the order of tens of micrometers, even locations not commonly noted for motion, such as the brain, move orders of magnitude more than the diffusive motion under investigation, and such motions can corrupt image quality. This effect can mimic increased diffusivity and yield diffusion coefficients that are higher than the true underlying values [30].

2.3.2.4 Diffusion-Tensor Imaging

Diffusion-tensor MR imaging (Fig.2.12) is a technique that has been developed more recently than isotropic (trace-weighted) DW imaging. Typical diffusion-tensor imaging techniques sample water motion in at least six non-

collinear directions (rather than in the three directions used in isotropic DW imaging), which provide information about both the rate and the direction of water motion. Diffusion-tensor imaging has shown applicability for a number of disease states owing to the fact that normal-brain white matter is highly structured, and fiber tracts impart a strong orientational bias toward microscopic water diffusion. The tendency for water molecules to diffuse in some directions rather than equally in all directions is termed “anisotropy.” Highly compact white matter fiber tracts exhibit a high degree of anisotropy, and less compact white matter pathways exhibit lesser degrees of anisotropy. All types of white matter typically show greater degrees of anisotropy than are seen in gray matter structures, which have a low degree of anisotropy. Thus, diffusion-tensor imaging provides a sensitive means to detect alterations in the integrity of white matter structures. In fact, in many settings,

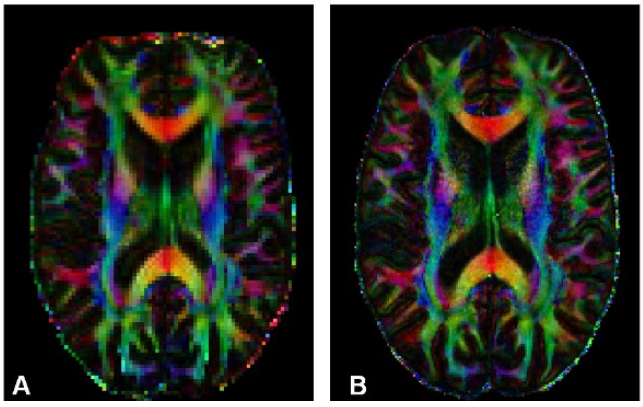

Fig.2.12 Diffusion Tensor Imaging (DTI) slices [31]

white matter abnormalities can be seen on diffusion- tensor images that are not evident on routine MR images [28] Diffusion- tensor imaging also provides a means of depicting white matter pathways (tractography), which may be useful for providing guidance in neurosurgical procedures by preoperatively depicting important white matter tracts. It also helps to determine infiltration of white matter tracts by tumor, and provides evidence of degeneration of white matter tracts proximal to tumor sites (ie, wallerian degeneration) [31].

2.3.2.5 Perfusion-weighted MRI

Perfusion-weighted MRI (PWI) is an evolving MRI technology for studying cerebral hemodynamics and blood flow (Fig.2.13). Hemodynamic maps of cerebral blood flow (CBF), cerebral blood volume (CBV), and mean transit time (MTT) can be created using PWI. These maps are based on mathematical analysis of the evolution of the intensity of the T2-weighted gradient or spin echo images after a gadolinium bolus administration or by using "labeled" water protons as endogenous, freely diffusible tracers. The advantages of these PWI techniques are their high resolution and non invasive nature compared with PET or CT based methods. PWI can be combined with other MRI techniques such as magnetic resonance angiography (MRA) to assess vessel patency and with DWI to assess ischemic injury. Several problems remain, however, regarding the use of PWI to non invasively quantify CBF and MTT in pathological states. The problems relate to the difficulty of measuring brain density and plasma hematocrit in pathological states and obtaining a value for the relaxivity of gadolinium contrast agent across a range of blood vessel sizes. Other pitfalls include the difficulty of measuring the arterial input function close to the voxel of interest, delay and dispersion of the contrast bolus [32].

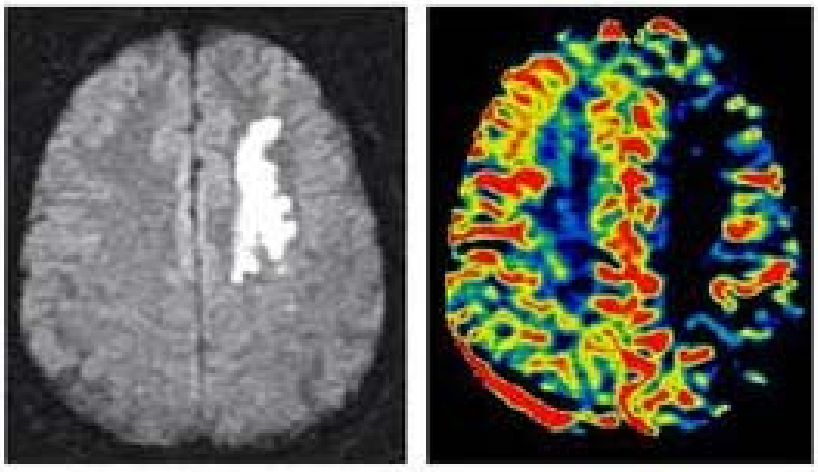

Fig.2.13 Perfusion weighted Imaging (PWI) [32]

These advanced MRIs are providing insights into tumor behavior that are not available from conventional MR imaging and will likely be more important for assessment of tumor response to therapy than for diagnosis. DWI may allow the cellularity of tumors to be graded noninvasively; because cells constitute a relative barrier to water diffusion, compared with extra cerebral space, tumors that are more cellular would be expected to show less of an increase in ADC than tumors that are less cellular. Studies of patients with brain tumors have shown that increases in water diffusion generally indicate positive response to therapy.

2.3.3 Noise in MR Imaging

Many image acquisition procedures (MRI, PET, SPECT, etc.) suffer from image degradation by noise. For Magnetic Resonance Imaging the primary source of random noise is thermal noise which forms a statistically independent random source entering the MR data in the time domain. Thermal noise is white and can be characterized by a Gaussian random field with zero mean and constant variance [33]. Hence the noise is not correlated with the signal or with itself. Apart from thermal noise, structured noise usually degrades the image quality as well due to MR system characteristics, physiological pulsations or object motion. The characteristics of noise depend on its source, as does the operator which reduces its effects. Noise, inhomogeneous pixel intensity distribution and blunt boundaries in the medical MR images caused by MR data acquisition process are the main problems that will affect the quality of MRI segmentation [33]. One principal source of noise is the ambient electromagnetic field picked up by the radiofrequency (RF) detectors acquiring the MR signal, and another is the object or body being imaged

In MRIs, raw data is intrinsically complex valued and corrupted with zero mean Gaussian distributed noise with equal variance. After inverse Fourier transformation, the real and imaginary images are still Gaussian distributed, given the orthogonality and linearity of the Fourier transform. MR magnitude images are formed by simply taking the square-root of the sum of the square of the two independent Gaussian random variables (real and imaginary images) pixel by pixel. After this nonlinear transformation, MR magnitude data can be shown to be Rician distributed.

In MRI, there is a trade off between signal-to-noise ratio (SNR), acquisition time and spatial resolution. The SNR is relatively high in most MRI applications, and this is accomplished implicitly and explicitly by averaging. The MRI data acquisition process can be affected by two averaging techniques: (1) Spatial volume averaging is required due to the discrete nature of the acquisition process and (2) In the case of some applications, the signal for the same k-space location is acquired several times and averaged in order to reduce noise.

The two averaging methods are interconnected. When a higher sampling rate of the frequency domain is used, higher resolution images are obtained. However, in order to receive a desired SNR at high spatial resolution a longer acquisition time is required, as additional time necessary for averaging. Conversely, the acquisition time, with the subsequent SNR and the imaging resolution, are practically limited by the patient comfort and the system throughput. Consequently, high SNR MRI images can be acquired at the expense of constrained temporal for spatial resolution. Also, high resolution MRI imaging is achievable at a cost of lower SNR for longer acquisition times.

Another important source of noise in MRI imaging is thermal noise in the human body. Common MRI imaging involves sampling in the frequency domain (also called "k-space"), and taking Inverse Discrete Fourier Transform. Signal measurements have components in both real and imaginary channels and each channel is affected by additive white Gaussian noise. Thus, the complex reconstructed signal includes a complex white additive Gaussian noise. Due to phase errors, usually the magnitude of the MRI signal is used for the MRI image reconstruction. The magnitude of the MRI signal is real-valued and is used for the image processing tasks, as well for visual inspection [34,35].

The way the magnitude MRI image is reconstructed results in a Rician distribution of noise. Since the Rician noise is signal-dependent, separating the signal from the noise is a very difficult task. In high intensity areas of the magnitude image, Rician distribution can be approximated to a Gaussian distribution, and in low intensity regions it can be estimated as a Rayleigh distribution. A practical effect is, a reduced contrast of the MRI image, as the noise increases the mean intensity values of the pixels in low intensity regions also increases. As explained, it is a fact that Rician noise degrades the MRI images in

both qualitative and quantitative senses, making image processing, interpretation and segmentation more difficult. Consequently, it is important to develop an algorithm to remove this type of noise.

2.3.3.1 Different Noise Models

Noise modeling in images is affected by capturing instrument, data transmission media, image quantization and discrete source of radiation.

a. Gaussian Noise

Gaussian noise is statistical noise that has a probability density function (abbreviated pdf) of the normal distribution (also known as Gaussian distribution). In other words, the values that the noise can take on are Gaussian-distributed. It is most commonly used as additive white noise to yield additive white Gaussian noise (AWGN). Gaussian noise is properly defined as the noise with a Gaussian amplitude distribution. This says nothing of the correlation of the noise in time or of the spectral density of the noise. Labeling Gaussian noise as 'white' describes the correlation of the noise. It is necessary to use the term "white Gaussian noise" to be correct. In Magnetic Resonance Images, raw data is intrinsically complex valued and corrupted with zero mean Gaussian distributed noise with equal variance. After inverse Fourier transformation, the real and imaginary images are still Gaussian distributed given the orthogonality and linearity of the Fourier transform. MR magnitude images are formed by simply taking the square-root of the sum of the square of the two independent Gaussian random variables pixel by pixel.

MR images are corrupted by Rician noise, which arises from complex Gaussian noise in the original frequency domain measurements [36]. The Rician probability density function for the corrupted image intensity x is given by Eqn.4.19

$$p(x) = \frac{x}{\sigma^2} exp(-\frac{x^2+A^2}{2\sigma^2})\, I_0\, (\frac{xA}{\sigma^2}) \qquad (4.19)$$

where A is the underlying true intensity, σ is the standard deviation of the noise, and I_0 is the modified zeroth order Bessel function of the first kind.

b.Speckle noise

A different type of noise in the coherent imaging of objects is called speckle noise. This noise is, in fact, caused by errors in data transmission [36]. This kind of noise affects the ultrasound images [33]. Speckle noise follows a gamma distribution and is given as Eqn.4.20

$$F(g) = [\frac{g^{\alpha-1}}{(\alpha-1)!a^{\alpha}} e^{\frac{g}{a}}] \quad (4.20)$$

where, a^2 is the variance, $\propto$ is the shape parameter of gamma distribution and g is the gray level. Speckle noise is a granular noise that inherently exists in and usually degrades the quality of the active radar and synthetic aperture radar (SAR) images and can also be present in MR images..

2.3.4 Partial volume effect

The partial volume effect (PVE) is the consequence of the limited resolution of the scanning hardware and the discretization procedures. It occurs in non-homogeneous areas, where several anatomic entities contribute to the gray level intensity of a single pixel/voxel. It results in blurred intensities across edges, making difficult the task of accurately deciding on the borders of two connected objects. An example of this type of artifact is the fat/water cancelling and emerging in regions containing both fat and water. Due to their opposing magnetization fields, the corresponding regions will appear dark [34].

Segmentations that allow regions or classes to overlap are called *soft segmentations*. Soft segmentations are important in medical imaging because of *partial volume effects*, where multiple tissues contribute to a single pixel or voxel resulting in a blurring of intensity across boundaries. Fig.2.14 illustrates how the sampling process can result in partial volume effects, leading to ambiguities in structural definitions. In Fig.2.14, it is difficult to precisely determine the boundaries of the two objects.

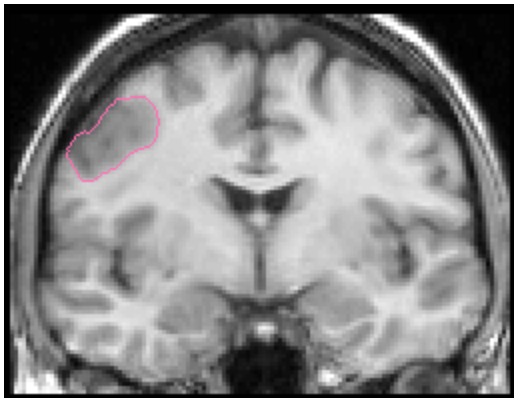

Fig. 2.14 A common example of Partial volume effect [7]

A *hard segmentation* forces a decision of whether a pixel is inside or outside the object. Soft segmentations on the other hand, retain more information from the original image by allowing uncertainty in the location of object boundaries. Note that the point spread function of an imaging device can be larger than the spatial extent of a single pixel or voxel. Thus, partial volume effects can cause boundaries to be blurred across significant portions of an image.

2.3.5 Intensity in-homogeneities

Another difficulty which has to be handled by segmentation techniques using MR images is the intensity in-homogeneities shortcoming. The intensity in-homogeneities can be caused by the imperfections in the RF coil that produces the magnetic field, or by various defects in the signal acquisition procedures. Also, the magnetic field can have a non-uniform distribution due to the local magnetic properties of the biological structure or because of a movement of the patient during the acquisition process. This effect can be identified as a shading artifact in the image data and can have a major consequence on the performances of the intensity based segmentation algorithms, considering that a certain tissue has a constant intensity distribution in the dataset [35].

Conclusions

The materials included in this chapter give primary information for the subsequent discussions of brain anatomy, Glioma, grades, MRI sequences giving basic idea about brain anatomy, tumor and the imaging techniques. This chapter also provides a basic idea about the extent to which the conventional MR imaging techniques are useful for grade detection and visualization of glioma tumors. The different imaging modalities and the different factors which affect the quality of MR image are also presented.

References

[1] www.abta.org -- American Brain Tumor Association

[2] www.cbtf.org -- Children's Brain Tumor Foundation

[3] www.virtualtrials.com -- Musella Foundation for Brain Tumor Research and Information

[4] www.braintumor.org -- National Brain Tumor Society

[5] www.neurosurgery.org -- American Association of Neurologic Surgeons

[6] www.cancer.org -- American Cancer Society

[7] www.cancer.gov -- National Cancer Institute

[8] www.asco.org -- American Society for Clinical Oncology

[9] www.cancer.gov/clinicaltrials -- Find clinical trials

[10] www.cancer.net -- Cancer.Net

[11] A. Michotte, Adamson C, Kanu OO, Mehta AI, Di C, Lin N, Mattox AK, et al. Glioblastoma multiforme: a review of where we have been and where we are doing. *Expert Opin Investig Drugs, vol.*18(8):pp.1061-83.(2009).

[12] D.C Bowers, Y Liu, W Leisenring, et al. Late-occurring stroke among long-term survivors of childhood leukemia and brain tumors: a report from the Childhood Cancer Survivor Study. *J Clin Oncol*, vol.24(33):pp.5277-82.(2006).

[13] J.C Buckner, P D Brown, O'Neill BP, Meyer FB, Wetmore CJ, Uhm JH. Central nervous system tumors. *Mayo Clin Proc, vol.*82(10):pp.1271-86.(2007).

[14] Chandana SR, Movva S, M Arora, et.al, Primary brain tumors in adults. *Am Fam Physician*, vol. 77(10):pp.1423-30.(2008).

[15] O O. Kanu, A Mehta, C Di, et al. Glioblastoma multiforme: a review of therapeutic targets. *Expert Opin Ther Targets*, vol.13(6):pp.701-18.(2009).

[16] D Krex, B Klink, C Hartmann, et al. Long-term survival with glioblastoma multiforme. *Brain, vol.*130(10):pp.2596-2606. (2007).

[17] D A Mitchell, J H Sampson. Toward effective immunotherapy for the treatment of malignant brain tumors. Neurotherapeutics, *vol.* 6(3):pp.527-538.(2009).

[18] P.C Nathan, S.K Patel, K Dilley, et al. Guidelines for identification of, advocacy for, and intervention in neurocognitive problems in survivors of childhood cancer: a report from the Children's Oncology Group. Arch Pediatr Adolesc Med, vol.161(8):pp.798-806,(2007).

[19] National Comprehensive Cancer Network. NCCN Clinical Practice Guidelines in Oncology: Central nervous system cancers. Vol.(2).(2009).

[20] S Sathornsumetee, D A Reardon, A Desjardins, et.al. Molecularly Targeted Therapy for malignant glioma. Cancer, vol.110(1):pp.13-24.(2007).

[21] R Stupp, F Roila; ESMO Guidelines Working Group. Malignant glioma: ESMO clinical recommendations for diagnosis, treatment and follow-up. Ann Oncol, vol.20(4):pp.126-128.(2009)

[22] Wen PY, Kesari S. Malignant Gliomas in adults. N Engl J Med, vol.359(5):pp.492-507, (2008).

[23] www.radiologyinfo.org -- RadiologyInfo

[24] M. Essig, N. Anzalone , S.E. Combs, et.al. 'MR Imaging of Neoplastic Central Nervous System Lesions: Review and Recommendations for Current Practice. AJNR Am J Neuroradiol,vol 33:pp. 803–17 May 2012

[25] W. Bian, I. S. Khayal, J. M. Lupo, et.al, Multiparametric Characterization of Grade 2 Glioma using magnetic Resonance Spectroscopic, perfusion, and Diffusion Imaging, Translational Oncology. Vol.2(4) pp.271-280, (2009)

[26] N. Bulakbasi, M. Kocaoglu, A. Farzaliyev et al. Assessment of Diagnostic Accuracy of Perfusion MR Imaging in Primary and Metastatic Solitary Malignant Brain Tumors, Am J Neuroradiol. Vol. 26(9) pp.2187–2199, (2005)

[27] J. M. Provenzale, , S. Mukundan,, P Daniel, et.al Diffusion-weighted and Perfusion MR Imaging for Brain Tumor Characterization and Assessment of Treatment Response Special Review Radiology, vol. 239(3): pp.632-649, (2006).

[28] Neuroimaging and Dissociative Disorders,Angelica Staniloiu1,2,3, Irina Vitcu3 and Hans J. Markowitsch, Chapter 2 Text book on Advances in Brain Imaging, Edited by Vikas Chaudhary, (2012).

[29] M. Law, S. Yang, H. Wang, et.al Glioma Grading: Sensitivity, Specificity, and Predictive Values of Perfusion MR Imaging and Proton MR Spectroscopic Imaging Compared with Conventional MR Imaging AJNR Am J Neuroradiol, vol.24:pp.1989–1998. (2003).

[30] J. M. Provenzale,S. Mukundan, D. P. Barboriak, Diffusion-weighted and Perfusion MR Imaging for Brain Tumor Characterization and Assessment of Treatment Response, Radiology**:** Volume 239, Number 3, June 2006.

[32] S.cha, Update on Brain Tumor Imaging: From Anatomy to physiology, Am J Neuroradiol, vol. 27 pp.475-87, (2006)

[33] J. Sijbers, P. Scheunders,N. Bonnet,D. Van Dyck, E. Raman. Magnetic Resonance Imaging, Vol. 14, Nr. 10, p. 1157-1163, (1996).

[34] M. V. Sarode, P. R. Deshmukh, Performance Evaluation of Rician Noise Reduction Algorithm in Magnetic Resonance Images, Journal of Emerging Trends in Computing and Information Sciences Volume 2 Special Issue ISSN 2079-8407 2010-11

[35] F. Balsiger, Brain Tumor Volume Calculation Segmentation and Visualization Using MR Images, Department of Biomedical Engineering, Bachelor Thesis, University of Applied Sciences and Arts of Northwestern Switzerland, Switzerland, July 2012.

[36] B. Shinde, D. Mhaske, M. Patare, A.R. Dani. Apply Different Filtering Techniques To Remove The Speckle Noise Using Medical Images. International Journal of Engineering Research and Applications (IJERA) vol. 2(1): pp.1071-1079.(2012).

Chapter 3

Biomedical Image Segmentation and Statistical Texture Classification Techniques – An Overview

Automatic Segmentation or extraction of tumor, tumor boundary, grey matter and white matter are the first stage of the proposed computer aided system for grade detection and 3D modeling of glioma. Texture based grade detection of glioma from segmented 2D slices using statistical features is the second stage of this system. In this chapter, we discuss the state of art approaches used in medical image segmentation including brain images and texture classification/detection of different pathological structures. The chapter gives a qualitative comparison, by pointing out the advantages and the disadvantages of these approaches. A review of validation techniques for various segmentation approaches are also discussed here.

3.1 Introduction

Accurate Segmentation of pathological structures is a crucial step in computer assisted grading and detection of glioma tumors. This chapter provides an overview of different approaches for segmentation of anatomical structures in brain MR images, and other modalities. With the increasing size and number of medical images, the use of computers in facilitating their processing and analysis has become necessary. In particular, computer algorithms for the delineation of anatomical structures and other regions of interest are a key component in assisting and automating specific radiological tasks. These algorithms, called image segmentation algorithms, play a vital role in numerous biomedical imaging applications such as the quantification of tissue volumes [1], diagnosis [2], localization of pathology [3], study of anatomical structures [1], treatment planning [4], partial volume correction of functional imaging data [5], and computer integrated surgery [6,7]. Methods for performing segmentations vary widely depending on the specific application, imaging modality, and other factors. For example, the segmentation of brain tissue has different requirements from the segmentation of the liver. General imaging artifacts such as noise, partial volume effects, and motion can also have significant consequences on the performance of segmentation algorithms.

As discussed in chapter 2, shape of pathological structures cannot be used as a feature for classification/detection process because of inconsistencies in shapes. Hence texture base classification/ detection are preferred in medical image analysis. Section 3.6 details a brief overview of various texture based classification techniques available in literature.

3.2 Image enhancement and Segmentation

The principal objective of image enhancement is to process an image so that the result is more suitable than the original image for a specific application. That means, the enhancing methods are different for different application; for example the approach used for enhancing X-ray image may not necessarily be the method used for MR image or satellite image. Usually enhancing an image is related to its visual evaluation of image quality. Image enhancement approaches

fall into two broad categories viz. spatial domain methods and frequency domain methods. Spatial domain refers to image plain itself, i.e., direct manipulation of pixels in an image. Frequency domain processing techniques are based on modifying Fourier transform of an image.

Low level methods of image processing, i.e., procedures and algorithms that are performed without prior knowledge about the specific content of an image, are mostly applied to pre- or post-processing of medical images. Traditionally, the purpose of segmentation is to partition the image into non-overlapping, constituent regions (or called classes, clusters, subsets or sub-regions) that are homogeneous with respect to intensity and texture [8].

3.3 Literature Review of Segmentation Methods

This review describes several common approaches that have appeared in the recent literature on medical image segmentation. We define each method, provide an overview of how the method is implemented, and discuss its advantages and disadvantages. Although each technique is described separately, multiple techniques are often used in conjunction with one another for solving different segmentation problems. The segmentation methods are divided into nine categories: (1) Intensity thresholding algorithms, (2) Region growing and split and Merge algorithms, (3) clustering approaches,(4) artificial neural networks (5) Markov random field models, (6)deformable models, (7) atlas guided approaches, (8)Watershed Methods, and (9) Level set methods. Other notable methods that do not belong to any of these categories are described in section 3.3.10.

3.3.1 Intensity thresholding algorithms

Thresholding is one of the oldest and easiest segmentation technique for scalar images and volumes [8]. Mainly, it takes into account only the intensity value of the pixels or voxels and creates a binary partition of the dataset. Single-threshold algorithms use only one intensity value, called threshold, which separates the dataset into two classes as follows: intensities higher than the threshold are clustered in one class and the rest of the pixels (voxels) are clustered in the other class.

When the analyzed dataset contains more than 2 classes, a multi-thresholding algorithm [8] has to be applied. It assumes that images are composed of regions with different gray level ranges, the histogram of which can be separated into a number of peaks (modes), each corresponding to one region and there exists a threshold value corresponding to the valley between the two adjacent peaks. A thresholding procedure determines an intensity value, called the threshold, which separates the desired classes. In case the dataset (image or volume) has to be clustered into *n* different classes, *n - 1* thresholds have to be applied.

The difficult task is to determine the threshold values which best differentiate the regions of interest. A simple case is the one in which the structures to be clustered have contrasting intensity values (or other features). Practically, the resulting segmentation is very sensitive to the used thresholds, which may be affected by the noise and intensity in-homogeneities (present in MRI images). Another important drawback of the approach is that it does not take into consideration the spatial distribution of the intensities. However, this method can be implemented in real-time and it is often used as an initialization step and can be combined with other segmentation techniques [9, 10]. It has been used in digital mammography, in which two classes of tissue are typically present healthy and tumorous [11, 12]. When the interested structures have distinctive quantifiable features, threshold-based algorithms are effective. Threshold-based algorithms do not need complex operations and are computationally efficient. Due to the noise influence and partial volume effect, the edges of organs or structures in medical images are usually not clearly defined and therefore algorithms based on threshold are seldom used alone [13]

Adaptive thresholding is an approach which aims to improve the performance of the algorithm in images corrupted by noise and intensity in-homogeneities (MRI images). Also called local or dynamic thresholding methods [14], they compute a distinct threshold for each pixel or voxel based on the local image properties. Kittler et al. [15] used the image statistics based on the gradient magnitude for the selection of an automatic threshold, while Kom et.al [16] applied adaptive threshold in order to segment dense masses in mammograms. Other medical image segmentation applications include extracting edges and maintain only the ones which respect some predefined similarity criteria [17] for segmenting

blood vessels [18], extracting anatomical structures in MR images [19] and endoscopic images [20] or 3D bone segmentation in CT scans [21]. Adaptive liver segmentation from CT using supervised thresholding and k-means clustering [22], anatomical region segmentation using supervised pixel level segmentation [23] are also discussed in literature. A survey on thresholding techniques is provided by R.B. Dubey, et.al and Z.Ma,et.al [24, 25].

3.3.2 Region growing and Split and Merge algorithms

The region growing method is a well-developed technique for image segmentation. It is a technique for extracting an image region that is connected, based on some predefined criteria. These criteria can be based on intensity information or edges in the image [26]. Compared to the thresholding techniques, it includes information related to the neighborhood configuration and it is designed to extract homogeneous regions which have higher probability to correspond to anatomical structures. It requires at least one seed point for each object to be segmented, which is used to select all the belonging pixels or voxels based on the homogeneity criteria. Therefore, the main disadvantage is that it requires manual intervention and is very sensitive to initialization. Results of region growing algorithms are highly influenced by noise and partial volume effects (specific for MRI images). Zhang et. al [27] used region growing as a post-processing step for the 3D adaptive thresholding of the CT images. Also, CT angiographic image segmentation has been realized using gradient based region growing [28]. Region growing has been improved by including topological information for 3D MRI cortex segmentation [29] or by adapting the algorithm to the fuzzy sets theory [30].

Split and merge algorithms are similar to region growing, but they overcome the need of seed points [31]. Similarly based on a predefined criterion, it successively splits the regions into a certain number of sub regions, and merges only the ones which satisfy the required conditions. The main drawback of this algorithm is that it requires a pyramidal grid structure of the dataset, which makes it very computationally expensive and undesirable for the huge array of data nowadays. Region growing is seldom used alone but usually within a set of image processing operations, particularly for the delineation of small, simple structures such as tumors and lesions [32, 33]. Segmentation of low grade glioma tumors by eliminating partial volume effect in brain using advanced gradient magnitude

region growing technique is proposed by S.Madhu kumar, et.al [34]. Its main limitations is that it requires manual interaction to obtain the seed point. Thus, for each region that needs to be extracted, a seed must be planted. Region growing can also be sensitive to noise, causing extracted regions to have holes or even become disconnected. These problems can be removed using a homotopic region-growing algorithm [35- 37].

3.3.3 Clustering

A cluster is a set of nodes. Clustering allows us to run applications on several parallel servers (cluster nodes). The load is distributed across different servers and even if any of the servers fails, the application is still accessible via other cluster nodes. Clustering is crucial for scalable enterprise applications, because we can improve performance by simply adding more nodes to the cluster. In general, clustering is the process of organizing objects into groups whose members are similar in some way. Clustering algorithms normally perform the same function as classifiers without the use of training data. That is why they are termed unsupervised methods. To compensate for the lack of training data, clustering methods iteratively alternate between segmenting the image and characterizing the properties of each class. In a sense, clustering methods train themselves using the available data.

Three commonly used clustering algorithms are the k-means algorithm, the fuzzy c-means algorithm, and the expectation-maximization algorithm [38–49]. The k-means algorithm computes the mean of the feature space for each class and then allocates every pixel or voxel to the class with the closest feature vector. The algorithm minimizes the dissimilarity of each class by iteratively reassigning the pixels or voxels to the iteratively computed classes. The fuzzy c-means algorithm generalizes the k-means algorithm, allowing for soft segmentations based on fuzzy set theory [49].

The expectation-maximization (EM) algorithm applies the same clustering principles with the assumption that the data follow a Gaussian mixture model [51]. Although clustering algorithms do not require training data, they do require an initial segmentation [52-56].The expectation-maximization (EM) technique assumes that the data can be modeled as a mixture of Gaussians and applies the

same clustering procedure. It iteratively estimates the mean, covariance, mixing coefficients and computes the posterior probabilities. Similar to classification techniques, no spatial distribution of the data is taken into account in the clustering process, and thus their outcomes can be easily corrupted by noise and intensity in-homogeneities. As they require initial parameters, sensitivity to initialization has been shown in the literature [56]. It also has been proved that EM has higher initialization sensitivity in comparison with K-means and fuzzy c-means clustering [57]. Nevertheless, improved robustness to noise and intensity in-homogeneities is obtained when these methods are combined with other techniques like Markov random fields and Bayesian approaches [58] and improved fuzzy clustering techniques [59] for MRI brain image segmentation. For the clustering algorithms, the number of clusters, the position of the initial points and the parameters should be properly selected. Lack of incorporating spatial characteristics is also an obstacle. Due to the large shape variations in medical images, the applications of these algorithms are constrained [60]. In order to overcome the noise and in-homogeneity sensitivity, the performance of the clustering methods has been improved using spatial information in the minimization function [61, 62].One of its most common applications is the brain tissue segmentation in MR images [63].

3.3.4 Artificial Neural Networks

A Neural Network is a powerful data modeling tool that is able to capture and represent complex input/output relationships. The motivation for the development of neural network technology stemmed from the desire to develop an artificial system that could perform intelligent tasks similar to those performed by the human brain. Neural Networks resemble the human brain in two ways: they acquire knowledge through learning and the knowledge is stored within inter-neuron connection strengths known as synaptic weights. The true power and advantage of neural networks lies in their ability to represent both linear and nonlinear relationships and in their ability to learn these relationships directly from the data being modeled. Traditional linear models are simply inadequate when it comes to modeling data that contains nonlinear characteristics. Artificial Neural Networks (ANNs) are parallel networks of processing elements or nodes that simulate biological learning. Each node in an ANN is capable of performing elementary computations. Learning is achieved through the adaptation of weights

assigned to the connections between nodes. A thorough abstraction on Neural Networks is given I.Khalifa et.al and J.W.Clark et.al [64, 65]. It is most widely used in medical imaging as a classifier [66, 67] in which the weights are determined by using training data and the ANN is then used to segment new data. ANNs can also be used in an unsupervised fashion as a clustering method [68, 69], as well as for deformable models [70-72]. Because of the many interconnections used in a Neural Network, spatial information can be easily incorporated into its classification procedures.

Classification techniques are known as supervised methods as they have to be first trained with pre-segmented data and then tested on new datasets for the automatic segmentation task [73]. The most used classifiers in the literature are: k-nearest neighbor [74, 75] (kNN) (each pixel or voxel is labeled as the same class in the training data set which is the closest in the feature space) and modified fuzzy c-means clustering [76, 77]. These are non-parametric classifiers, since in their clustering techniques implementation, no assumption is made with respect to the statistical structure of the data set [78]. Compared with threshold-based algorithms, the ones based on pattern recognition techniques can better utilize structural information and therefore can achieve good results. When the structures in medical images are regular and not much influenced by noises, applying pattern recognition techniques is effective. However, like the threshold-based models, pattern recognition models are also sensitive to noise. The results of these algorithms may depend on their initialization step. For the classifier-based algorithms, the segmentation results depend on the size of the training samples and the correctness of the manual segmentations [79].

Maximum likelihood or Bayes classifier is common parametric classifiers. It is assumed that the studied feature space is formed of independent samples which form a mixture of probability distributions [80]. Usually the distributions are Gaussian and the mixture is called finite mixture model. When it is trained, the Bayes classifier estimates the k-means, covariance and the mixing coefficients, in the case of Gaussian mixtures. In the segmentation process, each pixel or voxel receives the label with the highest posterior probability [81]. As mentioned, it is very important for the classifiers to work with distinct quantifiable features. Practically, it is very difficult to find feature spaces which easily distinguish

between the classes to be labeled. Another drawback of these techniques is that they do not perform spatial modeling, their results being vulnerable to noise corruption [82]. Also, manual interaction and gathering of the training data are very time consuming and laborious. However, as they are non-iterative, they are reasonably computationally effective and several feature spaces can be combined in the classification process. Maximum likelihood segmentation has been applied on ultrasound images and mammograms [83, 84] where the density probability distribution and the smoothness constraints of the gray level values are used to define the energy functional. Vrooman et. al [85] implemented the conventional kNN in combination with manual or atlas-based training, for the brain tissue classification in multispectral MR images.

3.3.5 Markov Random Field Models

Markov Random Field (MRF) Modeling is not a segmentation technique, but a statistical scheme which is often used with other segmentation techniques for results improvement. The main aim of the MRFs is to include the spatial information in the segmentation process by modeling the relationships between neighboring pixels or voxels [64]. MRFs model spatial interactions between neighboring or nearby pixels. These local correlations provide a mechanism for modeling a variety of image properties [85]. For example, in medical image processing, this method sets constraints on the inter connectivity between pixels or voxels representing the same organ. In this case it is considered that most of the pixels or voxels can be classified to be the same as their neighbors, because of the very low probability of existing organs represented by a very low number of pixels/voxels. MRFs are often incorporated into clustering segmentation algorithms such as the k - means algorithm under a Bayesian prior model [86- 89]. The segmentation is then obtained by maximizing a *posteriori* probability of the segmentation given the image data, using iterative methods such as iterated conditional modes [90] or simulated annealing [91]. A difficulty associated with MRF models is the proper selection of the parameters controlling the strength of spatial interactions [86]. The main disadvantages of this approach are the computational cost and the tuning of the parameters managing the strength of the spatial relationships between pixels/voxels [64]. Selecting too high parameters would result in an extremely smoothed segmentation, loosing important details of

the structures to be segmented. Nevertheless, these algorithms are widely used in medical image processing, due to their ability to model intensity in-homogeneities which are widely present in MR images [65].

3.3.6 Deformable Models

Deformable model is a powerful tool in the segmentation of biomedical images. Medical images and volumes usually contain complex and irregular structures; hence, segmentation and representation of these shapes with local descriptors are difficult. Deformable models are model-based techniques for delineating region boundaries by using closed parametric curves or surfaces that deform under the influence of internal and external forces. To delineate an object boundary in an image, a closed curve or surface must first be placed near the desired boundary and then allowed to undergo an iterative relaxation process. Internal forces are computed within the curve or surface, to keep it smooth throughout the deformation. They are routinely used in the reconstruction of the cerebral cortex from MRIs [92-104]. Deformable models are also used in the segmentation of cardiac images [95], of bone in computed tomography (CT) images [96] and ultrasound images [97].The main advantages of deformable models are their ability to directly generate closed parametric curves or surfaces from images and their incorporation of a smoothness constraint that provides robustness to noise and spurious edges. Standard deformable models can also exhibit poor convergence to concave boundaries. This difficulty can be alleviated somewhat through the use of pressure forces [97] and other modified external force models [99]. Another important extension of deformable model is the adaptive model topology by using an implicit representation rather than an explicit parameterization [98,100]. A survey on deformable models in medical image analysis is presented in automatic brain structure segmentation from brain MRI [102]. Due to the advantages of being able to handle structures with complex topology, easy to incorporate with other techniques, sub-pixel accuracy, noise insensitive and intuitive interaction mechanisms, etc. the deformable models are intensively investigated in the last few decades [103]. Parametric deformable models have high computational efficiency and are easy to incorporate with other techniques; Geometric deformable models have the advantage of naturally handling the topological changes. For the medical image segmentation, use of

parametric model or geometric model depends on the applications. In general, when structures have large shape variety or complicated topology, geometric deformable models are preferred; when the interested structures have open boundaries or the structures are thin or the algorithms need real-time operations, parametric models are preferred. However, deformable models usually contain number of parameters. To select proper parameters is critical to the final segmentation results while this is usually a time-consuming task.

Automatic segmentation of thalamus and corpus collasum by combining clustering and deformable models [104], 3-D deformable model-based approach for accurate, robust, and automated tissue segmentation of brain MRI data [105], hybrid segmentation technique incorporating a statistical as well as a geometric model in a unified segmentation scheme for brain tissue segmentation of magnetic resonance imaging (MRI) scans [106] are also presented in literature. A method for detecting and locating the brain structures of interest that can be used for fully automatic 3D functional segmentation of rodent brain MR images based on active shape model (ASM), Meta morph models and variational techniques [107], Automatic method for initialization of a segmentation method based on a combination of a deformable model and spatial relations, leading to a precise segmentation of the brain tumors in 3D MRI [108, 109], are also discussed in literature.

3.3.7 Atlas-guided Approaches

Atlas guided techniques are widely used in medical image analysis when templates or atlases are accessible. An atlas is created using the anatomical information of the structure to be segmented. Once the atlas is generated, it is used as a reference for the segmentation algorithm, translating the process to a registration problem [110]. An initial step is to determine a transformation which maps a pre-segmented atlas structure to a configuration in the analyzed image. This procedure is called atlas warping and is usually achieved using linear transformations [111]. Occasionally, the algorithm adapts to the anatomical variability of the studied structure by applying a sequence of linear and nonlinear transformations [112-114]. MR brain imaging is one of the most common application of the Atlas guided approaches. The great advantage is that during the segmentation process, the labels are also transferred to the studied data set. On the other hand, these techniques have proved deficit in segmenting very complex

structures. Also the results provided by these algorithms are affected by the variability of the anatomical structures between subjects. This is the reason for which their usage is recommended for structures which are stable over the studied population. An improvement has been proposed by Thompson and Toga [114] using probabilistic atlases, but this approach is more computationally expensive and requires manual interaction. Even with nonlinear registration methods, however, finding accurate segmentations of complex structures is difficult because of anatomical variability.

Automated approach guided by digital anatomical atlas, which segments white matter, grey matter and cerebrospinal-fluid [115], Atlas guided identification of brain structures by combining 3D segmentation and SVM classification[116]**,** Automatic atlas guided method for the segmentation of the first transverse temporal gyrus of Heschl (HG), the morphological marker for the primary auditory cortex in humans from brain MRs [117] ,3D brain image segmentation algorithm by fusing an adaptive atlas (generative) and informative features (discriminative) [118] are also discussed in literature.

3.3.8 Watershed Methods

Watershed segmentation is a well known edge-based segmentation algorithm. In geography, watershed line is defined as the line separating two catchment basins. The rain that falls on either side of the watershed line will flow into the same lake water. This idea can be used in digital images. The image gradient can be viewed as a terrain. The homogeneous regions in the image usually have low gradient values. Thus they represent valleys, whereas edges represent peaks that have high gradient values. The watershed algorithm uses concepts from edge detection and mathematical morphology to partition images into homogeneous regions. The main problem of watershed transform is its sensitivity to intensity variations and shading effect present, resulting in over- segmentation, which occurs when the image is segmented into an unnecessarily large number of regions. This can be avoided using markers placed in the region of interest which is brain as well as in the background [119-123]. The over segmentation is also reduced by watershed algorithm followed by fuzzy c-means clustering algorithm [124]. Three-dimensional (3-D) MRI images are segmented using an automatic algorithm composed of watershed, fuzzy clustering (Fuzzy C-Means) and re-

segmentation [125] and combining watershed algorithm with GVF snake model can also reduce the computational complexity, to improve the insensitiveness to noise, and capture range [127]. Segmentation of brain structures by watershed transform on tonsorial morphological gradient of diffusion tensor imaging (DTI), and then using the hierarchical watershed transform, can efficiently segment brain structures, such as the corpus callosum, the ventricles and the cortico-spinal tracts, and use the results for subsequent quantitative analysis of DTI parameters [126].

3.3.9 Level Set Methods

A level set method which is able to deal with intensity in-homogeneities in the segmentation that simultaneously segment the image and estimate the bias field, and this estimated bias field is used for intensity in-homogeneity correction as discussed in automatic segmentation of brain structures by integrating atlas based labeling and level set method [128]. By combining basic level set method to catch the accurate boundaries of the tumor area and applying the inverse thresholding for segmenting binary mask, the exact tumor region was extracted from the different MRI brain scans. [129]. L. Zhukov, et.al [130] used a level set approach to remove noise from the DT-MRI data of a human subject and to produce smooth, geometric models of the isotropic and strongly anisotropic regions of the brain. For obtaining boundaries of the contour, atlas-based segmentation method and level set function [131] are combined and used for segmentation.

Level set methods offer a powerful approach for the medical image segmentation because it can handle all concavities by convolution, splitting, or merging. However, this method requires specifying initial curves and can only provide good results if these curves are placed symmetrically with respect to the object boundary. Although level sets have demonstrated a great potential for 3D medical image segmentation, their usefulness has been limited by two problems. First, 3D level sets are relatively slow to compute [132]. Second, their formulation usually entails several free parameters, which can be very difficult to correctly tune for specific applications. The second problem is compounded by the first [133]. Thus, level set segmentation is not sufficient for the segmentation of complex medical images and they must be combined with powerful initialization techniques to produce successful segmentation. A new variational level set algorithm without

re- initialization to segment the MRI image and to implement a competent medical diagnosis system is also developed in literature [133].

3.3.10 Other Methods

Methods for segmentation of brain MRI using wavelet and Gabor transform[134] are also there. A fully automatic method for segmenting MR images showing tumor, both mass-effect and infiltrating structures using un-decimated wavelet transform and Gabor wavelets were proposed [135]. Symmetry axis based segmentation was used for extraction of stem cells [136]. Segmentation method using balloon inflation forces and a directed and weighted graph and performing a min-cut for optimal segmentation results for Grade IV glioblastoma, relies on detection of high intensity tumor boundaries [137] .

3.4 Validation Methods for the segmentation algorithm used in medical images- An overview

This Section discusses validation of different segmentation techniques. In medical image segmentation, the accuracy of extracted pathological structures is very important. Hence validation of segmented region of interest is needed.

While several systems for segmentation of medical data are currently in use in various research laboratories and hospitals, the issue of correct validation is often ignored. A validation method can be thought of as a combination of two components. One component is the notion of a 'ground truth' against which the results of an algorithm are to be judged. The second component is a measure for establishing the deviation of the results from this ground truth. In this section, we briefly summarize the methods that have been typically used for validation for different segmentation algorithms, their strengths and weaknesses.

A lot of methods are available in literature in order to evaluate the accuracy, and performance of segmentation algorithm in terms of its ground truth images. Segmentation of brain tissue by combining expectation maximization, binary mathematical morphology and active contour models from MRIs [138] were evaluated by number of pixels misclassified with respect to manual GT by

quantitative technique and also performed qualitative evaluation in terms of segmentation time with respect to GT.

The validation of automatic segmentation algorithm described in [139] was done by VALMET validation software, which finds overlapped segmented portions of the segmented region with respect to the manual ground truth, and also inter observer variability. The accuracy and performance of segmentation method [140] were evaluated in brain MRI using Dice Similarity Coefficient (DSC), which measures coincidence between two segmentations. In this technique, manual segmentation by an expert is considered as reference image and automatic segmentation was one using confidence connected segmentation algorithm (CCS) in ITK library. Automatic segmentation of non enhancing tumors in brain MRI [141] was validated by finding the correspondence ratio. This allows to discuss the way in which the segmented tumors corresponds in size and location to the ground truth tumor while weighing the importance of false positive (FP) and false negative (FN).

Performance of atlas based segmentation using expectation maximization technique was validated, i.e. with binary EM model and multiclass EM model using decision fusion method [142] with respect to manual gold standard. The computation time and memory requirement were also evaluated. The validation of automatic brain structure segmentation based on mean shift algorithm [143] was done by evaluating sensitivity, dice similarity coefficient and Tanimoto Index of the segmented brain structures with a reference atlas which consists of T1, T2 and PD weighted as well as pre-labeled map of tissues of interest. The validation of adaptive template moderate brain tumor segmentation [143] and automatic segmentation of low grade glioma and meningioma using brain MRI [144] were done by comparing the segmentation techniques with the manual segmentation carried out by 4 independent medical experts by considering inter-observer variability. Automatic Segmentation of liver tumor was done based on image partitioning into homogeneous primitives regions by applying a pseudo-watershed algorithm and image gradient magnitude. The algorithm was evaluated on Computed Tomography (CT) and Magnetic Resonance (MR) data using the dice similarity coefficient (DSC) as a statistical validation metric [145]. Automatic pancreas segmentation in contrast enhanced CT data using learned spatial anatomy

and texture descriptors [148] were evaluated in terms of positive prediction value which is a measure of TP and FP for measured overlapping pixels with respect to ground truth.

The evaluation of the quality of segmentation of an image, and the assessment of intra and interexpert variability in segmentation performance, has long been recognized as a difficult task. For a segmentation validation task, it may be effective to compare the results of an automatic segmentation algorithm to multiple expert segmentations. Recently an expectation-maximization (EM) algorithm for simultaneous truth and performance level estimation (STAPLE) was developed to this end to compute both an estimate of the reference standard segmentation and performance parameters from a set of segmentations of an image [146]. A statistical label fusion algorithm to estimate quality of segmentation, i.e., Consensus Level Labeler Accuracy and Truth Estimation (COLLATE), which is based on the simple idea that some regions of an image are difficult to label (e.g., *confusion regions*: boundaries or low contrast areas) while other regions are intrinsically obvious (e.g., *consensus regions*: centers of large regions or high contrast edges). Unlike its predecessors, COLLATE estimates the consensus level of each voxel and estimates differing models of observer behavior in each region [147].

A semi-automatic segmentation method for volume assessment of intestinal-type adenocarcinoma (ITAC) using Gaussian hidden Markov random field (GHMRF) model [148] that represents an advanced version of a finite Gaussian mixture (FGM) model was validated by computing Tanimoto index, percentage match, positive prediction value which are the TP, FP, and FN, with respect to manually segmented GT image, by an expert radiologist.

A semi-automatic image analysis system was developed using supervised artificial neural network classifier augmented with dedicated pre- and post processing algorithms, including anisotropic noise filtering and a surface-fitting method focused on the quantification of white matter lesions in the human brain [149] which was validated by using three different ways, i.e. 1) Average total tissue area over all slices; 2) Correlation coefficients of total tissue area between all measurement pairs on all slices; and 3) An index of similarity calculated between

each measurement pair with respect to manual GT. These are the currently available methods for validation of segmentation techniques in medical imaging.

3.5 An Overview of Texture based Classification/ Detection of Pathological subjects in Medical imaging

Texture based image classification techniques are widely used in classification/ detection procedure in medical image analysis. This section gives a brief overview of classification techniques used in literature for identification of pathological subjects using statistical/spectral texture analysis.

Computer aided discrimination between primary and secondary brain tumors on MRI using texture analysis was carried out by Georgiadis et.al [150]. Texture analysis and feature extraction were done using Halarick and Gray level run length matrix on T1 post contrast MRI series. Curvelet based multi resolution texture analysis for classifications of tissues in medical images on CT scan is also there in the literature [151]. Curvelet transform extracts contrast of pixel pairs in radial vedges. The results of this indicate that curvelet based texture descriptors significantly improves the wavelet based ridgelet based classification algorithm. Gray level cooccurence (GLCM) based texture descriptors and grey level run length model were used to quantify the difference between fine and course textures of normal tissues in computed tomography images [152]. Liver segmentation from multi slice CT scan was also done using GLCM features [153].

Medical image classification using cluster co-occurrence matrices of local relation features is a more robust method because the features extracted were implicitly invariant to additive illumination changes and other kinds of monotonic illumination changes. The author says that it is more flexible than other methods; here dimensionality of the feature vector is very large [154]. Pixel based classification algorithm was designed for localization of brain blood vessel in CT angiography [155].

In the classification approach for segmentation of normal tissue, chest and abdomen, from CT images by M. Kalinin [156], GLCM based features were extracted for pixel level classification using decision tree .Texture information as well as textual information of ROI using Halarick texture descriptors and run

length encoding descriptors were used for annotating internal organs by D.S. Raicu,et.al [157], from CT images.

The classification of tumors from abdominal CT images using probabilistic Neural Network (PNN) using selected feature sets is described by A. Depeursinge, et.al [158]. The features were extracted from segmented ROIs using bi-orthogonal wavelet transform to get the vertical, horizontal and diagonal details of images. From these details spatial grey level dependence matrix and second order statistical features were computed. The high resolution computed Tomography images (HRCT) of the chest were used for classification of lung tissues using different classifiers. The features were extracted using improved quincunx wavelet frames [159].

Supervised texture segmentation using Gabor filter [160] was carried out by S. S Sreejamole, et.al and S. Poonguzhali, et.al [162], since Gabor filters provide means for better spatial localization. However their usefulness is limited in practice because there is usually no single filter resolution at which one can localize a spatial structure in natural texture. In supervised classification of textures based on GLCM approach, local binary patterns were computed over a region [163]. An automatic detection system was developed for identification of cyst and malignant tumors from ultrasound liver images using combined features extracted using GLCM, GLRLM, spectral texture features, and Gabor wavelet based features [164]. Texture classification using logical operators were also thee in literature [165].

Statistical features can be calculated based on the grey level co- occurrence probabilities (GLCP) [166]. A feature extraction method using linear wavelets for the classification of textures using GMRF model is presented in classification using wavelet packet an Gaussian mixture model [167]. Texture features derived from six grid sizes of independent and different Gabor filter banks were incorporated into the CBIR system by additionally incorporating texture, shape and spatial information [168]. Texture classification of digital images based on the co-occurrence features obtained from the two-level wavelet packet decomposition is proposed in [169]. In the feature selection process of pattern classification for mammographic micro calcifications, GLCM and spatial information such as shape features were extracted [170].

Thus GLCM and GLRLM and other first order statistical moments are widely used for texture analysis and feature extraction tool for classification of pathological subjects in medical imaging.

Conclusions

A brief overview of various segmentation techniques used in literature for different modalities of medical images and the merits and demerits of each segmentation technique are discussed. Different validation techniques in literature used for analyzing the accuracy of segmentation techniques are also summarized. A summary of texture analysis methods used in medical imaging for classification/ detection of pathological subjects is also presented.

References

[1] S.M. Larie and S.S. Abukmeil. Brain abnormality in schizophrenia: a systematic and quantitative review of volumetric magnetic resonance imaging studies. *J. Psych.*, vol.172:pp.110–120, (1998)

[2] P. Taylor. Invited review: computer aids for decision-making in diagnostic radiology- a literature review. Brit. J. Radiol, vol.68:pp945–957,(1995).

[3] A.P. Zijdenbos and B.M. Dawant. Brain segmentation and white matter lesion detection in MR images. Critical Reviews in Biomedical Engineering, vol.22:pp.401–465, (1994).

[4] V.S. Khoo, D.P. Dearnaley, D.J. Finnigan, et.al, Magnetic Resonance Imaging (MRI): Considerations And Applications In Radiotheraphy treatment planning. Radiother.Oncol, vol. 42:pp.1–15, (1997).

[5] H.W. Muller-Gartner, J.M. Links, et al. Measurement of Radiotracer Concentration in Brain Grey Matter Using Positron Emission Tomography: MRI-based Correction for Partial volume effects. J. Cereb. Blood Flow Metab, vol.12:pp.571–583, (1992).

[6] N. Ayache, P. Cinquin, I. Cohen, et.al. Segmentation of Complex Three Dimensional Medical Objects: A Challenge and a Requirement for Computer-Assisted Surgery Planning And Performance. In R.H. Taylor, S.

Lavallee, G.C. Burdea, and R. Mosges, editors, Computer Integrated Surgery: Technology and Clinical Applications, pp.59–74. MIT Press, (1996).

[7] W.E.L. Grimson, G.J. Ettinger, T. Kapur, et al. Utilizing Segmented MRI data in Image-Guided Surgery. Int. J. Patt. Rec. Art. Intel., vol.11:pp.1367–1397, (1997).

[8] P. K Sahoo, S. Soltani, A. K. C. Wong, and Y. C Chen. A survey of thresholding techniques.Computer Vision, Graphics, and Image Processing, vol.41:pp.233-260, (1988). ACM ID:46079.

[9] H. R Singleton, G. M. Pohost. Automatic cardiac MR image Segmentation using Edge Detection by Tissue Classification in Pixel Neighborhoods, .Magn Reson Med vol.37:pp.418–424. (1997).

[10] L. Gordon , C. E. Webber, J. D. Adachi, et al. In Vivo Assessment of Trabecular Bone Structure at the Distal Radius from High-Resolution Computed Tomography Images. Phys Med Biol, vol.41:pp.495–508, (1996).

[11] W. R. Polakowski, D. A. Cournoyer, S. K. Rogers, et al. Computer-aided Breast Cancer Detection and Diagnosis of Masses Using Difference of Gaussians and Derivative-Based Feature Saliency. IEEE Trans Med Imaging vol.16: pp.811–819, (1997).

[12] H. D. Cheng, Y. M. Lui, R. I. Freimanis. A Novel Approach to Microcalcification Detection Using Fuzzy Logic Technique. IEEE Trans Med Imaging, vol.17:pp. 442–450, (1998).

[13] N.Sang, H.Li, W. Peng, and T. Zhang. Knowledge-based Adaptive Thresholding Segmentation of Digital Subtraction Angiography Images. Image Vision Comput.,vol.25 :pp.1263-1270, (2007).

[14] J. Kittler, J. Illingworth, and J. Fglein. Threshold Selection based on a Simple Image Statistic. Computer Vision, Graphics and Image Processing, vol.30 (2):pp.125-147, (1985).

[15] G. Kom, A. Tiedeu, and M. Kom. Automated Detection of Masses in Mammograms by Local Adaptive Thresholding. Computers in Biology and Medicine, vol.37 (1):pp.37-48,(2007).

[16] A. J. Burghardt, G. J. Kazakia, and S. Majumdar. A Local Adaptive Threshold Strategy for High Resolution Peripheral Quantitative Computed Tomography of Trabecular Bone. Annals of Biomedical Engineering, vol.35 (10):pp.1678-1686, (2007).

[17] S.A. Kostopoulus, D. Glostos, G. Kagadis et.al, Development of a Brain blood Vessel Segmentation Method in CT Angiography, Proceedings of 3rd European Medical & Biological Engineering ConferenceEMBEC'05, Prague, Czech Republic.(20 -25 November 2005).

[18] R. Khayati, M. Vafadust, F. Towhidkhah, and M. Nabavi. Fully Automatic Segmentation Of Multiple Sclerosis Lesions in Brain MRI Images using Adaptive Mixtures Method and Markov Random Field Model. Comput. Biol. Med, vol.38:pp.379-390,(March2008).

[19] H. Tian, T. Srikanthan, and K. Vijayan Asari. Automatic Segmentation Algorithm for the Extraction of Lumen Region and Boundary from Endoscopic Images. Medical & Biological Engineering & Computing, vol.39(1):pp.8-14,(2001).

[20] D. Li , M. Kallergi, L. P. Clarke, et al. Markov Random Field for Tumor Detection in Digital Mammography. IEEE Trans Med Imaging, vol.14:pp.565–576, (1995).

[21] J. Liu, Q. Hu, Z. Chen, et.al, Adaptive Liver segmentation from Multi slice CT Scans' Asian-Pacific Conference on Medical and Biological Engineering - 2008: pp-381-384.

[22] M. Kalinin, D.S.Raicu, J. D. Furst, et. al, A Classification Approach for Anatomical Regions Segmentation. The IEEE International Conference on Image Processing (ICIP), Genoa, Italy, September 11-14, (2005).

[23] D.L.Pham, C.Xu, J.L. Prince, et.al, A Survey of Current methods in Medical Image Segmentation, Annual Review of Biomedical Engineering. (1998)

[24] R. B. Dubey, M. Hanmandlu, S. K. Gupta, S. K. Gupta, et.al, The Brain MR Image Segmentation Techniques and use of Diagnostic Packages. Acad Radiol, vol.17:pp.658–671, (2010)

[25] Z.Ma, J. Manuel R. S. Tavares, R. M. Natal Jorge, A Review on the Current Segmentation Algorithms for Medical Images, Proceedings of the First International Conference on Computer Imaging Theory and Applications, Lisboa, Portugal, February 5-8, (2009).

[26] R. M. Haralick, L. G. Shapiro. Image Segmentation Techniques. Comp Vis. Graph Image Proc, vol.29:pp.100–132, (1985)

[27] J. Zhang, C.H. Yan, C.K. Chui, and S.H. Ong. Fast segmentation of bone in CT images using 3D adaptive thresholding. Computers in Biology and Medicine, vol.40(2):pp.231-236,(2010).

[28] G. N. Harikrishna Rai and T. R. Gopalakrishnan Nair. Gradient based seeded region grow method for CT angiographic image segmentation, International Journal of Computer Science and Networking, Vol.1(1),(2009).

[29] J. K. Udupa and S. Samarasekera. Fuzzy connectedness and object definition: Theory, Algorithms, and Applications in Image Segmentation. Graphical Models and Image Processing, vol.58(3):pp.246-261,(1996).

[30] J. F. Mangin, V. Frouin, I. Bloch, et.al. From 3D Magnetic Resonance Images to Structural Representations of the Cortex Topography using Topology Preserving Deformations. J. Math. Imaging Vis, vol.5:pp.297-318, (1995).

[31] I. N. Manousakas, P. E. Undrill, G. G. Cameron and T. W. Redpath. Split-and-Merge Segmentation of Magnetic Resonance Medical Images: Performance Evaluation and Extension to Three Dimensions. Computers

and Biomedical Research, an International Journal, vol.31 (6):pp. 393-412, (1998).

[32] P. Gibbs, D. L. Buckley, S. J. Blackband, et al. Tumor Volume Detection from MR images by Morphological Segmentation. Phys Med Biol, vol.41:pp.2437–2446. (1996).

[33] K. A. Pohlman, N. A. Powell, W. A. Obuchowski, et al. Quantitative Classification of Breast Tumors in Digitized Mammograms. Med. Phys, vol.23:pp. 1337–1345, (1996).

[34] S. Madhu kumar, N. Santhiyakumari, Elimination of Partial Volume Effect on Low Grade Gliomas Segmentation. International Conference on Communications and Signal Processing (ICCSP), pp. 344-347, (2011).

[35] N. Manousakas, P. E. Undrill, G. G. Cameron, et al. Split-and-merge Segmentation Of Magnetic Resonance Medical Images: Performance Evaluation and Extension to Three Dimensions. Comp Biomed Res, vol.31:pp.393–412, (1998).

[36] F. Mangin, V. Frouin, I. Bloch, et al. From 3D Magnetic Resonance Images to Structural Representations of the Cortex Topography using Topology Preserving Deformations. J Math Imaging Vis, vol.5:pp.297–318, (1995).

[37] K. Udupa, S. Samarasekera. Fuzzy Connectedness and Object Definition: Theory, Algorithms and Applications in Image Segmentation. Graph Models Image Process, vol.58:pp.246–261, (1996).

[38] W. Vannier, R. L. Butterfield, D. Jordan, et al. Multi Spectral Analysis of Magnetic Resonance Images. Radiology, vol.154:pp.221–224.(1985).

[39] T. Kapur, W. E. L. Grimson, R. Kikinis, et al. Enhanced Spatial Priors For Segmentation of Magnetic Resonance Imagery. Proc. Int Conf Med. Image Comp Assist Interv. Cambridge, MA, (1998).

[40] G. B. Coleman, H. C. Andrews. Image Segmentation by Clustering. Proc. IEEE, vol.5:pp.773–785, (1979).

[41] Z. Liang, J. R. MacFall, D. P. Harrington. Parameter Estimation and Tissue Segmentation from Multispectral MR Images. IEEE Trans Med Imaging, vol.13:pp.441–449, (1994).

[42] T. Lei, W. Sewchand. Statistical approach to X-ray CT imaging and its Applications in Image Analysis - A_New_Stochastic_Model-Based Image Segmentation Technique for X-Ray CT Image. IEEE Trans Med Imaging, vol.11:pp.62–69, (1992).

[43] A. K. Jain, R. C. Dubes. Algorithms for Clustering Data. Englewood Cliffs, NJ: Prentice Hall, (1988).

[44] K. Xiao, S. H. Ho, A. Bargiela, Automatic Brain Segmentation Scheme Based on Feature Weighting Factors Selection Based on Fuzzy C-Means Clustering Algorithms with Gaussian Smoothing. Int. J. Comput. Intelligence in Bioinformatics and System Biology, (2009)

[45] D .Selvathi, A. Arulmurgan, S. Thamarai Selvi, MRI Image Segmentation Using Unsupervised Clustering Techniques, Proceedings of the Sixth International Conference on Computational Intelligence and Multimedia Applications (ICCIMA'05), (2005).

[46] H. M. Moftah, A.E. Hassanien, and M. Shoman, 3D Brain Tumor Segmentation Scheme using K-mean Clustering and Connected Component Labeling Algorithms, 10th International Conference on Intelligent Systems Design and Applications. pp.320-324, (2010)

[47] J. C. Bezdek, L. O. Hall, and L. P. Clarke. Review of MR image segmentation techniques using pattern recognition. Medical Physics, vol.20 (4):pp.1033-1048, (1993).

[48] Z. Liang, J. R. MacFall, and D.P. Harrington. Parameter estimation and tissue segmentation from multispectral MR images. IEEE Transactions on Medical Imaging, vol.13(3):pp.441-449, (1994).

[49] H. Zaidi, T. Ruest, F. Schoenahl,et.al, Comparative assessment of statistical brain MR image segmentation algorithms and their impact on

partial volume correction in PET. NeuroImage, vol.32:pp.1591 – 1607.(2006).

[50] T. Lei and W. Sewchand. Statistical approach to X-ray CT imaging and its applications in image analysis. Statistical analysis of x-ray CT imaging. IEEE Transactions on Medical Imaging, vol.11(1):pp.53-61.(1992).

[51] L. A. Zadeh, Fuzzy sets. Inf. Control pp.338–353. (1965)

[52] H. Greenspan, A. Ruf, and J. Goldberger, Constrained Gaussian Mixture Model Framework for Automatic Segmentation of MR Brain Images, IEEE Transactions On Medical Imaging, vol. 25(9). pp.1323-1325, (2006).

[53] J. W. Davenport, J. C. Bezdek, R. J. Hathaway. Parameter Estimation for Finite Mixture Distributions. Comp Math, vol.15:pp.810–828.(1988).

[54] J. C. Rajapakse, J. N. Giedd,J. L. Rapoport. Statistical Approach to Segmentation of Single-Channel Cerebral MR Images. IEEE Trans Med. Imaging, vol.16:pp.176–186, (1997).

[55] D. L. Pham, J. L. Prince. An Adaptive Fuzzy C-Means Algorithm for Image Segmentation in The Presence of Intensity In-homogeneities. Pattern Recognit. Lett. Vol.20:pp.57–68, (1999).

[56] T. J. Hebert. Fast Iterative Segmentation of High Resolution Medical Images. IEEE Trans Nucl Sci, vol.44:pp.1363–1367, (1997).

[57] M. S. Yang and C. F. Su. On Parameter Estimation For Normal Mixtures Based on Fuzzy Clustering Algorithms. Fuzzy Sets Syst, vol.68:pp.13-28, (1994).

[58] A. F. Goldszal, C. Davatzikos, D. L. Pham, et.al, An image processing system for qualitative and quantitative volumetric analysis of brain images. Journal of Computer Assisted Tomography, vol.22(5):pp.827-837, (1998).

[59] A. Kouhi, H. Seyedarabi, A. Aghagolzadeh, A Modified FCM Clustering Algorithm for MRI brain image Segmentation Proceedings of Machine Vision and Image Processing Nov.-2011

[60] J. Wang, J. Kong, Y. Lu, M. Qi, and B. Zhang. A modified FCM algorithm for MRI Brain Image Segmentation Using both Local and Non-Local Spatial Constraints. Computerized Medical Imaging and Graphics: The Official Journal of the Computerized Medical Imaging Society, vol.32 (8):pp. 685-698, (2008).

[61] S. Chen and D. Zhang. Robust Image Segmentation Using FCM With Spatial Constraints Based on New Kernel-Induced Distance Measure. IEEE Transactions on Systems, Man, and Cybernetics- Part B: Cybernetics, vol.34 (4):pp.1907-1916, (2004).

[62] S. Z. Li. Markov Random Field Models in Computer Vision. In Proceedings of the Third European conference on Computer Vision (Vol. II), pages 361-370, Secaucus, NJ, USA, 1994. Springer-Verlag New York, Inc.

[63] K. Held, E. R. Kops, B. J. Krause, et.al, Markov random field segmentation of brain MR images. IEEE Transactions on Medical Imaging, vol.16 (6):pp.878-886, (1997).

[64] I. khalifa, A. Youssif , H. Youssry , Tissue segmentation Techniques of brain MR Images: A Review, Proc.International Conference on Intelligent Computational Systems (ICICS'2012) Jan. 7-8, 2012 Dubai pp.17-21

[65] J. W. Clark. Neural network modeling. Phys Med. Biol, vol.36:pp.1259–1317, (1991).

[66] S. Haykin Neural networks: a comprehensive foundation. New York: Macmillan, 2002.

[67] L. O. Hall, A. M. Bensaid, L. P. Clarke, et al. A Comparison of Neural Network and Fuzzy Clustering Techniques in Segmenting Magnetic Resonance Images of the Brain. IEEE Trans. Neural Netw, vol.3:pp.672–682, (1992).

[68] E. Gelenbe, Y. Feng, K. R. R. Krishnan. Neural Network Methods for Volumetric Magnetic Resonance Imaging of the Human Brain. Proc IEEE, vol.84:pp.1488–1496. (1996)

[69] J.C. Bezdek, L.O. Hall, L.P. Clarke. Review of MR Image Segmentation Techniques Using Pattern Recognition. Med. Phys, vol.20:pp.1033–1048, (1993).

[70] W.E. Reddick, J.O Glass, E.N. Cook, et al. Automated Segmentation and Classification of Multispectral Magnetic Resonance Images of Brain Using Artificial Neural Networks. IEEE Trans Med. Imaging, vol.16:pp.911–918, (1997).

[71] D.L. Vilarino, V.M Brea, D Cabello, et al. Discrete-Time CNN For Image Segmentation by Active Contours. Pattern Recognit Lett, vol.19:pp.721–734, (1998).

[72] M.C. Clark, L. O. Hall, D. B. Goldgof, et.al, Automatic Tumor Segmentation Using Knowledge based Techniques, IEEE Transactions On Medical Imaging, Vol. 17(2). pp.187-201, (1998).

[73] Q. Ain, G. Latif, S. B. Kazmi, M. A. Jaffar, et.al, Classification and Segmentation of Brain Tumor using Texture Analysis, Proceedings of the 9th WSEAS International Conference on Recent Advances In Artificial Intelligence, Knowledge Engineering And Data Bases, 20-22 February 2010, pp.147-155.

[74] J. Hussain, T. S. Savithri, P. V. Sree Devi, Segmentation of Tissues in Brain MRI Images using Dynamic Neuro-Fuzzy Technique. International Journal of Soft Computing and Engineering (IJSCE) ISSN: 2231-2307, vol.1 (6):pp.416 – 421, (2012).

[75] S. Shen, W. Sandham, M. Granatet.al, MRI Fuzzy Segmentation of Brain Tissue Using Neighborhood Attraction With Neural-Network Optimization, IEEE Transactions on information Technology In Biomedicine, Vol. 9(3):pp.459-467 (2005).

[76] W. M. Wells, W. L. Grimson, R. Kikinis, and F. A. Jolesz. Adaptive Segmentation of MRI data. IEEE Transactions on Medical Imaging, vol.15(4):pp.429-442, (1996).

[77] A. O. Malagelada, Automatic Segmentation in Mammographic images. Ph.D Thesis Department of Electronics. University of Girona, (2007).

[78] N. Sang, H. Li, W. Peng, and T. Zhang. Knowledge-based Adaptive Thresholding Segmentation of Digital Subtraction Angiography Images. Image Vision Comput, vol.25:pp.1263-1270,(2007).

[79] H. Andres, L. Aynla, J. Fncon , Automatic Segmentation of Brain MRI Through Learning by Example, International Conference on Image Processing (ICIP), pp.917-921. (2004).

[80] G. Gerig, N. Moon, S. Ho, et.al, Model-Based Segmentation of Brain Tissue and Tumor, Proceedings of the Second Joint EMBS/BMES Conference 2002, pp.1071-75

[81] H. A. Vrooman. kNN-based multi-spectral MRI brain tissue classification: manual training versus automated atlas-based training. In Proceedings of SPIE, pages 61443L- 61443L-9, San Diego, CA, USA, 2006.

[82] S. Z. Li. Markov random field modeling in computer vision. Springer, 1995

[83] T. N. Pappas. An Adaptive Clustering Algorithm for Image Segmentation. IEEE T. Signal Process, vol.40:pp.901–914, (1992).

[84] J. C. Rajapakse, J. N. Giedd, and J. L. Rapoport. Statistical Approach To Segmentation of Single-Channel Cerebral MR Images. IEEE T. Med. Imag., vol.16:pp.176–186,(1997).

[85] K. Held, E. R. Kops, B. J. Krause, W. M. Wells, R. Kikinis, et al. Markov Random Field Segmentation of Brain MR Images. IEEE T. Med. Imag, vol.16(6),(1997).

[86] A. F. Goldszal, C. Davatzikos, D. L. Pham, et.al. An Image Processing System for Qualitative and Quantitative Volumetric Analysis of Brain Images. Journal of Computer Assisted Tomography, vol.22:pp.827–837, (1998).

[87] J. Besag. On the Statistical Analysis of Dirty Pictures. CVGIP: Im. Understand., vol.57:pp.359–372,(1986).

[88] S. Geman and D. Geman. Stochastic Relaxation, Gibbs Distrutions, and the Bayesian Restoration of images. IEEE T. Patt. Anal. Mach. Intel., PAMI, vol.6:pp.721–741, (1984).

[89] C. Davatzikos, R. N. Bryan. Using a Deformable Surface Model To Obtain A Shape Representation of The Cortex. IEEE Trans Med Imaging, vol.15:pp.785–795, (1996).

[90] T. McInerney,D. Terzopoulos. Medical image Segmentation using Topologically Adaptable Surfaces. Lect Notes Comp Sci, vol.1205:pp.23–32, (1997).

[91] C. Xu, D. L. Pham, J. L. Prince, et al. Reconstruction of the central layer of the human cerebral cortex from MR images. In Proc Int Conf Med. Image, Comp Comp Assist Interv. Cambridge, MA; pp. 482–488, (1998).

[92] E. Bardinet, L. D. Cohen, N. Ayache. A Parametric Deformable Model to fit unstructured 3D Data. Comp Vis Image Underst, vol.71:pp.39–54, (1998).

[93] A. Neumann, C. Lorenz. Statistical Shape Model Based Segmentation of Medical Images. Comp Med. Image Graph, vol.22:pp.133–143, (1998).

[94] I. Mikic, S. Krucinski, J. D. Thomas. Automatic 3-D model-based Segmentation and Tracking in Echocardiograph Sequences: Active Contours Guided by Optical Low Estimates. IEEE Trans Med Imaging, vol.17:pp.274–284, (1995).

[95] L. D. Cohen. On Active Contour Models and Balloons. CVGIP: Image Underst, vol.53:pp.211–218, (1991).

[96] V. Caselles, F. Catte , T. Coll, et al. A Geometric Model for Active Contours. Number vol.66:pp.1–31, (1993).

[97] C. Xu, J. L. Prince. Snakes, shapes, and gradient vector flow. IEEE Trans. Image Proc. Vol.7:pp.359–369, (1998).

[98] T. McInerney, D. Terzopoulos. Topologically Adaptable Snakes. In: Proc Int. Conf Comp Vis. Cambridge, MA: IEEE Comp Soc, pp.840–845. (1995).

[99] T. McInerney, D. Terzopoulos. Deformable Models in Medical Image Analysis: A Survey. Med. Image Anal, vol.1:pp.91–108, (1996).

[100] J. B. M. Maintz, M.A. Viergever. A Survey of Medical Image Registration. Med. Image Anal, vol.2:pp.1–36, (1998).

[101] J. Talairach, P. Tournoux. Coplanar Stereotaxic Atlas of the Human Brain. 3Dimensional Proportional System: An Approach to Cerebral Imaging. Stuttgart, Germany: Thieme, 1988.

[102] Q. He, K. Karsch, and Y. Duan, A Novel Algorithm for Automatic Brain Structure Segmentation from MRI, ISVC 2008, Part I, LNCS 5358, pp. 552–561, (2008)

[103] A. Huang,, R. Abugharbieh, R. Tam, A Hybrid Geometric–Statistical Deformable Model for Automated 3-D Segmentation in Brain MRI, IEEE Transactions on Biomedical Engineering, Vol. 56(7):pp.1838-1848, (2009).

[104] A. Huang1, R. Abugharbieh1, R. Tam, Automatic MRI Brain Tissue Segmentation Using a Hybrid Statistical and Geometric Model, Proceedings of the IEEE International Symposium on Biomedical Imaging: From Nano to Macro, USA, pp.394-397,(2006).

[105] H. Khotanlou, O. Colliot and I. Bloch, Automatic Brain Tumor Segmentation Using Symmetry Analysis and Deformable Models, Fuzzy Sets and Systems

Volume 160 (10), pp.1457-1473, (2009)

[106] O. Colliot, J. Atif, I. Bloch, 3D Brain tumor Segmentation in MRI Using Fuzzy Classification, Symmetry Analysis and Spatially Constrained Deformable Models, Fuzzy Sets and Systems,vol.160:pp.1457–1473. (2009).

[107] J. B. A. Maintz and A. Max. Viergever. A Survey of Medical Image Registration. Medical Image Analysis, vol.2 (1):pp.1-36, (1998).

[108] N. C. Andreasen, R. Rajarethinam, T. Cizadlo et.al Automatic Atlas-Based Volume Estimation of Human Brain Regions from MR Images. Journal of Computer Assisted Tomography, vol.20(1):pp.98-106, (1996).

[109] E. G. Christensen, S. C. Joshi, M. I. Miller,. Volumetric Transformation of Brain Anatomy. IEEE Transactions on Medical Imaging, vol. 16:pp.864-877, (1997).

[110] L. Collins, C. J. Holmes, T. M. Peters, and A. C. Evans. Automatic 3-D Model-Based Neuro-Anatomical Segmentation. Human Brain Mapping, vol.3(3):pp.190-208, (1995).

[111] Christos Davatzikos and Christos Davatzikos. Spatial Normalization of 3D Brain Images Using Deformable Models. Journal of Computer Assisted Tomography, vol.20:pp.656-665,(1996).

[112] S. Bourouis, K.Hamrouni, N.Betrouni, Automatic MRI Brain segmentation with Combined Atlas based Classification and Level set Approach, Proceedings of the 5th International Conference on Image Analysis and Recognition, 2008, pp. 770-778

[113] A. Akselrod-Ballin , M. Galun , M.J. Gomori, et.al, Atlas Guided Identification Of Brain Structures by Combining 3D Segmentation and SVM classification.MICCAI- pp:209-16.(2006).

[114] C. Yi Liu, J. Eugenio Iglesias, A. Toga, et.al. Fusing Adaptive Atlas and Informative Features for Robust 3D Brain Image Segmentation,IEEE International Symposium on Biomedical Imaging: From Nano to Macro, 848-851, (2010).

[115] J. Wang ; Y. Lu ; J. Zhang ; et.al, A Novel Approach for Segmentation of MRI Brain Images, Electrotechnical IEEE Mediterranean Conference, 2006. MELECON 2006. pp: 525-528

[116] L. Vincent, P. Soille. Watersheds in Digital Spaces: an Efficient Algorithm Based On Immersion Simulation. IEEE Trans Pattern Anal Mach Intell,vol.13:pp.583–598.(1991).

[117] J. Sijbers, P. Scheunders, M. Verhoye, et al. Watershed-Based Segmentation of 3D MR Data for Volume Quantization. Magn Reson Imag, vol.15:pp.679–688, (1997).

[118] C. E. Priebe, D. J. Marchette, G. W. Rogers. Segmentation of Random Fields via Borrowed Strength Density Estimation. IEEE Trans Pattern Anal Mach Intell, vol. 19:pp.494–499, (1997).

[119] D. Goshal1, P. P. Acharjya, MRI Image Segmentation Using Watershed Transform International Journal of Emerging Technology and Advanced Engineering, Vol.2(4):pp. 373-376, (2012).

[120] A. Salem Hamed , Segmentation of Magnetic Resonance Brain images Using Watershed Algorithm, *Segmentation of Magnetic Resonance Brain Images Using Watershed Algorithm*. Masters Thesis, University Putra Malaysia, (2004)

[121] J. Wang, J. Kong, Y. Lu, Segmentation of 3-D MRI Brain Images Using Information Propagation, MIAR 2006, LNCS 4091, pp. 348 – 355

[122] T. Sai kumar, P. Yugander, P.S.Murthy et.al, MRI Brain Image Segmentation Algorithm Using Watershed Transform and Kernel Fuzzy C-Means Clustering on Level Set Method, International Conference on Information and Network Technology, 2011, pp-188-195.

[123] L. Rittner, S. Appenzeller, R. Lotufo, Segmentation of Brain Structures by Watershed Transform on Tensorial Morphological Gradient of Diffusion Tensor Imaging, Brazilian Symposium on Computer Graphics and Image Processing (SIBGRAPI),pp. 126 - 132 (2009)

[124] D. Jayadevappa, S. Srinivas Kumar, and D. S. Murty, A Hybrid Segmentation Model based on Watershed and Gradient Vector Flow for the Detection of Brain Tumor, International Journal of Signal Processing, Image Processing and Pattern Recognition, Vol. 2(3):pp.-29-42(2009).

[125] C. Li, R. Huang, Z. Ding, et.al, A Level Set Method for Image Segmentation in the Presence of Intensity In-homogeneities with Application to MRI, IEEE Transactions on Image Processing, Vol. 20(7): pp. 2007-2016,(2011).

[126] N. S. Zulpe and V. P. Pawar, Level set and Thresholding for Brain Tumor Segmentation, International Journal of Computer and Electrical Engineering, vol.4(1),(2012).

[127] L.Zhukov, K.Museth, D. Breen, et.al, Level Set Modeling and Segmentation of DT-MRI Brain Data, *J. Electron. Imaging*. 12(1), 125-133 (Jan 01, 2003)

[128] M. Shaker, H. Soltanian-Zadeh, Automatic segmentation of brain structures from MRI integrating atlas-based labeling and level set method, Canadian Conference on Electrical and Computer Engineering, pp. 001755 – 001758. (2008)

[129] C. Baillard, P. Hellier, C. Barillot, Segmentation of brain 3D MR images using level sets and dense registration, Medical Image Analysis, vol.5:pp.185–194. (2001).

[130] K. Aloui, and M. S. Naceur, 3D Brain Tumor Segmentation Using LevelSets Method and Meshes Simplification from Volumetric MR Images, World Academy of Science, Engineering and Technology, vol.57: pp.127-131(2009).

[131] P. Chandra Barman,. S. Miah, Bi. Chandra Singh, MRI Image Segmentation Using Level Set Method And Implement an Medical Diagnosis System, Computer Science & Engineering: An International Journal (CSEIJ), Vol.1(5). (2011).

[132] G. Mirajkar, B. Barbadekar, Automatic Segmentation of Brain Tumors from MR Images using Undecimated Wavelet Transform and Gabor Wavelets, 17th IEEE International Conference on Electronics, Circuits, and Systems (ICECS), 2010. pp.-702-705.

[133] Y. Xiao, T. D. Pham , J.Chang, Symmetry-based Presentation for Stem-Cell Image Segmentation, In Proceedings of ICCABS. pp. 196-201.(2011).

[134] J.Egger, D. Zukic., M. H. A Bauer., D.Kuhnt, et.al, A Comparison of Two Human Brain Tumor Segmentation Methods for MRI Data, Proc. of the 6th Russian-Bavarian Conference on Bio-Medical Engineering

[135] T. Kapur, W. E.L . Grimson, W. M. wells, . kikinis, Segmentation of Brain Tissue From Magnetic Resonance Images, Medical image Analysis, vol. 1(2):pp.109-127.(1996).

[136] R. Xu, L. Luo and J. Ohya,Segmentation of Brain MRI,chapter 8, A Text Book of Advances in Brain Imaging, Edited by Vikas Chaudhary, publisher: InTech

[137] M. Prastawa, E. Bullit, S. Ho, G. Geirg. A Brain tumor segmentation framework based on outlier detection, Medical Image Analysis, vol.8:pp.275-283((2004).

[138] I. Diaz, P.Boulanger, R.Griener, A.Mutha. A Critical Review Of Effects Of Denoising Algorithms On MRI Bain Tumor Segmentation, 33rd annual international conference on IEEE EMBS,USA, 2011, pp.3934-37.

[139] L.M.Fletcher-Heath, L.O.Hall, D. B. Goldof, F. R. Mutagh. Automatic Segmentation of Non Enhancing Brain Tumors in Magnetic Resonance Images

[140] T. Rohlfing, D. B. Russakoff, and C. R. Maurer, Performance-Based Classifier Combination in Atlas-Based Image Segmentation Using Expectation-Maximization Parameter Estimation, IEEE Transactions On Medical Imaging, Vol. 23.(8): 983.(2004).

[141] C. Farmaki, K. Mavrigiannakis, K.Marias, M. Zervakis, V,Sakkalis. Assesment of Automated Brain Structures Based on Mean Shift Algorithm: Application In Brain Tumor.IEEE 2010, pp. 435–460

[142] M.K aus, S.K. Warfield, F.A.Jolesz, R. Kikins. Adaptive template moderated brain tumor segmentation in MRI, Bildverarbeitung fur die Medizin, 102-106. Springer Verlag(1999)

[143] M.Kaus, S.K. Warfield,A. Nabavi,P.M.. et.al. Automated segmentation of MR Images of brain tumors, Radiology 2001;218,pp.586-591

[144] P. Rodrigues ,J. L. Vilaça ,J. Fonseca, An Image Processing Application for Liver Tumour Segmentation, Portuguese Meeting in Bioengineering, February 2011 , Portuguese chapter of IEEE EMBS

[145] M. Erdt, M. Kirschner, K. Drechsler, et.al, Automatic Pancreas Segmentation In Contrast Enhanced Ct Data Using Learned Spatial Anatomy And Texture Descriptors, IEEE,pp.2076-2082,(2011).

[146] O. Commowick and S. K. Warfield, Estimation of Inferential Uncertainty in Assessing Expert Segmentation Performance from STAPLE IEEE Transactions On Medical Imaging, Vol. 29(3): pp.771- 786, (2010).

[147] A. J. Asman, , and B. A. Landman, Robust Statistical Label Fusion Through Consensus Level, Labeler Accuracy, and Truth Estimation (COLLATE) . IEEE Transactions On Medical Imaging, Vol. 30(10): pp.1779,(2011).

[148] K. M. Passera, P. Potepan, L.Brambilla et.al, ITAC volume assessment through a Gaussian hidden Markov random field model-based algorithm, 30th Annual International IEEE EMBS Conference Vancouver, British Columbia, Canada, (August 20-24, 2008)

[149] A. P. Zijdenbos, B.M. Dawant, Morphometric Analysis of White Matter Lesions in MR Images: Method and Validation IEEE Transactions on Medical Imaging, Vol. 13(4).(1994).

[150] L. Semler, L. Dettori, Curvelet Based Texture Classification in Computed Tomography, Computers in Biology and Medicine, Volume 37 (4), 2007, pp. 486-498

[151] D. Xu, J. Lee, D.S.Raicu et al, Texture Classification of Normal Tissues in Computed Tomography, , Computer-Based Medical Systems, 2005. Proceedings. 18th IEEE Symposium on, 23-24 June 2005, pp**.** 593 - 598

[152] J. Liu, Q. Hu, Z. Chen et al, Adaptive Liver Segmentation from Multi Slice CT Scan, 7th Asian-Pacific Conference on Medical and Biological Engineering, IFMBE Proceedings Volume 19, pp 381-384, (2008)

[153] L. Setia, A.Teynor, A. Halawani et al,Image Classification using Cluster Cooccurance Matrices of Local Relational Features, Proceeding MIR '06 Proceedings of the 8th ACM international workshop on Multimedia information retrieval, PP. 173-182

[154] S.A. Kostopoulos, D. Glotsos, G. Kagadis et al, Development of a Brain Blood Vessel Segmentation Method in CT Angiography, Proceedings of 3rd Europian Medical and Biological Engineering Conference 2005

[155] M. Kalinin, D. S. Raicu, J.D. Furst,et.al, A Classification Approach for Anatomical region Segmentation, IEEE International Conference on Image Processing, ICIP 2005, 1262-1265 (2005).

[156] D.S. Raicu, J.D. Furst , D. Channin, et.al, A Texture Dictionary for Human Organs Tissues'classification, In Proc.8th World Multiconf. on Systemics, Cybernetics and Informatics,Orlando, USA, Jul 2004

[157] K. Mala, V. Sadasivan and S.A. Alagappan, Neural Network based Textutre Analysis of Liver Tumor from Computed Tomography images, International Journal of Biological and Life Sciences. 2(1) pp:33-40.,2005

[158] A. Depeursinge, A. Geissbuhler, A. Platon, et.al, A classification framework for lung tissue categorization, J Digit Imaging. ; 23(1): pp.18–30. (2010)

[159] Vibha S. Vyas and Priti Rege, Automated Texture Analysis with Gabor filter, GVIP Journal, Volume 6, Issue 1, July 2006, pp

[160] S.S. Sreejamole and L. Ganesan, Supervised classification of images using Textural features, International Journal of Soft Computing, 4(3), ,2009, pp.122-126

[161] S. Poonguzhali and G. Ravindran , Automatic classification of focal lesions in ultrasound liver imagers using combined texture features. Information Technology Journal, 7(1), 205-209, 2008

[162] V. Manian, R. Vásquez, and P. Katiyar Texture Classification Using Logical Operators, IEEE Transactions On Image Processing, Vol. 9, NO. 10, October 2000, pp. 1693-1703

[163] Hong-Choon Ong, Hee-Kooi Khoo, Improved Image Texture Classification Using Grey Level Co-occurrence Probabilities with Support Vector Machines Post-Processing, European Journal of Scientific Research, Vol.36, No.1 (2009), pp.56-64

[164] B.V. Ramana Reddy, M. Radhika Mani, K.V. Subbaiah, Texture Classification Method using Wavelet Transforms Based on Gaussian Markov Random Field, International Journal of Signal and Image Processing (Vol.1-2010/Iss.1), pp 35-39.

[165] M.E. Osadebey, Integrated Content-Based Image Retrieval Using Texture, Shape and Spatial Information , Master Thesis Report in Media Signal Processing, Department of Applied Physics and Electronics, Umea University, Umea , Sweden.

[166] P.S.Hiremath, S.Shivashankar, Texture Classification using Wavelet Packet Decomposition, GVIP Journal, Volume 6, Issue 2, September, 2006,pp. 77-80,

[167] S. C. Kim, T. J. Kang, Texture classification and segmentation using wavelet packet frame and Gaussian mixture model, Pattern Recognition 40 (2007) pp.1207 – 1221

[168] J.C. Fu, S.K. Lee, S.T.C. Wong, et.al., Image segmentation feature selection and pattern classification for mammographic microcalcifications, Computerized Medical Imaging and Graphics 29 (2005) 419–429

[169] M. Tuceryan and Anil K. Jain, Texture Analysis, The Handbook of Pattern Recognition and Computer Vision (2nd Edition), by C. H. Chen, L. F. Pau, P. S. P. Wang (eds.), pp. 207-248, World Scientific Publishing Co., 1998.

[170] H. Wibawanto, A. Susanto, T. S. Widodo, Discriminating Cystic and Non Cystic Mass using GLCM and GLRLM-based Texture Features, International Journal of Electronic Engineering Research, Volume 2, Number 4 (2010) pp. 569–580

Chapter 4

Basic Theory of Image Segmentation and Texture Quantification Techniques

The basic image processing techniques involved in this research are explained in this chapter. The main techniques used are based on segmentation, representation and description. The theoretical back ground of segmentation includes binary and gray level mathematical morphological operations, different thresholding techniques and correlation filtering techniques. Validation methods used for segmentation of medical images are also discussed in this chapter. As a part of external representation, boundary extraction and as internal representation, texture analysis is also presented. Statistical texture feature extraction methods using first order statistics and gray level co-occurrence matrices are also explained. The chapter includes uses of box plot in feature selection procedures and an overview of decision tree and its applications in detection/ classification methods. A theoretical explanation of performance evaluation using Receiver operating characteristic curve is also presented in this chapter.

The initial step of any image processing application (after image enhancement) is segmentation of the object of interest. The various operations used for segmentation in this work are morphological operations, spatial domain filtering and thresholding.

4.1 Mathematical Morphology

This section gives an introduction to the theory and implementation details of morphological filtering techniques. Mathematical morphology is an algebraic method based on set theory that probes an image by a structuring element (SE) to filter or quantify an image according to the manner in which the SE fits (or does not fit) within the image [2]. The structuring information of the morphologically processed image depends on the size and shape of the SE. The basic morphological operations are dilation, erosion, opening and closing, applied to both binary and grayscale images.

Structuring elements are available in different shapes and types which are useful for segmentation, reconstruction and noise removal from images. Some of them are box, disk and line.

4.1.1 Binary Morphology

4.1.1.1 Erosion and Dilation

The basic fitting operation of mathematical morphology is erosion of an image by a structuring element. The erosion is computed by scanning the image with the structuring element. When the structuring element fits completely inside the image, the scanning position is marked. The erosion consists, boundary of all scanning locations where the structuring element fits inside the image. The erosion of set A by B is denoted by $A \ominus B$ and defined by Eqn. (4.1)

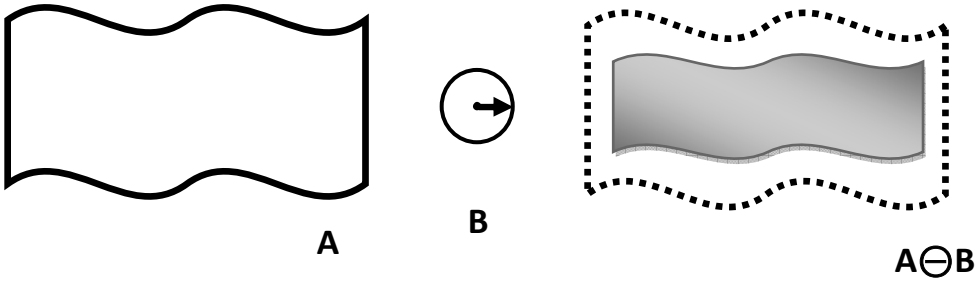

(a) (b) (c)

Fig.4.1 The erosion process. (a) Image A (b) Structuring element B with radius d/2 with origin at dotted point (c) Eroded image

$$A \ominus B = \{x : B_x \sqsubset A\} \quad (4.1)$$

where, A is the input image and B is the structuring element , $\sqsubset$ denotes the subset relation and $Bx = \{b+x : b \in B\}$ is the translation of set B by a point 'x'. Thus the shaded region in Fig.4.1 constitutes erosion of A by B. The boundary of the shaded region shows the limit beyond which further displacement of the origin of B, causes B to go outside the image boundary (beyond which B is fully contained in A).

One of the simplest uses of erosion is for eliminating irrelevant details from a binary image. A binary image is formed by the foreground and background pixels. In mathematical morphology, for every operator that changes the foreground, there is a dual operator that changes the background. The dual operator for erosion is dilation. Since dilation involves a fitting into the complement of an image, it represents a filtering on outside, where as erosion represents a filtering on the inside.

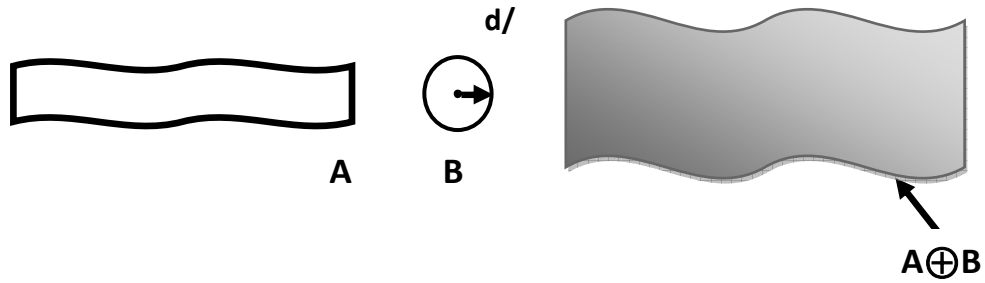

Fig 4.2 The dilation process. Figures from left to right- A is the image, B is the structuring element with radius d/2. Dilated image A⊕B

Formally, the dilation of set A by B, denoted by $A \oplus B$, is defined by Eqn.(4.2)

$$A \oplus B = (A^c \ominus \breve{B})^C \qquad (4.2)$$

where A^c denotes the set-theoretic complement of A and $\breve{B}=\{-b: b \in B\}$ is the reflection of B, i.e., a 180^0 rotation of B about the origin. Foreground is generally associated with white color while background is associated to black color. But note that in compression works, the inverse convention is sometimes used. Even though dilation process is based on set operations, the basic process of flipping the structuring element B, about its origin and successively displacing it so that it slides over set (image) A is analogous to the convolution process.

Dilation has the expected expanding effect as shown in Fig.4.2, filling in small intrusions into the image and erosion has a shrinking effect, eliminating small extrusions. As dilation by a disk expands an image and erosion by a disk shrinks an image, both can be used for finding boundaries of binary images. The three possibilities are:

1. *External boundary*: dilation minus the image.
2. *Internal boundary*: the image minus the erosion.
3. *Combined boundary*: dilation minus erosion.

The latter straddles the actual Euclidean boundary and is known as the morphological gradient, which is often used as a practical way of displaying the boundary of the segmented objects [2, 3].

4.1.1.2 Opening and Closing

Besides the two primary operations of erosion and dilation, there are two important operations that play key roles in morphological image processing, they being opening and its dual, closing. The opening of an image A by a structuring element B, denoted by $A \circ B$, is the union of all structuring elements that fit inside the image (Fig. 4.3)

$A \circ B = \cup\{B_x : B_x \subseteq A\}$ where $\cup\{\bullet\}$ denotes the union of all sets inside the braces.

or

$$A \circ B = (A \ominus B) \oplus B \tag{4.3}$$

Thus the opening of set A by B is defined as an erosion of A by B followed by a dilation by B. Opening generally smoothes the contour of an object, breaks narrow isthumuses and thin protrusions [2]. The opening operation has a simple geometric interpretation as shown in Fig 4.3, the boundary of $A \circ B$ is established by the points in B that geometrically fits with boundary of A. The opening of A by B by taking the union of all translates of B that fit into A.

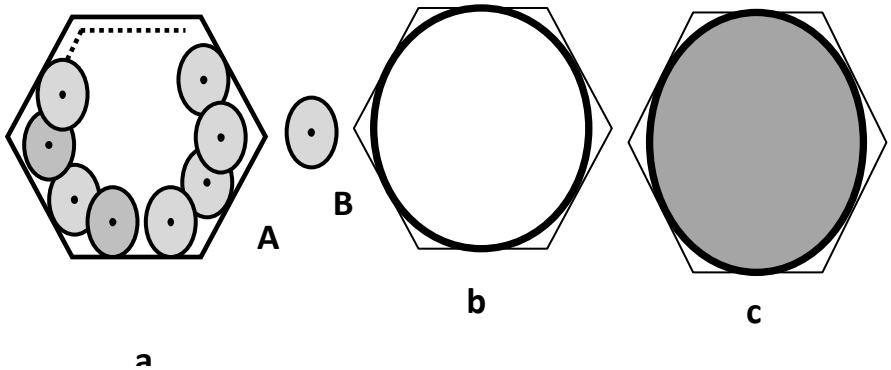

Figure 4.3 Morphological opening. a) Structuring element B rolling along inner boundary of A ,b) the heavy line is the outer boundary of the opening. c) Completed opening (shaded)

Dual version of opening, called 'closing' (Fig. 4.5, right), which is defined by

$A \bullet B = (A^c \circ \check{B})^C$ or
$A \bullet B = (A \oplus B) \ominus B$ (4.4)

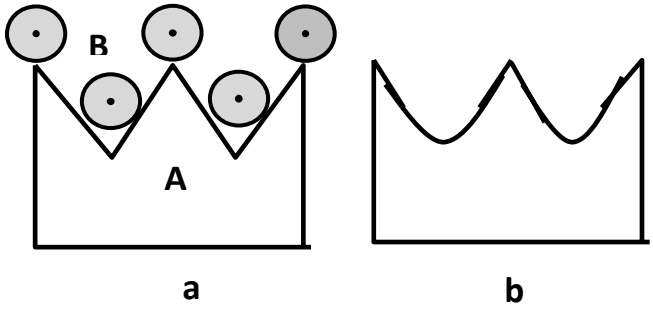

Figure 4.4 Morphological closing operation a) Structuring element B rolling outer boundary of set A, b) Set A after closing.

Closing has same geometric interpretation as opening, except that structuring element B is rolling on outside the boundary. Geometrically, a point *w* is an element of $A \bullet B$, if and only if, $B_x \cap A \neq \emptyset$, for any B_x that contains *w*. Fig.4.4 illustrates the basic geometrical properties closing. Closing of A by B is simply the dilation of A by B, followed by the erosion of the result by B. From Fig.4.4, it can be noted that the inward pointing corners were rounded, whereas outward pointing corners remain unchanged, when a circular shaped structuring element is used.

Closing tends to smooth sections of contours, narrow breaks and long thin gulfs, eliminates small holes, fills gap in the contour. These operations can be used to construct filters similar to other types of spatial filters. It can reduce noise with light element on a dark background and as dark elements on the light background. A morphological filter consisting of opening followed by closing can be used to accomplish this objective. The back ground noise can be completely eliminated in the erosion stage of opening, if the structuring element selected is physically larger

than the noise component. The net effect of opening is to eliminate all noise components in both background and image. The opening followed by closing clean of noise specks, but has the disadvantage that images containing print ridges are not fully repaired [3].

As a filter, opening can clean the boundary of an object by eliminating small extrusions; however, it does this in a much finer manner than erosion, the net effect being that the opened image is a much better replica of the original than the eroded image. Analogous remarks apply to the closing, the difference being the filling of small intrusions.

When there is both union noise and subtractive noise, one strategy is to open to eliminate union noise in the background and then close to filling subtractive noise in the foreground. The open-close strategy fails when large noise components need to be eliminated but a direct attempt to do so will destroy too much of the original image. In this case, one strategy is to employ an Alternating Sequential Filter (ASF). Open-close (or close-open) filters are performed iteratively, beginning with a very small structuring element and then proceeding with ever-increasing structuring elements.

Note that whereas the position of the origin relative to the structuring element has a role in both erosion and dilation, it plays no role in opening and closing. However, opening and closing have two important properties [4]:

1. Once an image has been opened (closed), successive openings (closings) using the same structuring element produce no further effects.
2. An opened image is contained in the original image which, in turn, is contained in the closed image (Fig. 4.3 & 4.4).

As a consequence of this property, we could consider the subtraction of the opening from the input image, called opening top-hat, and the subtraction of the image from its closing called closing top-hat, respectively defined by Eqn. (4.5) and (4.6)

$$A\,\hat{o}\,B = A - (Ao\,B) \tag{4.5}$$

$$A\,\hat{\bullet}\,B = (A \bullet B) - A \tag{4.6}$$

4.1.2 Gray –Scale Morphology

In this section we extend to gray scale images the basic operations of dilation, erosion, opening and closing. Here, we deal with digital image functions of the form *f(x, y)* and *b(x, y),* where *f(x, y)* is the input image and *b(x ,y*) is the structuring element, itself a sub image function..

Mathematically, dilation and erosion of an image is represented as per Eqn. (4.7) & (4.8) using a SE '*b* 'to obtain I_1 and I_2 respectively.

$$I_1 = (f \oplus b) = max\{f(x-x', y-y') + b(x', y') \mid (x', y') \in D_b\} \qquad (4.7)$$

$$I_2 = (f \ominus b) = min\{f(x+x', y+y') - b((x', y') \mid (x', y') \in D_b\} \qquad (4.8)$$

where D_b is the domain of *b*, and *f (x, y)* is assumed to be equal to -∞ outside the domain of *f*. Eqn.4.7 implements a process similar to the concept of spatial convolution, with max operations replacing the sums of convolution and the additions replacing the products of convolution. Gray level dilation operation is rotating the structuring element about its origin and translating it to all locations in the image, just as convolution kernel is translated and rotated and then translated about the image. Fig.4.5 shows the dilated image when a disc shaped structuring element is used.

(a) (b)

Fig.4.5 Image after Gray level dilation with a disc shaped structuring element. (a) Original Image (b) Image after gray level dilation

One important difference between convolution and gray scale dilation is

that, in dilation, D_b a binary matrix defines which locations in the neighborhood are included in the max operation. In other words, for an arbitrary pair of coordinates (x_0,y_0) in the domain of D_b, the sum $f(x-x_0,y-y_0)+b(x_0,y_0)$ is included in the max computation only if D_b is 1 at those coordinates. If D_b is 0 at (x_0,y_0), the sum is not considered in the max operation.In gray scale operation, gray scale dilation usually is performed using flat structuring elements in which the value (height) of b is 0 at all coordinates over which D_b is defined. That is, $b(x',y')=0 \quad for\ (x',y') \in D_b$

In this case, the max operation is specified completely by the pattern of 0s and 1s in the binary matrix D_b, and the gray scale dilation equation simplifies to Eqn. 4.9

$$I_1 = (f \oplus b) = max\{f(x-x',y-y') \mid (x',y') \in D_b\} \qquad (4.9)$$

At each translated pixel location, the rotated SE values are added to the image pixel values and maximum is computed. The general effect of performing dilation on a gray scale image is two-fold: (1) if all values of structuring element are positive, the output image tends to be brighter than the input. (2) Dark details either are reduced or eliminated, depending upon how their values and shapes relate to the SE used for dilation.

The flat gray scale erosion is a local minimum operator, in which the minimum is taken over the set of pixel neighbors determined by the shape of D_b. gray scale erosion as per Eqn.4.8, translating the structuring element to all locations in the image. At each translated locations, the SE values are subtracted from the image pixel values and the minimum is taken. As with dilation, grayscale erosion is most often performed using flat structuring elements. Eqn.4.9 is similar in form to 2-D correlation, with the min operation replacing the sums of correlation and subtraction replacing the products of correlation. The equation for flat grayscale erosion is reduced to Eqn. 4.10

$$I_2 = (f \ominus b) = min\{f(x+x',y+y') \mid (x',y') \in D_b\} \qquad (4.10)$$

Thus, gray scale erosion is a local minimum operator, in which the minimum is taken over a set of pixel neighbors determined by the shape of D_b as shown in Fig. 4.6.

Fig.4.6 Image after Gray level erosion with a disc shaped structuring element. (a) Original Image (b) Image after gray level erosion

Erosion reduces the size of a segment and dilation leads to enlargement according to the size of the structuring element used and combination of these operations enable underlying object shapes to be identified and reconstructed from their noisy distorted forms. Dilation and erosion can be combined to achieve variety of effects. Subtracting an eroded image from its dilated version produces a morphological gradient of the image [2, 4].

4.1.2.1 Gray level Opening and closing

The expressions for opening and closing of gray scale images have the same form as their binary counter parts. The opening of f by the structuring element b denoted $f\ o\ b$, is defined as Eqn.4.11. The morphologically opened image is given Fig.4.7

$$fob = (f \ominus b) \oplus b \tag{4.11}$$

As before, this is simply the erosion of *f* by *b*, followed by the dilation of the result by b. Similarly closing of f by *b*, denoted *f•b*, is dilation followed by erosion (Eqn.4.12)

(a) (b)

Fig.4.7 Image after Gray level opening (a) Original Image (b) Image after gray level opening with a disc shaped structuring element

$$f \bullet b = (f \oplus b) \ominus b \tag{4.12}$$

Because opening suppresses bright details smaller than the structuring element, and closing suppresses dark details smaller than the structuring element, they are used often in combination for image smoothing and noise removal. This is shown in Fig.4.8.

(a) (b)

Fig.4.8 Image after Gray level closing with a disc shaped structuring element. (a) Original Image (b) Image after gray level closing

Opening removes small details of the outline of the segment without affecting the total size of the relevant regions. After opening operation, the output image undergoes closing operation. The closing is able to remove holes in the interior of a region and smooth its contour [4]. The size of segment is almost

maintained after the closing operation. The combination of opening followed by closing or closing followed by opening can suppress noise sufficiently [3, 4].

4.2 Spatial filtering techniques using convolution and Correlation

The principle objective of enhancement is to process an image, so that the result is more suitable than the original image for a specific application. Image enhancement technique falls into two broad categories: spatial domain methods and frequency domain methods. The term spatial domain refers to the image plane itself, and approaches in this category are based on direct manipulation of pixels. Frequency domain processing techniques are based on modifying the Fourier transform of an image.

The term spatial domain refers to the aggregate of pixels composing an image. Spatial domain methods are procedures that are directly on these pixels values. Spatial domain processes are denoted by the expression.

$$g(x,y) = T[f(x,y)] \tag{4.13}$$

where, *f(x, y)* is the input image, *g(x, y)* is the processed image, and *T* is an operator on *f*, defined over some neighborhood of *(x, y)*. In addition *T* can operate on a set of input images, such as, performing the pixel by pixel sum of *K* images for noise reduction.

The neighborhood was defined about a point *(x, y)* by using square sub area centered at *(x, y)* as shown in Fig.4.9. The center of the sub image is moved from pixel to pixel starting, at the top left corner. The operator T is applied at each location *(x, y)* to yield the output, '*g*', at that location. The process utilizes only the pixels in the area of the image spanned by the neighborhood [5].

Correlation and Convolution are basic operations for extracting information from images. They are in some sense the simplest operations that are performed on an image, but they are extremely useful. Moreover, because they are simple, they can be analyzed and understood very well, and they are also easy to implement and can be computed very efficiently. These operations have two key features: they are *shift-invariant*, and *linear*. Shift invariant means, performing the

same operation at every point in the image. Linear means, it replaces every pixel with a linear combination of its neighbors. These two properties make these operations very simple.

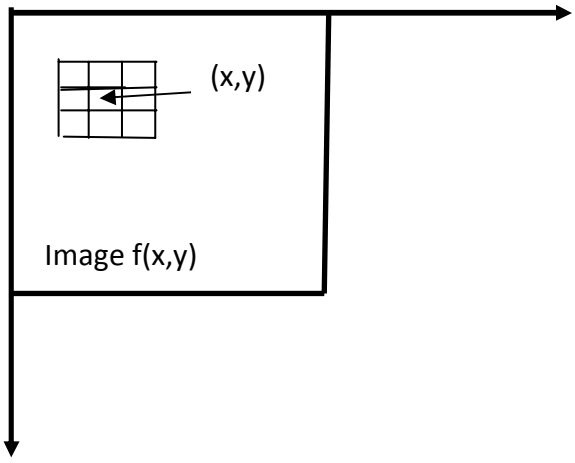

Fig.4.9. A 3x3 neighborhood about a point (x ,y) in an image

4.2.1 Correlation

Consider a square filter. Then the results of correlation can be computed by aligning the center of the filter with a pixel, and then multiply all overlapping values together, and add up the result. The corresponding mathematical expression can be written as Eqn.4.14.

$$F \circ I(x,y) = \sum_{i=0}^{N-1} \sum_{j=0}^{N-1} F(i,j) I(x+i, y+j) \qquad (4.14)$$

The importance of correlation is that, it is useful to find locations in an image that are similar to a template. To do this, consider the filter as a template and then slide it around the image looking for a location where the template overlaps the image so that values in the template are aligned with similar values in the image and the real correlation value is maximum[6]. The example for filtering using correlation shown in Fig.4.10

(a) (b)

Fig.4.10 Example for Correlation filtering. (a) Original Image (b) Image after correlation filtering

4.2.2 Convolution

Convolution is just like correlation, except that flip it over the filter before correlating. In the case of convolution, flip the filter both horizontally and vertically. This can be written as Eqn.4.15

$$F * I(x,y) = \sum_{i=0}^{N-1} \sum_{j=0}^{N-1} F(i,j) I(x-i, y-j) \quad (4.15)$$

Correlation and convolution are identical when the filter is symmetric. The key difference between the two is that convolution is associative[7]. That is, if *F* and *G* are filters, then Eqn.4.16

$$F*(G*I) = (F*G)*I. \quad (4.16)$$

In general, people use convolution for image processing operations such as smoothing, and they use correlation to match a template to an image. Correlation is not associative, because it does not really make sense to combine two templates into one with correlation, whereas in the case of convolution, two filters may be often combined together.

4.3 Thresholding

Suppose that gray level histogram shown in Fig.4.11 corresponds to an image *f (x,y)*, composed of light objects on a dark background, in such a way that objects on a dark background have gray levels grouped into two dominant modes. One obvious way to extract the objects from the background is to select a threshold *T* that separates these modes. Then at any point *(x, y)* for which *f(x, y) >T* is called an object point, otherwise, the point is called a background point.

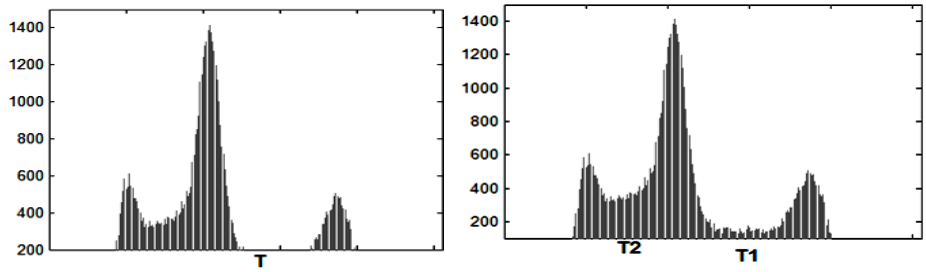

(a) (b)

Fig.4.11 Gray level histograms that can be partitioned by a) A single threshold b) Multiple thresholds

Fig. 4.11 (b) shows three different levels characterizing the image histogram. Here, multilevel thresholding classifies a point *(x, y)* as belonging to one object class if to other object class if $f(x,y) > T2$, and to the background if $f(x,y) \le T1$. Example for thresholded image is shown Fig.4.12

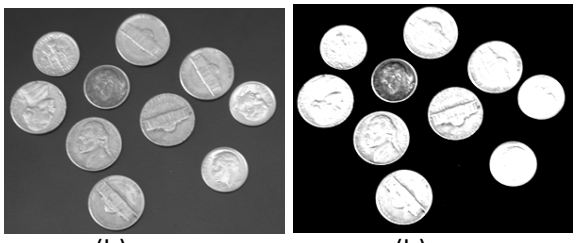

(b) (b)

Fig. 4.12 Example for Thresholding. (a) Original Image (b) Image after Thresholding

Thresholding can also be defined as the test against a function T of the form as represented in Eqn 4.17

$$T = T[x, y, p(x, y), f(x, y)] \tag{4.17}$$

where *f(x, y)* is the gray level of point *(x, y)* and *p(x, y)* denotes some local property of the point. A thresholded image *g(x, y)* is defined as Eqn 4.18

$$g(x, y) = \begin{cases} 1, & if\ f(x, y) > T \\ 0, & if\ f(x, y) \leq T \end{cases} \tag{4.18}$$

Thus, pixels labeled as 1 corresponds to objects, whereas pixels labeled as 0 corresponds to the background. When *T* depends only on *f(x, y)* (gray level values) the threshold is called *global*. If T depends on both *f(x, y)* and *p(x, y),* the threshold is called *local*. If, in addition, T depends on spatial coordinates x and y the threshold is called *dynamic or adaptive*.

In the case of global thresholding, partition the image histogram by using a single global threshold *T*. Segmentation is thus achieved by scanning the image pixel by pixel and labeling each pixel as object or background, depending on whether the gray level of that pixel is greater or less than the value of T. When applying a single threshold T midway between maximum and minimum gray levels, any pixel ≤ T is labeled as black (0) and any pixel with a gray level $> T$ is labeled as white (1) thus generating a binary object.

4.3.1 Adaptive Thresholding

In this case, the thresholds are fixed up automatically, which will produce minimum average segmentation error.

For choosing a threshold automatically, following iterative procedure has to be followed [2].

1. Select an initial estimate for T. Usually initial estimate is the midpoint between the minimum and maximum intensity values in the image.
2. Segment the image using *T*. This will produce two groups of pixels: G_1, consisting of all pixels with intensity values$\geq T$, and G_2, consisting pixels with values $< T$.

3. Compute the average intensity values μ_1 *and* μ_2 for the pixels in regions G_1 and G_2.

4. Compute a new threshold value: $T = \frac{1}{2}(\mu_1 + \mu_2)$.

5. Repeat steps 2 through 4 until the difference in T in successive iterations is smaller than a predefined parameter T_o.

4.4 Extraction and Labeling of Connected Components

The extraction of connected components in a binary image is central to many automated image analysis applications. The term connected component is defined in terms of a path, and the definition of a path in turn depends on adjacency. A pixel p at coordinates *(x,y)* has two horizontal and two vertical neighbors whose coordinates are *(x+1,y), (x-1,y), (x,y+1)* and *(x,y-1)*. This set of 4-neighbors of *p,* denoted N_4 *(p)*, is shaded in Fig.4.13a. The four diagonal neighbors of *p* have coordinates *(x+1,y+1), (x+1,y-1), (x-1,y+1)*, and *(x-1,y-1)* are denoted as $N_D(p)$. The $N_4(p)$ and $N_D(p)$ are the 8-neighbors of *p,* denoted $N_8(p)$ (Fig.4.13b). Two foreground pixels p and q are said to be 4-connected if there exist a 4-connected path between them, consisting entirely of foreground pixels (Fig 4.13c). For any foreground pixel *p,* the set of all foreground pixels connected to it, is called the connected component containing *p.* Identification and labeling of connected component in binary images (see Fig. 4.14) are widely used for automatic segmentation systems [2].

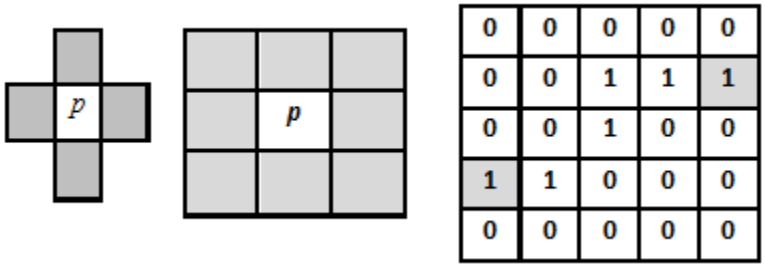

Fig. 4.13 Structure of a connected component. a) Pixels p and its 4-neighbours $N_4(P)$, b) Pixels p and its 8-neighbours c) The shared pixels are both 4 connected and 8 connected.

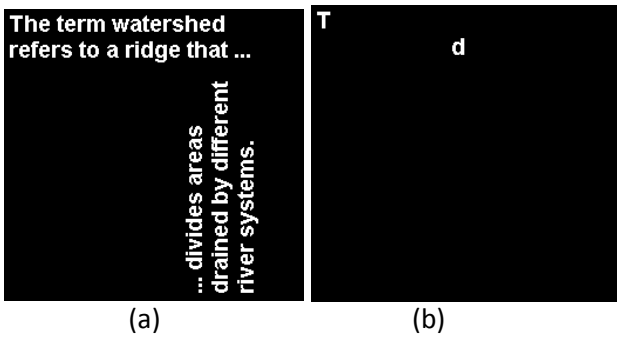

Fig.4. 14 Example for connected component labeling. (a) Original Image (b) Image after connected component labeling

4.5 Validation Methods for segmentation algorithm used in medical images- A Theoretical approach

In medical imaging, the accuracy of segmentation technique is very important. Hence all segmentation methods have to be evaluated. While several systems for segmentation of medical data are currently in use in various research laboratories and hospitals, the issue of correct validation is often ignored. A validation method can be thought of as a combination of two components. One component is the notion of a 'ground truth' against which the results of an algorithm are to be judged. The second component is a measure for establishing the deviation of the results from its ground truth. For their second component, most validation schemes use standard statistical methods of finding means, modes, variances, standard deviations, or root mean squared errors. The first component requires developing the notion of a ground truth for a segmentation algorithm and that is where one tends to run into difficulty. The problem is not that there is no ground truth for medical data, but that the ground truth is not typically available to the segmentation systems in any form that they can readily be used. In this section, the methods that have been typically used for validation of segmentation algorithms is briefly summarized.

The following are representative of schemes used for validation of medical segmentation results.

- Method 1: visual inspection
- Method 2: comparison with manual segmentation
- Method 3: testing on synthetic data
- Method 4: use of fiducials on patients
- Method 5: use of fiducials and/or cadavers

Visual inspection and comparison with manual segmentation are very strenuous and are not reliable since the amount of data to be processed is usually large. Here, we depict three different measures for quantitatively evaluating segmentation results.

(1) The misclassification rate (MCR) is the percentage of misclassified pixels and is computed as (background pixels were ignored in the MCR computation)

$$MCR = \frac{number\ of\ misclassified\ pixels}{Total\ number\ of\ all\ pixels} \times 100\% \qquad (4.19)$$

(2) The root mean squared error (RMSE) is to quantify the difference between the true partial volumes and the algorithm estimations. The RMSE of an estimator $\hat{\theta}$ with respect to the estimated parameter θ is defined as [8]:

$$RMSE(\hat{\theta}) = \sqrt{\mathrm{MSE}(\hat{\theta})} = \sqrt{\left(\mathrm{E}(\hat{\theta} - \theta\right)^2} \qquad (4.20)$$

E-is the error between two images,ie original image and noise added image.

Let N_{fp} be the number of pixels that do not belong to a cluster and are segmented into the cluster, N_{fn} be the number of pixels that belong to a cluster and are not segmented into the cluster, N_p be the number of all pixels that belong to a cluster, and N_n be the total number of pixels that do not belong to a cluster. Three parameters in this evaluation system may now be defined as follows [9]

- Under segmentation (*UnS*): $UnS = \frac{\mathrm{N}fp}{\mathrm{N}n}$, representing the percentage of negative false segmentation;
- Over segmentation (*OvS*): $OvS = \frac{\mathrm{N}fn}{\mathrm{N}p}$, representing the percentage of positive false segmentation;
- Incorrect segmentation (*InC*): $\frac{\mathrm{N}fp+\mathrm{N}fn}{N}$, representing the total percentage of false segmentation.

Correct segmentation means there is no under segmentation and over segmentation.

4.6 Representation

After an image has been segmented into regions based on the methods mentioned above the segmented pixels can be represented and described in a form suitable for further processing. Basically representing a region can be done in two ways- First one is, in terms of its boundary (external characteristics) and second one, in terms of pixels comprises its regions (internal characteristics). Representation scheme is chosen for making analysis of the selected region. An external representation is chosen when the primary focus is on shape characteristics. An internal representation is selected when the primary focus is on regional properties, such as color and texture. In either case, the features selected as descriptors should be as insensitive as possible to variations in size, translation, and rotation [10].Choosing a representation of a region is only a part of making data useful to analysis. Next task is to describe the region based on chosen representation. This chapter is giving special emphasis on internal characteristics of segmented region, that is, texture, texture description and quantification of its texture content.

4.6.1 Boundary of a region

Boundary of a region classified in terms of external characteristics of a region. A region is a connected component, and the boundary of a region is set of pixels in the region that have one or more neighbors that are not in the region. The points on a boundary are ordered, if they form a clockwise or counter clockwise sequence. A boundary is said to be minimally connected if each of its points has exactly two 1-valued neighbors that are not 4-adjacent. In order to find out the boundaries, the 2D coordinates are organized as *npx 2* arrays, where each row is an *(x, y)* coordinate pair, *np* is the number of points in the region or boundary. The exterior boundary of a region can be obtained with desired 4 or 8 connectivity with specified direction. Fig 4.15 shows the boundary of a set of regions with 4-connectivity [2].

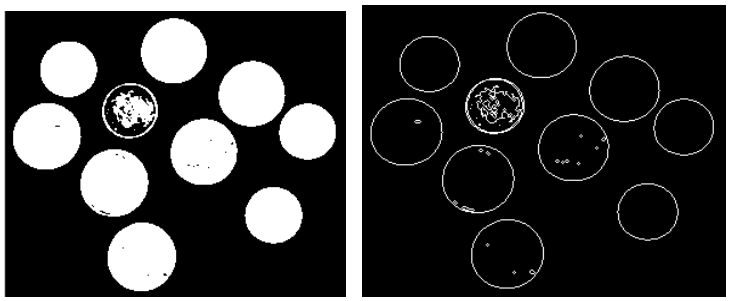

(a) (b)

Fig.4.15 Boundary representation a) Original Image b) 4-connected boundary

4.6.2 Texture

Texture is an internal representation of a region. A texture perceived by humans is a visualization of complex patterns composed of spatially organized, repeated sub patterns, which have a characteristic, somewhat uniform appearance. The local sub patterns within an image are perceived to demonstrate specific brightness, color, size, roughness, directivity, randomness, smoothness, granulation, etc. A texture may carry substantial information about the structure of physical objects [1].

The main challenge has been to describe the properties of texture in an image numerically for meaningful quantitative analysis. Quantitative analysis in textures is essential in many tasks such as classification of images based on their textures, segmentation of an image into homogeneous regions, synthesizing texture for computer graphics and image retrieval based on texture. However, it is very difficult to describe in precise terms what we visually perceive as texture, even though being able to visually distinguish one texture from another comes to us naturally. As a result, there is no unique definition for texture. We can characterize a texture by its properties as we perceive them based on visual and tactile senses. For example, we can describe a certain texture with such terms as ‘net-like’, ‘rough’ or ‘smooth’. Therefore, a good approach to quantitative analysis of textures is to first describe a texture in a way that is perceptually and intuitively meaningful and then try to measure these properties in order to approximate visual perception

[5]. Spectral approaches are based on the properties of Fourier spectrum and are particularly suited to periodic or semi-periodic shapes. Three important things can be done using Fourier spectrum: Dominant peaks of the spectrum show the main texture feature direction which depicts the fundamental spatial period of the texture from the peak frequency and isolates non-periodic objects by filtering out periodic components of the spectrum [6].

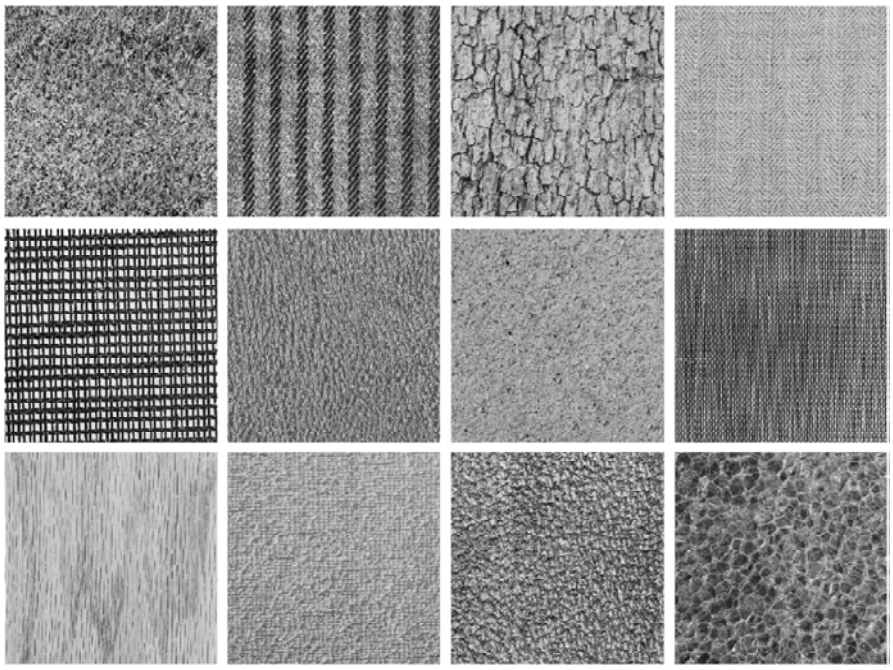

Fig.4.16. Examples of different types of Textures

4.6.2.2 Statistical Methods

Numerous texture analysis methods have been proposed in the past four decades for measuring textural properties. One of the first and most widely used methods is the extraction of second order statistics based on *pairs* of gray-level distributions in the image [5]. In statistical texture analysis, texture features are computed from the statistical distribution of observed combinations of intensities at

specified positions relative to each other in the image. According to the number of intensity points (pixels) in each combination, statistics are classified into first-order, second-order and higher-order statistics.

In medical image processing, texture is especially important, because it is difficult to classify human organ tissues using shape or gray level information. Some of the challenges are: 1) the shape of each organ is not consistent throughout all slices of a 3D medical image and may change quickly where the inter-slice distance is large, and 2) the gray level intensities overlap considerably for soft tissues. On the other hand, organs are expected to have consistent and homogeneous textures within tissues [3].

The most important characterizing factor of the texture is coarseness [4]. An image must have a certain level of coarseness for it to have meaningful texture and this is determined by the size of its textural primitives or equivalently, the scale of the image. At one extreme, the textural primitives can be so small that they become dots, indicating the highest level of fineness, in which case, the image can be described as white noise. On the other extreme, the textural primitive can be so large that only one can fit in the image. In both cases, there is no meaningful texture in the images. Once we ensure that there is a certain level of texture in an image, the challenge is to characterize the texture in meaningful terms.

4.6.2.2.1 First order statistics

Simple first-order statistical texture properties can also be computed directly from the image. These methods measure basic statistical variations in gray-levels and are mostly based on the histogram of an image, which counts the total number of pixels with a given gray value within the image. Hence, a normalized histogram gives the probability that a given pixel in the image has a certain gray level value. Some simple first-order statistics include mean, variance and skewness of the distribution of gray-levels. One of the simplest approaches for describing texture is to use statistical moments of gray level histogram of an image or region. Let z be a random variable denoting gray levels and let $p(z_i)$, i=0,1,2….L-1, be the corresponding histogram, where L is the distinct gray levels.

A frequently used approach for texture analysis is based on the statistical properties of histogram. One class of such measures is based on statistical moments (Eqn.4.21).

$$\mu_n = \sum_{i=0}^{L-1}(z_i - m)^n p(z_i) \quad (4.21)$$

where m is the mean value of z (average gray level) given by

$$m = \sum_{i=0}^{L-1} z_i p(z_i) \quad (4.22)$$

'm' is a measure of average intensity (n=0) (Eqn.4.22).

$$1. Stanard\ deviation\ \sigma = \sqrt{\mu_2(z)} = \sqrt{\sigma^2} \quad (4.23)$$

$\mu_2(z)$, the second moment, is. σ^2, the variance (Eqn.4.23) which is a measure of average contrast.

For any region of interest, the *mean* and the *standard deviation* of the gray values in the region can be used to measure the spread of gray values of the pixels within that region. For example, a relatively *dark* region with a texture that can be characterized as *homogeneous* has a relatively low mean and a low standard deviation, assuming that the lowest gray level value is black and the highest is white on the gray color spectrum. The mean and standard deviation represent the gray level distribution in the region of interest.

$$2. Smoothness\ R = 1 - \frac{1}{1+\sigma^2} \quad (4.24)$$

Smoothness R measures relative smoothness of intensity in a region. R is 0 for a region of constant intensity and approaches 1 for regions with large excursions in the values of its intensity levels.

3.Third moment $\mu_3 = \sum_{i=0}^{L-1}(z_i - m)^3\, p(z_i)$ (4.25)

It, measures the skewness of a histogram. This measure is 0 for symmetric histograms, positive for histograms skewed to the right and negative for histograms skewed to the left.

4.Uniformity $U = \sum_{i=0}^{L-1} p^2\,(z_i)$ (4.26)

This measure is uniform when all gray levels are equal.

5. Entropy $e = -\sum_{i=0}^{L-1} p(z_i) \log_2 p(z_i)$ (4.27)

Entropy is a measure of randomness. Another useful statistics is entropy [13], which can be used in regions of interest from both raw and texture images. Given a region of interest in a grayscale image, entropy is a function of pixel intensities (or probabilities), which measures *uncertainty* in the region of interest. If the histogram of the region, which describes the frequency distribution of the gray level values, is taken to be a probabilistic distribution, then the entropy computed using the histogram, is a measure of the region's *randomness*. Let $h = h1, \ldots\ldots, hn$ be a normalized histogram of an image, where hi for $i = 1, \ldots\ldots, n$ is the frequency of gray values that fall into bin i. Then the entropy for the image is given by equation 4.27.

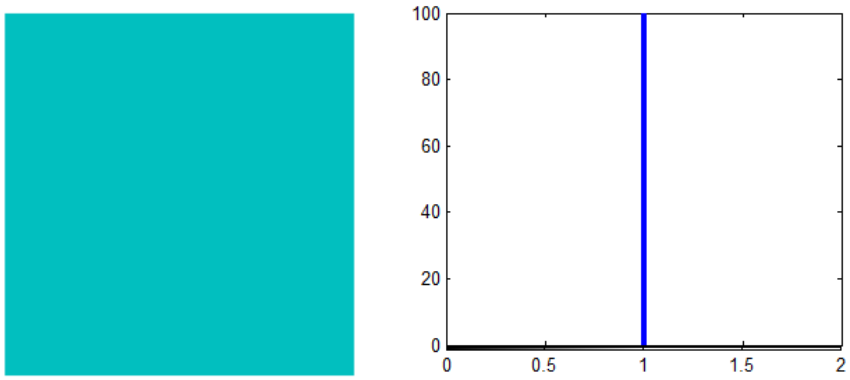

Fig. 4.17 An image with gray level value equal 1: entropy 0

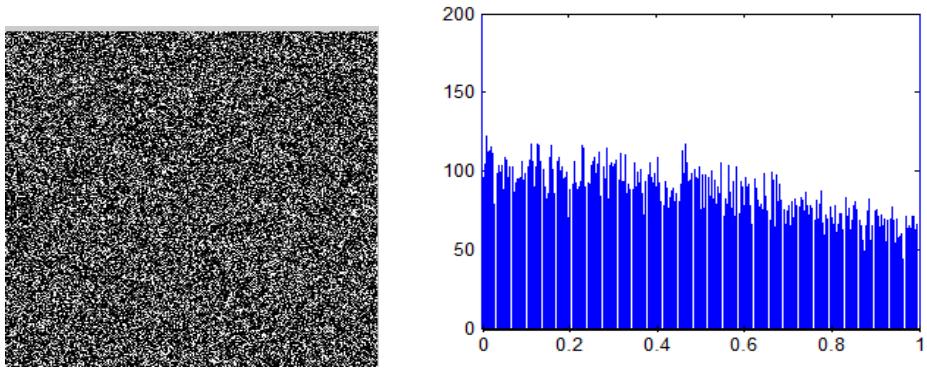

Fig. 4.18 An image with uniform noise: entropy 4.15

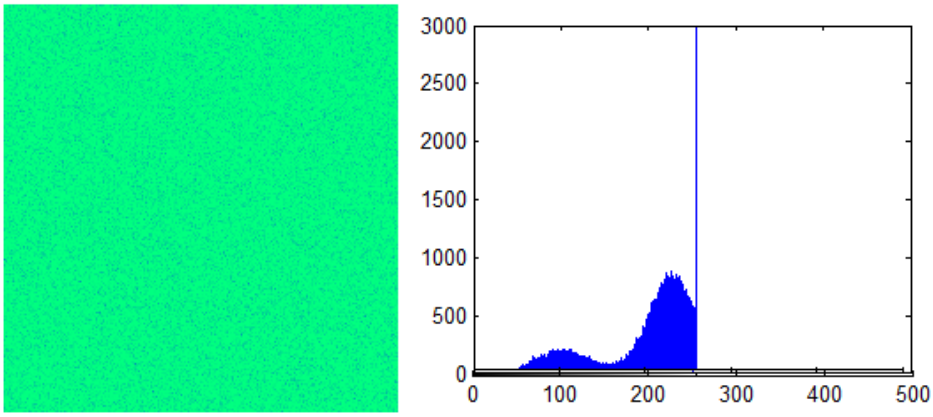

Fig.4.19 An image added with Gaussian noise: entropy 5.6

The smoothness, coarseness and periodicity of image regions can be assessed by using these first order statistical features. For example, the entropy of the coarse region is higher than the smoother regions because the values of pixels in that region are more random than the values in the other regions. This is also true when contrast and average intensity is high. Then that region is less smoother and less uniform than other images. Third moment of coarse texture region is less symmetric than other regions. An image with a *uniform* distribution of gray values has a high rate of randomness. In other words, the probability that a given pixel has a certain gray value is equal to the probability that the pixel has any other gray value. In this case the uncertainty is maximum. As an example, consider an image whose pixels have only binary values: 1 or 0. Also assume that half the pixels in the image are 1 and the rest are 0 (in which case the distribution is uniform). In this case, given a random pixel in the image, one cannot say with a high level of certainty that this pixel has a value of 1 (or 0), since the probability of any value occurring is 0.5. Therefore, the entropy, or equivalently the randomness, is 0.5. On the other hand, if an image has only values of 1, then one can say with 100% certainty that any given pixel in the image will have the value 1. Therefore, the uncertainty for such an image is minimized and the entropy is 0. Fig. 4.17, Fig.4.18

and Fig. 4.19 show three images with their corresponding histogram and entropy measures; Fig. 4.18 generated by uniform noise, Fig. 4.19 generated by Gaussian noise and in Fig. 4.17, all pixels have the value one and entropy =0 respectively.

4.6.2.2.2 GLCM based second order statistics

The basic statistical tools, introduced earlier, extract *first order* features. First order statistics are measures that do not take into account the location of gray values relative to each other. Therefore, if the pixels in a region of interest were to be scrambled, these statistical results would remain the same. Gray Level Co-occurrence Matrices (GLCM), first introduced by Halarick, et.al [6], uses *second order statistics*. The central idea behind GLCMs is that gray values of pairs of pixels and their relative positions characterize certain textural properties. Haralick et al. introduced a method based on Gray-Tone Spatial Dependence Matrices (also known as Gray-Level Co-occurrence Matrices), which assumes that the textural properties of a region can be determined from the overall or average spatial relationship between the gray levels in an image [5]. More specifically, a co-occurrence matrix collects information regarding the distribution of pairs of pixels within an image according to a displacement rule, which is defined by a distance and an angle.

For a given distance d and angle θ, the entry (i, j) in a normalized co-occurrence matrix $P(d, \theta)$is the joint probability that a pixel with gray value j appears at a distance d and angle θ with respect to a pixel with gray value i. Fig. 4.20 shows the direction of GLCM generation. From the center ($\oplus$) to the pixel 1 representing direction = 0° with distance d =1, to the pixel 2 direction = 45° with distance d = 1, to the pixel 3 direction = 90° with distance d = 1, and to the pixel 4 direction = 135° with distance d = 1. Second-order statistics have a higher correlation with human visual perception [7].

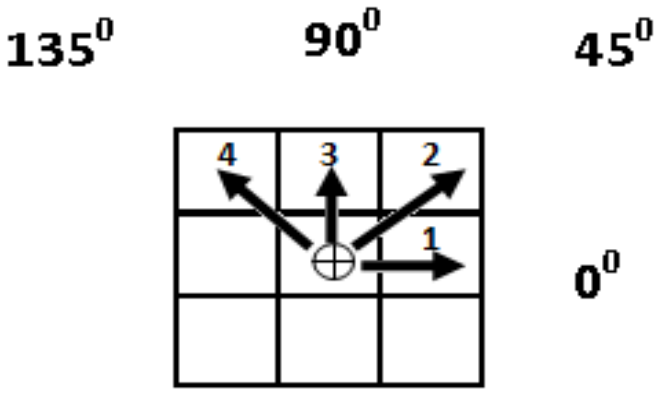

Fig.4.20 Direction of GLCM generation.

1. GLCM Construction

The first step in building co-occurrence matrices is to specify a neighborhood structure, which in turn is used to construct the co-occurrence matrices from the region of interest in the grayscale image. Then second order statistics are computed on the co-occurrence matrices to characterize certain textural properties in the region of interest.

If there are' n' gray levels in an image, for a given region of interest in the image, the dimension of each co-occurrence matrix is *n*-by-*n*. The number of co-occurrence matrices is equal to the number of offsets in the neighborhood structure. Each row of a co-occurrence matrix represents the gray level of a pixel being referenced and the columns represent the gray levels of pixels that are offset to the reference pixel. Therefore, the number *kij* located at row *i* and column *j* of the co-occurrence matrix representing offset *O*, indicates the number of times gray level *gi* appears with gray level *gj* offset by *O* [8-10].

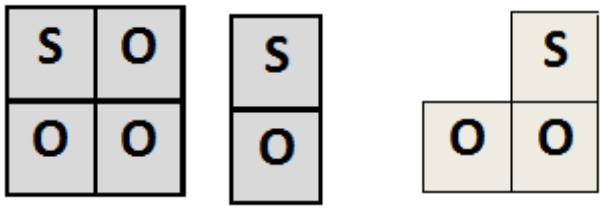

Fig. 4.21: Sample gray scale neighborhood structures, having two offsets.

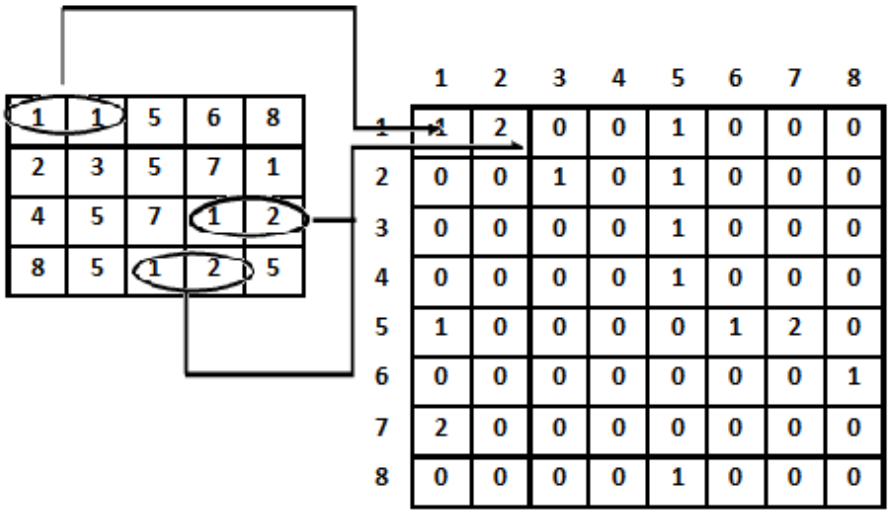

Fig. 4.22 Construction of GLCMs.

Figure 4.21 shows the co-occurrence matrices built for a sample gray scale image using a neighborhood structure that has two offsets, each located at a distance of one from the reference pixel. Once the gray level co-occurrence matrices are constructed (Fig.4.22), then each matrix *M* is normalized to transform the values *Mij* from number of co-occurrences to probabilities (*Pij)* of co-occurrences (Eqn.4.28): On the left, the grayscale image has 8 gray levels with values 1 to 8. Therefore, each co-occurrence matrix is 8-by-8. The neighborhood

structure has 2 offsets and there is one co-occurrence matrix for each offset. In each matrix, the rows represent the gray levels of reference pixels and the columns represent the gray levels of offset pixels. For example, in the matrix for the offset left, as demonstrated in the Figure, gray level 1 appears two times with gray level 2 to its left. Such properties include energy (which measures 'orderliness'), contrast, correlation (which measures gray-level linear dependencies) and more. Many of these properties correlate with each other, thus computing all of them would be redundant. Given normalized co-occurrence matrices, certain statistical properties can be measured that describe certain textural properties of the image. For example, the co-occurrence values appearing along the diagonal of a co-occurrence matrix represent the frequency at which pixels with the same gray levels occur together in the image. If for a certain image, the values along the diagonals of its co-occurrence matrices are large, then this image must have little contrast as this means adjacent pixels have similar values. On the other hand, if the values farther away from the diagonal of the co-occurrence matrices are more significant, then the image must have high contrast. The following are some statistical tools used to extract textural properties from a normalized co-occurrence matrix.

$$P(i,j) = \frac{M_{ij}}{\sum_{i=1}^{n}\sum_{j=1}^{n} M_{ij}} \tag{4.28}$$

$$P = (P_{i,j}) \tag{4.29}$$

A number of texture features may be extracted from the GLCM [12]. We use the following notation: G is the number of gray levels used. μ is the mean value of P (Eqn. (4.29) μ_x, μ_y, σ_x and σ_y are the means and standard deviations of P_x and P_y. $P_x(i)$ (Eqn.4.30)is the ith entry in the marginal-probability matrix obtained by summing the rows of $P(i, j)$ and $P_y(j)$ (Eqn. 4.31) jth entry in the marginal-probability matrix obtained by summing the columns of $P(i, j)$ [11,12].

$$P_x(i) = \sum_{j=0}^{G-1} P(i,j) \tag{4.30}$$

$$P_y(j) = \sum_{i=0}^{G-1} P(i,j) \tag{4.31}$$

$\mu_{\mathrm{x}} = \sum_{\mathrm{i}=0}^{\mathrm{G}-1} \mathrm{i} \sum_{\mathrm{j}=0}^{\mathrm{G}-1} P(i,j) = \sum_{\mathrm{i}=0}^{\mathrm{G}-1} \mathrm{i} \sum_{\mathrm{j}=0}^{\mathrm{G}-1} P_x(i,j)$

$\mu_{\mathrm{y}} = \sum_{\mathrm{j}=0}^{\mathrm{G}-1} \mathrm{j} \sum_{\mathrm{i}=0}^{\mathrm{G}-1} P(i,j) = \sum_{\mathrm{j}=0}^{\mathrm{G}-1} \mathrm{j} P_x(i,j)$

$\sigma_x{}^2 = \sum_{i=0}^{G-1} (i - \mu_{\mathrm{x}})^2 \sum_{j=0}^{G-1} P(i,j) = \sum_{i=0}^{G-1} (P_x(i) - \mu_{\mathrm{x}}(i))^2$

$\sigma_y{}^2 = \sum_{j=0}^{G-1} (j - \mu_{\mathrm{x}})^2 \sum_{i=0}^{G-1} P(i,j) = \sum_{i=0}^{G-1} (P_y(j) - \mu_{\mathrm{y}}(j))^2$

and $P_{x+y}(k) = \sum_{i=0}^{G-1} P(i,j) \qquad i + j = k$

for k = 0, 1, ..., 2(G − 1).

$P_{x-y}(k) = \sum_{i=0}^{G-1} P(i,j) \qquad |i - j| = k$

for k = 0, 1, ...,G − 1.

The following features are some of the important features that are widely used:

1.Homogeneity, Angular Second Moment (ASM) :

$$ASM = \sum_{i=0}^{G-1} \sum_{j=0}^{G-1} \{P(i,j)\}^2 \qquad (4.32)$$

ASM is a measure of homogeneity of an image. A homogeneous scene will contain only a few gray levels, giving a GLCM with only a few but relatively high values of *P(i, j)*. Thus, the sum of squares will be high.

2.Contrast :

$$CONTRAST = \sum_{n=0}^{G-1} n^2 \sum_{i-0}^{G-1} \sum_{j=0}^{G-1} P(i,j) \qquad |i - j| = n \qquad (4.33)$$

This measure of contrast or local intensity variation will favour contributions from *P(i, j)* away from the diagonal, i.e. $i \neq j$.

3.Entropy :

$$ENTROPY = \sum_{i=0}^{G-1}\sum_{j=0}^{G-1}(\mathrm{P(i,j)} \times \log(\mathrm{P(i,j)}) \quad (4.34)$$

Homogeneous scenes have low first order entropy

4.Correlation :

$$CORRELATION = \sum_{i=0}^{G-1}\sum_{i=0}^{G-1}\frac{\{i\times j\}\times P(i,j)-\{\mu_{\mathrm{x}}\times\mu_{\mathrm{y}}\}}{\sigma_x\times\sigma_y} \quad (4.35)$$

Correlation is a measure of gray level linear dependence between the pixels at the specified positions relative to each other [13].

5.Sum of Squares, Variance :

$$VARIANCE = \sum_{i=0}^{G-1}\sum_{j=0}^{G-1}(i-\mu)^2\,P(i,j) \quad (4.36)$$

This feature puts relatively high weights on the elements that differ from the average value of *P(i, j)*.

6.Sum Average :

$$AVER = \sum_{i=0}^{2G-2} iP_{x+y}(i) \quad (4.37)$$

7.Sum Entropy :

$$SENT = -\sum_{i=0}^{2G-2} P_{x+y}(i)\log\left(P_{x+y}(i)\right) \quad (4.38)$$

8.Difference Entropy :

$$DENT = -\sum_{i=0}^{G-1}(P_{x+y}(i)\log\left(P_{x+y}(i)\right) \quad (4.39)$$

9.Cluster Shade :

$$SHADE = \sum_{i=0}^{G-1}\sum_{j=0}^{G-1}\left\{i+j-\mu_{\mathrm{x}}-\mu_{\mathrm{y}}\right\}^3\times P(i,j) \quad (4.40)$$

10.Cluster Prominence

$$PROM = \sum_{i=0}^{G-1}\sum_{j=0}^{G-1}\left\{i+j-\mu_{\mathrm{x}}-\mu_{\mathrm{y}}\right\}^4\times P(i,j) \quad (4.41)$$

11.Energy

$$E = \sqrt{\sum_{i=0}^{G-1}\sum_{j=0}^{G-1}P^2}\,(i,j) \quad (4.42)$$

Energy is a measure of how uniform the texture is. Entropy is negatively correlated to energy and is a measure of randomness. When entropy is calculated based on co-occurrence matrices, it is a measure of randomness in co-occurrences,

as opposed to entropy that is calculated based on the values in a raw image. Contrast is also negatively correlated with homogeneity.

4.7. Box plot and its uses

Box plots are widely used for statistical analysis and interpretation of data [14]. It is a very useful tool for graphically portraying empirical distribution of data and its statistics, central location, skewness, outliners etc. The box plot of Fig.4.23 displays the characteristics of the empirical distribution for single data at a glance: location, spread, skewness, tail lengths and outliers ("wild" values). The box represents

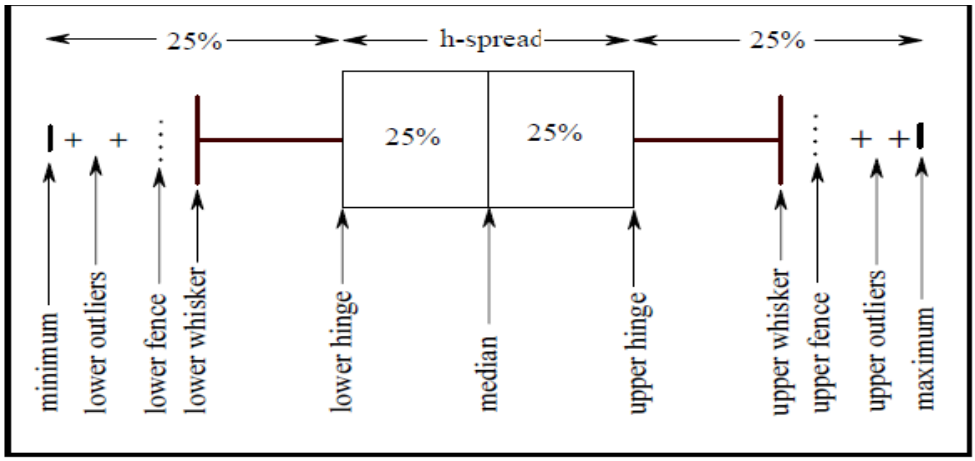

Fig.4.23 Box plot and its properties

50% of ordered data stretching between the lower hinge and the upper hinge which represent the lower and the upper quartile of the data respectively. The bar in this box indicates the median, which, by its position depicts the symmetry or skewness of the data. The two hinges, the median and the two extreme values (lowest and highest) are known as the 5-number summary. The box also describes the spread of the data symbolized by the h-spread, whereas its width shows the sample size. The whiskers include all data, from the hinges up to the lower and the upper fences which define the outliers (“wild data”) cutoffs. The cutoffs are found by

subtracting or adding a step (1.5 of the h-spread) to the lower and to the upper fences respectively. This means, in a given data set, 25% of the data can be arbitrarily wild without significantly affecting the median and hinges; and since the outlier cutoffs are defined by the h-spread, they are not affected by the outlier data and therefore can resist disturbances due the data. Comparing box plot medians is like a visual hypothesis test, analogous to the t test used for means. Box plots are very useful for finding the statistical significance between two datasets.

4.8 An overview of decision system

A decision tree is a classifier expressed as a recursive partition of the instance space. The decision tree consists of nodes that form a *rooted tree*, meaning it is a *directed tree* with a node called "root" that has no incoming edges. All other nodes have exactly one incoming edge. A node with outgoing edges is called an *internal* or test node.

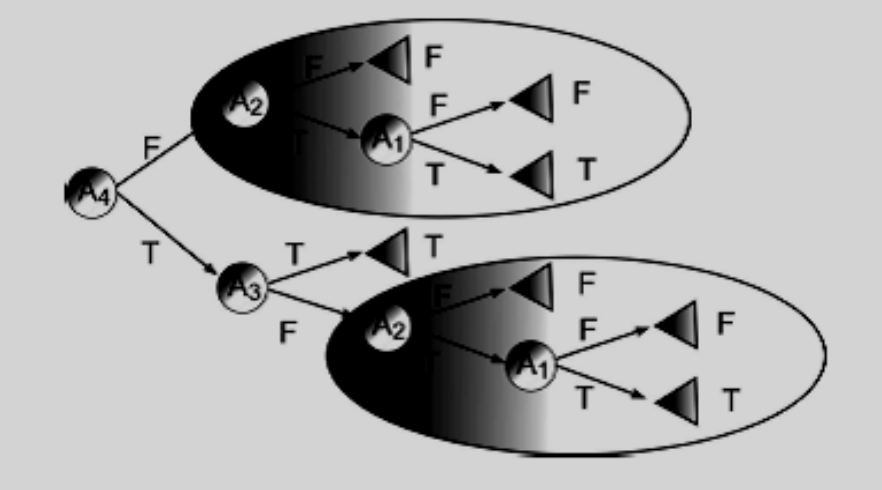

Fig.4.24. Illustration of decision Tree with Replication [14]

All other nodes are called leaves (also known as terminal or decision nodes). In a decision tree, each internal node splits the instance space into two or more sub-spaces according to a certain discrete function of the input attributes

values. In the simplest and most frequent case, each test considers a single attribute, such that the instance space is partitioned according to the attribute value. In the case of numeric attributes, the condition refers to a range. Each leaf is assigned to one class representing the most appropriate target value. Alternatively, the leaf may hold a probability vector indicating the probability of the target attribute having a certain value. Instances are classified by navigating them from the root of the tree down to a leaf, according to the outcome of the tests along the path [14]. Fig.4.24 shows the representation of decision trees.

4.8.1 Properties of Decision Trees

Several properties of the decision tree as a classification tool have been pointed out in the literature [24]:

1. Decision trees are self–explanatory and when compacted they are also easy to follow. In other words if the decision tree has a reasonable number of leaves, it can be grasped by non–professional users. Furthermore decision trees can be converted to a set of rules. Thus, this representation is considered as comprehensible. Decision trees are capable of handling datasets that may have missing values.
2. Decision trees can handle both nominal and numeric input attributes and its representation is rich enough to represent any discrete value classifier.
3. Decision trees are capable of handling datasets that may have errors.

4.9 Performance Assessment with Receiver Operating Characteristics (ROC) Curve

A binary classification model classifies each instance into one of two classes; say a *true* and a *false* class. This gives rise to four possible classifications for each instance: a true positive (TP), a true negative (TN), a false positive (FP), or a false negative (FN). This situation can be depicted as a confusion matrix (also called contingency table) given in Fig. 4.25. The confusion matrix juxtaposes the observed classifications for a phenomenon (columns) with the predicted classifications of a model (rows). In Fig. 4.25, the classifications that lie along the major diagonal of the table are the correct classifications, that is, the true positives

and the true negatives. The other fields signify model errors. For a perfect model we would only see the true positive and true negative fields filled out, the other fields would be set to zero. It is common to call true positives *hits*, true negatives *correct rejections*, false positive *false alarms*, and false negatives *misses*. A number of model performance metrics can be derived from the confusion matrix.

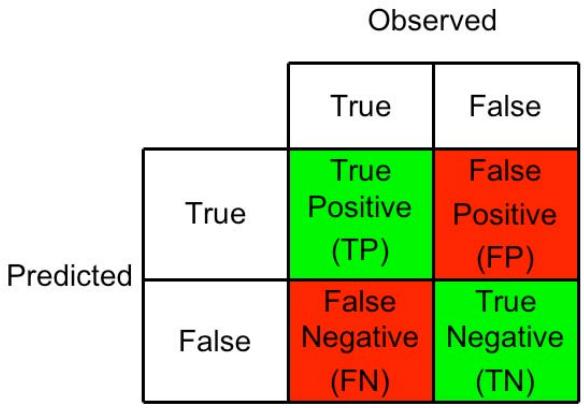

Fig. 4.25: Format of a Confusion Matrix

ROC curves are two-dimensional graphs that visually depict the performance and performance trade-off of a classification model [14]. ROC curves were originally designed as tools in communication theory to visually determine optimal operating points for signal discriminators [15]. Two new performance metrics need to be introduced to construct ROC curves (defined here in terms of the confusion matrix),- the *true positive rate* (TPR) and the *false positive rate* (FPR): To evaluate the performance of detection/classification model, specificity and sensitivity of detection were considered. Sensitivity and specificity are terms that show the significance of a test related to the presence or absence of the disease. Eqs. (4.43) and (4.44) are used to calculate these two parameters, respectively

$$Sensitivity = \frac{TP}{TP + FN} = TPR \tag{4.43}$$

$$Specificity = \frac{TN}{TN + FP} = TNR \tag{4.44}$$

ROC graphs are constructed by plotting the true positive rate (TPR) against the false positive rate (see Fig. 4.26).

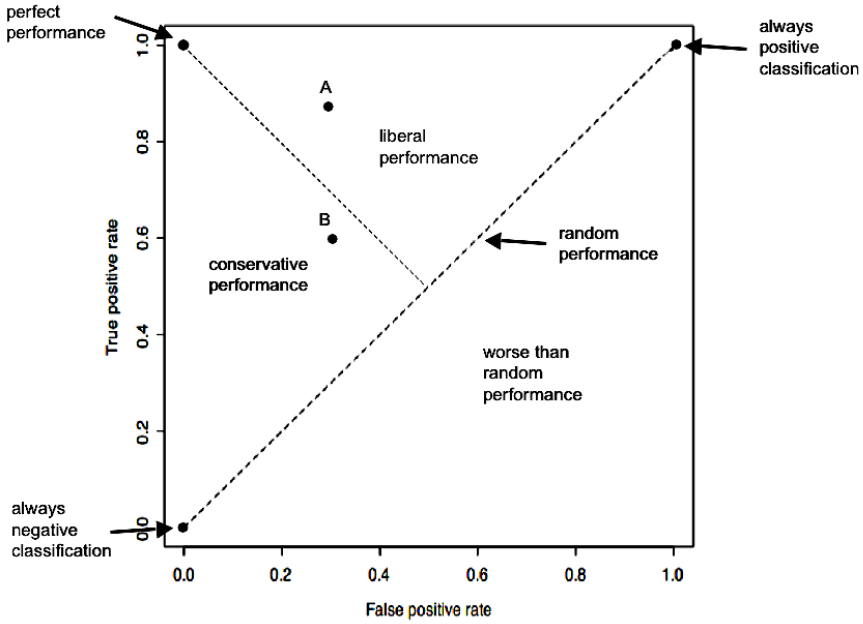

Fig.4.26: ROC curve: regions of a ROC graph

Identify a number of regions of interest in a ROC graph. The diagonal line from the bottom left corner to the top right corner denotes random classifier performance, that is, a classification model mapped onto this line produces as many false positive responses as it produces true positive responses. To the left bottom of the random performance line we have the conservative performance region. Classifiers in this region commit few false positive errors. In the extreme case, denoted by the point in the bottom left corner, a conservative classification model will classify all instances as negative. In this way it will not commit any false positives but it will also not produce any true positives. The region of classifiers

with liberal performance occupies the top of the graph. These classifiers have a good true positive rate but also commit substantial numbers of false positive errors. Again, in the extreme case denoted by the point in the top right corner, we have classification models that classify every instance as positive. In that way, the classifier will not miss any true positives but it will also commit a very large number of false positives. Classifiers that fall in the region to the right of the random performance line have a performance worse than random performance, that is, they consistently produce more false positive responses than true positive responses. However, because ROC graphs are symmetric along the random performance line, inverting the responses of a classifier in the "worse than random performance" region will turn it into a well performing classifier in one of the regions above the random performance line. Finally, the point in the top left corner denotes perfect classification: 100% true positive rate and 0% false positive rate. The ranking values are typically normalized to values between 0 and 1 (the default decision threshold for most classifiers is set to 0.5, if the ranking value expresses the actual probability value of the instance being classified as true). At each threshold increment, the performance of the model is computed in terms of the true positive and false positive rates and plotted. This traces a curve from left to right (maximum ranking to minimum ranking) in the ROC graph. It means that the left part of the curve represents the behavior of the model under high decision thresholds (conservative) and the right part of the curve represents the behavior of the model under lower decision thresholds (liberal).

Fig. 4.27 shows some typical examples of ROC curves. Part (a) depicts the ROC curve of an almost perfect classifier where the performance curve almost touches the 'perfect performance' point in the top left corner. Part (b) and part (c) depict ROC curves of inferior classifiers. At this level the curves provide a convenient visual representation of the performance of various models where it is easy to spot optimal versus sub-optimal models.

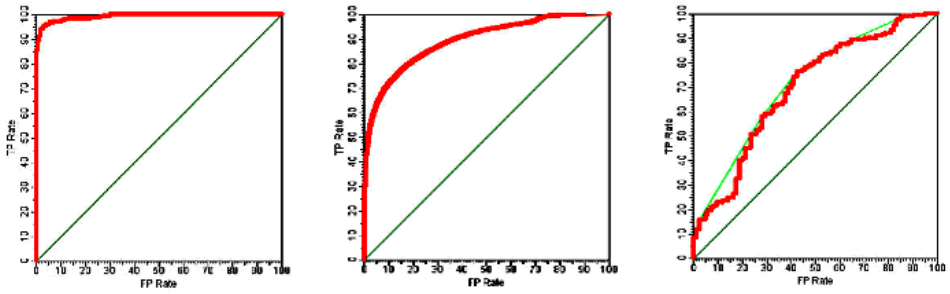

(a) (b) (c)

Fig.4.27 ROC curves: (a) an almost perfect classifier (b) a reasonable classifier (c) a poor classifier

When using ROC curves for checking the performance of classifiers to distinguish between normal an deceased cases, ROC curve parameters are sensitivity and specificity. Sensitivity indicates the number of subjects who have the disease and are accurately identified by positive test. Thus, it is a measure of the probability of correctly diagnosing a condition [15]. Specificity indicates the number of subjects who do not have the disease, and are accurately identified by negative test. Thus, it is a measure of the probability of correctly distinguishing when the condition is not present in a subject. Other statistical method known as relative operating characteristic (ROC) curve is also used to analyze the experimental results. ROC curve is a graphical plot of the sensitivity against specificity for a binary classifier system as its discrimination threshold is varied [15]. The ROC can also be represented equivalently by plotting the fraction of true positive rate (TPR) against the fraction of false positive rate (FPR). An ROC curve demonstrates the tradeoff between sensitivity and specificity in which, the closer the curve to the 45° diagonal of the ROC space, the less accurate the test. At the same time, the area under the curve (AUC) is also a measure of the accuracy. The AUC is largely adopted to represent the expected performance of a classifier. The AUC of a classifier is equivalent to the probability that the classifier will rank a randomly chosen positive instance higher than a randomly chosen negative instance.

Conclusions

Theoretical explanations of spatial domain filtering techniques such as mathematical morphological filtering techniques, different thresholding methods and correlation filtering techniques were explained in this chapter. Image representation using boundary extraction and statistical texture analysis using first order and second order gray level co-occurrence matrix were also detailed in this chapter. It also includes theoretical explanation of validation methods for segmentation, overview of decision systems and performance evaluation method using receiver operating characteristics curves. The following chapter presents the development and implementation of the theoretical study discussed in this chapter, for the extraction of glioma tumors and other pathological subjects and also the grade detection of glioma tumors.

References

[1] R.C. Gonzalez, R. E. Woods ,Digital Image Processing,Text book, 2nd Edition, Pearson Education,India, (2002)

[2] T. M.Deserno, Fundamentals Of Biomedical Image Processing, Thomas M. Deserno,Biomedical Image Processing, Springer, USA, ,pp 1-50 (2011).

[3] MR Kaus, SK Warfield, A Nabavi, et.al. Automated Segmentation of MR Images of Brain Tumors. , Radiology, vol.218(2):pp.586–591.(2001).

[4] RB Dubey, M Hanmandlu , SK Gupta An Advanced Technique for Volumetric Analysis. International Journal of Computer Applications. vol.1(1):pp.102-106.(2011).

[5] S Dube, J J Corso, TF Cloughesy . Automated MR image processing and analysis of malignant brain tumors: enabling technology for data mining. AIP Conf Proc. , vol.953:pp.64-84.(2007).

[6] D.S. Saif and A.B. Ahmed Segmentation of tumor tissue in gray medical images using watershed transformation method. International Journal of Advancements in Computing Technology, vol.2(4):pp.123-127.(2010).

[7] MP Katia, P Paolo, L Brambilla , et.al. ITAC volume assessment through a Gaussian hidden Markov random field model-based algorithm. Proceedings of 30th Annual International IEEE EMBS conference (2008).

[8] T Rohlfeng, DB Russakov, C R Maurer Performance- Based classifier Combination in Atlas-Based Image segmentation using Expectation – Maximization Parameter Estimation. IEEE transactions on Medical Imaging, vol.23(8):pp.983-994.(2004).

[9] M. Heydari, Prognosis of Glioblastoma Multforme using textural properties on MRI, Thesis work in Master of Science, Univesity of Alberta, 2009

[10] F. Albregtsen, Statistical Texture Measures Computed from Gray Level Cooccurrence Matrices, Image Processing Laboratory, Department of Informatics, University of Oslo (2008)

[11] A Mohd. Khuzi, R Besar, WMD Wan Zaki, et.al. Identification of Masses in Digital Mammogram using Gray Level Co-Occurrence Matrices, Biomed Imaging Interv J. 8 (1) (2009) e5.

[12] S.Ananda Resmi and T. Thomas,'Texturedescription of low grade and high grade glioma using statistical features in brain MRIs, Int. J. of Recent Trends in Engineering and Technology, Vol. 4(3), pp.27-33, (2010)

[13] M. Bounessah, The Boxplot: A Robust Exploratory Data Analysis Tool For The Definition of the threshold for outlier data, Asian Journal of Chemistry, Vol.14, pp. 1772-74, (2002).

[14] L. Rokach, O. Maimon, Decision Trees, Chapter 9, Data Mining And Knowledge Discovey Handbook pp.166-192

[15] L. Hamel, Model Assessment with ROC curves. Encyclopedia of Data Warehousing and Mining, IGI Global, 2nd Edition, pp-1316-1323, (2009)

Chapter 5

Automatic Extraction of Glioma Tumors and other Pathological brain Tissues

Different approaches for segmentation of pathological brain subjects have been proposed in recent years, but, none of them obtained good performances for all studied cases. In this chapter, two new methods for extracting glioma tumors using spatial domain techniques are presented. The first method is applicable only for extracting tumor regions from T2 weighted MRIs. Using the second method named as Adaptive Gray level algebraic set Segmentation Algorithm(AGASA), we can extract Tumor, Tumor boundary, Grey Matter and White Matter from the joint intensities of T2 weighted and T1 FLAIR MR Images. The performance and accuracy of segmentation techniques are validated on different datasets with respect to manual Ground Truth and the result obtained are very promising. A comparative study of the two methods with respect to fuzzy c-means clustering technique is also provided in terms of qualitative and quantitative measurements.

5.1 Introduction

Automated medical image segmentation is becoming an increasingly important image processing step for a number of clinical and research applications including but not limited to brain volumetry, treatment planning in radiation therapy, surgical planning, and image-guided intervention procedures. The principal objective of segmentation is to extract a region of interest (ROI) from an image for a specific application and the methods used for extracting the ROIs are specific and problem oriented. Segmentation of pathological tissues from conventional brain MRI is a difficult and time consuming task because of its complex structure. Usually MR images are affected by noise and partial volume effect which causes accurate segmentation and boundary determination of tumor a difficult task; Most of the segmentation techniques used so far have limitations, as they require more computation time, go under segmented, over segmented, have problem with variation in intensity levels etc. The existing methods can be combined and modified for reducing the limitations to a certain extent [1].

This chapter details the development of methods for extraction of various brain components including tumor and tumor boundary, from magnetic resonance images. A novel and robust algorithm for the extraction of definable objects such as white Matter (WM), grey Matter (GM), tumor and tumor boundary by preserving its shape and gray level information are developed, by using spatial domain processing techniques. The term spatial domain refers to the aggregate of pixels composing an image.

Section 5.2 explains the development method for extracting tumor from a single modality T2 weighted MRIs. The implementation, robustness of the method with respect to different noise levels, the results obtained with respect to different datasets and validation of results are also presented. Section 5.3 details the method for extracting complex brain structures such as grey matter, white matter, tumor and tumor boundary from the joint intensities of T1-FLAIR and T2 weighted MRIs. The accuracy of segmentation determines the eventual success or failure of any computer assisted method. The validation of segmented ROIs with manual ground truth and its discussions are explained in Section 5.4. Section 5.5 gives a qualitative and quantitative comparative study of the two methods with respect to

the most widely used segmentation method in brain MRI segmentation, the Fuzzy c-means clustering method. These segmented tumors are used for tumor grading and 3D modeling of tumors for finding the volume of tumors, as explained in the forthcoming chapters.

5.2 A Novel Technique for Extraction of low grade and high grade Glioma Tumor from T2-Weighted MRI (Method 1)

5.2.1 Method Development

This section illustrates development of a novel and robust method for extraction of low and high grade glioma using conventional T2-weighted MR images. Different imaging modalities in conventional MRI and its specialties were already discussed in Chapter 2. T2 weighted image shows high contrast to tumor lesions. The following section detail the method of extraction of tumors from T2 weighted MR images. Fig. 5.1 shows the flow chart for pre-processing and segmentation.

5.2.1.1 Pre-processing and Extraction of Tumor

Normalization is the first stage of pre-processing. Normalization is done to reduce the variability of raw image intensities and subject orientation; this is important both for the segmentation and consistent feature evaluation. For further analysis of segmented region of interest (ROI) using statistical textural properties, it is important to distinguish the ROI from its surroundings. So the pre- processed images should be segmented from brain MRI with minimum loss of tumor tissue. This can be done by using mathematical morphological operations, correlation filtering and thresholding [2, 3]. Fig.5.1 shows the flow chart of the various operations done on the raw MRI to obtain the segmented ROI.

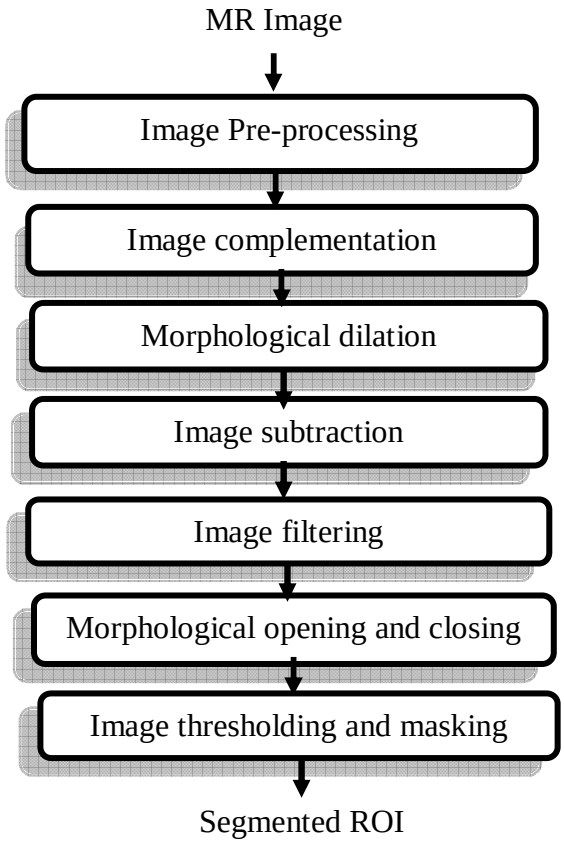

Fig. 5.1 The flow chart for Segmentation of ROI

The operations are done as given below.

Step 1:

Normalization is done by dividing each pixel gray level values by the absolute maximum gray level pixel value present in the image. After normalization, the range of gray level pixel values will be between 0 and 1.

Step 2:

As first part of the segmentation procedure, the pre-processed image (Fig. 5.2(b)) is complimented and dilated (Fig.5. 2 c) using square shaped (gray level) SE, for intensity adjustment. The complemented and dilated image is subtracted from the normalized image. This is for reducing noise artifacts and partial volume effect present in the image and enhancing tumor boundary [9]. The resulting image undergoes spatial domain filtering by correlation method with a filter mask, $w = [1, 1]$. The filtered output (Fig.5. 2d) undergoes morphological opening with a disk shaped SE. The main challenge in the tumor segmentation procedure is that usually tumor boundaries will not be clearly defined from the other regions and tumors may have heterogeneous borders and will have infiltrating nature. This boundary intrusions and protrusions are clearly visible after opening.

The main disadvantage of morphological dilation is over segmentation [4, 5]. This can be reduced to a great extent by using morphological opening (Fig. 5. 2e) operation with a disc shaped SE of suitable radius. The dimension and shape of the SE is selected empirically and held constant for the entire image dataset. Opening operation (Fig.5.2e) is erosion followed by dilation. The opening removes small details of the outline of the segment without affecting the total size of the relevant regions. After the opening operation, the output image undergoes closing operation (Fig.5.2f) in order to correct the variation in small details. The tumor boundary and region of the resulting image is visually enhanced. The repeated morphological operations with structuring elements of varied dimension and shape is for achieving accurate segmentation. The resultant image is thresholded (Fig.5.2g) to obtain a binary image. It is then morphologically labeled using connected component labeling technique to obtain the segmented ROI. The binary segmented tumor mask (Fig.5.2h) thus obtained is masked with the original normalized image to obtain the original gray level image of the corresponding ROI, as shown in Fig.5. 2i.

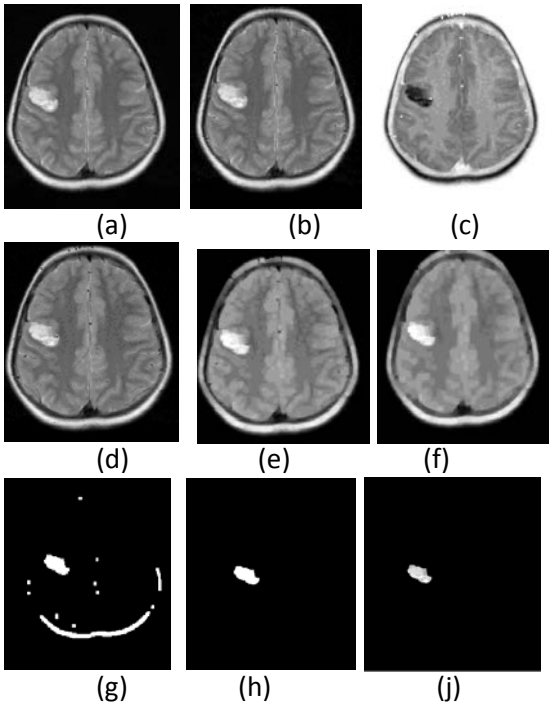

Fig.5.2 Extraction technique for high grade tumor from T2 weighted MRI slice a)Original image b)Pre-processed image c)Complemented and dilated image d) Filtered image e) Image after opening f) Image after closing g) Thresholded image h) Morphologically labeled image using connected component labelling i) Segmented gray level image

5.2.2 Implementation of method I

The developed method is implemented and tested on the entire image database. The robustness of the method with respect to Gaussian noise and speckle noise is also tested. Accuracy of the method is validated with respect to manual ground truth. This method also checks how much it reduces over- segmentation and under -segmentation.

5.2.2.1 Image Database

The MRI database consists of T2 weighted axial MRI data sets of 105 patients, with each set containing twenty images. The thickness of each slice is 5mm and the inter slice distance is 2mm. All patients underwent biopsy or surgical resection of the tumor with histopathological diagnosis. Out of this hundred and five histopathologically tested image database, forty five sets were of high grade and fifty five were of low grade and five normal image datasets. MRI images were collected from the department of Radiology in the Sree Chitra Institute of Medical Sciences and Technology (SCIMST) and Regional Cancer Centre, Trivandrum, Kerala, India. The images were gray scale images with each pixel level represented by 16 bits. Fig. 5.3 shows the sample T2 weighted image slices for segmentation

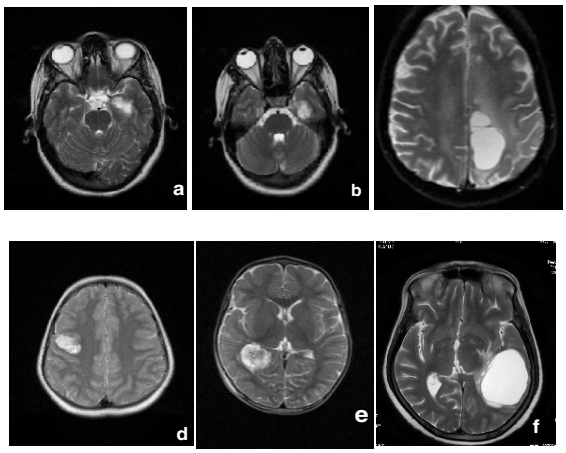

Fig.5.3 T2 weighted images of low grade and high grade glioma tumors a), b) and c) Low Grade Glioma d), e) and f) High Grade Glioma

5.2.2.2 Evaluation of segmentation algorithm

The evaluation of brain tissue classification is a complex issue in medical image processing [4]. A validation method can be thought of as a combination of two components. One component is the notion of ground truth (GT) against which result of an algorithm is to be judged [6]. The second component is a measure of establishing the deviation from the GT, i.e., an evaluation with actual segmentation is needed to assess how it deviates from the real one.

In the case of segmentation of brain tissues from MRIs, there is indeed a true boundary of the brain tissue for each patient, but it is not correctly known. Approximations to the true boundary can be obtained in the form of manual segmentation algorithm by experts of neuro-anatomy; however manual segmentation is subject to inter observer variability and human error [7]. To minimize the influence of these factors, while maintaining a means of measuring the segmentation accuracy of the individual raters, the standard was defined on the basis of independent human observers. Randomly selected 20 images from 20 patients' image datasets were manually segmented by the radiology expert in our group. These images were selected as ground truth (GT) images for validation.

Here there are two different measures for evaluating the segmented results obtained with the automatic segmentation algorithm developed. They are accuracy evaluation using quantitative techniques and qualitative techniques.

1. Accuracy evaluation using quantitative techniques

With the GT images in the dataset, three indices were calculated [2] by Eqns.5.1, 5.2, and 5.3.

$$Tanimoto\ Index: TI[\%] = \frac{TP}{TP+FP+FN}.100; \quad (5.1)$$

$$Percent\ Match: PM[\%] = \frac{TP}{TC}.100; \quad (5.2)$$

$$Positive\ Prediction\ Value: P+[\%] = \frac{TP}{TP+0.5FP}.100 \quad (5.3)$$

where TP=true positives, i.e. pixels labeled as ROI in the GT and by the algorithm, FP= false positives, i.e pixels labeled as ROI in the GT, but not in algorithm and FN= false negative, i.e. pixels labeled as ROI in algorithm, not in GT. TC =pixels manually labeled as ROI in GT. The 0.5 coefficient for FP is introduced taking into

account that, for treatment purposes, the immediate area around the tumor will also be treated and a certain degree of FP is usually acceptable.

Tanimoto index (TI) represents the percentage ratio between the number of pixels labeled as tumor by GT and the algorithm, and the number of pixels classified as tumor by the algorithm and/or by GT. The value of 100% signifies that there are no FP and FN. Percentage match (PM) index shows the correspondence between the GT and the segmentation algorithm. An ideal PM value is 100 %, which means algorithm localizes GT perfectly with ROI. Conversely, positive prediction value (P+) index estimates the correspondence in size and location between the segmented ROI and GT. For performance evaluation, computation time and accuracy of the automatic method with manual segmentation method are considered.

5.2.2.3 Robustness of the method with respect to Gaussian noise and Speckle noise

The presence of noise and also low contrast of the MRI data make it difficult to precisely delineate regions of interest between tumor and other brain subjects. Many methods are reported in literature to reduce noise in MRIs. The MRI de-noising algorithms can be divided into four major categories; finite impulse filters, anisotropic diffusion, wavelet, and nonlocal mean algorithms. The algorithms using Modified Fuzzy c-means clustering algorithm [17], data processing algorithm based on least mean squared adaptive filtering to suppress structured noise in MR images[17],classical techniques like spatial averaging, low pass or median filtering are usually applied to the noisy image to increase the SNR [14] are also used for de-noising MRI data. Most of the segmentation algorithms found in literature tend to be very sensitive to noise, intensity in-homogeneities and low contrast.

Almost all image processing filters are based on Gaussian assumption and do blur discontinuities between regions [8]. This is the main challenge in de-noising MRI data for segmentation application, i.e. to preserve the edges and details but at the same time to reduce noise in uniform regions. Most of the de-noising algorithms are not strong enough to retrieve the boundaries, to improve the contrast and in-homogeneities beyond a certain extent.

This section describes the effect of Gaussian and speckle noise in the 105 MRI data set containing low and high grade glioma and the robustness of the developed segmentation technique discussed in the previous section, in terms of accurate segmentation and visualization, for the noise-added image dataset.

The presence of noise in T2 weighted MRI data make it difficult to precisely delineate regions of interest between tumor and normal brain issues. Hence it is necessary to pre-process MR image to reduce noise and to enhance the contrast between regions. In order to check the robustness of this algorithm with respect to noise, Gaussian noise and speckle noise at different noise levels were added to the MR images and segmentation was carried out using the newly developed algorithm, without using pre-processing filters. Signal-to-noise ratio (SNR) is used as a synthetic index to quantify the totality of noise influence and to characterize the effectiveness of MRI examination [9]. The SNR aims at exploring how much the noise has been reduced.

5.2.3 Results and Discussions (Method I)

5.2.3.1 Implementation of the algorithm for extraction of Tumor Region

The method for automatic segmentation of low grade and high grade glioma tumors developed as mentioned in Section 5.2.1 was tested on 105 patients' T2 weighted axial MRI data sets and obtained promising results. Out of this 105 histopathologically tested image database, forty five sets were of high grade, fifty five were of low grade and 5 were normal dataset. Each image dataset contains 20 slices, out of which, tumor will be present only in six to eight slices. Fig 5.4 shows the effect of the segmentation algorithm on sample image slice of a low grade glioma tumor. Usually low grade tumor contains intensity in-homogeneity and partial volume effect. Here tumor region is accurately segmented according to the manual ground truth images.

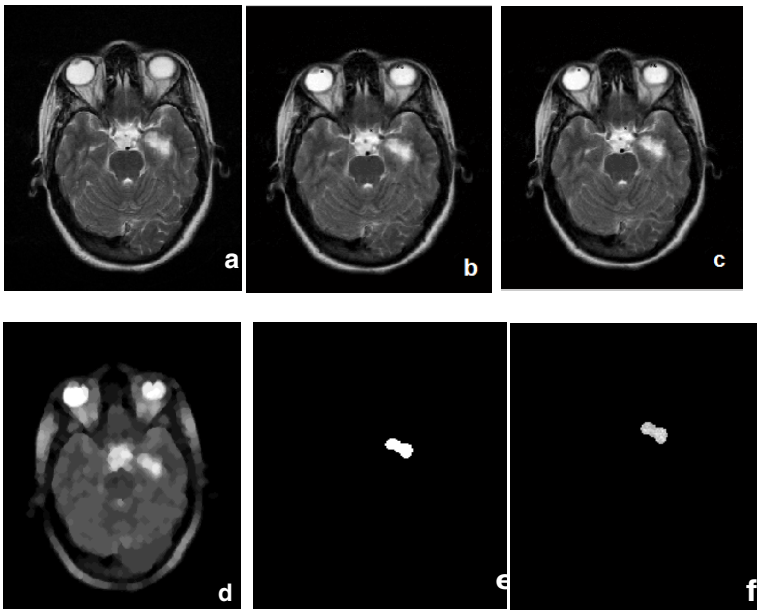

Fig.5.4 Segmentation procedures for extracting low grade glioma tumor from a T2 weighted MR image a) Original Image b) Normalized and Subtracted Image c) Image after Dilation and Correlation filtering d) Image after morphological opening and closing e)Image after thresholding f)Segmented gray level tumor

Fig.5.4a shows the T2 weighted MR image of low grade glioma without a clear boundary. As discussed in Section 5.2.2 the boundary of the tumor is clearly visible after correlation filtering (Fig.5.4c), which was already complemented, dilated and subtracted from the normalized image. The structuring element used for dilation operation was a square shaped SE of small dimension. Thus square shaped SE of suitable dimension is selected for retaining the exact shape of the tumor. Fig. 5.4d is the result after morphological opening and closing with a disk shaped SE of suitable radius. After these operations, the boundary of the tumor is defined. It reduces partial volume effect. The shape of SE was determined and fixed by applying SE of different shape and dimension on the same image. Comparing the shape and size of the segmented tumor with respect to GT, the SE with suitable dimension was manually selected, later applied on different image datasets and

finally automated for every slice. Image after morphological operation is thresholded (Fig.5.4e). The levels of thresholds were selected from the average gray level values in the tumor region. Initially, these values are selected manually for slices from different image datasets and finally automated for every slice. Connected component labeling was done after thresholding as shown in Fig.5.4f for selecting the largest connected component, which specifies the location also the binary mask of tumor. This operation was done for retaining the tumor mask only while removing the other background details which were present after the thresholding operation. The final segmented tumor (Fig.5.4f) retains the original gray level value of the tumor.

Fig. 5.5 and Fig.5.6 show the application of this algorithm for automatic extraction of high grade glioma from a sample image slice and also for studying the effect on sample normal image slice. The procedure is the same as was explained in the previous paragraph of extraction low grade glioma. It can be noted that, in the case of high grade glioma, the segmented tumor slices are retaining the gray level values (Fig.5.5h) and hence these segmented ROIs are used for grade detection using texture analysis using statistical quantification techniques, which will be useful for prognosis [10] and treatment planning. Another application of this segmentation technique is that, these segmented slices are used for 3D modeling of glioma tumors for obtaining volumetric size and further analysis of the tumor.

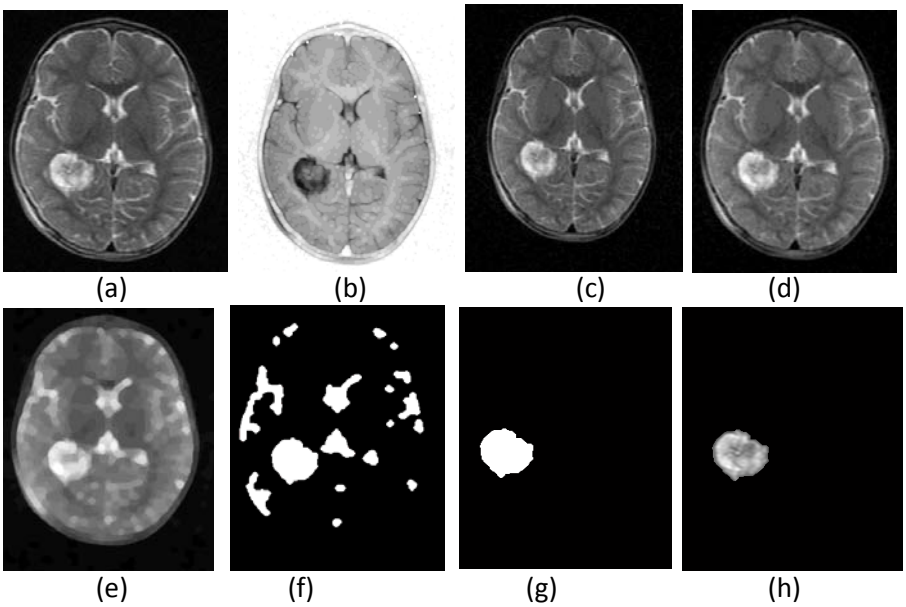

Fig.5.5 Segmentation procedures for extraction of high grade glioma tumor from a T2 weighted MR image a) Original image b) Complemented and dilated image c) Image after correlation filtering d.) Image after morphological opening e) Image after closing g) Thresholded image g) Segmented binary tumor h) Gray level tumor

Fig.5.6 shows the effect of the segmentation algorithm in normal images. The final output is a blank image showing that the slice is a normal one with no tumor. From this, it can be well observed that the algorithm automatically detects the presence of tumor, by indicating the ROI with actual gray level values, if the slice contains tumor region or otherwise the resulting image will be a blank image. This technique is more reliable, more accurate, robust and less time consuming, with reduced complexity than other existing system. The comparison of this method with respect to other techniques and also the effect of noise on this algorithm are discussed in the next sections.

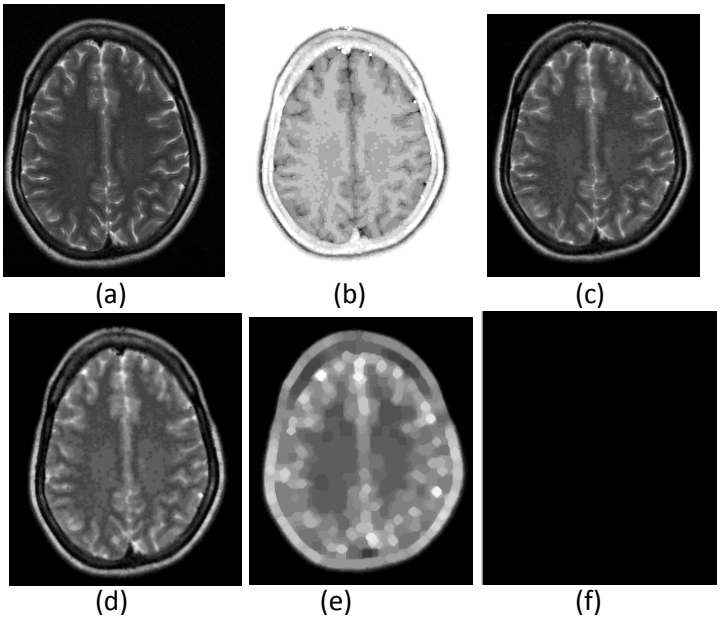

Fig.5.6 Automatic extraction method applied on normal image slice a) Normal image b) Complemented and dilated image c) Filtered and subtracted image d) Image after morphological opening e) Image after morphological closing c) Final output after thresholding and labeling

5.2.3.2 Validation of the method with manual Ground truth

Accuracy and performance of this automatic segmentation method was evaluated by comparing with manual ground truth images (ROI). The method was then validated by randomly selecting 40 images each from 40 image datasets. The accuracy of the method was determined by computing Tanimoto index (TI) by validating against the manually labeled image, by Dr. Bejoy Thomas, Additional Professor, Imaging Sciences and Interventional Radiology, Sree chithra Tirunal Institute of medical sciences and Technology. The images are manually labeled as shown in Fig.5.7b. Fig.5.7c is the automatically segmented tumor. In Fig.5.7d, the manually segmented image slice (GT) is superimposed on automatically segmented image for the visual validation of the method. From this, it can be observed that,

there is no pixel missing with respect to GT tumor region or overlapping with background. True Positive (TP), False Positive (FP) and False Negative (FN) values of the pixel count in the ROI, were calculated for finding TI. The TP, FP, and FN, TI values of low and high grade glioma are provided in the Table 5.1 and 5.2 respectively.

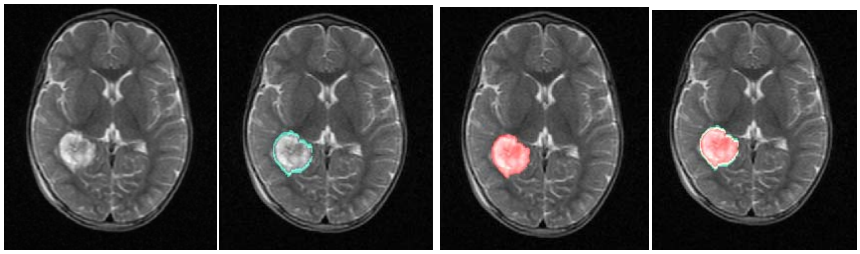

Fig.5.7 Automatically labeled Tumor with respect to manual ground truth Original image b) Ground Truth image c) Automatically labelled tumor d) Labelled tumor with manual ground truth boundary superimposed.

Table 5.1 TP, FN, FP and TI computed values of randomly selected segmented low grade tumor for 10 images

Low grade Tumor	FN	TP	FP	TI
tumor_low 1	27	3143	57	97.397
tumor_low 2	56	1896	24	95.951
tumor_low 3	27	3534	42	98.085
tumor_low 4	48	2326	26	96.917
tumor_low 5	27	3736	122	96.165
tumor_low 6	54	4313	77	97.052
tumor_low 7	87	3467	39	96.493
tumor_low 8	45	2925	79	95.933
tumor_low 9	39	5056	19	98.866
tumor_low 10	66	1978	72	93.478

Table 5.2 TP, FN, FP and TI computed values of randomly selected segmented high grade tumor for 10 images

High grade Tumor	FN	TP	FP	TI
tumor_high 1	10	7718	23	99.57
tumor_high 2	17	6585	60	98.84
tumor_high 3	19	8195	78	98.83
tumor_high 4	15	9875	62	99.23
tumor_high 5	21	7087	34	99.23
tumor_high 6	17	8987	69	99.05
tumor_high 7	16	5975	42	99.04
tumor_high 8	5	8586	68	99.16
tumor_high 9	12	9908	54	99.34
tumor_high 10	26	6458	25	99.22

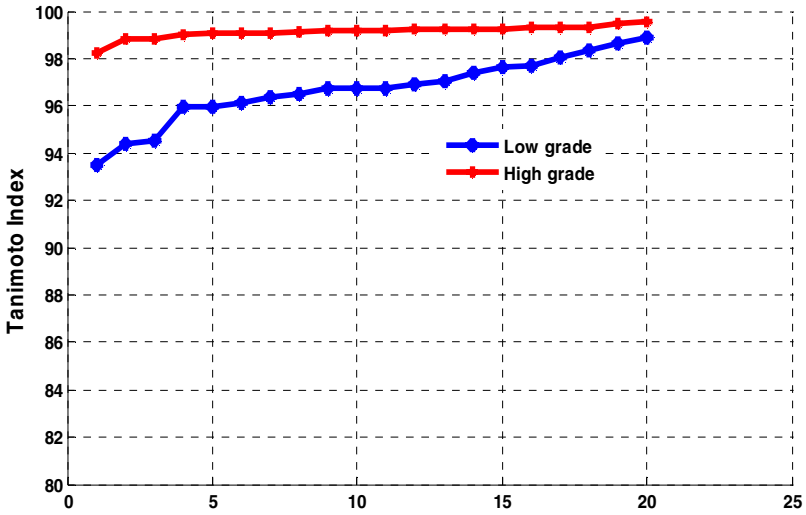

Fig.5.8 The Tanimoto Index computed for segmentation of low and high grade glioma, The ranges of values for low and high grade glioma are 93.4-98.7 and 98.2-99.6 respectively.

From these calculated parameters, it can be well observed that, the accuracy of the method in terms of TI, for extraction of low and high grade tumor is 93.4 - 98.7 and 98.2-99.6 respectively and hence the performance of the method is highly appreciable. A plot of Tanimoto Index for the 20 low grade and high grade glioma is shown in Fig.5.8. The Graph depicts accuracy of the method. When comparing the accuracy of segmentation between two grades, extraction of high grade tumor is more accurate than low grade. Usually low grade glioma shows a non enhancing boundary so that the boundary determination of low grade glioma is more challenging than high grade glioma.

5.2.3.3 Robustness of the method on noisy MR images

This section details the segmentation results obtained for images degraded with Gaussian noise and speckle noise with different signal to noise ratio (SNR). This was achieved by varying the mean and variance of the noise, which is added to the original image. The developed method was implemented on these noisy MR images. It was observed that, this algorithm could remove the noise level effect up to a PSNR of 10db, when Gaussian noise with different mean and standard deviation was added. Fig.5.9 and Fig.5.10 show segmentation results obtained, when the original image was superimposed with Gaussian noise and without using any pre-processing filters for de-noising. From Fig. 5.9d, it was observed that the effect noise was reduced considerably after correlation filtering and morphological opening and closing. Also, it can be note that the segmented tumor coincides with the superimposed GT ROI.

In the case of image added with speckle noise, the algorithm worked effectively up to a PSNR of 12 dB without using any preprocessing filters. For a PSNR of less than 12 dB, further processing with Weiner filter is needed. Fig.5.11 and Fig.5.12 shows the details of segmentation of noisy low grade and high grade glioma images of 12dB, added with speckle noise. The segmentation algorithm discussed in this chapter had proved its robustness with respect to noise, by correctly segmenting images with Gaussian noise added noisy image of 10db PSNR and speckle noise added noisy image of PSNR 12db. From this, it can be inferred that, the method is useful for de-noising MRI data as well as for tumor segmentation from noisy back ground.

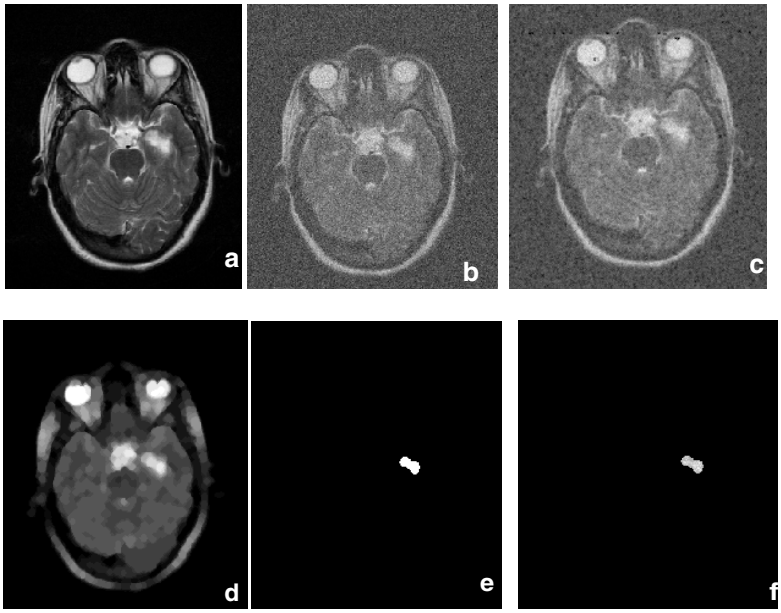

\

Fig.5.9 Segmentation of low grade glioma tumor from a noise added image a) T2 weighted MR image b) Gaussian noise added image of PSNR 10db c) Image after dilation and correlation filtering d)Image after morphological opening and closing e) Image after thresholding f) Segmented gray level tumor

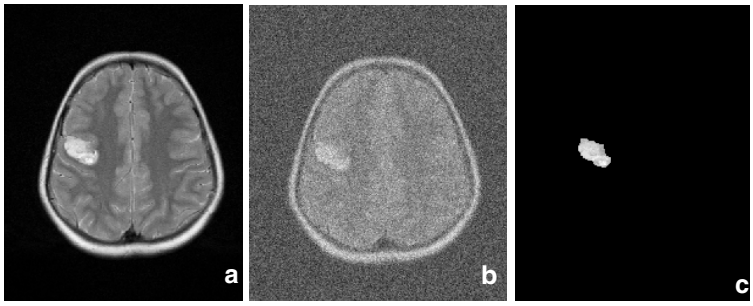

Fig.5.10 High grade glioma tumor segmented from Gaussian noise added image of PSNR 10db a) T2 weighted image b) Noise added image c) Segmented tumor from noise added image using morphological filtering technique and thresholding

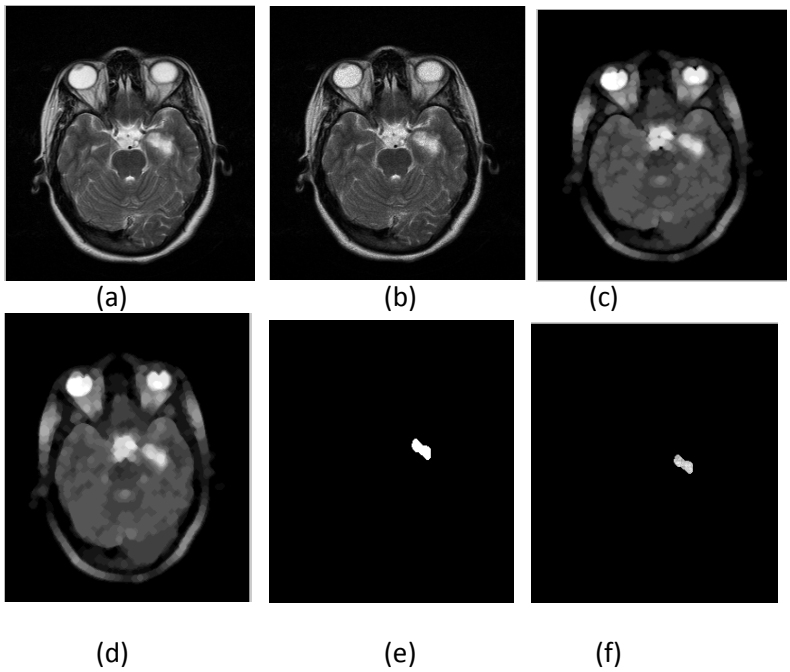

Fig.5.11Segmentation of low grade glioma tumor in speckle noise added image with PSNR of 12 db. a) Original image b) Speckle noise added image c) Image after opening d) Image after closing e) Thresholded binary image f) Segmented gray level image

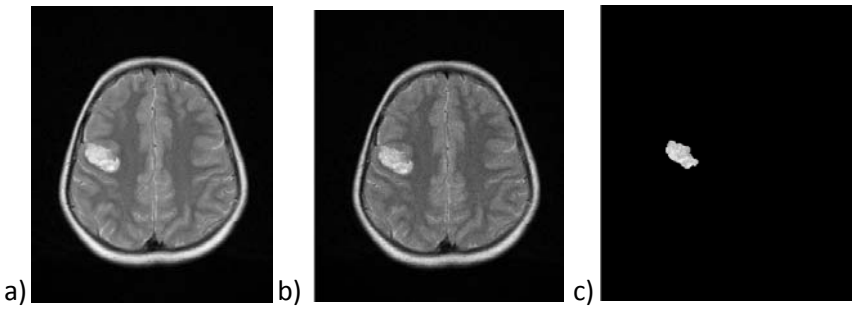

Fig.5.12 High grade glioma tumor segmented from Speckle noise added image of PSNR 12db a) T2 weighted image b) Noise added image c) Segmented tumor from noise added image using morphological filtering technique and thresholding

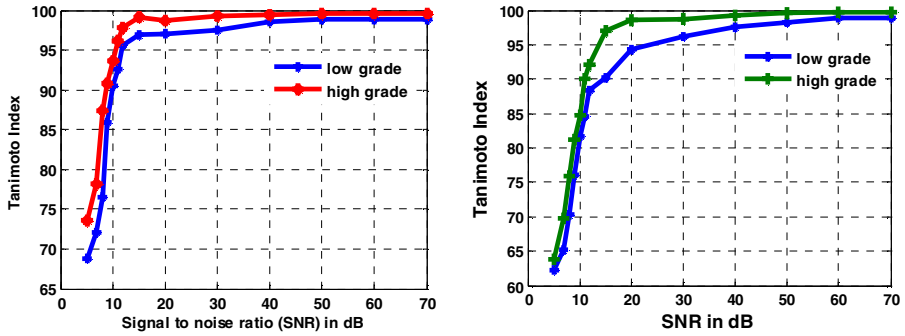

Fig.5.13 Tanimoto Index of the segmented of low and high grade glioma with respect to SNR at different noise levels. (a) Gaussian noise added images with different noise levels ,(b) Speckle noise added images with different noise levels

The Graph shown in Fig.5.13 depicts the accuracy of segmentation at different SNR which is degraded by Gaussian noise and speckle noise. As per Fig.5.13a it can be observed that Tanimoto Index is greater than 90% at 10dB for low and high grade glioma and from 5.13b, TI is greater than 90% at 12dB for low and high grade glioma. From the graph it can be clearly observed that, as the image quality degrades up to a SNR of 10db for Gaussian noise and 12db for speckle noise, the method remains robust.

5.3 A Novel Automatic Extraction Technique for Pathological Subjects and other Brain Tissues from T1 FLAIR and T2-weighted MR images using Adaptive Gray level Algebraic Set Segmentation Algorithm (AGASA)

The preceding section details the method of extraction of the tumor region alone, using T2 weighted MR images. This section discusses the method of extraction of tumor, tumor boundary, WM and GM from T1-FLAIR and T2 weighted MR images using Adaptive Gray level Algebraic set Segmentation

Algorithm (AGASA). The organization of this section is follows: Method development, implementation of the method followed by results and discussion.

5.3.1 Method Development

An accurate segmentation of low grade glioma is critical, because of the presence of undesired partial volume effect, which lies on the boundary between high and low intensity regions, making unerring boundary determination a difficult task. The segmentation of other pathological subjects in the brain like GM, WM CSF are also important for detecting various abnormalities in the brain. Hence a new method was developed for the extraction of all these constituents of the brain. Both T1 – Flair and T2 weighted slices of the MR images were used for the purpose.

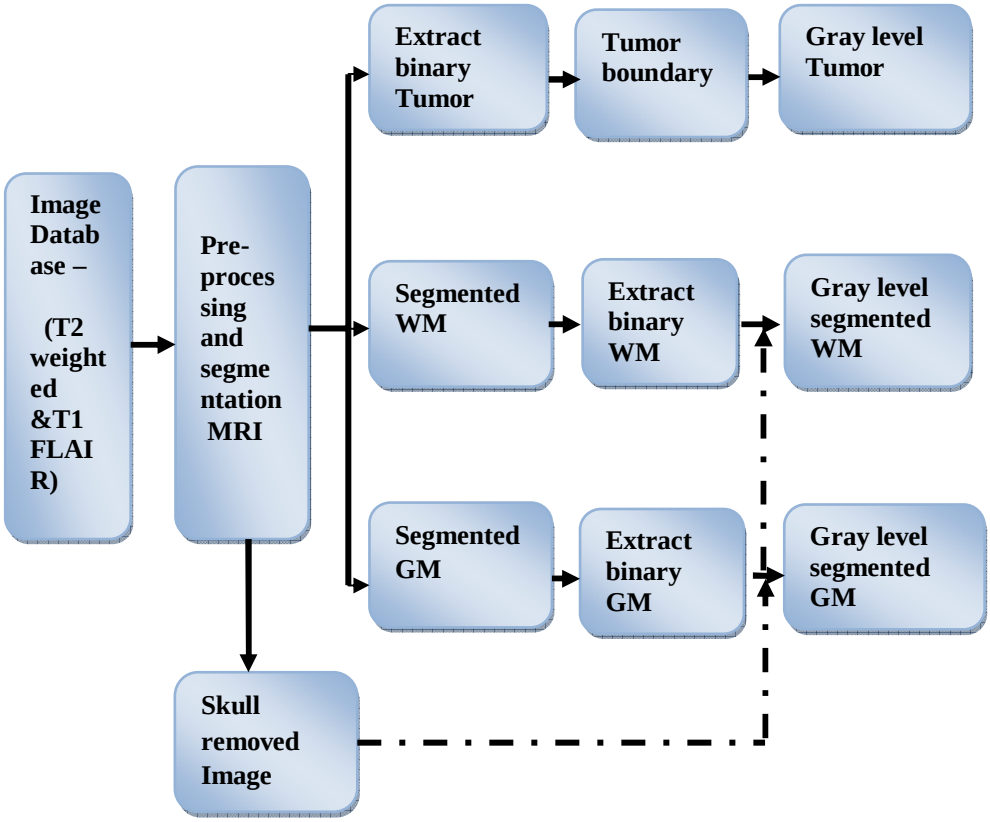

Fig.5.14 Block diagram for the Adaptive Gray level Algebraic set Segmentation Algorithm

In this section, a novel method, named as Adaptive Gray level Algebraic Algorithm (AGAA) is presented for the automatic extraction of tumor boundary, glioma tumors, WM and GM, by using spatial domain filtering techniques, which mainly involves morphological methods, adaptive thresholding and correlation filtering. There are three general steps involved in this method. They are: 1) skull removal, 2) segmentation of brain tissue into GM and WM, and 3) extract the low grade and high grade tumor and tumor boundary. The block diagram of the algorithm is shown in Fig.5.14.

5.3.1.1 Image pre processing and segmentation

A brain image consists of five regions – grey matter (GM), white matter (WM), cerebral spinal fluid (CSF), meninges (the protective membranes surrounding the brain) and skull, muscle, fat, skin or air. These regions are considered as five different classes. The goal of the segmentation process in this work is to assign tissue class labels (background, GM, WM, CSF, and low grade glioma or high grade glioma tumor and its boundary) to each slice in an image dataset which contains 20 slices. Using single modality conventional MRI, it is difficult to extract pathological subjects other than tumor. So joint intensities of both T1-FLAIR and T2 weighted images are used for differentiating tissue classes.

As an initial procedure, pre-processing was done based on the image profile. The pre-processing stage is a fundamental step in MR image analysis.

5.3.1.2 Skull Stripping

The skull and non brain intracranial tissues like fat, muscle, skin etc., that surround the surface of brain cortex and cerebellum in the brain should be removed. This is needed to avoid the misclassifications of surrounding tissues, skin and scalp as WM or GM. By removing these it will get rid of non-brain tissues and will be left with only soft tissues. This was done by gray level erosion using a disc shaped structuring element, which result in the removal of thin connections between brain and non brain portions. Thus a skull removed brain mask was obtained and this method was automated for every image slice [11].

The extraction of various tissue classes from an MRI slice involves various spatial domain processing. The main methods involved for pre-processing and segmentation of brain tissues were gray level morphological erosion, dilation,

image subtraction, adaptive thresholding, Correlation filtering, morphological labeling, segmentation of ROI and finally extraction of tumor boundary and other components like WM and GM.

5.3.1.3 Extraction of Tumor and boundary of the Tumor

In this work, low and high grade glioma were extracted using T1 FLAIR (Fig.5.15a) and T2 weighted (Fig.5.15b) images of the same slice. Following steps shows the procedures for extracting tumors,

1. Perform an erosion operation on T2 weighted image with a disc shaped structuring element of suitable radius corresponding to the thickness of the connectors between brain and the cranium (determined empirically, and held constant over scans), in order to eliminate connections from the brain to any misclassifiable non-brain structure like skull, meninges etc. (Fig .5.15c).
2. T1 FLAIR image (Fig.5.15a) is subtracted from the T2 weighted image (Fig.5.15b) for adjusting intensity of resulting image the subtracted image.
3. Dilate the brain component obtained in the step 2 by a SE slightly smaller in size than the one used in the morphological erosion, for conditioning brain labels in the input image. This is for restoring the boundaries of the brain component that were distorted in the erosion step (Fig.5.15d).
4. Dilated image is complemented and subtracted the resulting image with dilated image for adjusting intensity as shown in Fig .5.15e and it is thresholded to obtain regions with gray levels above certain threshold (Fig 5.15f).
5. Again, erosion with disc shaped SE of smaller radius is performed to remove unwanted gray level region and the resulting image is thresholded to obtain binary thresholded image (Fig.5.14g). The gray level erosion followed by dilation is done for avoiding under segmentation or over segmentation, partial volume effect and other noise present in the image.
6. Binary tumor mask is extracted using connected component labeling from the binary thresholded image in the previous step.

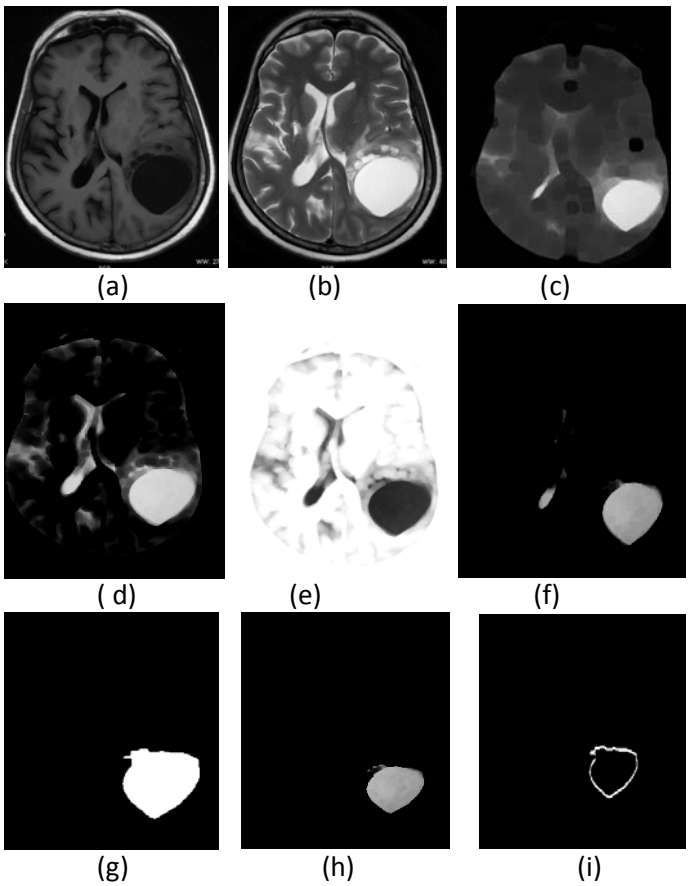

Fig. 5.15 The various steps for segmentation tumor and boundary a)T1 FLAIR b) T2 weighted c) Skull removed d) Subtracted and dilated e) Complemented image f) Intensity adjusted image g) Thresholded and labeled image h) Segmented gray level tumor i). Tumor boundary

7. Step 6 lead to obtain a binary mask of the brain tumor. A gray level is obtained by masking the initial MR image by this mask. In this way, all pixels outside the region were set to 0, while the tumor region had their initial value retained (Fig.5.14h). This can be used for further analysis.

8. The heterogeneous tumor border (Fig.5.15i) of the segmented tumor was obtained using boundary extraction technique. The maximum perimeter of the tumor can be determined if the benchmark images are used for tumor boundary extraction. Bench mark images are the slices which provide maximum information about tumor shape and size.

5.3.1.4 Extraction of Grey Matter

This section deals with the segmentation of the grey matter, with tumor region removed. The algorithm for extracting grey matter is as follows;

1. The intensity adjusted image (Fig.5.15d) of *section 5.3.1.3* used for extraction of tumor, is considered for adjusting gray level values of GM and WM
2. The intensity adjusted image is filtered using correlation filter with a filter mask *w= [1 1]* for enhancing the image.
3. Perform adaptive thresholding operation by finding the minimum and maximum values of GM for obtaining the binary mask of GM with skull boundaries. Here threshold is determined for every pixel position (pixel adaptive). A binary GM with outer boundaries is obtained (Fig.5.16b).
4. A gray level GM with outer boundaries is obtained by masking the gray level skull stripped image (Fig.5.16c). with the binary grey matter mask .The resulting image is dilated with disc shaped structuring element for restoring the components of grey matter as shown in (Fig .5.16c)

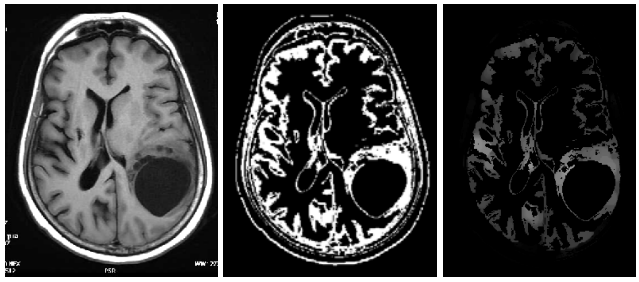

Fig. 5.16 Segmentation of grey matter with tumor removed. a) Enhanced image b) Binary mask of GM with outer layers c**)** Extracted GM with outer layers removed.

5.3.1.5 Segmentation of White Matter with tumor portion removed

The procedure for extracting white matter is quite similar to the extraction of grey matter up to step 2 of Section 5.3.1.4. After step 2, pixel adaptive thresholding is used for obtaining the binary mask of white matter. The highest and lowest gray level values in white matter are selected as levels in adaptive thresholding operation by selecting an initial gray level value as threshold. The binary mask thus obtained is masked with the original T2 weighted image for obtaining gray level image. Fig.5.17 gives the details of extraction of white matter.

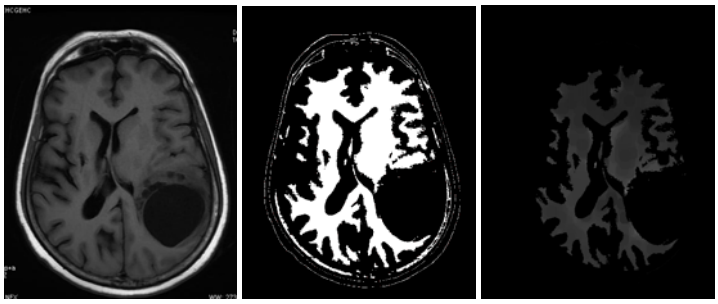

Fig. 5.17 Segmentation of white matter with tumor removed a) Enhanced image b) Binary mask of white matter with tumor removed c) White matter with skull removed

5.3.2 Implementation of the Adaptive Gray level Algebraic set Segmentation Algorithm

The method developed was implemented on seventy MR image data sets with each image dataset containing 20 slices. Out of this, forty sets were of high grade and twenty were of low grade glioma and ten normal image datasets. Image database development and validation of the algorithms were based on this MRI database which was already manually identified and segmented by the Radiologist. The selected images were histo-pathologically tested by the radiologists and have confirmed the presence of the disease. In this method, axial slices of T2 weighted and T1 FLAIR brain MRI data as shown in Fig.5.18 were considered. The images are gray level images and pixel levels are represented by unsigned 16bit integers.

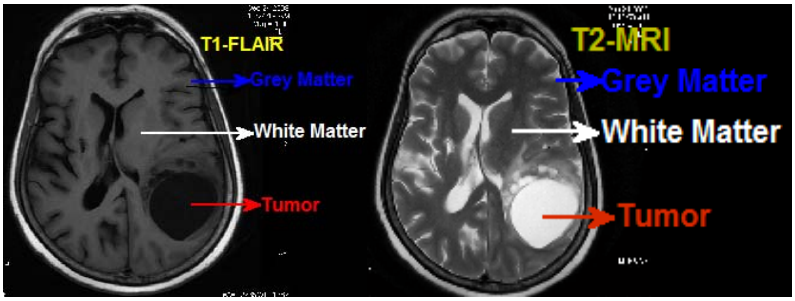

Fig.5. 18 Sample raw data from a patient volume used segmentation.
T1-FLAIR andT2-weighted MRI slice

5.3.3 Results and Discussion

This Section contains the experimental results of new method named as Adaptive Gray level Algebraic set Segmentation Algorithm (method II) and validation results.

5.3.3.1 Segmentation of tumor, Grey Matter and White Matter

This section presents the results of segmentation of tumor, tumor boundary, and GM and WM regions. Examples of segmented ROIs of low grade glioma, high grade glioma and normal images are shown in Fig.5.19, 5.20 and Fig.5.21 respectively. Even in the presence of partial volume effect, intensity in-homogeneities and infiltrative nature of tumor, the method is robust enough for defining the tumor boundary and extracts tumor and other pathological structures from the joint intensities T1-FLAIR and T2-weighted images. Benchmark images, two or three slices from each patient, are selected for obtaining exact area and perimeter of the tumor and its boundary. Gray level morphological filtering technique is the major procedure in this method. The main drawback of morphological segmentation is, under or over segmentation. This was reduced to a great extent using this method (Fig.5.19e). This was eliminated by repeated dilation and erosion with slightly varied dimension in the structuring element. Disk shaped SE of varied dimension is used for different morphological operations performed in this method. The same algorithm is used for extraction of pathological subjects

from low and high grade glioma MR images and normal images. Thus, this algorithm is also effective for extraction of WM and GM from normal images. The other advantage of this segmentation procedure is that, segmented structures are preserving the gray level values of the original T2 weighted image. For further texture description and classification/tumor grading using texture quantification, gray level intensity images are very essential.

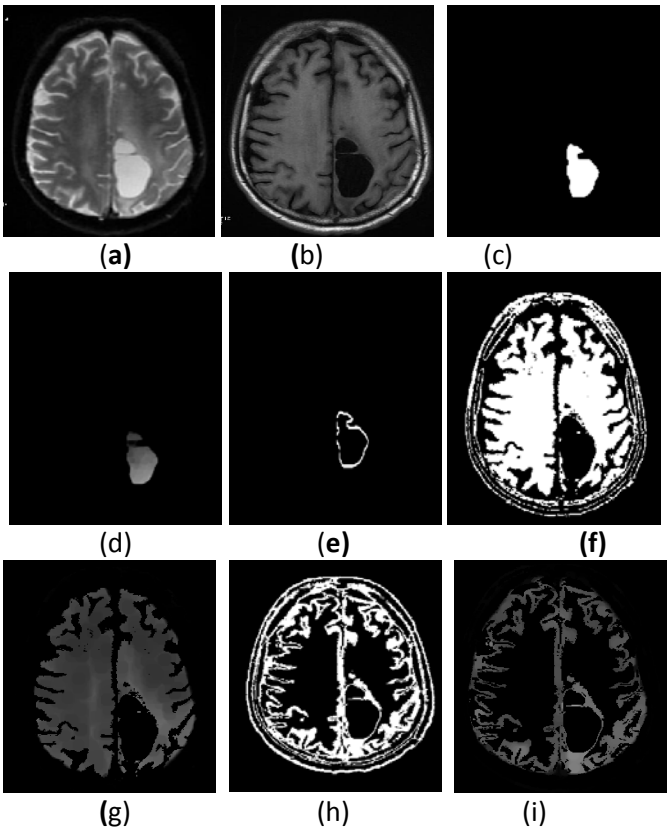

Fig. 5.19 Example of segmented ROIs of low grade glioma tumor from MR image slices. *a)* T2 weighted b)T1 FLAIR MR image c) Segmented binary low grade glioma tumor d) Gray level tumor e) extracted tumor boundary. f*)*Binary segmented WM with tumor portion removed g) Gray level WM with outer layers removed h) Segmented binary GM i) Gray level GM with outer layers removed.

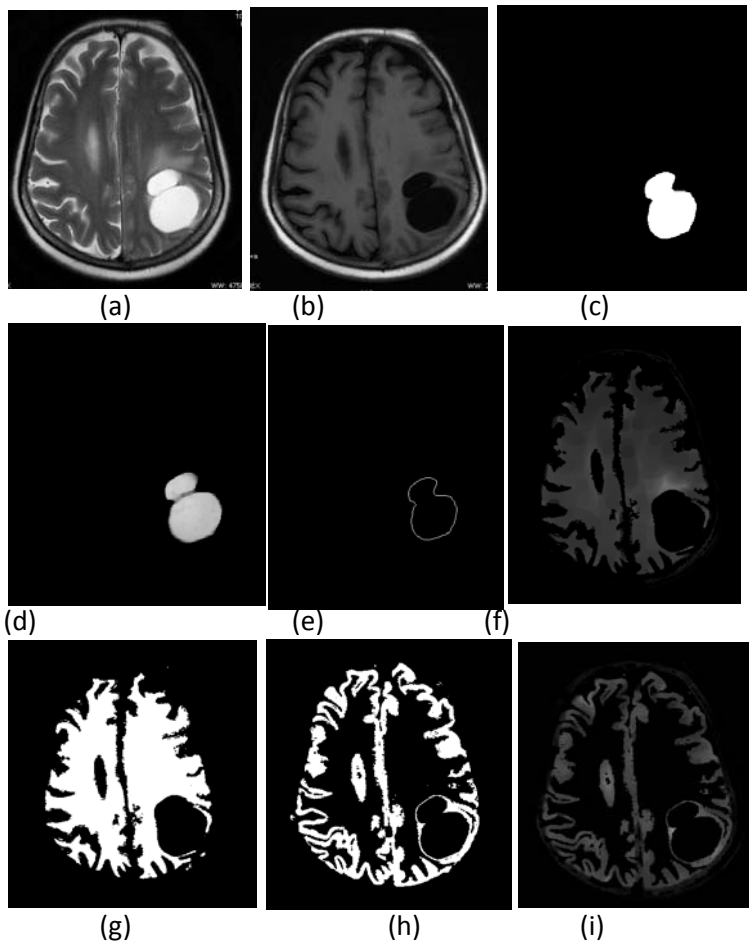

Fig. 5.20 Example of segmented ROIs of high grade glioma tumor patient from MR image slices. a) T1 FLAIR image b) T2 weighted image c) Segmented binary tumor d) Gray level tumor e) Extracted tumor boundary f) Gray level WM g) Binary segmented WM with outer layers removed h) Segmented binary GM i) Gray level GM with outer layers removed

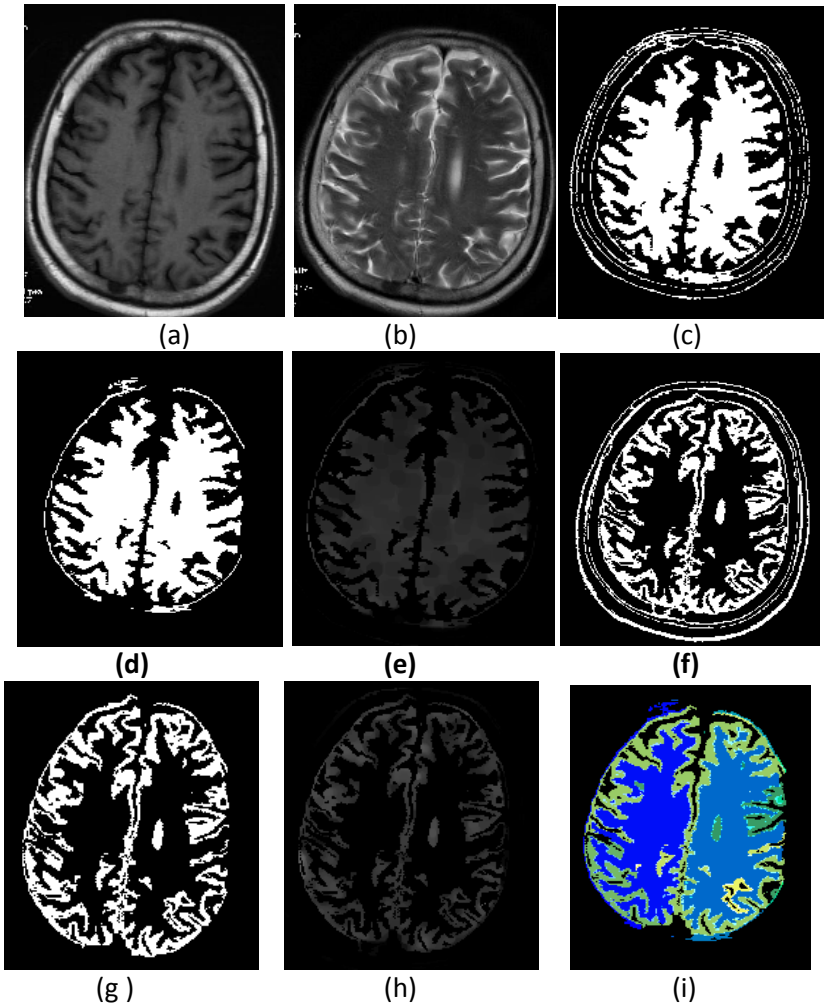

Fig.5.21. Example for Extraction method applied on a Normal Image. a) T2-Weighted Image b) T1 FLAIR image c) Binary WM with d) Binary segmented WM with outer layers removed e) segmented gray level WM f)segmented binary GM g) Binary GM with outer layers removed h) Gray level GM i) segmented and labeled image

The method is tested for over segmentation and under segmentation as shown in Fig.5.22. Most of the segmentation methods in literature are prone to

under segmentation or over segmentation. The method is validated in terms of Tanimoto Index, Positive Prediction Value and Percentage Match with respect to manual Ground Truth images.

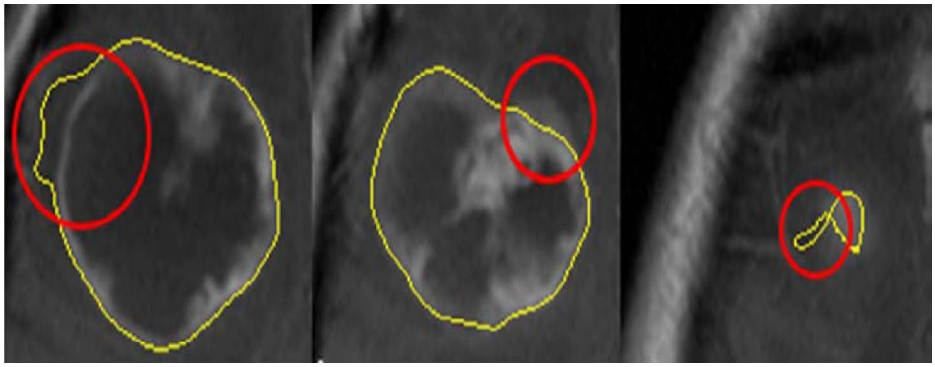

(a) (b) (c)

Fig. 5.22 Segmentation problem cases, (a) Under-segmentation, (b) Over-segmentation (c) Clustering. Segmented boundaries are in yellow; red circles indicate errors.

5.3.3.2 Results of Validation against the manual Ground Truth

The goal of this automated segmentation algorithm is to make segmentation of MR images more practical by replacing manual outlining of the tumor by radiologist without any loss in accuracy. In order to evaluate the efficiency, accuracy, and computation time of the segmented method described here, with respect to segmented WM, GM, and tumor from T1 FLAIR and T2-weighted MRIs, the authors used 20 images from 20 patients' image dataset (10 low grade glioma and 10 high grade glioma).

1. Visual similarity using labeling technique for measuring Efficiency

Examples of automatically labeled GM, WM and tumor with respect to GT are shown in Fig 5.23. From the figures, it can be well observed that the algorithm is very efficient with respect to manual GT. Manually segmented ROIs were superimposed and labeled into automatically segmented image for visual validation of the algorithm. Visual similarity between automatic method and GT can be

observed using this labeling technique. The dataset images included pre-labeled maps of tissues of interest (WM, GM, and tumor).

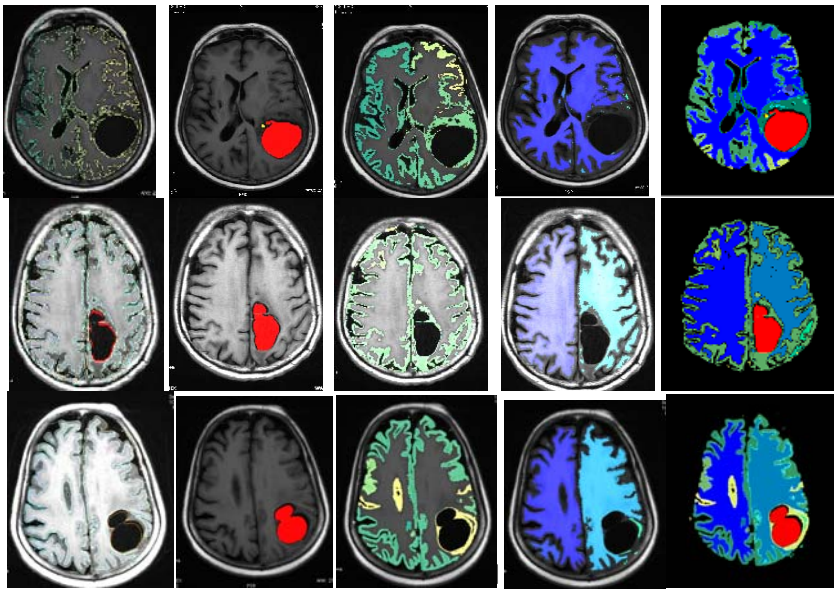

Fig.5.23 Manually outlined Brain components on T1 FLAIR images (ground Truth) by expert Radiologist and automatically labeled brain components of high grade and low grade glioma tumors on T1-FLAIR images; *1column* . Manually segmented T1 FLAIR images containing high and low grade tumor, *2nd column*. Automatically segmented and labeled high and low grade tumors, *3rd column* Automatically segmented and labeled GM, 4th *column* Automatically segmented and labeled WM, 5th *column* Automatically segmented and labeled tumor, GM, and WM with outer layers removed.

2. Accuracy measurement using Tanimoto Index, Percentage Match and Postive prediction value

The algorithm was quantitatively compared with GT for accuracy performances. To measure the agreement between automated and standard segmentations, the no. of pixels in the tumor, WM and GM regions obtained from the automatic method were compared with the pixels in the standard segmentation or GT in each slice.

TP, FP, FN are measured in each case. Accuracy of segmentation was quantitatively evaluated by calculating Tanimoto index (TI), Percentage match (PM) and Positive prediction (P+) values of this algorithm with respect to GT. Tables 5.3 and 5.4 show the FN,TP,FP,TI, PM, and P+ of High and low grade Tumor, Tables 5.5 and 5.6 shows these parameters for WM (low and high grade) and Table 5.7 and 5.8 show typical values of FN,TP,FP,TI, PM, and P+ for high and low grade GM for 10 sample images. From the tables, it can be observed that the TI of low grade and high grade glioma tumor ranges from 97.07%-99.8% and 98.28%- 99.6 %, TI of WM for low grade and high grade ranges are 97.97%-99.79% and 97.12%-99.55% and TI of GM for low and high grade ranges of values are 91.4%- 98.4% and 93.9% -96.6% respectively. Fig.5.24 shows the same results for TI for this algorithm with respect to GT for low and high grade tumor, WM, and GM of randomly selected 20 images from 20 image datasets. That is, the percentage of misclassified pixels is very low or in other words, FP and FN also give a measure of the 0.02-0.06%, 0.01-0.07% for tumor 0.03-0.1%, 0.04-0.12% for the WM and 0.04-.0.12% and 0.08-0.13% respectively including all segmented ROIs. FP and FN also a measure of number of over segmented pixels and number of under segmented pixels with respect to GT. TI of 100% signifies that there are no FP and FN. Thus the new method shows excellent performance for the three segmented ROIs.

Table 5.3 Performance analysis for segmented high grade tumor in MRI images

High grade Tumor	FN	TP	FP	TI	PM	P+[%]
tumor_high 1	4	8791	33	99.367	99.626	99.813
tumor_high 2	7	6985	20	99.388	99.714	99.857
tumor_high 3	9	7195	54	98.941	99.255	99.626
tumor_high 4	5	7875	60	98.957	99.244	99.620
tumor_high 5	21	7087	34	99.202	99.523	99.761
tumor_high 6	7	7005	22	99.362	99.687	99.843
tumor_high 7	6	6975	14	99.472	99.800	99.900
tumor_high 8	7	7587	62	98.892	99.189	99.593
tumor_high 9	33	7499	34	99.246	99.549	99.774
tumor_high 10	6	6941	41	99.086	99.413	99.706

Table 5. 4 Perfomance analysis for segmented low grade tumor in MRI images

Low grade Tumor	FN	TP	FP	TI	PM	P+[%]
tumor_low 1	17	4135	42	98.009	98.994	99.495
tumor_low 2	16	1746	14	98.422	99.205	99.601
tumor_low 3	7	4334	36	98.366	99.176	99.586
tumor_low 4	43	4345	16	99.269	99.633	99.816
tumor_low 5	27	2736	20	98.559	99.274	99.636
tumor_low 6	14	3313	27	98.396	99.192	99.594
tumor_low 7	24	2445	19	98.470	99.229	99.613
tumor_low 8	19	1925	29	97.075	98.516	99.252
tumor_low 9	4	4096	4	99.805	99.902	99.951
tumor_low 10	6	1748	12	98.646	99.318	99.658

Table 5. 5 Perfomance analysis of segmented high grade WM for 10 sample images

ROI	FN	TP	FP	TI	PM	P+[%]
WM_high 1	91	44298	193	99.14	99.57	99.78
WM_high 2	82	40982	400	98.09	99.03	99.51
WM_high 3	196	39675	221	98.90	99.45	99.72
WM_high 4	41	42489	172	99.20	99.60	99.80
WM_high 5	406	40069	594	97.12	98.54	99.26
WM_high 6	66	43967	99	99.55	99.78	99.89
WM_high 7	168	43464	304	98.62	99.31	99.65
WM_high 8	43	43198	129	99.41	99.70	99.85
WM_high 9	72	43526	146	99.33	99.67	99.83
WM_high 10	18	43895	123	99.44	99.72	99.86

Table 5. 6 Perfomance analysis of segmented low grade WM for 10 sample images

ROI	FN	TP	FP	TI	PM	P+[%]
WM_low 1	440	42987	1098	95.14	97.51	98.74
WM_low 2	429	42086	900	95.90	97.91	98.94
WM_low 3	167	41023	344	98.35	99.17	99.58
WM_low 4	340	39228	412	97.94	98.96	99.48
WM_low 5	417	40261	1494	93.09	96.42	98.18
WM_low 6	398	38241	1583	92.35	96.03	97.97
WM_low 7	420	40964	1120	94.82	97.34	98.65
WM_low 8	343	40965	378	98.19	99.09	99.54
WM_low 9	396	38156	1447	92.95	96.35	98.14
WM_low 10	362	39163	699	96.55	98.25	99.12

Table 5. 7 Perfomance analysis of segmented high grade GM for 10 sample images

ROI	FN	TP	FP	TI	PM	P+[%]
GM high 1	26	25583	455	96.57	98.25	99.12
GM high 2	235	22845	730	93.99	96.90	98.43
GM high 3	112	20107	1005	90.91	95.24	97.56
GM high 4	186	17869	780	91.97	95.82	97.86
GM high 5	186	16031	155	98.10	99.04	99.52
GM high 6	233	22893	830	93.24	96.50	98.22
GM high 7	260	18755	505	94.89	97.38	98.67
GM high 8	317	21617	700	93.92	96.86	98.41
GM high 9	60	19879	481	95.38	97.64	98.80
GM high 10	192	18790	470	95.24	97.56	98.76

Table 5. 8 Perfomance analysis of segmented low grade GM for 10 sample images

ROI	FN	TP	FP	TI	PM	P+[%]
GM low 1	260	21088	172	98.39	99.19	99.59
GM low 2	62	16820	642	92.91	96.32	98.13
GM low 3	27	20511	516	95.21	97.55	98.76
GM low 4	196	18962	721	92.93	96.34	98.13
GM low 5	66	18924	642	93.65	96.72	98.33
GM low 6	200	19982	1218	89.13	94.25	97.04
GM low 7	185	18100	420	95.56	97.73	98.85
GM low 8	147	18670	877	91.41	95.51	97.71
GM low 9	256	27054	302	97.82	98.90	99.44
GM low 10	214	21065	589	94.70	97.28	98.62

Percentage Match and Tanimoto Index are measures of accuracy. The WM and tumor segmentation had better PM and TI, than GM. The PM values for the new segmentation algorithm with respect to GT are excellent. From this, it is well observed that segmentation accuracy in terms of the segmented location area and size of ROI's are very high. Because positive prediction value of ROIs are greater than 98%.

Fig.5.25 shows the Percentage Match (PM) of the segmentation algorithm with respect to GT. The median values of PM obtained from the box plot (Fig.5.25) for low grade tumor, GM and WM are 99.8, 97.5 and 99.6 respectively and for high grade the median values tumor, GM and WM are, 99.4, 97.2 and 97.8 respectively. The whiskers show the range of values. The horizontal bars are the median values, the boxes shows the percentiles. Its ranges values for low and high grade tumor 99.01-99.86, and 98.9-99.49, WM 99.10-99.90 and 96.1-98.89 and GM are 95.26- 98.9 and 94.2-99.01 respectively

The algorithm developed in this method is based on customorized mathematical morphology and adaptive thresholding techniques which incorporates spatial information. We tested the distribution of FP and FN was tested by computing TI.

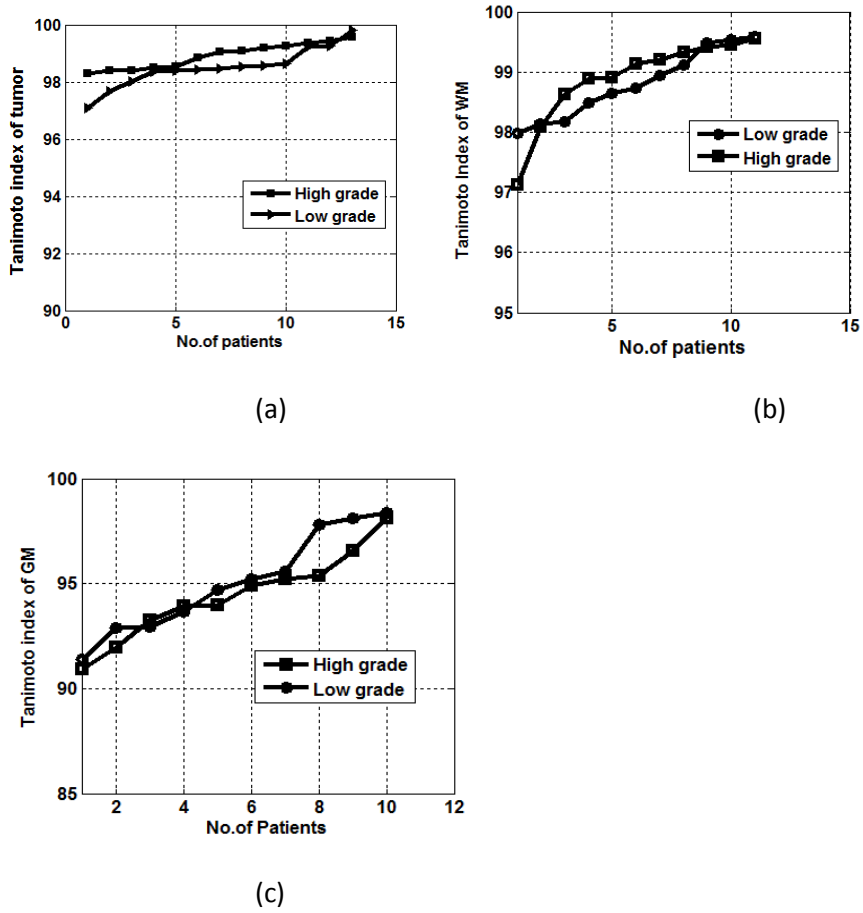

Fig.5.24**.** Tanimoto index (TI) of high grade and low grade Tumor , WM, and GM of 20 patients.

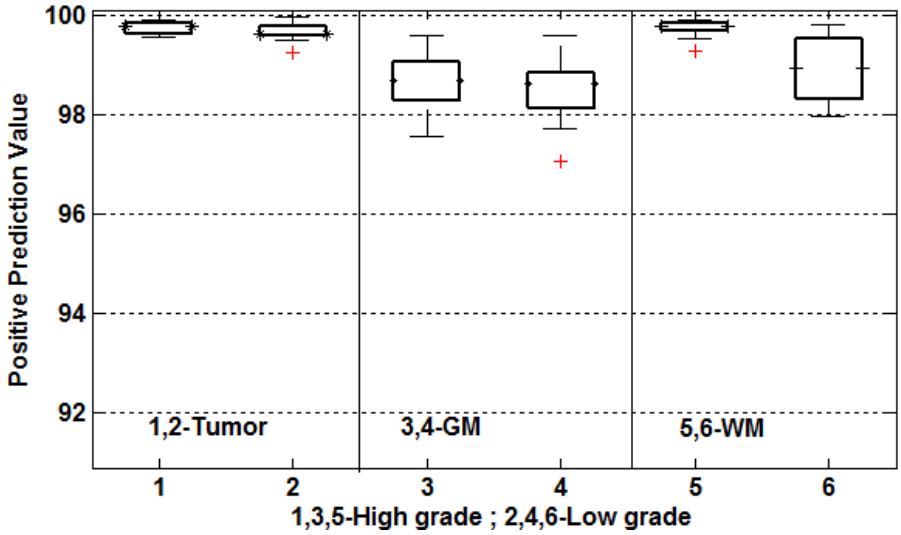

Fig.5.26 Positive prediction (P+[%]) values of high and low grade tumors, GM, and WM respectively.

The positive prediction value, the correspondence with the location and size of segmented ROIs are also excellent as shown in Fig.5.25. P+ index estimates the correspondence in size and location between the Segmented ROI and GT. The ranges of values for low and high grade tumors 99. 3- 99.6%, 99.5- 99.85%, GM - 98.1-99-1%, 98.3- 99.2% and WM are 98.3-99.5%, 99.5-99.8% respectively. The median positive prediction values obtained from the box plot (Fig. 5.25) of low and high grade tumor- 99.4 and 99.5, GM -98.7 and 98.8 and WM are 99.1 and 99.6 respectively.

3. Computation Time

For manually segmenting pathological areas of the brain, it takes at least 30 minutes for each slice. The maximum time required for segmentation of ROIs using this method is only 0.1second, which makes the method attractive to clinicians. So the laborious manual segmentation can be dispensed with this automated method can aid radiologist to a great extent.

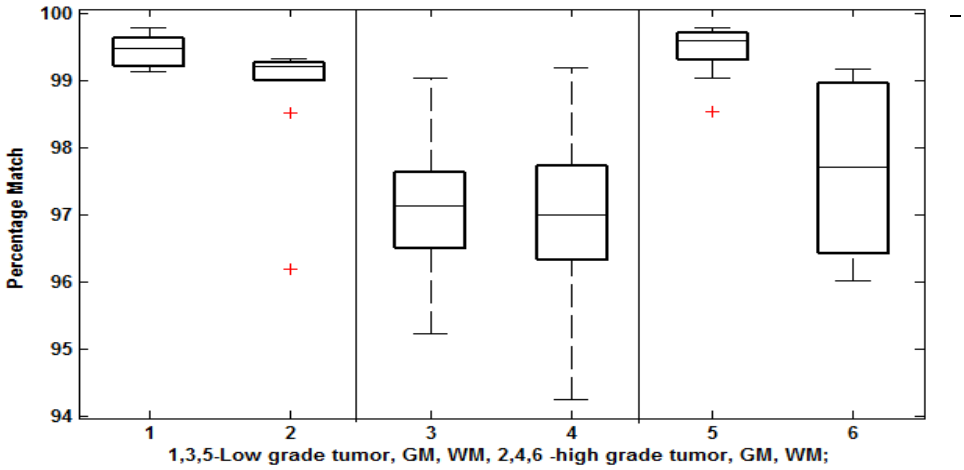

Fig 5.25 The percentage match of low grade and high grade glioma tumor, GM and WM is shown using box plot.

A user friendly software package has been developed and is presented in chapter8. The computation time and accuracy of atlas based segmentation using expectation maximization [6], segmentation based on hidden Markov random field model based algorithm [12], Adaptive template moderated brain tumor segmentation [3], Segmentation of brain tissue from expectation maximization, mathematical morphology and active contour models [10], and assessment of automated brain structures segmentation based on the mean shift algorithm [13] are validated in the literature. Of these methods, segmentation discussed here, is more accurate with much less computation time. Our validation study was designed to determine how closely this method correlated with GT. The size of the structure depends on segmentation accuracy. Segmentation errors occur on the boundary of surfaces. Thus, larger the surface of an object, more number of pixels are misclassified. So accuracy is lower with larger objects than smaller objects. The incorporation of T2-weighted images, which distinguish tumor as hyper intense tissues, may enable the precise definition of tumor boundaries. Accuracy in terms of TI, PM, P+ and reproducibility is almost same when considering two grades.

5.4 A comparative study between Fuzzy C-Means clustering Technique and the two methods

So far two novel methods for segmentation of tumor,GM and WM have been discussed. These two methods have to be compared with existing method that is widely accepted for segmentation of brain structures. The next section discuss the comparison of performance of the two methods with Fuzzy C-Means Clustering algorithm. Comparison was done qualitatively and quantitatively.

5.4.1 Fuzzy C-Means Clustering Technique

Fuzzy C-Means clustering technique is a widely used technique for segmentation of pathological tissues from brain MRI, which was already discussed in chapter 3. In general, cluster analysis refers to a broad spectrum of methods which try to subdivide a data set X into c subsets (clusters) which are pair wise disjoint, all non-empty, and reproduce X via union. The clusters are then termed a hard (i.e., non-fuzzy) c-partition of X. Fuzzy c-means (FCM) is a method of clustering which allows one piece of data to belong to two or more clusters[14]. It is based on minimization of the following objective function [15]:

$$J_m = \sum_{i=1}^{N}\sum_{j=1}^{C} U_{ij}^{m}\left\|x_i - c_j\right\|^2, \qquad 1 < m < \infty$$

where m is any real number greater than 1, u_{ij} is the degree of membership of x_i in the cluster j, x_i is the ith of d-dimensional measured data, c_j is the d-dimension center of the cluster, and ||*|| is any norm expressing the similarity between any measured data and the centre. Fuzzy partitioning is carried out through an iterative optimization of the objective function shown above, with the update of membership u_{ij} and the cluster centers c_j by:

$$U_{ij} = \frac{1}{\sum_{k=1}^{c}\left[\frac{\left\|x_i - c_j\right\|}{\left\|x_i - c_k\right\|}\right]^{\frac{2}{m-1}}}, \quad where\ c_j = \frac{\sum_{i=1}^{N} U_{ij}^{m}.x_i}{\sum_{i=1}^{N} U_{ij}^{m}}$$

This iteration will stop when $\max_{ij}\left\{\left|u_{ij}^{(k+1)}-u_{ij}^{(k)}\right|\right\}<\varepsilon$, where ε is a termination criterion between 0 and 1, whereas k are the iteration steps. This procedure converges to a local minimum or a saddle point of J_m. The algorithm is composed of the following steps:

1. *Initialize* $U=[u_{ij}]$ *matrix,* $U^{(0)}$
2. *At k-step: calculate the centers vectors* $C^{(k)}=[c_j]$ *with* $U^{(k)}$

$$c_j=\frac{\sum_{i=1}^{N}u_{ij}^{m}\cdot x_i}{\sum_{i=1}^{N}u_{ij}^{m}}$$

3. *Update* $U^{(k)}$, $U^{(k+1)}$

$$u_{ij}=\frac{1}{\sum_{k=1}^{C}\left(\frac{\|x_i-c_j\|}{\|x_i-c_k\|}\right)^{\frac{2}{m-1}}}$$

4. *If* $||\ U^{(k+1)}-U^{(k)}\ ||<\varepsilon$ *then STOP; otherwise return to step 2.*

5.4.2 Implementation of the Fuzzy C-Means Algorithm

The Fuzzy C Means Algorithm (FCM) method is implemented for the image database of method I and method II. The method is also validated quantitatively by computing Tanimoto Index and qualitatively in terms of computation time.

5.4.3 Results and Discussions

This section details the results obtained for the FCM method. Fig.5.27a shows a sample T2 weighted image and Fig.5.27b shows the tumor region detected. Fig.5.28 shows the visual validation of the method. Tumor and its boundary is extracted using iterative procedure and the extracted tumor boundary is superimposed on T1-FLAIR image. It can be well observed that the entire tumor region is not segmented out fully using this method; the tumor region is under segmented. The regions left out is marked in Fig. 5.28d

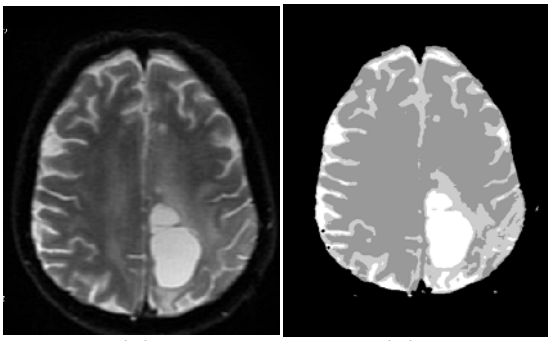

Fig.5.27 Example for Fuzzy c-means algorithm
(a) T2 weighted image (b)Segmented Image using fuzzy c-means algorithm

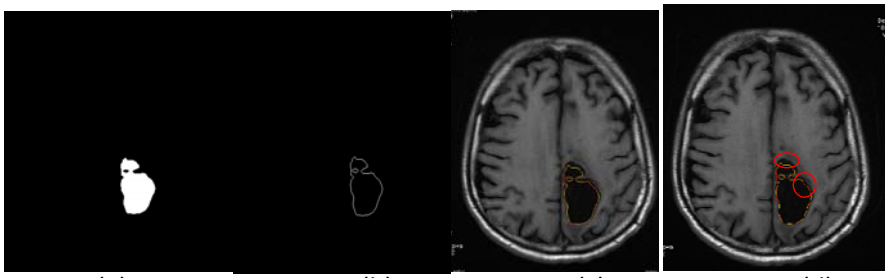

Fig.5.28 Visual validation of fuzzy c-means clustering technique
(a) Segmented using the FCM algorithm (b) Tumor boundary (c) extracted boundary super imposed on T1 weighted image (d) under segmentation detected in the rounded portions

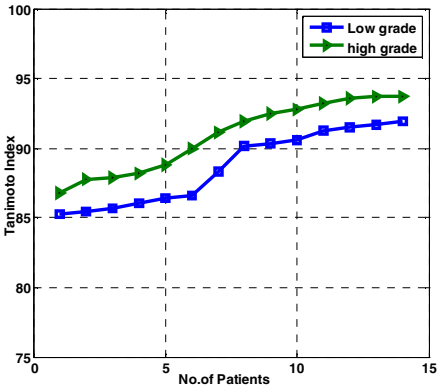

Fig.5.29 Tanimoto index of low and high grade glioma using Fuzzy c-means clustering Algorithm.

Table 5.9 Performance Analysis of FCM method

FCM	TI	FP	Computation time	TI	FP	Computation time
Image 1	85.28	245	38	86.80	256	36
Image 2	85.44	342	34	87.78	312	32
Image 3	85.67	451	32	87.91	434	33
Image 4	86.09	298	35	88.21	297	25
Image 5	86.40	381	38	88.84	343	28
Image 6	86.62	254	39	90.01	259	29
Image 7	88.32	314	36	91.15	326	26
Image 8	91.68	356	39	93.74	306	39
Image 9	91.97	212	34	93.69	223	24
Image 10	92.00	235	35	93.70	275	35

The Accuracy of segmentation of low and high grade glioma is calculated using Tanimoto index as shown in Fig.5.29. From Table 5.9 the percentage ranges of accuracy of segmentation for low and high grade glioma is 86.2-92.3 and 87.1-93-2 respectively. The computation time and FP are also provided in the Table 5.9 for low and high grade patients' image dataset. That is, in this method, number misclassified pixels are high. Hence this method is not accurate as the two methods discussed in this chapter.

5.4.3.1 Performance Comparison of Method I and Method II with respect to Fuzzy C-Means Clustering Technique

This Section gives a comparative study between the results obtained for method I and AGASA (method II) with respect to Fuzzy C-means clustering algorithm.

Table 5.10 Comparative study of proposed method I and Method II with respect to FCM method

Parameter for comparison	Method I	AGASA (Method II)	FCM
Segmentation Accuracy(TI%)	98%	98%	90%
Average No. of Misclassified pixels (FP or FN)	120	130	300
Computation Time	1 Seconds	2 Seconds	36 Seconds

The accuracy of these segmentation methods were already discussed in the previous sections as part of validation procedure and is given in Table 5.10. Accuracy of the FCM method is already computed using Tanimoto Index and visual validation was done by labeling procedure in all cases. From the Table 5.10, it is noted that the average values for TI is 98% for method I and Method II, and 90% for FCM. The average number of misclassified pixels is measured interms of average FP is 120 for method I, 130 for AGASA (Method II) and 300 for FCM. The positive prediction value, the correspondence with the location and size of segmented ROIs are also excellent as shown in Fig.5.25. P+ index estimates the

correspondence in size and location between the Segmented ROI and GT. The ranges of values for low and high grade tumors 99. 3- 99.6%, 99.5- 99.85%, GM - 98.1-99-1%, 98.3- 99.2% and WM are 98.3-99.5%, 99.5-99.8% respectively. The median positive prediction values obtained from the box plot (Fig. 5.25) of low and high grade tumor- 99.4 and 99.5, GM -98.7 and 98.8 and WM are 99.1 and 99.6 respectively.

Computation time for FCM is 36 seconds compared to 1second and 2second time for method I and method II. From the above values, it is clear that method I and method II have better segmentation performance than the FCM method. The FCM method is quite complex and time consuming than the proposed methods.

Method I uses T2 weighted images only and it extracts the tumor region, whereas AGASA (Method II) is able to extract White matter, Grey matter and Tumor from the joint intensities of T1 FLAIR and T2 weighted images. The Accuracy and performance of two methods are almost same.

Conclusions

A new simple, accurate and robust method for automatic extraction of low and high grade tumors from T2 weighted MRI was explained in this chapter. The robustness of the algorithm with respect to Gaussian noise and speckle noise was also demonstrated. The main drawback of this algorithm is that using the single modality T2 weighted images it is difficult to extract other brain subjects such as White matter and Grey Matter. The segmentation accuracy of the methods is computed using Tanimoto index.

This difficulty was overcome by developing a novel and robust algorithm named as Adaptive Gray level Algebraic set Segmentation Algorithm (AGASA) for the extraction of definable objects such as White Matter, Grey Matter, tumor and tumor boundary, which preserves its shape and gray level information. The spatial domain processing technique used mainly involves mathematical morphological methods, correlation filtering and adaptive thresholding technique. Here, we make use of joint intensities of two modalities of MRI. The method is validated against manually segmented images by an expert radiologist as Ground Truth images. The accuracy of method in terms of segmented region of interests was validated by computing TP, FP, FN with respect to Ground truth images. The

Tanimoto Index, Percentage Match, Positive Prediction Value obtained and its ranges shows excellent performance of the new methods.

The developed methods were compared with the widely used Fuzzy c-means clustering technique and it is seen that, the new methods showed much better performance than FCM algorithm.

The main goal of development of this automated segmentation method is to make segmentations of MR images more practical by replacing manual outlining, which reduces operator time, without accuracy loss and to improve reproducibility. This segmentation method is suitable for image registration for surgical planning, detection of tumor growth and thus by determining prognosis of patients in the case of high grade tumors. Partial volume effects were very much reduced in low grade tumor as defined by the boundary of the tumor. It may be noted that, this method is fairly simple when compared with other frequently used methods. The segmented ROIs were retaining the gray level values of each pixel. Hence these segmented tumors are used for statistical texture analysis and grade detection of glioma tumor. Segmented gray level tumors are also used for 3D rendering of glioma tumors for volumetric analysis. A software package is developed which can be operated by the users and thus by assisting radiologist to a great extend for replacing the manual outlining of pathological subjects in brain MRI.

References

[1] D. L. Pharm, C. Szu, A survey of current methods in image segmentation. Technical Report JHU/ECE 99-01, Publication to Annual Medical Review of Biomedical Engineering, pp.1-27. (1998).

[2] S. Ananda Resmi and T. Thomas,B. Thomas A Novel Automatic Segmentation Method for Extraction of Glioma Tumor, White matter and Grey matter from Brain MRI, Biij(accepted for publication), vol.e21(2) (2013)

[3] S. Ananda Resmi, Tessamma Thomas, A semi-automatic method for segmentation and 3D modeling of glioma tumors from brain MRI , J. Biomedical Science and Engineering, 2012, 5, 378-383

[4] R. Xu, L Luo and J Ohya. Segmentation of brain MRI, A text book of Advances in brain Imaging.In Tech Publishers, pp.143-169.(2002).

[5] T Kapur, W Eric, L Grimson, et.al. Segmentation of brain tissue from magnetic resonance images, Medical Image Analysis, Oxford University Press, vol.1(2):pp.109–127.(1996).

[6] M P Katia, P Paolo, L Brambilla , et.al. ITAC volume assessment through a Gaussian hidden Markov random field model-based algorithm. Proceedings of 30th Annual International IEEE EMBS conference (2008).

[7] M R Kaus, SK Warfield, A Nabavi, et.al. Automated Segmentation of MR Images of Brain Tumors. , Radiology, vol.218(2):pp.586–591.(2001).

[8] B. Shinde, D. Mhaske, M. Patare, A.R. Dani. Apply Different Filtering Techniques To Remove The Speckle Noise Using Medical Images. International Journal of Engineering Research and Applications (IJERA) vol. 2(1): pp.1071-1079.(2012).

[9] M. N. Nobi and M. A. Yousuf , A New Method to Remove Noise in Magnetic Resonance and Ultrasound Images. J. Sci. Res, vol.3(1):pp.81-89.(2011).

[10] S. Ananda Resmi, Tessamma Thomas, Automatic Segmentation framework for Primary tumors from brain MRIs using Morphological filtering Techniques, Proceedings of 5th International Conference on BioMedical Engineering and Informatics (BMEI'12) , 16-18 October 2012, in Chongqing, China

[11] HD Jude, S Kezi, C Vijila, Fuzzy Based Experimental Verification of Significance of Skull Tissue removal in Brain Tumor Image segmentation', International Journal of Computer Applications, vol.1(29):pp.56-61.(2010).

[12] T Rohlfeng, DB Russakov, C R Maurer Performance- Based classifier Combination in Atlas-Based Image segmentation using Expectation – Maximization Parameter Estimation. IEEE transactions on Medical Imaging, vol.23(8):pp.983-994.(2004).

[13] C Farmaki, K Mavrigiannakis Assessment of Automated Brain Structures Segmentation based on the Mean-shift Algorithm', 10th IEEE International Conference on Information Technology and Applications in Biomedicine (ITAB). :pp.1-5.(2010)

[14] J.C. Bezdek, R. Ehrlich and W. Full. FCM- Fuzzy c-means clustering Algoithm.Computers and GeoSciences, vol.10(2-3),pp:191-203, (1984)

[15] Y. Yang, S. Huang, Image Segmentation by Fuzzy C-Means Clustering Algorithm with a Novel Penalty Term, Computing and Informatics, Vol. 26, pp. 17–31,(2007).

Chapter 6

Technique for Grade Detection of Glioma Tumors from Conventional MRI using Statistical Methods

Different approaches for classification/detection of abnormalities of human organs and other pathological subjects including brain tumors from various imaging modalities have been proposed in recent years, but none of them obtained 98% performance. In this chapter, a new efficient method for grade detection of glioma tumors is presented based on texture analysis. The images used for texture analysis contains only the segmented tumor regions which retain the normalized gray level values of the original image. Initially, Statistical texture analysis of segmented images from the database is performed using first order statistical methods and Gray level co-occurrence matrix (GLCM) based second order statistics, for feature extraction and feature set formulation. Then, a decision system was developed based on the thresholds fixed by selected discriminant features in the feature sets. The performance of the method, which is tested by using twenty patients' image dataset and performance of detection system was evaluated using ROC analysis, which showed 98% above accuracy.

6.1 Introduction

The characterization and grading of glioma tumors, via image derived features, for diagnosis, prognosis, and treatment response has been an active research area in medical image computing. This chapter presents the development of a new method for grade detection of glioma tumors from conventional T2 weighted MR images. The steps involved in this work are texture analysis, feature extraction, feature selection and detection. Statistical texture analysis was done on the segmented tumor region using first order statistical features and gray level co-occurrence matrix (GLCM) based second order statistical features.

The organization of this chapter is as follows. Section 6.2 presents texture analysis for feature extraction using first order and second order GLCM based features, feature selection using box plots and feature set formulation based on the thresholds fixed by the selected features, for detection of high grade and low grade glioma tumors from conventional T2 weighted MR images. The implementation of the technique is detailed in section 6.3. Section 6.4 discusses results obtained from implementation of the method and development of a decision system for detection. Performance evaluation of the method using ROC analysis is also presented.

6.2 A Novel Technique for grade Detection of Glioma

Method Development

The steps involved in technique are shown in the flowchart of Fig.6.1. They are texture analysis and feature extraction, feature selection, feature set formulation and development of the decision system based on the thresholds fixed by the selected features in the feature set.

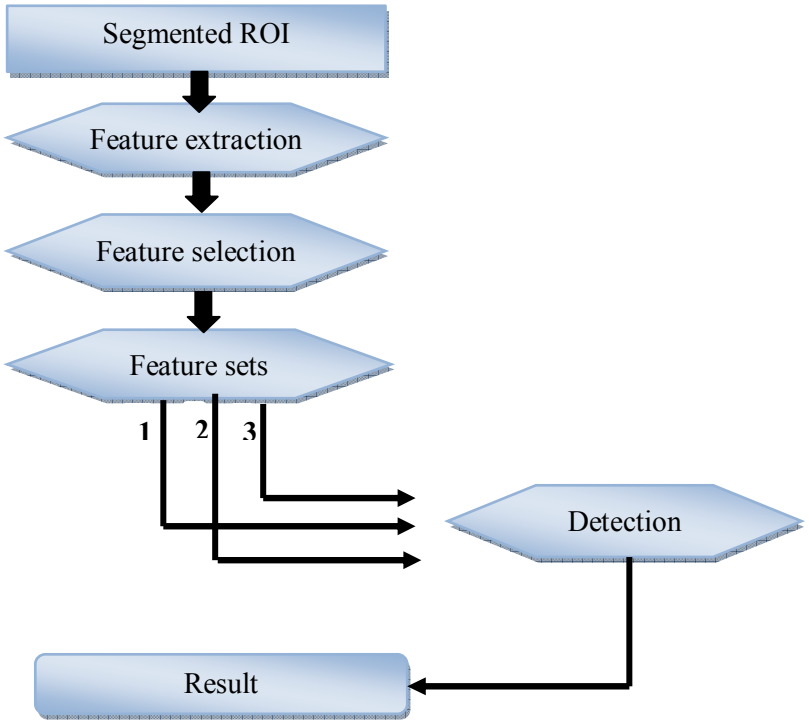

Fig.6.1 Show the flow chart for decision system for grade detection of glioma

6.2.1 Texture Analysis and Feature Extraction

After an image has been segmented into regions of interest, the resulting segmented pixels or regions are usually represented and described in a form suitable for further analysis.

The segmented regions can be represented in terms of its external (boundary) or internal characteristics (pixels comprising the region). External representation is chosen when the primary focus is on shape characteristics. An internal representation is selected when the primary focus is regional properties such as color and texture. Choosing a representation of a region is only a part of making

data useful for analysis. Next task is to describe the region based on the chosen representation. Special emphasis is given here on texture, description and quantification of its content. Texture analysis is very important in brain tumor detection, as it is difficult to differentiate between various types of tumor tissues using shape [2, 3]. The main challenge is that the shape of a tumor is not consistent throughout all slices of MR image and may change quickly if the inter-slice distance is large. But, tumors are expected to have consistent textures for all slices [3] and hence prominent MRI slices are chosen from each patient data slice for grade detection.

Texture features have proved useful in differentiating normal and abnormal tissues [4] in different organs using different types of imaging modalities. The segmented ROI was considered for texture analysis in the detection method described in this chapter.

As part of method development, two types of texture analysis were considered

1. By considering only 16x16 sub image of entire segmented tumor region as done by earlier researchers
2. By considering the entire segmented tumor region

A set of textural descriptors is calculated for each ROI, using first order statistics (of texture type 1 and 2) and GLCM based second order statistics (Type 2). The discriminant features that are suitable for properly differentiating the two tumor grades were selected from these descriptors.

6.2.1.1 First-order statistics

For any segmented ROI, the mean (average intensity) and the standard deviation (average contrast) of the level values in the region can be used to measure the spread of gray level values of the pixels within that region (Histogram)[1,4 - 6]. One class of such measures is based on statistical moments. Here statistical moments such as mean, standard deviation, entropy, kurtosis and skewness are calculated from a 1)16x16 sub image or blocks of the segmented ROI (Fig 6.2) and also the entire segmented tumor area. This is for the purpose of correctly detecting the grade of glioma. Intensity pattern in the tumor region is calculated using histograms of segmented ROI (SROI).

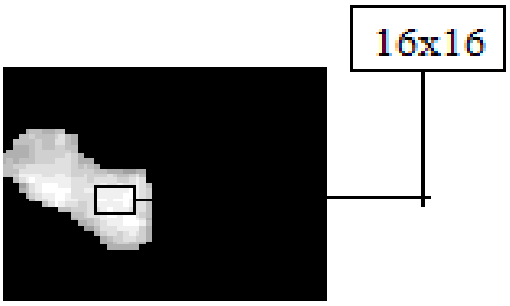

Fig.6.2sub image selected from the segmented tumor region

Using first order statistical moments it is able to describe the underlying structures that leads us to perceive the texture in terms of 'coarseness', 'uniformity', 'roughness' and so on. Table 6.1 and 6.2 shows the typical values of five descriptors for 20 images (from 20 patients' image dataset) calculated from a 16x16 sub image of the segmented low grade and high grade glioma tumors respectively. Tables 6.3 and 6.4 show the same values, considering the whole segmented tumor regions, with respect to the same 20 images. From the table 6.1 and 6.2, it can be observed that the typical values of all descriptors are not statistically significant. From these tables, it can be observed that the ranges of values average intensity for low grade 49-98; and high grade glioma 52-190 ; Standard deviation for low grade 8-30 and high grade glioma 10-110; Kurtosis for low grade 2.2-8.5 and high grade glioma 3-42; entropy for low grade 0.59-1.98 and high grade glioma 0.4-8;

But the descriptors in the Table 6.3 and 6.4 are statistically significant. From these Tables 6.3 and 6.4 it can be well observed that the ranges of values of average intensity for low grade is 70-160 and for high grade is190-230; ranges of values observed for standard deviation for low grade is10-60 and high grade is 90-130 ; Range of values for entropy for low grade is 0.5-3 and high grade is 6.5-11. Range of values for kurtosis for low grade is 2-12 and high grade is 115-152 and the ranges of values observed for low grade-0.2-15 and high grade is10-20.

So it can be observed that considering only a small region does not give sufficient statistical information for differentiating between low and high grade glioma. Hence the whole region is considered for calculating the discriminating features in later sections.

Table 6.1 Typical values of First order statistical features from 16x16 segmented tumor sub image of 20 high grade dataset

High grade	Intensity	Std. dev	Kurtosis	entropy	Skewness
Image 1	100.75	93.64	65.79	1.04	10.9
Image 2	65.95	83.02	80.09	7.53	8.08
Image 3	91.15	98.04	17.2	7.03	5.08
Image 4	119.68	25.72	19.17	9.73	12.45
Image 5	74.88	12.13	12.05	10.23	1.52
Image 6	60.08	24.8	6.74	11.29	16.27
Image 7	75.28	14.56	10.13	7.81	15.02
Image 8	80.48	22.97	1.87	0.87	3.76
Image 9	195.68	18.82	3.41	1.71	15.88
Image 10	90.88	19.51	2.49	1.14	15.63
Image 11	186.08	22.99	2.33	1.23	1.81
Image 12	181.28	21.4	5.34	1.45	1.04
Image 13	76.48	56.73	6.73	0.67	5.61
Image 14	198.95	105.02	34.67	1.71	3.89
Image 15	85.28	38.27	36.42	2.95	4.35
Image 16	100.48	95	76.73	0.78	6.75
Image 17	88.22	85.27	69.94	5.67	11.33
Image 18	87.9	88.52	51.79	8.02	6.65
Image 19	144.41	71.77	11.45	3.78	8.79
Image 20	70.5	78.02	25.21	7.53	9.17

Table 6. 2 Typical values of First order statistical features of 16x16 segmented tumor sub image from 20 low grade glioma image dataset

Low grade	Intensity	Std. dev	Kurtosis	entropy	Skewness
Image 1	67.81	26.74	1.9	1.91	1.91
Image 2	46.59	30.82	10.05	1.07	1.07
Image 3	52.94	15.55	6.74	0.87	0.2
Image 4	67.59	26.72	10.13	1.71	1.61
Image 5	65.16	11.13	1.87	1.14	0.98
Image 6	79.73	24.60	3.41	1.23	2.02
Image 7	74.3	13.40	2.49	1.45	1.32
Image 8	81.87	20.30	0.33	0.67	1.28
Image 9	73.44	14.82	1.34	0.71	1.11
Image 10	98.01	19.51	2.16	0.95	0.95
Image 11	89.58	27.99	4.34	0.78	0.78
Image 12	97.15	20.04	1.02	0.61	0.61
Image 13	91.72	22.09	1.13	1.81	1.81
Image 14	86.29	19.64	6.39	1.04	1.04
Image 15	80.86	16.54	5.24	0.56	3.61
Image 16	77.59	12.65	2.95	1.01	3.89
Image 17	70	8.77	0.97	1.14	4.33
Image 18	75.69	9.22	8.54	0.94	1.65
Image 19	71.16	10.08	9.08	0.67	2.72
Image 20	82.29	15.93	9.62	0.4	3.10

Table 6. 3 Typical values of First order statistical features of the same low grade glioma patients' image dataset considering the whole tumor region.

Low grade	Intensity	Std. dev	Kurtosis	entropy	Skewness
Image 1	157.81	56.76	11.87	2.91	2.91
Image 2	146.59	50.82	12.39	2.07	2.07
Image 3	152.94	45.55	9.74	2.00	2.00
Image 4	137.59	36.73	10.13	1.71	1.71
Image 5	135.16	31.13	1.87	1.14	1.14
Image 6	129.73	24.60	5.81	2.36	2.36
Image 7	124.30	18.06	2.49	1.45	1.45
Image 8	118.87	11.53	0.33	1.28	1.28
Image 9	113.44	52.82	1.57	1.11	1.11
Image 10	108.01	40.45	3.46	0.95	0.95
Image 11	102.58	43.18	7.34	0.78	0.78
Image 12	97.15	39.84	1.02	0.61	0.61
Image 13	91.72	34.88	11.13	2.81	2.81
Image 14	86.29	29.64	8.39	1.04	1.04
Image 15	80.86	26.54	138.27	2.00	12.61
Image 16	127.59	22.65	95.00	1.71	13.89
Image 17	70.00	18.77	8.00	1.14	14.33
Image 18	75.69	14.22	8.54	0.94	16.65
Image 19	71.16	10.08	9.08	0.67	18.79
Image 20	82.29	15.93	9.62	0.40	20.17

Table 6. 4 Typical values of First order statistical features of the same set of high grade glioma considering whole tumor region

High grade	Intensity	Std. dev	Kurtosis	entropy	Skewness
Image 1	200.95	93.64	115.79	6.04	9.00
Image 2	195.95	103.02	120.29	7.53	18.08
Image 3	205.31	98.04	117.20	7.03	7.08
Image 4	209.10	93.64	119.17	9.73	12.48
Image 5	217.28	99.62	119.88	10.23	10.52
Image 6	200.95	112.64	118.38	11.29	16.27
Image 7	193.31	117.04	131.89	7.81	15.02
Image 8	205.31	115.52	121.99	9.08	13.76
Image 9	220.10	118.77	134.71	10.97	15.88
Image 10	225.86	122.02	127.76	9.66	15.63
Image 11	218.40	75.27	115.01	9.59	16.45
Image 12	220.40	128.23	134.90	8.66	16.77
Image 13	222.39	156.73	136.73	11.01	17.24
Image 14	214.39	135.02	134.67	6.53	17.71
Image 15	226.73	138.27	136.42	8.82	12.61
Image 16	228.38	95.00	116.73	8.75	13.89
Image 17	230.38	125.27	139.94	8.67	14.33
Image 18	232.38	128.52	151.69	8.02	16.65
Image 19	234.38	131.77	110.45	7.78	18.79
Image 20	216.37	138.02	125.21	7.53	20.17

6.2.1.2 Second order statistics

GLCM is a widely used tool for analyzing statistical textural properties [4-22] of different types of tissues in biomedical imaging. As part of feature extraction from the segmented tumor using GLCM features, 10 Halarick descriptors are calculated to quantify the spatial dependence of gray level values. These descriptors are computed from the co-occurrence matrices of size [16x16], and are constructed at a distance of $d = 1$ and for direction $\theta = 0°$. The texture descriptors considered from GLCM are : Correlation, Contrast, Energy, Entropy, Homogeneity, Maximum probability; Inverse Difference Moment, Dissimilarity, Cluster Prominence and Cluster Shade of level values and the other descriptors are relative values of these features. Contrast measures the amount of local variations present in an image, while energy is the sum of squared elements in GLCM. Energy may also be referred to as uniformity or the angular second moment. Lastly, correlation will show how correlated a pixel is to its neighbor over the whole image. Inverse Difference Moment (also called homogeneity) IDM is also influenced by the homogeneity of the image. The result is a low IDM value for inhomogeneous images, and a relatively higher value for homogeneous images.

The quantitative values of GLCM based features such as contrast, dissimilarity, energy, entropy; cluster shade; cluster prominence and correlation of the whole segmented ROI of high grade and low grade glioma of all datasets were computed and is provided in the Table 6.5 and 6.6 respectively for 20 patients' image dataset. The ranges of values observed for cluster prominence of low grade 425-650 and for high grade 1300-1700; ranges of values of cluster shade for low grade 20-80 and high grade 100-200; ranges of values of auto correlation for low grade 10-30 and high grade 40-75; ranges of values of entropy for low grade 0.2-1.5 and high grade 6-15; ranges of values of dissimilarity for low grade 0.5-10 and high grade 50-250; ranges of values of energy for low grade 3-15 and high grade 0.2-1.5; ranges of values of contrast for low grade 0.2-1.5 and high grade 6-15; ranges of values of inverse difference moment for low grade 0.8-0.9 and high grade 0.87- 0.99; ranges of values of entropy for low grade 0.2-1.5 and high grade 6-15 and ranges of values of maximum probability for low grade 4 - 6 and high grade 3.3-7.

Table 6. 5 Typical values of GLCM features for randomly selected 20 images from high grade glioma patients' image dataset

High Grade	Autocorrelation	Contrast	Cluster prominence	Cluster shade	Dissimilarity	Energy	Entropy	Max. Probability	Inverse difference moment
Image 1	42.91	25.71	1295.03	-110.05	67.92	0.39	14.97	4.31	0.99
Image 2	45.61	43.61	1315.00	-125.05	79.17	0.49	9.68	3.70	0.97
Image 3	52.67	23.83	1218.00	-105.26	90.42	0.49	4.39	3.09	0.91
Image 4	55.68	51.08	1487.00	-126.68	101.67	0.65	10.90	2.49	0.88
Image 5	41.23	24.46	1378.00	-106.27	112.92	0.86	5.61	6.16	0.97
Image 6	48.65	24.28	1439.99	-185.86	124.17	0.93	3.22	6.42	0.91
Image 7	53.16	44.42	1473.78	-198.78	135.42	0.31	1.69	5.64	0.89
Image 8	50.68	24.64	1507.58	-168.37	69.17	0.62	10.15	6.92	0.88
Image 9	62.34	24.79	1541.37	-157.95	91.67	0.39	18.62	7.58	0.87
Image 10	73.12	24.93	1575.16	-149.21	94.17	0.91	27.09	8.25	0.85
Image 11	53.90	25.08	1408.96	-137.79	107.67	0.69	31.56	8.92	0.99
Image 12	54.68	25.22	1642.75	-126.38	109.67	0.86	18.03	9.58	0.97
Image 13	44.81	25.37	1376.54	-114.97	111.67	1.39	11.28	3.70	1.03
Image 14	53.69	54.71	1510.34	-131.73	166.67	0.09	10.93	3.09	1.08
Image 15	49.14	25.63	1744.13	-148.40	215.67	0.90	12.08	2.49	0.85
Image 16	48.09	26.02	1577.93	-155.24	117.67	1.86	13.24	6.16	0.99
Image 17	47.04	24.09	1609.90	-157.00	219.67	0.61	4.39	2.49	1.12
Image 18	45.99	23.90	1623.70	-168.75	126.67	0.79	15.54	6.16	0.88
Image 19	43.54	25.39	1637.49	-177.02	223.67	1.41	6.70	6.42	0.97
Image 20	21.79	32.42	1651.28	-182.50	125.67	0.75	7.85	5.64	0.91

Table 6. 6 Typical values of GLCM features for randomly selected 20 images from low grade glioma patients' image dataset

Low Grade	Autocorrelation	Contrast	Cluster prominence	Cluster shade	Dissimilarity	Energy	Entropy	Max. Probability	Inverse difference moment
Image 1	30.08	15.88	606.09	-58.21	5.29	3.86	1.50	5.90	0.98
Image 2	11.07	12.88	507.00	-59.45	9.17	4.86	0.97	6.16	0.99
Image 3	23.94	14.28	456.00	-60.91	3.04	4.93	0.44	6.42	0.89
Image 4	30.08	13.87	489.00	-61.59	3.58	6.49	1.09	5.64	0.88
Image 5	29.51	13.07	567.00	-64.12	2.46	0.65	0.56	5.90	0.87
Image 6	29.29	14.60	496.16	-65.04	1.33	9.31	0.32	6.16	0.82
Image 7	29.07	13.74	486.55	-66.44	1.21	3.06	0.17	2.47	0.79
Image 8	12.96	13.18	476.93	-5.78	12.17	6.15	1.02	3.83	0.75
Image 9	25.81	13.16	467.31	-78.20	1.13	3.86	1.86	6.98	0.72
Image 10	20.78	12.99	458.33	-34.43	2.10	9.08	0.71	3.13	0.68
Image 11	27.80	13.82	447.24	-30.65	2.76	6.93	0.16	7.28	0.97
Image 12	16.10	13.65	436.14	-26.88	13.64	8.56	1.30	5.64	0.91
Image 13	25.44	5.48	425.05	-23.10	3.32	13.86	1.13	5.07	1.03
Image 14	24.77	14.31	589.00	-45.67	4.10	0.86	1.09	5.01	0.89
Image 15	27.10	13.87	542.90	-36.63	4.88	9.01	1.21	4.95	0.88
Image 16	11.46	13.28	566.81	-38.12	10.51	14.65	1.32	4.89	0.87
Image 17	28.45	11.74	590.73	-62.34	1.17	6.09	0.44	4.84	0.82
Image 18	22.02	13.18	614.64	-79.95	2.33	7.93	1.55	4.78	0.79
Image 19	21.58	9.75	610.55	-39.62	3.30	14.06	0.67	3.72	0.88
Image 20	14.15	12.29	620.46	-39.25	3.64	7.51	0.78	4.96	0.89

From the above ranges of values, it can be observed that, GLCM features computed except maximum probability and inverse difference moment are considered for discriminating between low and high grade glioma.

6.2. 2 Feature selection and feature set formulation

Feature selection and feature set formulation are very important, because the selected features must be sufficiently discriminating and suitably adapted for the application, since they fundamentally impact the resulting quality of the detection system. Box plots are used for feature selection and detection process. A detailed theoretical explanation for box plot and its uses are given in chapter 4. By using box plot, most relevant and discriminant textural descriptors can be identified and selected for detection of low grade and high grade glioma. Fifteen feature descriptors are extracted from the first order statistical model and GLCM model.

Initially, intensity based 5 first order statistical features of 16x16 sub images of segmented tumors were used for feature extraction and feature selection. As a second step, the entire regions of segmented tumors were considered. The next procedure is the feature selection which is implemented using box plot. From the box plot of the extracted features it can be well observed whether the extracted feature is statistically discriminant or not, or how much discriminant it is. Similarly, from the 10 extracted GLCM features of entire segmented images, the discriminant features which are useful for detection procedure are identified using box plot. That is, Box plot identifies the statistical significance of a feature.

6.2. 3 Results of feature selection and feature set formulation

1. Selection of first order statistics

After the features were extracted using first order statistical features and GLCM based features, feature selections were done using box plot. Initially, the first order statistical features extracted from 16x16 sub-images of the segmented tumors were tested using box plot.

The box plots of mean (Fig.6.3), standard deviation (Fig.6.4), kurtosis (Fig.6.5) and entropy (Fig.6.6) for16x16 sub image of segmented low grade and high grade tumors were plotted and it is well observed the ranges of values are not discriminant.

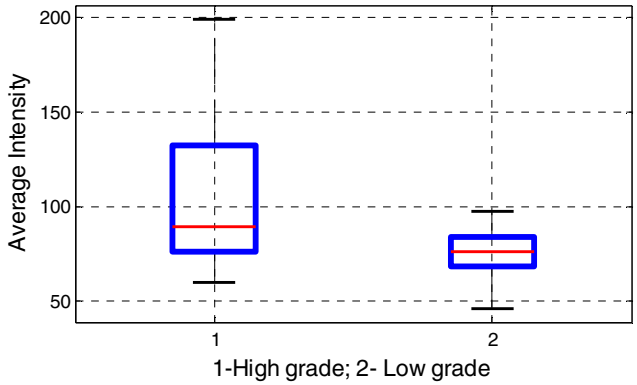

Fig.6.3 Box plots of Average Intensity for 16x16 sub-image of segmented low and high grade glioma.

The ranges values of average intensity of low and high grade are 49-98 and 52-190 respectively. Ranges of values of Standard deviation for low grade 8-30; and high grade glioma 10-110 and the median values are 50 for high grade and 18 for low grade. The ranges values for kurtosis for low and high grade glioma are grade 2.2-8.5and 3-42 respectively and for entropy the ranges of values of these low and high grades are 0.59-1.98 and 0.4-8 respectively. For all features, the ranges for low and high grade glioma are overlapping and hence it can be inferred that randomly selected 16x16 sub image of the tumor sub region is not sufficient to discriminate between the two grades of tumor. Hence the 16x16 sub images of the segmented tumor region were not taken for further Analysis. The clinical observation also conforms to this observation.

The diagnosis and detection of glioma currently rely on the histopathologic examination of biopsy specimens, but variations in tissue sampling for these heterogeneous tumors and restrictions on surgical accessibility make it difficult to be sure that the samples obtained are representative of the entire tumor [13].Hence we have to consider entire tumor region for analysis.

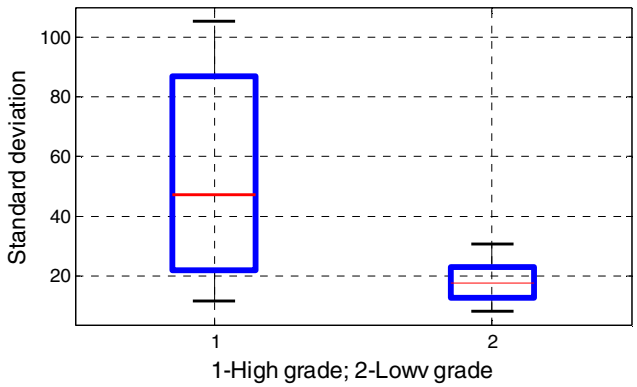

Fig. 6.4 Box plot of Standard deviation for 16x16 sub-image of segmented low and high grade glioma.

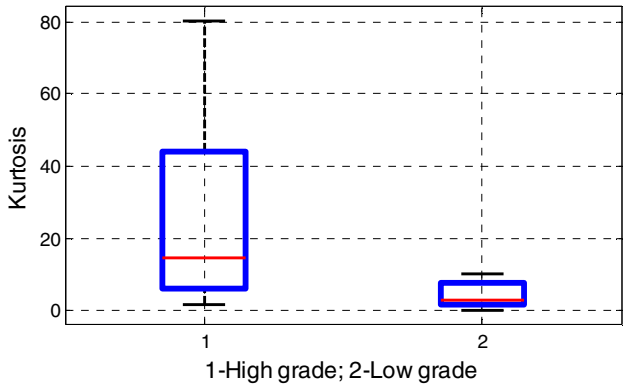

Fig. 6.5 Box plots of Kurtosis for 16x16 sub-image of segmented low and high grade glioma.

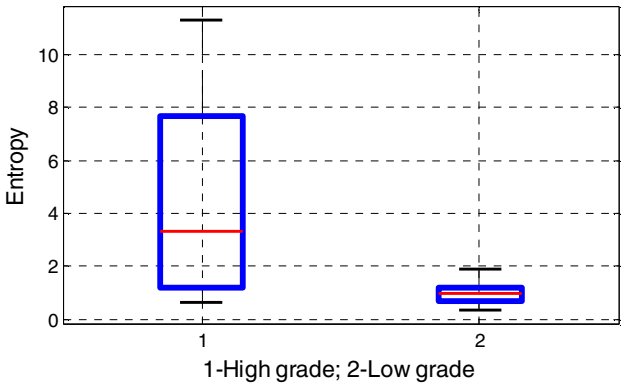

Fig. 6.6 Box plots of Entropy for 16x16 sub-image of segmented low and high grade glioma.

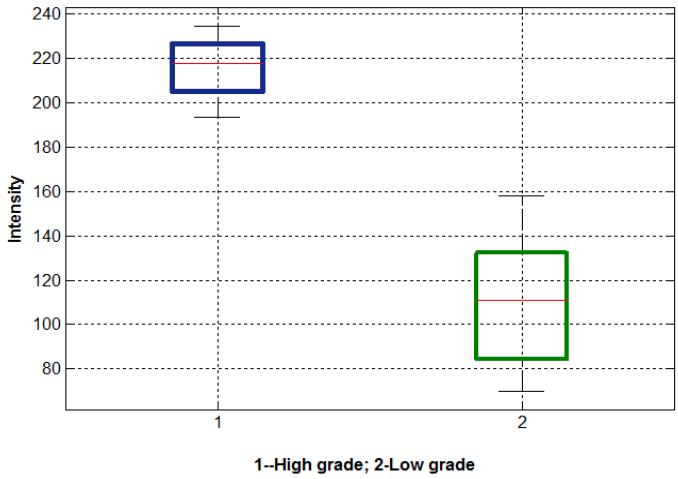

Fig.6.7 Box plot of mean (Intensity) levels for forty five sets of high grade and fifty five sets of low grade glioma patients.

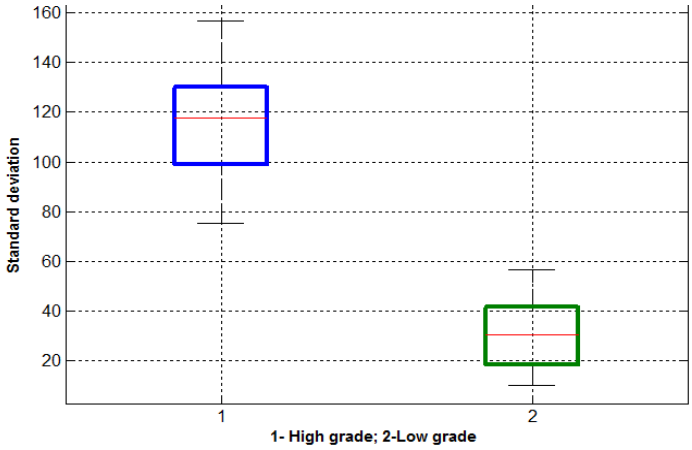

Fig. 6.8 Box plot of standard deviation using first order statistics for forty five sets of high grade and fifty five sets of low grade glioma patients

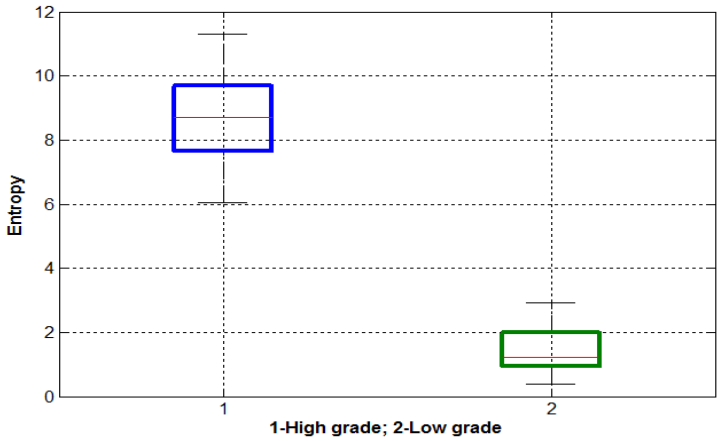

Fig. 6.9 Box plot of histogram based entropy distribution for forty five sets of high grade and fifty five low grade glioma patients ;

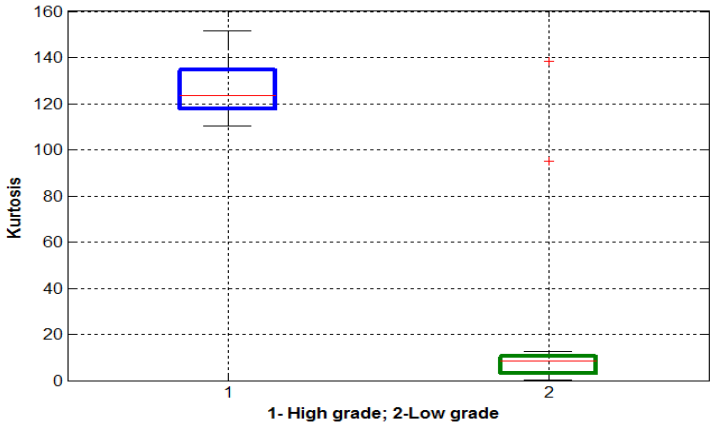

Fig.6.10 Box plot of kurtosis using first order statistics for forty five sets of high grade and fifty five low grade glioma patients.

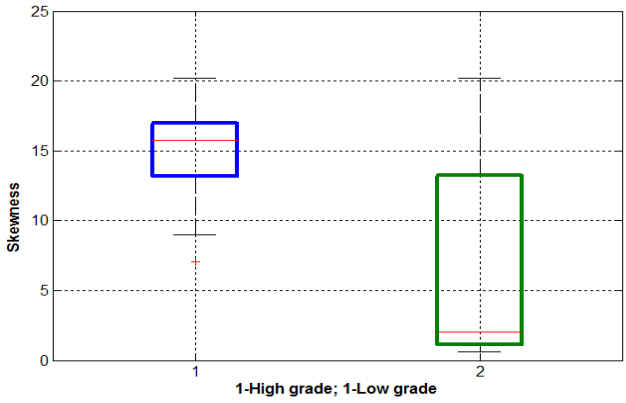

Fig.6.11 Box plots of intensity based parameter-skewness for forty five sets of high grade and fifty five sets for low grade glioma patients

Next, the box plots of intensity based 5 first order statistical features, for low and high grade glioma was calculated for entire tumor area and plotted. The box plots of mean (intensity), standard deviation, entropy, kurtosis, and skewness are shown Fig.6.7, Fig.6.8 Fig.6.9, Fig.6.10 and Fig. 6.11 respectively the ranges of values of high and low grade tumor. It can be observed that these descriptors are well discriminated between high and low grades. From the box plot, it is inferred that all features other than skewness have distinct values for high and low grade glioma. The ranges of values obtained for entropy, standard deviation, kurtosis and intensity are high for high grade glioma and low for low grade and these are also well differentiated between two grades. Hence, these features are selected as prominent features in detection procedure.

From the plot of skewness, it can be observed that, the feature is not well differentiated between two grades as that of the other descriptors. From the box plots of first order statistical descriptors, we can infer some of the properties of high grade and low grade glioma. These statistical descriptors yield characterization of high grade glioma texture as coarse texture. Usually coarse textures show heterogeneous behavior. Mean, standard deviation, kurtosis and entropy are high for high grade glioma. Highly malignant glioma (grade IV) tumors contain heterogeneous tumor texture [26]. Hence, as malignancy increases, tumor heterogeneity also increasing and hence these values should also increase.It is observed that, Intensity, Standard deviation, Third moment (Skewness), Kurtosis, and Entropy are low in low grade glioma, as low grade glioma has smooth texture when compared to high grade. This proved the effectiveness of first order statistical descriptors for glioma grade detection.

Table 6.7 The ranges of values of first order statistical features for segmented low grade and high grade glioma tumors

Texture	Intensity	Std. dev	Kurtosis	entropy	Skewness
High Grade	190-240	90-150	115-152	6.5-15	8-25
Low grade	70-160	10-60	1.5-12	0.5-5.2	0.2-3.0

Table 6.7 portrays the ranges of values for first order statistical descriptors, such as intensity, standard deviation, entropy, kurtosis, and skewness for the two grades of glioma tumors. The ranges of values determined from the statistical

quantification of 100 MRI datasets of segmented ROIs (55-low grade, 45- low grade). From the Table 6.5 and Fig 6.6, Fig 6.7, Fig 6.8 and Fig 6.9, it is observed that Intensity, Standard Deviation, Third Moment (Skewness), Kurtosis, and Entropy is higher for high grade glioma and all these features are well discriminated between two grades. So these features are selected for differentiating between two grades. The feature skewness has overlapping values is hence knocked off.

2. Selection of Second order Statistics

The quantitative values of GLCM based features such as Cluster Prominence, Cluster Shade, Correlation, Entropy, Dissimilarity, Energy, Contrast, Maximum Probability and Inverse Difference Moment of segmented ROI for high grade and low grade glioma of all datasets were computed and its box plots are plotted. The box plots of cluster prominence (Fig.6.12), cluster shade (Fig.6.13), auto correlation (Fig. 6.14), Entropy (Fig. 6.15), dissimilarity (Fig.6.16), energy (Fig.6.17), contrast (Fig.6.18), inverse difference moment (Fig.6.19) and maximum probability (Fig.6.20) for high grade and low grade Glioma tumors are plotted.

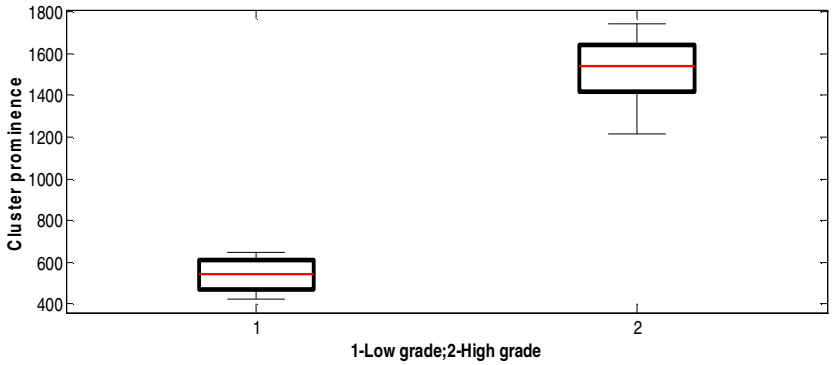

Fig.6.12 Box plots of Cluster prominence for forty five sets of high grade and fifty five sets of low grade Glioma patients .

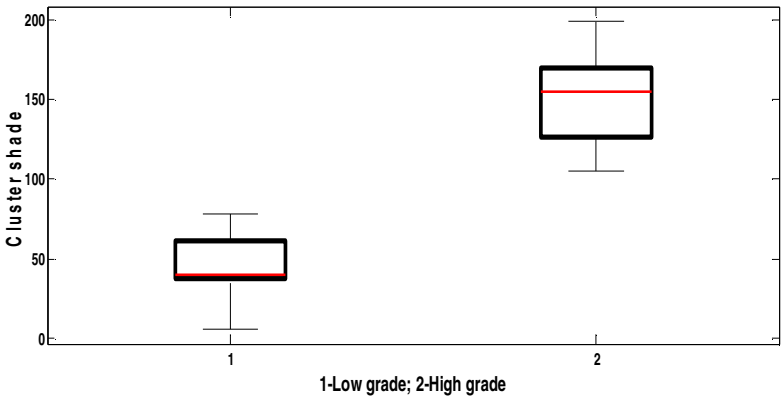

Fig.6.13 Box plots of Cluster shade forty five sets of high grade and fifty five sets are low grade glioma patients.

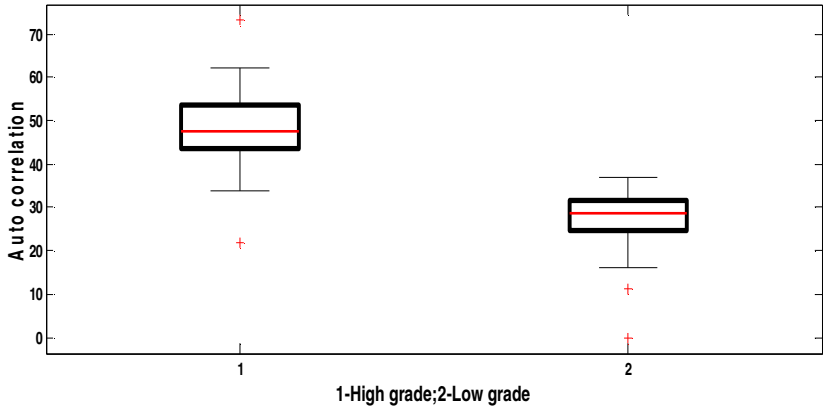

Fig.6.14 Box plots of Auto correlation for forty five sets of high grade and fifty five sets of low grade glioma patients.

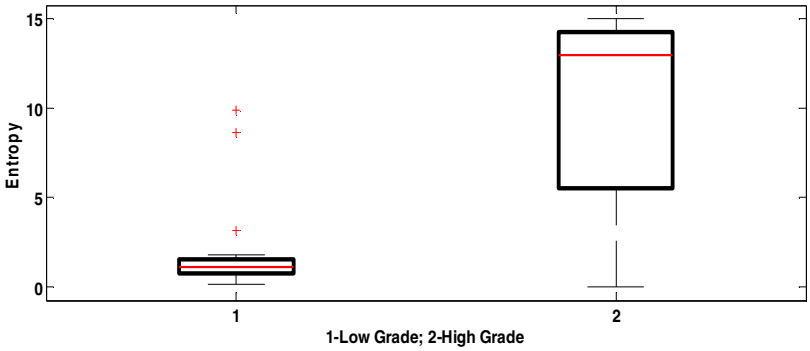

Fig.6.15 Box plots of Entropy forty five sets of high grade and fifty five low grade Glioma patients

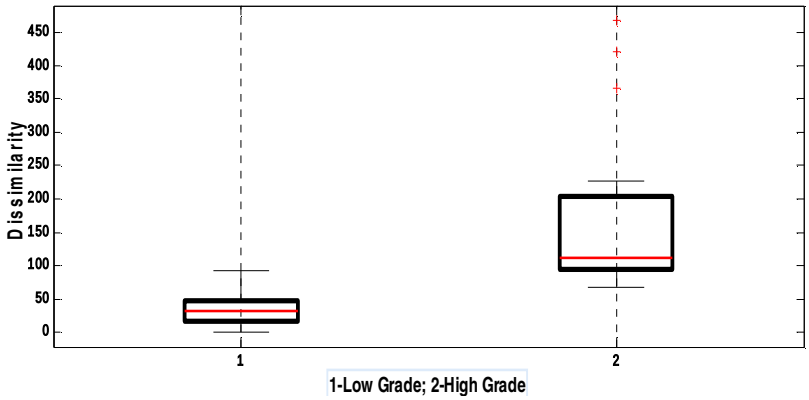

Fig.6.16 Box plots of Dissimilarity for forty five sets of high grade and fifty five low grade Glioma patients

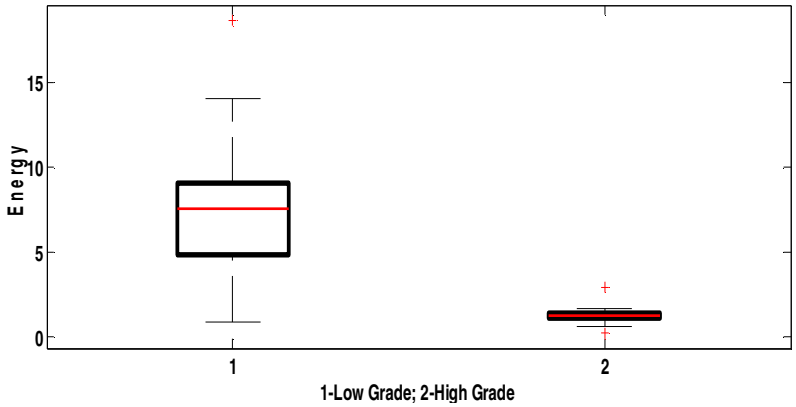

Fig.6.17 Box plots of Energy for forty five sets of high grade and fifty five low grade glioma patients

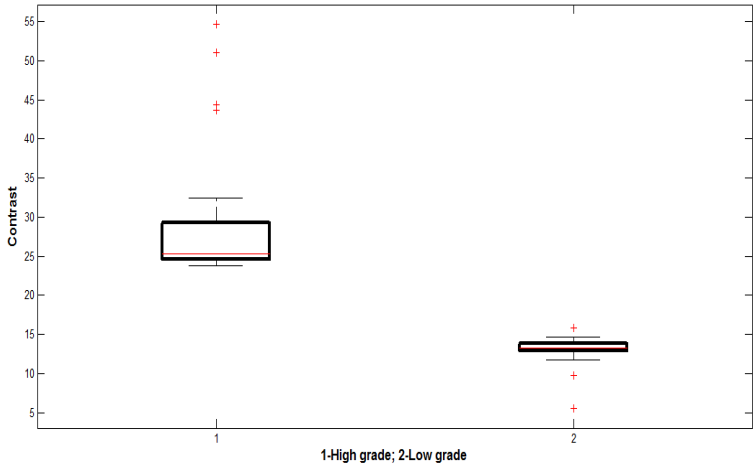

Fig.6.18 Box plots of Contrast for forty five sets of high grade and fifty five low grade glioma patients.

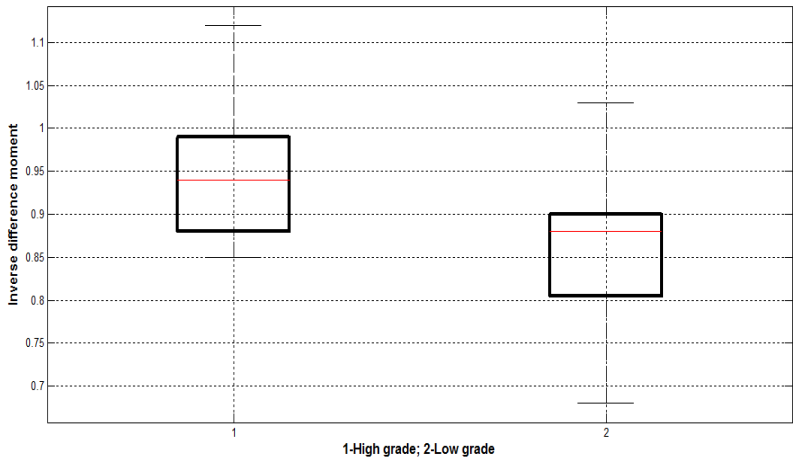

Fig. 6.19 Box plot of Inverse difference moment for forty five sets of high grade and fifty five low grade glioma patients

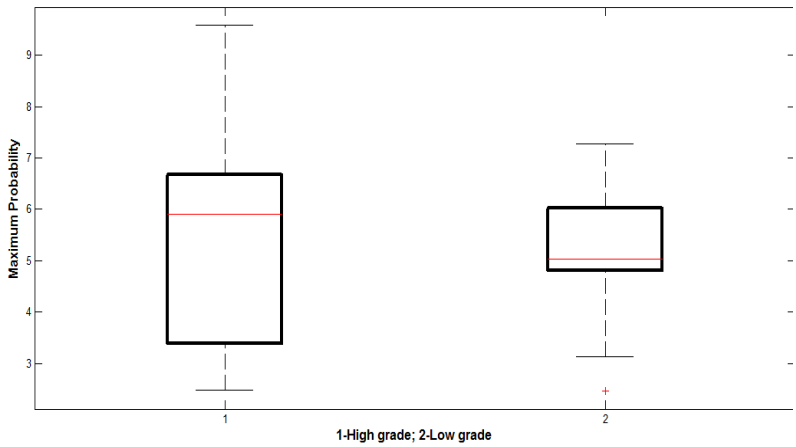

Fig.6.20 Box plot of maximum probability computed using GLCM based second order statistics for forty five sets of high grade and fifty five low grade glioma patients

Ranges of values for the different features are given in Table 6.8. Thus, it is quite evident from these plots that these features are well discriminative between two types of tumors and cluster prominence, cluster shade and contrast are shown to be the most effective discriminators. Inverse difference moments and maximum probability have their ranges of values to be overlapping for high and low grade tumors, and cannot be selected as a good feature for detection. GLCM based texture descriptors like, cluster prominence, cluster shade, dissimilarity, entropy, contrast and auto correlation is high and energy is low for high grade glioma texture. Dissimilarity, Entropy, cluster prominence, cluster shade and energy are measure of non uniformity or randomness of a texture and it is strongly correlated with texture heterogeneity [20]. When tumor malignancy increases, tumor heterogeneity also increases and patient prognosis decreases. In the case of low grade glioma, these texture descriptors are low; showing that low grade glioma tumor textures are smoother than high grade as expected. This proves the effectiveness of the GLCM based texture descriptors for differentiating between two grades.

Table 6. 8 Ranges of values of GLCM features for the segmented ROI, with respect to low grade and high grade glioma tumors obtained using boxplot

Texture	Auto Correlation	Contrast	Cluster prominence	Cluster Shade	Entropy	Dissimilarity	Energy
High Grade	40-75	25-55	1300-1700	100- 200	6-15	50-250	0.2-1.5
Low grade	10-30	5.0-16	425-650	20-80	0.2-1.5	0.5-10	3-15

After determining the discriminant features using first and second order statistical features and its ranges values for low and high grade glioma, three feature sets are formulated.

6.2.4 Development of grade Detection system

Classification of high and low grade glioma tumors were tried using 3 sets of features.

Feature sets	Thresholds for high grade	Thresholds for low grade
Feature Set 1-First order statistics		
Mean	**≥190**	**≤160**
Standard deviation	**≥90**	**≤60**
Kurtosis	**≥100**	**≤12**
Entropy	**≥6.5**	**≤2**
Skewness	**≥8**	**≤3**
Feature Set 2-GLCM		
Cluster Prominence	**≥1300**	**≤650**
Correlation	**≥40**	**≤30**
Energy	**≤1.5**	**≥3**
Entropy	**≥5**	**≤1.5**
Contrast	**≥30**	**≤16**
Dissimilarity	**≥50**	**≤10**
Cluster Shade	**≥100**	**≤80**
Feature Set 3-First order statistics + GLCM (set3)		
Mean	**≥190**	**≤160**
Standard deviation	**≥90**	**≤60**
Kurtosis	**≥100**	**≤12**
Entropy	**≥6.5**	**≤2**
Skewness	**≥8**	**≤3**
Correlation	**≥40**	**≤30**
Energy	**≤1.5**	**≥3**
Entropy	**≥5**	**≤1.5**
Cluster Prominence	**≥1300**	**≤650**
Contrast	**≥30**	**≤16**
Dissimilarity	**≥50**	**≤10**
Cluster Shade	≥100	≤80

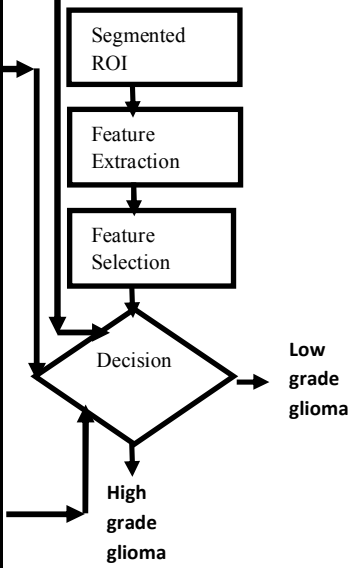

Fig.6.21The flow chart of the grade detection system based on the thresholds of feature sets

First feature set consisted of chosen five first order features like: first order statistical features like mean, standard deviation, kurtosis, entropy and skewness. Second feature set was formed using seven selected GLCM based features like Cluster Prominence, Cluster Shade, Correlation, Entropy, Dissimilarity, Energy and Contrast. Finally a third set of feature vectors were formulated by combining first and second feature set (12 features).

A statistical decision system was developed based on the feature sets generated from the selected discriminant features for grading of glioma tumors. The three feature sets was formulated and the thresholds for each feature in the feature sets were fixed based on the range of values determined from the boxplot. The flow chart for the decision system is shown in Fig.6.21. The decision system is chosen for grade detection of glioma, because the features selected for detection of glioma is highly discriminant between two grades. Hence it is very easy to develop a rule based detection system based on the thresholds of each features and this decision system is very efficient to discriminate between two grades.

6.3 Implementation of the developed system

The implementation procedure of the developed decision system is discussed in this section. This decision system does not make any assumptions about the distribution of data. A training set consisting of 80MRI data was used to build the decision system, while test set with a group of different data was used to estimate the accuracy of the system. Selected statistical moment descriptors of each segmented ROI image were compared with the feature set 1, 2 and 3 and decision levels are checked. The feature sets value of a segmented ROI for the decision level is true is considered as high grade or otherwise it is a low grade tumor. The details of image database used and performance evaluation using ROC Analysis are detailed here.

6.3.1 Image Database

T2 weighted axial MRI data sets of 100 patients were taken for analysis and detection. All patients underwent biopsy or surgical resection of the tumor with histopathological diagnosis. Out of this, hundred histopathologically tested image database, forty five sets were of high grade and fifty five were of low grade. The images were gray scale images. Segmented tumors from MR images in the database were taken as the data set for texture analysis, feature selection and in formulating the detection criteria. Eighty percentage of images in the data sets were used for training and unused twenty percentage images of the data sets were used for test purposes. Sample images in the dataset are shown in Fig.6.22

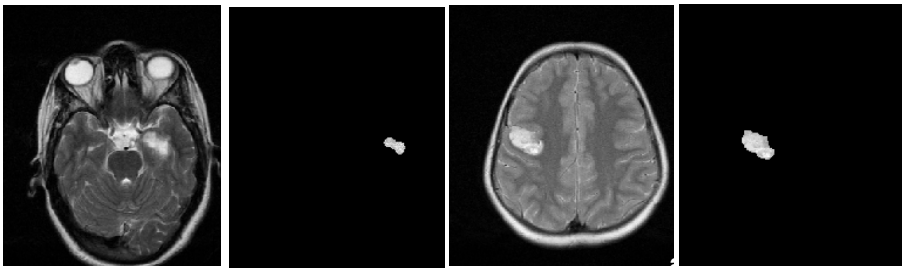

Fig.6.22 Sample images from the image database a) Original T2 weighted image with low grade tumor b) Segmented gray level low grade tumor c) Original T2 weighted image with high grade tumor d)Segmented gray level tumor

6.3.2 Implementation Steps

1. The images in the training set were processed and ROI of the tumor region was extracted.
2. The 12 features already chosen consisting of five features based first order statistics and seven features based on GLCM based second order statistics were evaluated by considering the whole segmented / extracted tumor region in each case.
3. Thresholds were fixed for high and low grade glioma detection.

4. Performance evaluation based on ROC analysis was done for the 3 sets of features, mentioned in section 6.4.1
5. For the 20% of the test data also, steps 1 to 4, were repeated.

5.3.3 Performance Evaluation of the glioma Detection Method

Performance evaluation of the detection method was done using ROC analysis. For this purpose the values for True positive (TP), False positive (FP), False Negative (FN), True Negative (TN), Sensitivity (TPR), Specificity and Area under the curve (AUC) of the detection system was evaluated. The detection is considered as TP, if the region of interest overlaps with the ground truth circle, otherwise it is FP. The definitions of this case are given in the Table 6.7. Sensitivity of a diagnostic test is the proportion of patients whose outcome is positive, that are correctly identified by the test. The specificity is proportion of patients for whom the outcome is negative that are correctly identified by the test. The AUC of a classifier is equivalent to the probability that the classifier will rank a randomly chosen positive instance higher than a randomly chosen negative instance. ROC curves in this study were plotted using MATLAB 7.1 An area of 1 represents a perfect test, while an area of 0.5 represents a worthless test.

In particular, Sensitivity is a measure of the probability of correctly diagnosing a condition. Specificity is equal to 1 – FPR. Thus, it is a measure of the probability of correctly distinguishing when the condition is not present in a subject. Other statistical method known as receiver operating characteristic (ROC) curve [25] was also used to analyze the experimental results. The area under the curve (AUC) is also a measure of accuracy. The AUC of a classifier is equivalent to the probability that the classifier will rank a randomly chosen positive instance higher than a randomly chosen negative instance.

Table 6. 9 Definition for TP, FP, FN, and TN for developed detection system

TP	high grade glioma is present and result detected is true
FP	high grade glioma present and result detected is false
TN	high grade glioma absent and result is detected true
FN	high grade glioma is absent and result detected is false

6.4 Results and Discussions

6.4.1 Results of Performance evaluation of the detection system using Receiver operating characteristic curves

The detection performance of the three feature sets was evaluated using ROC curve. The ROC curves for the three feature sets are shown in Fig. 6.23, Fig.6.24, and Fig.6.25. The graph depicts the tradeoff between the true-positive and false-positive rates. The area under the curve of feature set 3 was more as compared to the other two methods. The AUC for feature sets1, 2, and 3 are 0.8743, 0.9083 and 0.9735 respectively. The sensitivity and specificity using feature sets1, 2, 3 in detecting grade of tumors are 94.56, 97.13, 99.03 and 77.72, 83.042, 92.53 respectively. Table 6.10 shows the performance parameters TPR, TNR, AUC and its typical values.

Table 6. 10 Performance evaluation of Feature set1, Feature set2 and Feature set3

Performance Parameters	Feature set 3	Feature set 2	Feature set 1
TPR (%)	99.03	97.13	94.56
TNR (%)	92.53	83.04	77.2
AUC (%)	97.35	90.083	87.43
FPR (%)	1.49	4.35	4.66

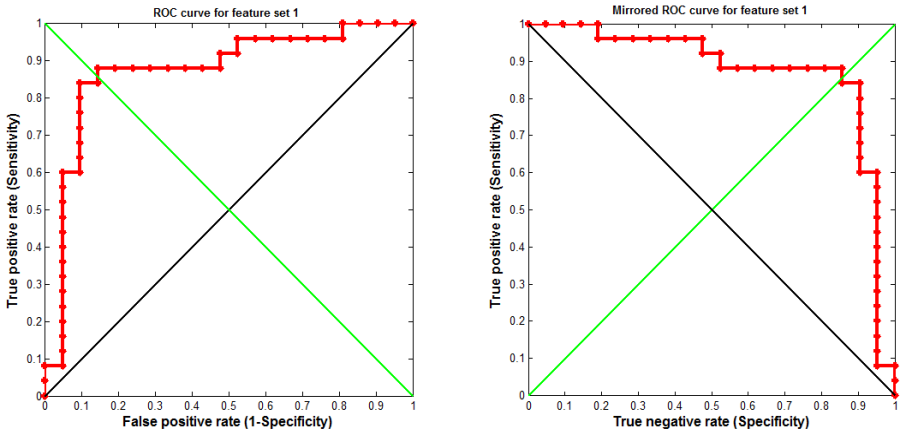

Fig.6.23 The ROC curve for feature set 1. Area under the curve (AUC)-87.43%, sensitivity -94.56%, specificity-77.2%, Performance of detection-Good test

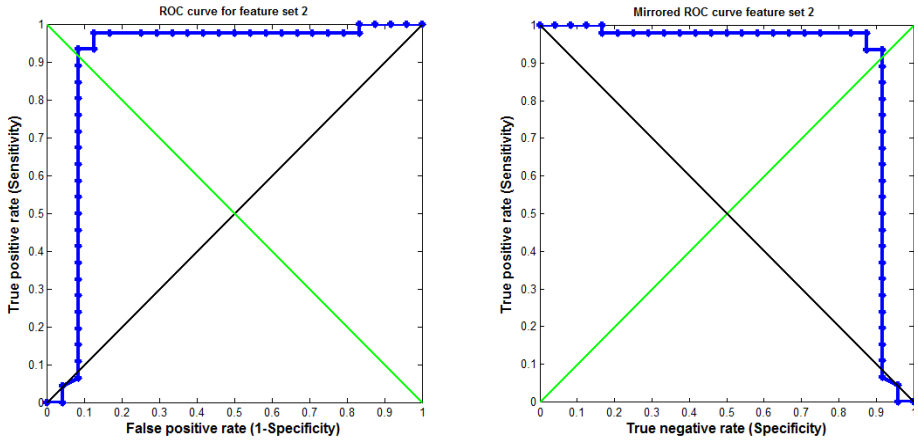

Fig.6.24 The ROC curve for feature set 2. Area under the curve (AUC)-90.083%, sensitivity -97.13%, specificity-83.04.2%, Performance of detection-Excellent test

It is very evident from the above results that the feature set 3 based detection gives more accurate results than feature set 1 and feature set 2 for the method. For comparing the performance of detection system the histogram (Fig.6.26) of different feature sets used for detection in terms of its sensitivity, specificity and AUC are plotted. For comparing the performance of the detection system, histogram of sensitivity (TPR), specificity (TNR) and AUC were plotted for the three feature sets. Detection based on feature set 3 showed best performances as it produced lesser error than the other two detection methods.

Generally the performance of the algorithm in this chapter shows better performance than the other existing methods [8, 20, and 21] in terms of its TPR and TNR. In literature, classification of type and grade detection of tumor using Support Vector Machines (SVM) from multi-parametric MRIs [27] is discussed. The SVMs are computationally complex and time consuming. In this work, the features selected are well discriminated between two grades and hence a decision system is sufficient for detection process. As per citations [8, 24, and 29], tumor heterogeneity and degree of malignancy are directly related and well established using this developed texture analyses. A comparison table for evaluating the performance of feature set 1, feature set 2, and feature set 3is shown in Table 6.10.

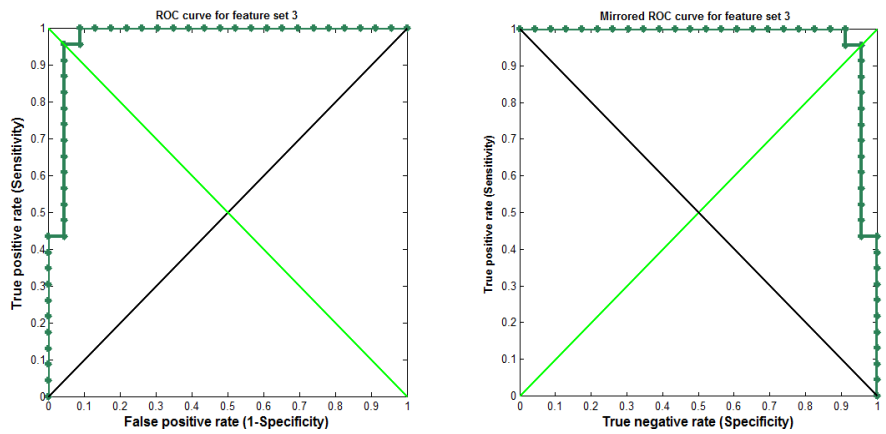

Fig.6.25 The ROC curve for feature set 3 Area under the curve (AUC) - 97. 35%, sensitivity -99.03%, specificity-92.53%, Performance of detection-Excellent test

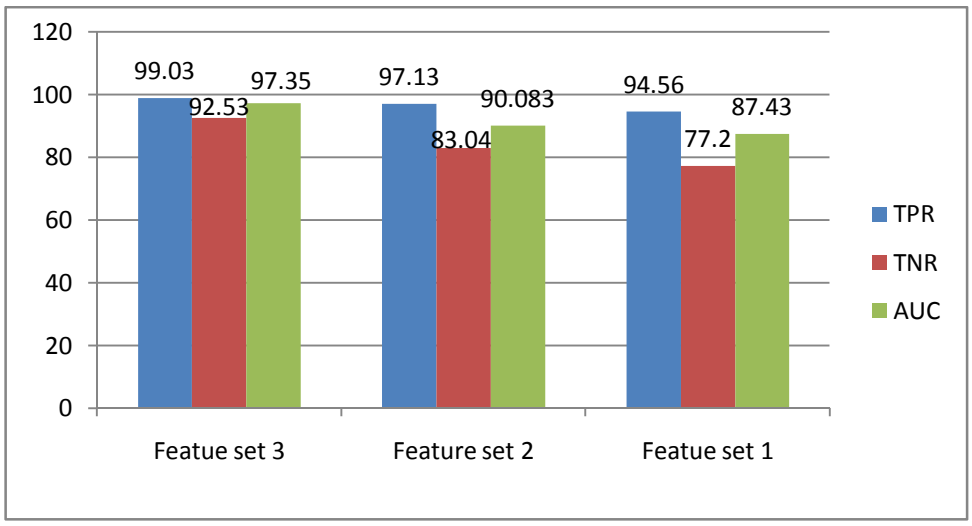

Fig.6.26 Performance comparison of different feature sets for detection of high and low grade Glioma tumors . TPR(%)-True Positive Rate(%); AUC(%)-Area under the curve; TNR(%)-True Negative Rate

Conclusions

A novel method for grade detection of glioma tumors from segmented MRIs is presented in this Chapter. Entire segmented region of interest was considered for texture analysis. Segmentation is important in this method because this work considered only the tumor texture. Statistical quantification of tumor texture was done using first order and GLCM based second order statistics. Of the three feature sets formed the feature set (12 features)containing 5first order statistical features and 7 GLCM based gave the best result for tumor grade detection

It should be noted that all features were extracted using grey level averaging and therefore not sensitive to small differences in delineation of ROIs. Along with the statistical features, by incorporating histopathological properties, edema properties, tumor shape etc., more sophisticated and robust system could be developed for detecting all grades and sub types of glioma

References

[1] R.C. Gonzalez, R. E. Woods ,Digital Image Processing,Text book, 2nd Edition, Pearson Education,India, (2002)

[2] T. M.Deserno, Fundamentals Of Biomedical Image Processing, Thomas M. Deserno,Biomedical Image Processing, Springer, USA, ,pp 1-50 (2011).

[3] P. Georgiadis, D. Cavouras, I. Kalatzis et.al, Computer Aided Discrimination Between Primary and Secondary Brain Tumors on MRI: From 2D to 3D Texture Analysis, e-Journal of Science & Technology (e-JST) vol. 8 pp. 9-18, (2008).

[4] N. Sharma, A.K. Ray, S.Sharma , et.al. Segmentation and Detection of Medical Images using Texture-Primitive Features: Application of BAM-Type Artificial Neural Network, Journal of Medical Physics. 33(3) (2008) 119–126 (2008)

[5] S.Ananda Resmi and T. Thomas, Segmentation and Texture Analysis of Brain MRIs using Statistical Features for low grade and high Grade Glioma detection'(Manuscript No. IF12A05-MICR1) Special issue of Information Fusion in Medical Image Computing Systems, Elsevier (under revision)

[6] S.Ananda Resmi and T. Thomas,'Texturedescription of low grade and high grade glioma using statistical features in brain MRIs, Int. J. of Recent Trends in Engineering and Technology, Vol. 4(3), pp.27-33, (2010)

[7] N. Bulakbasi, M. Kocaoglu, A. Farzaliyev et al. Assessment of Diagnostic Accuracy of Perfusion MR Imaging in Primary and Metastatic Solitary Malignant Brain Tumors, Am J Neuroradiol.vol. 26(9) pp.2187–2199, (2005)

[8] E. I. Zacharaki, S. Wang, S. Chawla, et.al, Classification of brain tumor type and grade using MRI texture and shape in a machine learning scheme, Magn Reson. Med. 62(6) (2009) 1609–1618.

[9] D. S. Raicu, J. D. Furst, D. Channin, et.al. A Texture Dictionary for Human Organs Tissue Classifications, Proceedings of the 8th world Multiconference on Systemic, Cybernetics and Informatics. (SCI-2004) 18-21.

[10] A Mohd. Khuzi, R Besar, WMD Wan Zaki, et.al. Identification of Masses in Digital Mammogram using Gray Level Co-Occurrence Matrices, Biomed Imaging Interv J. 8 (1) (2009) e5.

[11] Poonguzhali , G. Ravindran. Automatic Classification of Focal Lesions in Ultrasound Liver Images using combined Texture Features, Information Technology Journal. 7(1) (2008) 205-208

[12] M. Heydari, Prognosis of Glioblastoma Multforme using textural properties on MRI, Thesis work in Master of Science, Univesity of Alberta, 2009

[13] F. Albregtsen, Statistical Texture Measures Computed from Gray Level Co occurrence Matrices, Image Processing Laboratory, Department of Informatics, University of Oslo (2008)

[14] Hong-Choon Ong , Hee-Kooi Khoo, Improved Image Texture Detection Using Gray Level Co-occurrence Probabilities with Support Vector Machines Post-Processing, European Journal of Scientific Research.vol. 36(1) pp. 56-64, (2009).

[15] H. Wibawanto, A. Susanto, T.S. Widodo et. al. Discriminating Cystic and Non Cystic Mass using GLCM and GLRLM-based Texture Features, International Journal of Electronic Engineering Research,vol. 2 (4) pp.569–580, (2010)

[16] T. kalpalatha Reddy , N. Kumaravel. Texture Analysis of Bone CT Images for Detection and characterization of Bone Quality, International Journal for Soft computing.vol.4(5) pp.223-228, (2009)

[17] L. M. Fletcher-Heath, L.O. Hall, Dmitry B. Goldgof Automatic Segmentation of Non-enhancing Brain Tumors in Magnetic Resonance Images, Artificial Intelligence in Medicine, vol. 21 (1) pp.43-63, (2001)

[18] V. S. Vyas and P. Rege. Automated Texture Analysis with Gabor filter, GVIP Journal,Vol. 6 (1) pp. 35-41, (2006)

[19] G.W. Jiji, L.Ganesan, S.S. Ganesh. Unsupervised Texture Detection, Journal of Theoretical and Applied Information Technology, vol.5 (4) pp.373-381, (2009).

[20] Guo-Zheng Li, Jie Yang, Chen-Zhou Ye, et.al. Degree Prediction of Malignancy in Brain Glioma using Support Vector Machines, Computers in Biology and Medicine Vol. 36 (3), pp. 313-325, (2006)

[21] S. K. Ganeshan B, T. Good , G. Critchley , et.al. Imaging heterogeneity in gliomas using texture analysis, Cancer Imaging.Vol. 11 ,pp.5112-5117, (2011)

[22] P.A. Eliot, D. Olivie, S. Saikali, et.al. Can Dynamic Contrast-Enhanced Magnetic Resonance Imaging Combined with Texture Analysis Differentiate Malignant Glioneuronal Tumors from Other Glioblastoma?, Neurology Research International. Article ID 195176 (2012).

[23] M. Bounessah, The Boxplot: A Robust Exploratory Data Analysis Tool For The Definition of the threshold for outlier data, Asian Journal of Chemistry, Vol.14 ,pp. 1772-74, (2002).

[24] L. Rokach, O. Maimon, Decision Trees, Chapter 9, Data Mining And Knowledge Discovey Handbook pp.166-192

[25] L. Hamel, Model Assessment with ROC curves. Encyclopedia of Data Warehousing and Mining, IGI Global, 2nd Edition, pp-1316-1323, (*2009)*

[26] S. Dube, Jason J. Corso, F. Timothy. Cloughesy, et.al. Automated MR image processing and analysis of malignant brain tumors: enabling technology for data mining. Data Mining, Systems Analysis And Optimization In Biomedicine, AIP Conference Proceedings. Vol. 953 pp.64-84, (2007)

[27] Wi Bian, I. S. Khayal, J.M. Lupo, et.al, Multiparametric Characterization of Grade 2 Glioma using magnetic Resonance Spectroscopic, perfusion, and Diffusion Imaging, Translational Oncology. Vol. 2(4) ,pp. 271-280, (2009)

Chapter 7

3D Modeling of Segmented Glioma tumors from Brain MRI

Volumetric change in glioma tumors over time is a critical factor in treatment decisions. Typically, the tumor volume is computed on a slice-by-slice basis using MRI scans obtained at regular intervals. The objective of this chapter is to calculate precise volumes of gliomas from MR images. This includes tumor segmentation and 3-dimensional (3D) visualization of the tumor. The appearance of high grade tumor on MR images varies greatly, due to tissue variation inside the tumor and the diffuse growth of the tumor. Hence a robust and accurate segmentation method should be chosen to distinguish the tumor tissue from the surrounding brain to gain exact volume values. Moreover, the segmented tumors should be visualized to get an opinion about the tumor's shape and location in the brain. This chapter presents an efficient method for volume rendering (3Dmodelling) of glioma tumors from segmented 2D MRI datasets, by replacing the manual segmentation required in the state of art methods. For clinical follow-up, the evaluation of the pre-operative tumor volume is essential.. The 3D modeled tumor consists of gray level values of the original image with exact tumor boundary. The 3D modeling was also done using segmented 2D slices with the help of medical software package called 3D DOCTOR. The results were validated with the ground truth models by the Radiologist.

7.1 Introduction

The extraction of 3D objects and its visualization is one of the most important steps in the analysis of the pre-processed medical image data, which can help in performing diagnosis, treatment planning, and treatment delivery. Thus in practice, radiation oncologists spend a substantial portion of their time performing the segmentation task manually, using available visualization and segmentation tools [1]. Also, there may be cases where the automatic methods fail or perform poorly. Another consideration is that medical doctors must always have final control over the segmentation [2].

Due to the biological behavior, gliomas of WHO grade II to IV cannot be cured with surgery alone. The multimodal therapeutical concept involves maximum safe resection followed by radiation and chemotherapy, depending on the patient's functional impairment scale. The survival rate is still only approximately 15 months, despite new technical and medical accomplishments such as multimodal navigation during microsurgery, stereotactic radiation or the implementation of alkylating substances [4]. The clinical follow-up of tumor volume is essential for an adaptation of the therapeutical concept. Therefore, the exact volume evaluation is fundamental to reveal a recurrent tumor or tumor progress as early as possible.

7.1.1 Back ground

Volumetric change in glioblastoma multiforme (GBM) over time is a critical factor in treatment decisions. Typically, the tumor volume is computed on a slice-by-slice basis using MRI scans obtained at regular intervals. (3D)Slicer – a free platform for biomedical research – provides an alternative to this manual slice-by-slice segmentation process, which is significantly faster and requires less user interaction. Methods that use all slices to calculate the tumor boundaries have more information available to make accurate predictions of tumor volume. Simpler methods such as geometric models provide only a rough estimate of the tumor volume and may not be sufficient for accurate determination of tumor burden. Geometric approximations use one or several user-defined diameters to estimate the tumor volume

The driving problem to be discussed for 3D modeling is segmentation of 3D brain tumors from magnetic resonance image data. Tumors vary in shape, size, location, and internal texture, and hence tumor segmentation is known to be a very challenging problem [3].Various promising computer-assisted techniques to extract tumors and blood vessels from 2D MRI have been described in chapter 3. Since fully automated segmentation often fails to match human judgments of tumor boundaries, a number of interactive segmentation algorithms have been proposed [4]. Of these, Tumor and boundary extraction using graph cuts [5], deformable models [5] , snakes[6], balloons[7] Active contour models[7]are efficient algorithms to segment objects where pixel and region based methods fail e.g. because of the variability of object shapes, diffuse boundaries, noise or artifacts [8]. Active contours are especially suitable for objects with variable boundary intensity [9].When manual tracing by a knowledgeable operator is used as ground truth, the overall agreements for the results of automatic methods are ranging from 82% to 94% [10]. For some of these methods, the time required for the computations has been reported to vary from several hours to several tens of hours. Presumably, with modern computing platforms, this time can be reduced to several minutes or several tens of minutes [10].

The 3D segmentation of tumors from 3D image data sets by stacking up a sequence of 2D tumor contours detected by 2D level-sets method in the parallel cross-sectional MRI images [11, 12], IARD segmentation techniques [13] which operates efficiently for certain regions of MRI, and hierarchical segmentation method using variational tools that extract bones and blood vessels as two separate 3D objects [14], are some of the 3D segmentation techniques available in literature. Volumetric rendering of Glioblastoma (high grade) tumors using nearest neighbor algorithm [15] and surface modeling algorithm [7] for tracking growth rate of the tumor in order to find out patients survival time and prognosis is described by R. Rajeswari and P. Anand kumar[16]. Comparison between the above two methods is also done [6]. Segmented MRI slices using Grow cut with region growing method and volumetric modeling is also done using (3D) slicer [6]. Segmentation and 3D modeling using active contour model and volume Delaunay triangulation method are also presented in literature [19-20].

This chapter highlights the development of a novel method for brain tumor

segmentation and volumetric rendering of segmented tumor, which overcomes some of the above mentioned difficulties. The method consists of automatic segmentation of tumors from 2D MRI slices, which is already mentioned in Chapter 5 and these segmented tumor slices are exported to a 3D rendering using MATLAB. For the verification of rendered 3D tumor volume, the 3D-DOCTOR software package that is usually used by Radiologists was used.

7.2. A Novel Method for Volume Rendering of Glioma Tumor from the Segmented Axial Slices

This section contains a description of the methods to perform the segmentation, visualization and volume calculation of tumors. The flow chart for the entire procedure is shown in Fig.7.1. The method consists of mainly two parts. The First part is automatic segmentation of tumor regions from the acquired slices having presence of tumor, in the MRI dataset. The second part involved stacking 2D slices of the segmented tumor and performing volumetric rendering using 3D Doctor and MATLAB.

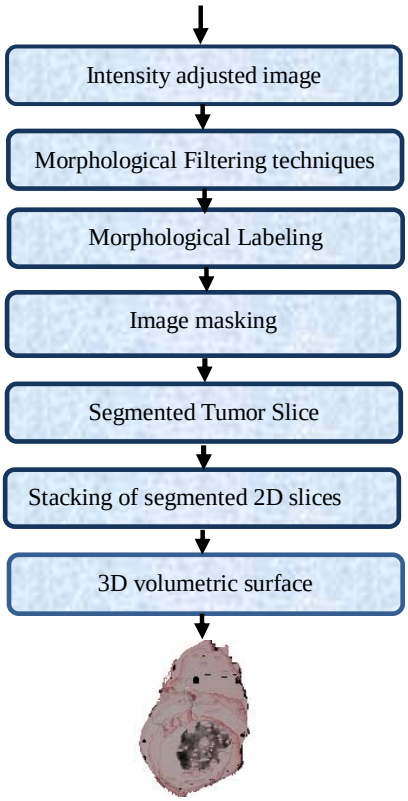

Fig. 7.1 The flow chart for 2D Segmentation and Volumetric 3D rendering of tumor

7.2.1 Choice of Segmentation

The method selected for segmentation is very crucial, since the segmented regions should have a true boundary, that is, there will not be any type of over segmentation or under segmentation. In consideration of the high diversity of the appearance of high grade and low grade glioma, pixel based methods are inappropriate. To prevent over-segmentation due to weak boundaries region based segmentation is not considered suitable either. Model based methods are able to segment results as desired but because of unavailable amount of sample data and the variant form of tumors, it is not possible to extract a statistically significant shape model. In conclusion, to fulfill the segmentation requirements spatial domain segmentation technique discussed in chapter 5 is chosen.

7.2.2 Segmentation Based on Spatial Domain Filtering Techniques

In this chapter, for segmentation, the second method described in Chapter 4, using T1 Flair and T2 weighted images was considered. Fig.7.2 shows an example of the segmentation technique already developed. This segmentation technique is applied for all images in a dataset. Fig. 7.2(d) and Fig. 7.2(e) show the segmented tumor and its boundary. Tumor boundary is superimposed on T2 weighted MR image for displaying the segmentation accuracy.

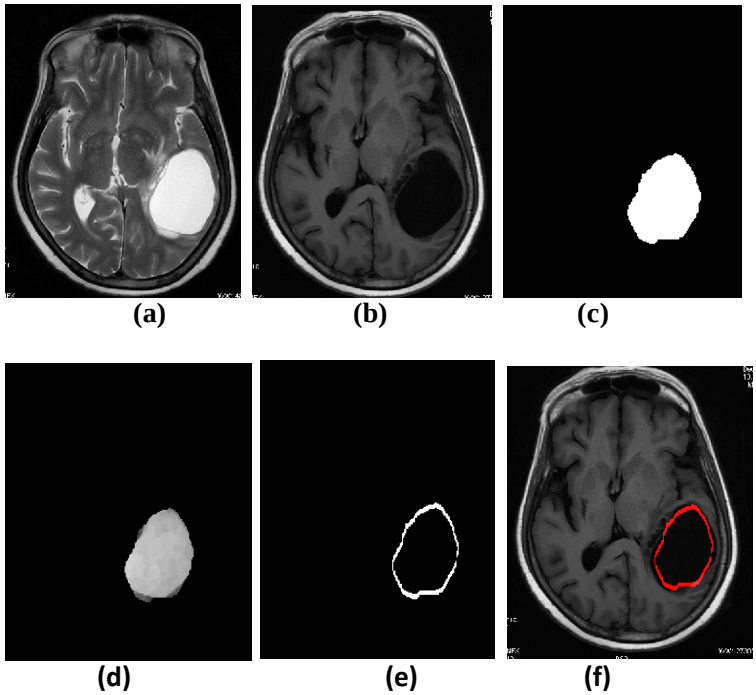

Fig 7.2 The example for development of tumor segmentation and Boundary Extraction techniques. (a) & (b) Axial slices of T2 weighted and T1 FLAIR image in a patient image dataset. (c) Segmented binary tumor (d) Segmented Gray level tumor (e) Tumor boundary (f) Extracted boundary is superimposed T1 FLAIR image.

7.2.3 Volume Rendering and Visualization

Many software packages are available for volumetric rendering of biomedical images in order to assist radiologist, surgeons and oncologists. But volume rendering of any abnormality present in an organ is quite difficult, time consuming and prone to error, because, each slice should be segmented manually. In order to avoid the time-consuming manual slice-by-slice segmentation for 3D modeling, in the software package, 3D slicer, a new known segmentation method called Grow Cut tool is introduced [17]. In the method , the tumor contour needs to be first segmented on the MR slices using the active contour segmentation

method. Then the contour points are used to build up a 3D set of points ("point cloud"), which allowed generating a tetrahedral mesh using the Delaunay triangulation. To generate the final surface plot of the tumor model the surface of the tetrahedral mesh is visualized. The surrounding area of the tumor and the tumor tissue itself can be explored by adding moveable image slices in all three anatomical planes [18].

The main steps to create 3D models and volume rendering from 2D slice images are [19]:

1. Create an empty space for 3D volume.
2. Each image pixel's x and y coordinate on 2D space (Fig. 7.3 a) is transferred to the empty space. The slice number (considering thickness of each slice) with respect to the distance between each slice is taken as z coordinate. If a pixel is adjacent to another pixel, the 3D points will be connected together.
3. Repeat the previous 2 steps until all slices are done. All the points in the 3D space will be connected to form a mesh [19] structure.
4. Finally 3D volume rendering is done.

For the correct rendering of stacked image slices, all 2D images are of the same dimension and thickness with equal spacing. All connected components together form a mesh like structure and correspondingly a 3Dsurface is modeled. In this way, we can perform a hierarchical volume rendering of the segmented slices.

In clinical practice, the pre-operative and post-operative tumor volumes are often based on the surgeon's impression or by measuring the greatest axis of the tumor in x, y and z directions [19]. In this method, the volume of the tumor is calculated in two stages. Initially, volume of segmented regions of interest in each slice is calculated and the sums of slice volumes give the total volume of the tumor. The volume of each slice is computed by measuring the cross product transverse area of the tumor and the thickness of each slice.

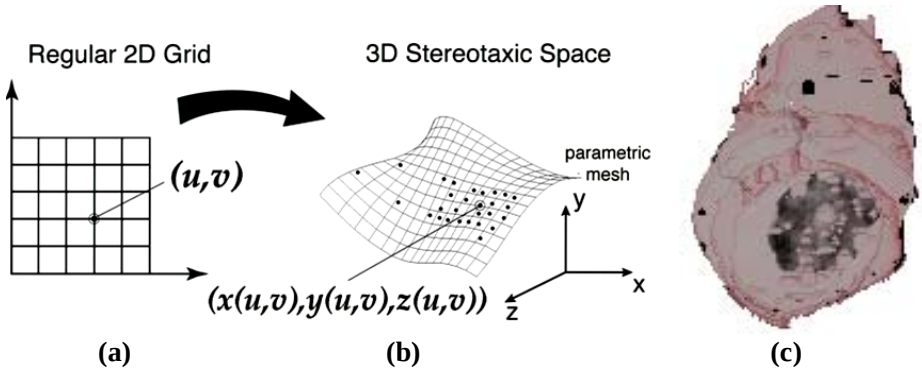

Fig.7.3 The basic principles behind the 3D modeling algorithm. (a) 2D Image (b) Transformed 3D points for the 2D image (c) 3D modeled tumor

7.2.4 Volume rendering using 3D DOCTOR

3D-DOCTOR is an advanced 3D modeling, image processing and measurement software for MRI, CT, PET, microscopy, scientific, and industrial imaging applications. It supports both grayscale and color images stored in DICOM, TIFF, Interfile, GIF, JPEG, PNG, BMP, PGM, MRC, RAW or other image file formats and creates 3D surface models and volume rendering from 2D cross-section images in real time. It is very useful for surgical planning, simulation, quantitative analysis, finite element analysis (FEA) and rapid prototyping applications. The user can calculate 3D volume and make other 3D measurements for quantitative analysis. 3D-DOCTOR's vector-based tools support easy image data handling, measurement, and analysis.3D CT/MRI images can be re-sliced easily along an arbitrary axis. Multi-modality images can be registered to create image fusions. Misaligned slices can be automatically or semi-automatically aligned using 3D-DOCTOR's image alignment functions. This package is developed using object-oriented technology and provides efficient tools to process and analyze 3D images.

Its main drawback is that, for 3Dmodelling of specific region of interest

automatic boundary extraction is not possible. Hence the users have to perform manual segmentation for extracting the boundary. It is time consuming and prone to error in the absence of an expert radiologist.

In order to overcome this difficulty, an automatic method is developed here for 3D modeling of tumors by using the surface rendering and visualization methods in 3D Doctor Environment. This is achieved by selecting all automatically segmented tumor slices in a dataset, extracted using the newly developed segmentation method named as Adaptive Gray level Algebraic Segmentation Algorithm (AGASA) and then surface rendering using 3D DOCTOR.

7.2.5 Validation

Segmented tumors are validated using the same method used for validating the performance of segmentation mentioned in Chapter 5. That is, by computing Tanimoto index (TI), Percentage Match and Positive Prediction value. In the case of 3D modeled images, intra- and inter-subject repeatability and reproducibility were maximized by repeated image assessment. Repeatability of a dataset is assessed by calculating the ratio of percentage of mean values of error and the volume computed by the same user and Reproducibility means ratio of percentage of mean values of error and the volume computed by the different user

7.2.6 Growth rate assessment

Growth rates were calculated in terms of halving times or doubling times for change in tumor enhancement volumes according to the following formula given in Eqn.(7.1).

$$T^* = \frac{t(ln\ 2)}{\ln\left(\frac{v}{v_0}\right)} \tag{7.1}$$

where T^* is the doubling time or halving time, t is the interval time in days, and Vo and V are the volumes at the onset of the interval and at the end of the interval period, respectively. Growth rates are sensitive enough to determine response to treatment [20].

7.3. Implementation of the Method

7.3.1 Image Database used

The method developed is implemented on 10 patients' brain MRI datasets which contains 22 axial slices of T2 weighted and T1 FLAIR images. Out of 10 datasets, six were of high grade glioma and four sets low grade glioma. The 3D rendering operation was performed using MATLAB 3D modeling functions. The thickness of each slice is 5mm with inter slice distance is 2mm. For 3D rendering operation, segmented slices which contain tumor portions are considered. The selected images were histopathologically tested and have confirmed the presence of the disease. In this work, MRI images were collected from the Department of Radiology, Regional Cancer Centre, Thiruvananthapuram, Kerala, India. The images were gray scale images. The entire procedure was done using MATLAB 7.5 and 3D DOCTOR.

7.3.2 Implementation

Segmentation method was applied for the entire images in the dataset. The number of slices in a dataset containing tumor will vary from 8 to15. The Segmented slices which contain the tumor portions are only considered for volume rendering. The segmented slices are already validated with the Ground Truth in chapter 5.

The order for stacking of segmented slices is very important and it should be arranged according to the order of the slices in the MRI dataset. The Volume rendering was performed in all the 10 image datasets.

The segmented slices in each datasets are exported to 3D DOCTOR software package and 3D volume of the tumor is rendered and visualized. Out of the 6 datasets, 4 datasets are MRI details of the same Glioblastoma patient acquired at different times, in order to analyze the response to chemotherapy and evaluate the prognosis of the patient in 420 days. From the volumetric modeling of the 4 datasets, tumor growth rate was computed. The 3D modeled tumor was validated with the Ground truth.

7.3.3 Results and Discussions

The results of the segmentation and volume rendering processes are separately discussed below.

7.3.3.1 Results of Segmentation

All slices in the datasets are considered for segmentation and tumor regions were extracted from the slices which contain tumor portions. Fig.7.4 and 7.5 are the examples of tumor regions extracted from two sample datasets.From these figures it can be noted that the area, shape and intensity of the tumor (ROI) regions in each slice varying and 3D modeling of these slices will give a clear idea of tumor nature. The accuracy and performance of the segmentation method is most important because these factors determine the accuracy of the 3D modeled tumor.

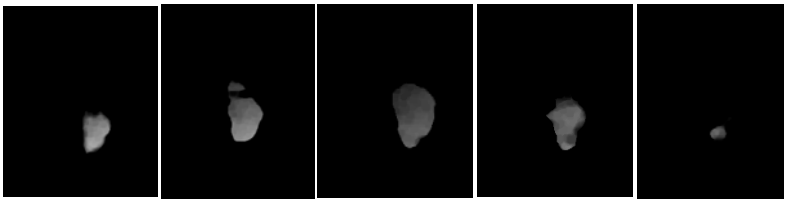

Fig.7.4Sample slices of segmented low grade glioma tumor in a dataset

Accuracy of the segmented tumor in each slice is depicted in Table 5.3 and Table 5.4. Its accuracy is indicated by Tanimoto Index and its ranges of low grade and high grade are 97.07%-99.8% and 98.28%-99.6% respectively and the time required for computation is 1 second. From Fig. 7.4, it can be observed that numbers of slices which contain tumor region are only five and hence the volume of tumor will be low, whereas in Fig. 7.5, the number of slices containing tumor is ten and hence the volume of the tumor will be big enough to visualize. Usually sizes of low grade tumor are lesser and they have lower contrast when compared to high grade tumor. These segmented slices in an image dataset are the input data sets for the3D modeling algorithms using 3D DOCTOR and software using MATLAB.

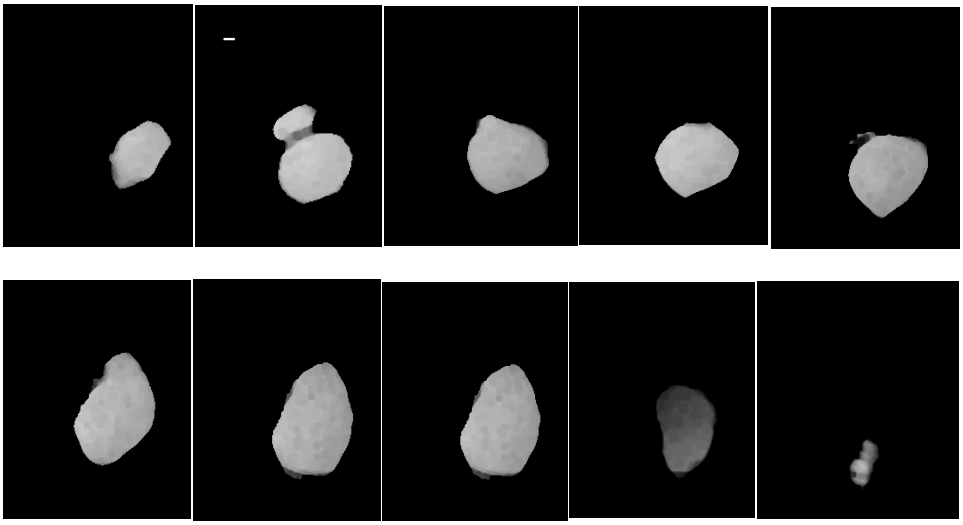

Fig.7.5Sample slices of Segmented Glioblastoma (high grade) tumor in a dataset

For manual segmentation of tumor region, neuro-surgeons took three to nineteen minutes (mean: ten minutes), in comparison to the new automatic segmentation using the spatial domain filtering method implementation which took only 20% of that time (mean: 2 minutes).

7.3.3.2 Results of Volume Rendering and Visualization

The 3D modelled images using the new automated method are given in Fig.7.6. Here entire size of the image was considered for 3D surface rendering. 3D modelled tumor using MATLAB with different elevation angles are shown in Fig 7.6 (a) and Fig.7.6 (b). Fig.7.6c gives a clear idea of 3D reconstructed high grade glioblastoma in MATLAB environment. Fig.7.7 shows 3D modelled tumor using the automatically segmented slices containing tumor region with 3D DOCTOR. In this method, only one anatomical plane, that is axial, is considered and volume with respect to that plane is also calculated. The volumes of 10 image datasets were computed using these two methods.

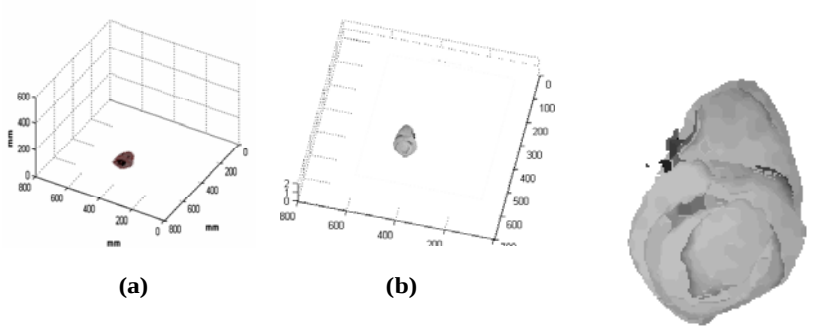

(a) **(b)** (c)

Fig.7.6 3D modeled images using the method. (a) 3D modeled image of low grade glioma (b) 3D modeled image of glioblastoma (high grade) (c) 3D visualization of high grade tumor

For validation of these two methods, 3D modelling of tumor from MRI slices was done manually using 3D DOCTOR by an expert radiologist and the results were compared with respect to volume of tumor and computation time. It is seen that the volume calculated using the two methods are approximately same and is given in the Table 7.1.The volumetric tumors are retains gray level value, hence it will be useful for texture based analysis.

The calculated tumor volumes of five different image datasets 1 are shown in Table 7.1.Every data set was segmented on axial anatomical plane for five times by the same user (repeatability columns). All segmentation properties were the same for the users. From Table7.1, it can be observed that, the repeatability is high. That is the accuracy is also high for the two methods and almost the same as that obtained using manual method. The Volume Calculation of data sets were implemented using MATLAB using the formula i.e, sum of [(Total area of all slices) x (sum of Thickness of each slice and spacing between two slices)]. The Segmentation result was strongly related to the accuracy of boundary, thus the volume calculation results are influenced by the segmentation results. The time of computation is very much reduced for two methods when comparing with manual methods which take at least 60 minutes.

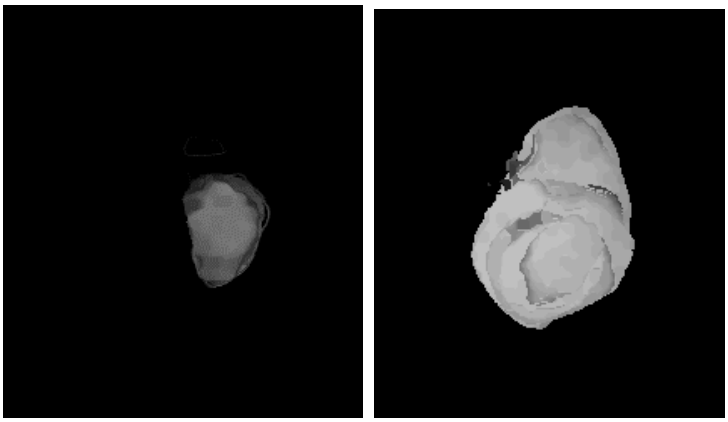

Fig.7.7 shows 3D modeled images of low and high grade Glioblastoma tumors. (a) Low grade tumor (b) Glioblastoma

Table 7. 1 Performance of the 3D Modelling algorithm with respect to Manual method

Data Sets	Volume Calculated (cm^3)	Volume calculated using 3D DOCTOR(Automated) (cm^3)	Repeatability (%)	Repeatability (%)3D DOCTOR (Automated)	Time of computation (Seconds) 3D DOCTOR (Automated)	Time of computation (Seconds)
Data Set1	63.57	63.565	99.92	99.22	120	130
Data Set2	45.54	45.54	99.98	99.28	115	126
Data Set3	38.76	38.72	99.87	99.16	108	118
Data Set4	62.53	62.51	99.95	99.57	119	120
Data Set5	22.39	22.409	99.82	99.01	90	100

The volume visualization allows exploring the tumor itself as 3D model in axial anatomical plane. Furthermore it is possible to explore the brain from each point of view. The 3D modelled gray level tumor provides the user with an

excellent impression about the patient's pathological state. To get an assumption about the tumor dimensions, the visualization displays the size in millimetres.

To get a statement about the accuracy of the segmentation and thus the calculated volumes, the segmentation results should be compared with a neuro-radiologist's opinion. According to him, in the cases of well defined tumor boundaries, the segmentation led to an accurate tumor volume.

7.4 Merits of the Method

Growth rates are sensitive enough to determine response to treatment. The growth can be determined by the algorithm and Fig 7.8 shows change in volume of a tumor with respect to number of days. By generating volumetric data across time, the patient may be tracked and response or non -response to therapy documented.

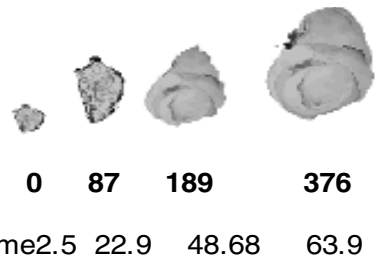

Fig. 7.8 The growth rates computed from a 3D modelled tumor over a 376-day period in a 42-year-old subject.

The automatic segmentation method followed by 3D surface modelling algorithm is capable of accurately and reliably determining the volume of low and high grade gliomas. Gray level volumes determined through the segmentation algorithm were highly correlated with measurements from manually segmented images using 3D DOCTOR. This approach will provide an accurate quantitative approach to assess the tumor changes in individual patients at different times per stages to give a progressive assessment to doctors. In addition, the structural models generated by this method represent 3D structural maps that may be correlated with data from other techniques for direct comparison or partial volume

correction[21].The models generated are very useful for follow up in patients and to determine whether they are responding to therapy. It is useful in creating structural models highlighting focal change, which may be analyzed to determine the effects of multiple therapies (egs. whether the therapies act synergistically or antagonistically).

The segmentation technique adopted in this method, it provides stable segmentation as shown in Table 5.3 and 5.4. It is also robust to changes in scanner protocol (TR/TE), including changes in the noise level of the images; and it is one of the quickest algorithms in terms of operator input and execution time as already explained in Chapter 5. Hence its volumetric model also has the same advantages.

The main objectives of this method is to develop a novel 3D modelling method with minimal human intervention, by replacing manual slice by slice automatic segmentation and reducing execution time considerably. A lot of methods are there in literature for 3D modelling algorithms like surface modelling [7], model-based approach [7], nearest neighbour algorithm [6], Active contour model and Delaunay triangulation [7] of the segmented data, etc. Main drawback of these algorithms is that much human intervention is required and it requires more execution time with a minimum time of 30 minutes. Using this method, maximum execution time is only 1minute. 3D modelling using the software 3D DOCTOR with automatic segmented slices will reduce the execution time. Replacing the manual method by automatic segmentation and 3D volumetric modelling can greatly enhance the capability in terms of fast computation time and accurate volumetric measurement of the tumor at various stages of growth.

Conclusions

A novel method for the 3D modeling of glioma tumors using 2D segmented slices is presented in this chapter. Manual segmentation of 2D slices is more time consuming and is very much prone to error. This interactive 3D modeling method is very accurate and less time consuming than any other method. These volumetric tumors can be used for volumetric analysis because it is preserving the gray level values of the original image for processing.

The volumes of 10 segmented 3D modeled image data sets were calculated using the method with reduced execution time of each data set and without much

human intervention. Manual slice by slice segmentation in 3D Doctor Software package is replaced by automatic segmentation .Tumor growth rate is also calculated using this method.

The Volumetric tumor representations are suitable for image registration, surgical planning for detection of tumor growth and also for determining prognosis of patients in the case of high grade tumors. It may be noted that, the use of this method is fairly simple when compared to the other frequently used methods. Since it is preserving the gray level values, it will be very useful for texture quantification using statistical, structural and spectral approach.

References

[1] R. Robb, D. Hanson, R. Karwoski, et.al Analyze: A comprehensive, operator interactive software package for multi-dimensional medical image display and analysis, Computerized Medical Imaging and Graphics, Vol.13:pp 433–454, (1989).

[2] N. Birkbeck, D. Cobzas, M. Jagersand, An Interactive Graph Cut Method for Brain Tumor Segmentation. Proceedings of IEEE Workshop on Applications of Computer Vision (WACV 2009), pp. 1-7, (December 2009).

[3] P. Kleihues, The WHO classification of tumors of the nervous system. Journal of Neuropathology & experimental Neurology, Vol. 61,:pp.215-229, (2002).

[4] J. Egger, D. Zukic, M.H.A. Bauer, et.al. A Comparison of Two Human Brain Tumor Segmentation Methods for MRI Data, Proceedings of 6th Russian-Bavarian Conference on Bio-Medical Engineering, State Technical University, Moscow, Russia, (Nov. 2010).

[5] S. Ho, E. Bullitt, G. Gerig, Level-Set Evolution with Region Competition: Automatic 3-D Segmentation of Brain Tumors. Proceedings of International conference on Pattern Recognition. Pp.532-535,(2002).

[6] J. Egger, T. Kapur, A. Fedorov, et.al, GBM Volumetry using the 3D Slicer Medical Image Computing Platform, Scientific Reports | 3 : 1364 | DOI: 10.1038/srep01364,Published4March2013

[7] F.Balsiger, Brain Tumor Volume Calculation Segmentation and Visualization Using MR Images,Department of Biomedical Engineering, Bachelor Thesis, Department of Biomedical Engineering,Linköping University,(April – July 2012)

[8] S. M. Haney, P. M. Thompson, T. F. Cloughesy, et.al, Tracking Tumor Growth Rates in Patients with Malignant Gliomas: A Test of Two Algorithms, *AJNR Am J Neuroradiol, vol.*22:pp.73–82,(January 2001)

[9] K.L.Chow,Y.P.Gobin,T.Cloughesy,et.al, Prognostic Factors in Recurrent GlioblastomaMultiforme and Anaplastic Astrocytoma Treated with Selective Intra-arterial Chemotherapy, *AJNR Am J Neuroradiol, Vol.*21:pp.471–478, (March 2000)

[10] M. Ahmed, D. B. Mohammad, Segmentation of Brain MR Images for Tumor Extraction by Combining Kmeans Clustering and Perona-Malik Anisotropic Diffusion Model, International Journal of Image Processing, Vol. 2:pp 27-34, (2008)

[11] Y. Wang, J. Cao, L. Liu, et.al. An Automatic Tumor Segmentation System of Brain Tumor from MRI Based on A Novel Energy Functional. Journal of Convergence Information Technology (JCIT), Vol.6:pp.59-67. (2011).

[12] A. Constantin, R. Bajcsy, S. Nelson, Unsupervised Segmentation of Brain Tissue in Multivariate MRI. Proceedings of Internarnational Symposium on Biomedical Imaging from Nano to Macro,pp.89-92, (April 2010).

[13] T. Kapur, W. Eric, L. Grimson, et.al, Segmentation of brain tissue from magnetic resonance images, Medical Image Analysis, Oxford University Press, Vol.1:pp.109–127, (1996).

[14] S. Roy, A. Saha , Prof. S. K. Bandyopadhyay, Brain Tumor Segmentation and Quantification from MRI of Brain, Journal of Global Research in Computer Science Vol.2:pp.155-160,(2011).

[15] M. Kumar, K. Mehta, A Modified Method to Segment Sharp and Unsharp Edged Brain Tumors in 2D MRI Using Automatic Seeded Region Growing Method, International Journal of Soft Computing and Engineering (IJSCE), Vol.1:pp.37-40, (2011).

[16] R. Rajeswari, P. Anandhakumar, Segmentation and Identification of Brain Tumor MRI Image with Radix4 FFT Techniques, European Journal of Scientific Research, Vol.52:pp.100-109, (2011).

[17] M. Kaus, S. K. Warfield, F.A. Jolesz, et.al., Adaptive Template Moderated Brain Tumor segmentation in MRI. Bildverarbeitung fur die Medizin, Springer Verlag, *pp.*102-106. (1999).

18] M. B. Cuadra, C. Pollo, A. Bardera, et.al. Atlas-Based Segmentation of Pathological MR Brain Images Using a Model of Lesion Growth. IEEE Transactions On Medical Imaging, Vol.23:pp.1301-1314, (2004).

[19] S.Ananda Resmi , T. Thomas, A Semi-automatic method for segmentation and 3D modeling of glioma tumors from brain MRI, J. Biomedical Science and Engineering,Vol. 5(7),(2012)

[20] GulMoonisa, J. Liub, K. Jayaram. et.al. Estimation of Tumor Volume with Fuzzy-Connectedness Segmentation of MR Images. AJNR, Vol. 23:pp. 356-363, (2002).

[20] K. Aloui, M. S. Naceur, 3D Tumor Segmentation from Volumetric Brain MR Images Using Level-Sets Method. Diagnostic Techniques and Surgical Management of Brain, InTech publisher,pp.117-138, (2011).

[21] K. Aloui, M. S. Naceur, 3D Segmentation, Compression and Wireless Transmission of Volumetric Brain MR Images. International Journal of Biological and Life Sciences,Vol.7,(2011).

[22] M. H. Gazit, R. Kimmel, N. Peled, et.al. Segmentation of thin structures in volumetric medical images. IEEE Transactions on Image Processing, Vol.15:pp. 354-363, (2006).

Chapter 8

AVG Glioma-A Software System for the Visualization and Grade Detection of Glioma

'AVG Glioma' A software system with a front end (Graphical User Interface) designed based on the techniques developed in the ealier chapters, and it is detailed in this chapter. A discussion on the applications of the developed technique and concluding remarks are also outlined in this Chapter. The front end of the system is user friendly allowing non-expert computer users to be able to extract pathological subjects in the brain including tumor and its boundary. The grade detection of the extracted glioma tumors from a set of MRI slices is implemented using GUI. Implementation of 3D modelled tumor from segmented slices is also included in this system.

8.1 Development of a Graphical User Interface system

The Block Diagram for the techniques developed in Chapter 5, Chapter 6 and Chapter 7 are integrated into a system and given in Fig.8.1, which incorporates automatic extraction of glioma tumors, tumor boundary, GM and WM from the joint intensities of T1FLAIR and T2 Weighted MRIs, glioma tumor extraction from T2 weighted MRI only. Automatic grade detection from segmented glioma tumors is possible. It also incorporates volumetric modelling using segmented slices. Based on this block diagram, a GUI is developed for the system. The main motive behind the development of a GUI is to make the system more user friendly as possible, allowing non-expert computer users to be able to segment and detect the grade of glioma.

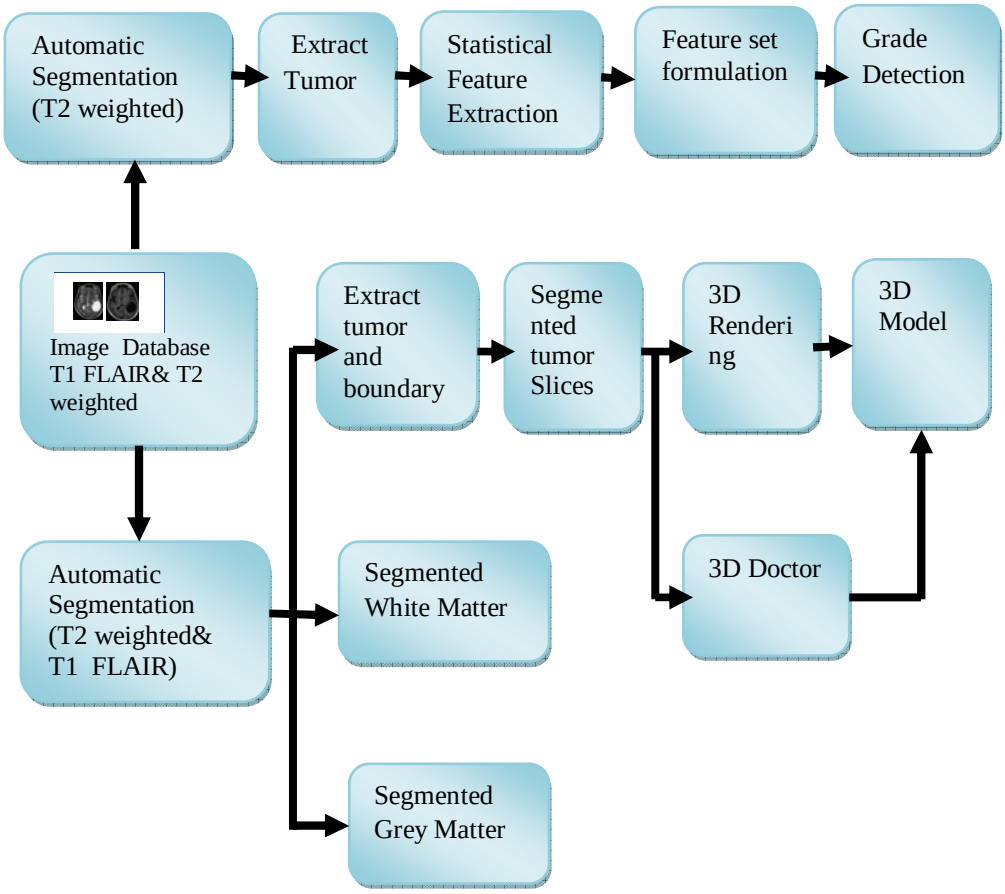

Fig.8.1 Basic Block diagram for the entire Techniques used in the AVG glioma

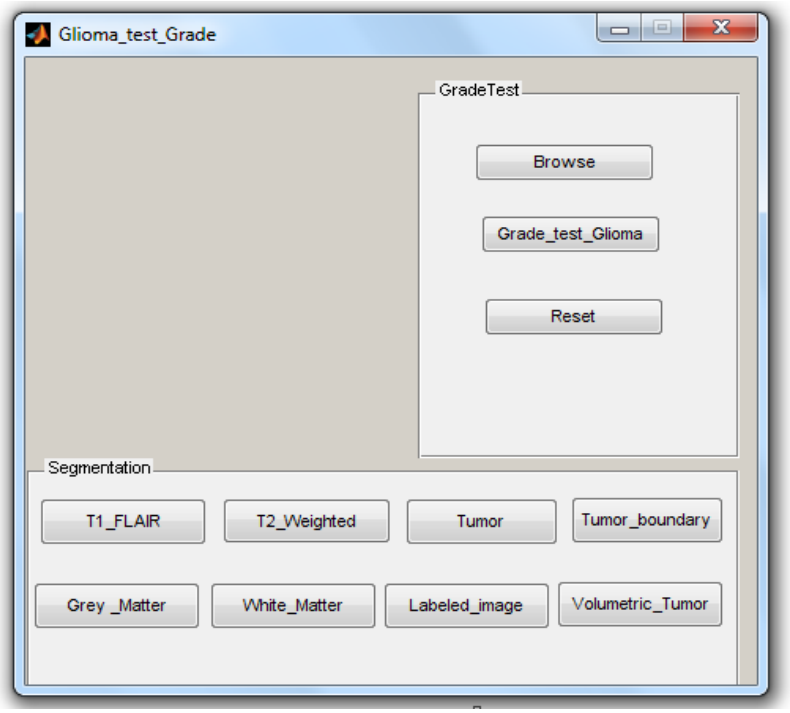

Fig.8.2 Developed Graphical User Interface for 'AVG glioma'

There are two main windows in the GUI, one is *Segmentation* window and the other one is *Grade_ test* as shown in Fig.8.2. The Segmentation window entries are "T1 FLAIR", "T2_Weighted", "Tumor", "Tumor_boundary", "Grey_Matter", "White_Matter", Labeled_image and Volumetric_Tumor. Using these entries, automatic segmentation of Tumor, Tumor boundary, Grey matter and white Matter can be extracted from the Database of T1 FLAIR and T2 Weighted images. The segmented slices in a database can be combined to get volumetric model of the extracted tumor. Each of these entries is enabled using push buttons allowing a set of actions. In the case of Grade Test Window, it contains Browse; Grade _test_Glioma and Reset push buttons which also include a series of actions for grade test.

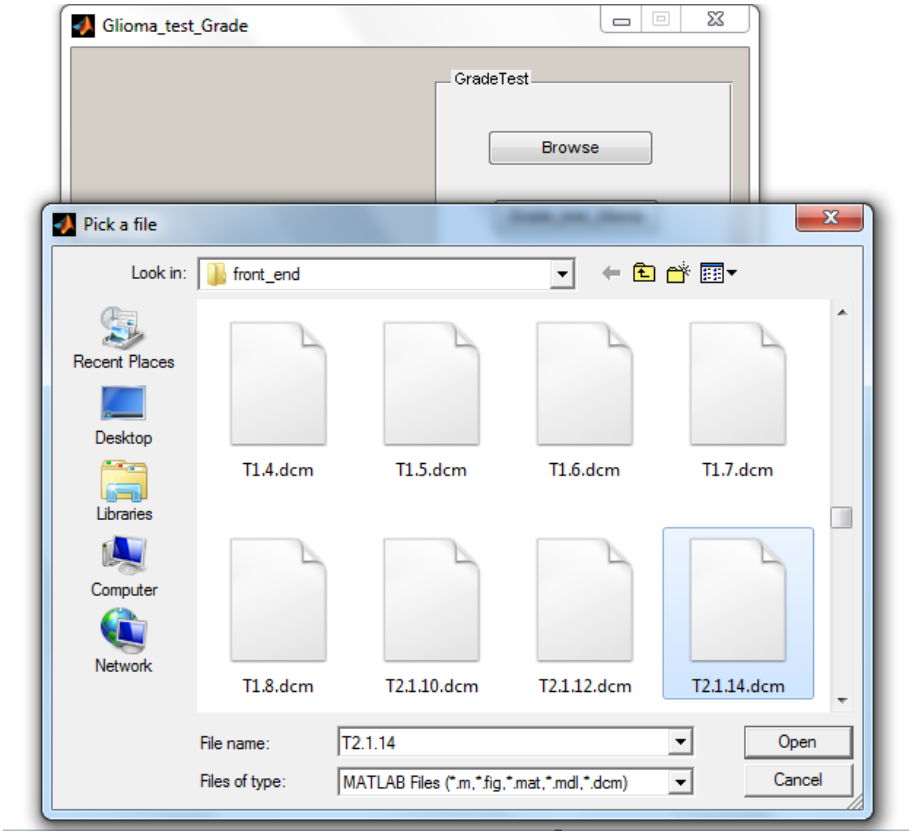

Fig.8.3 The image selection from an image database for automatic segmentation and grade detection using browse button

Browse Button: Allows opening of an image from the database, for segmentation and further procedures, that is, for grade detection or for 3Dmodelling. Using the Browse button, the users can select images in DICOM, TIFF or JPEG format. Fig.8.3 shows the image of GUI and database where the images are stored when Browse button is enabled.

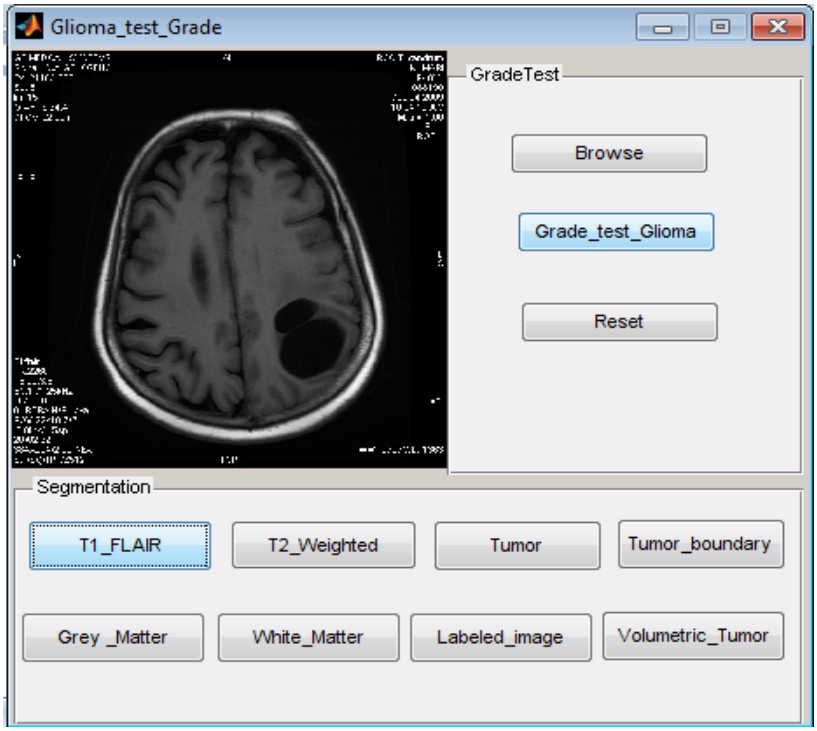

Fig 8.4 T1 FLAIR image when the push button T1_FLAIR is enabled. This is for selecting one of the input image for segmentation

In the segmentation window, it contains two buttons for image selection. T1_FLAIR and T2_Weighted. These images are of JPEG or TIFF formats.

T1_FLAIR: It is a push button used to input and display T1 FLAIR image into the figure window of GUI as shown in Fig. 8.4 when it is enabled.

T2_Weighted: It has the same function as that of T1_FLAIR push button discussed above, with only difference; instead of T1 FlAIR it displays T2 weighted images in the figure window of GUI as shown in Fig. 8.5 when it is enabled.

Tumor: This entry is for segmentation of tumor as per the method discussed in chapter5. When Tumor push button is enabled, it automatically extracts tumor region from the selected input slice as shown Fig. 8.6

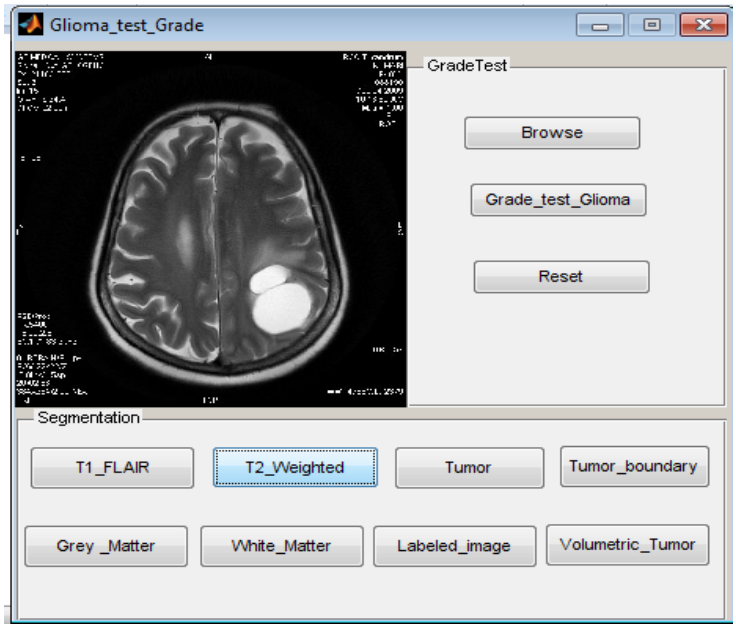

Fig 8.5 T2 Weighted image when the push button T2 Weighted is enabled. This is for selecting one of the input image for segmentation

Tumor_boundary: This entry is used for extracting tumor boundary from segmented tumors. Its execution time is less than 1 second .Fig 8.7 shows the extracted tumor boundary by enabling push button Tumor_boundary.

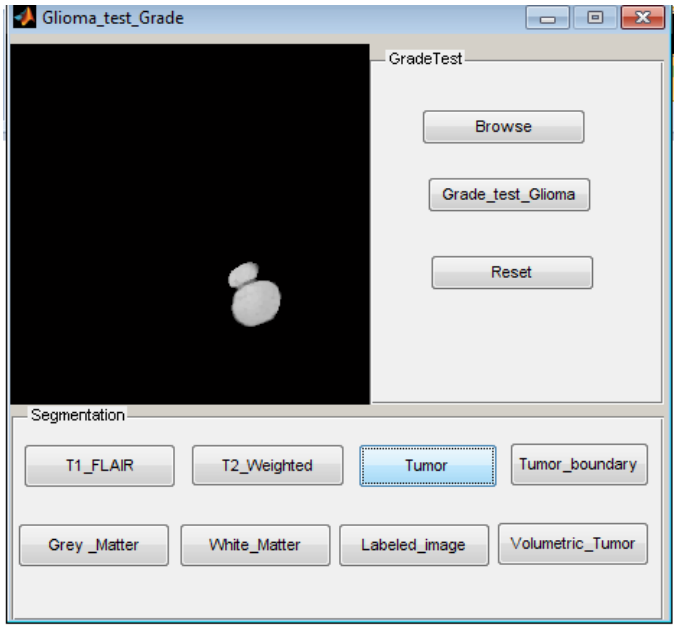

Fig.8.6 The automatic extraction of Tumor region when Tumor button is activated from the selected set of images

_bound

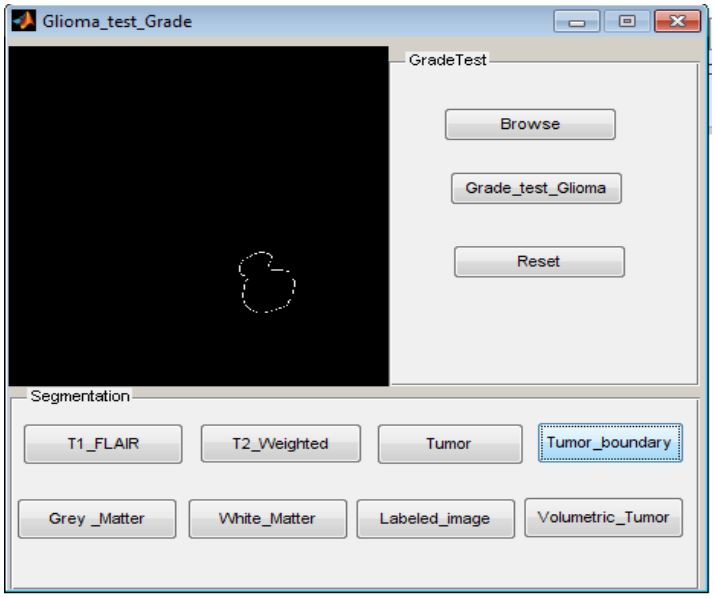

Fig.8.7 Boundary extraction while enabling the push button Tumor

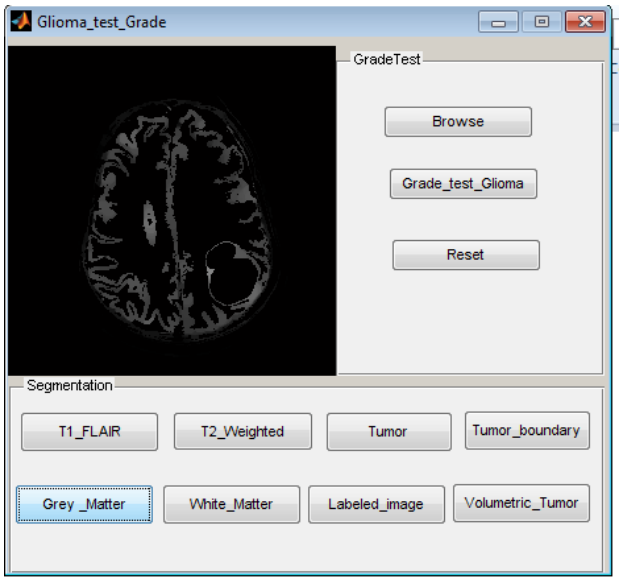

Fig.8.8The extraction of Grey Matter when Grey_matter push button is enabled

Grey_Matter: when this entry is activated, it will extract the Grey matter. Fig.8.8 shows segmented Grey matter when the push button *Grey_Matter* is activated from the given set of input image.

White_Matter: white Matter can be extracted and displayed in the figure window of GUI on pressing the push button *White_Matter* as shown in

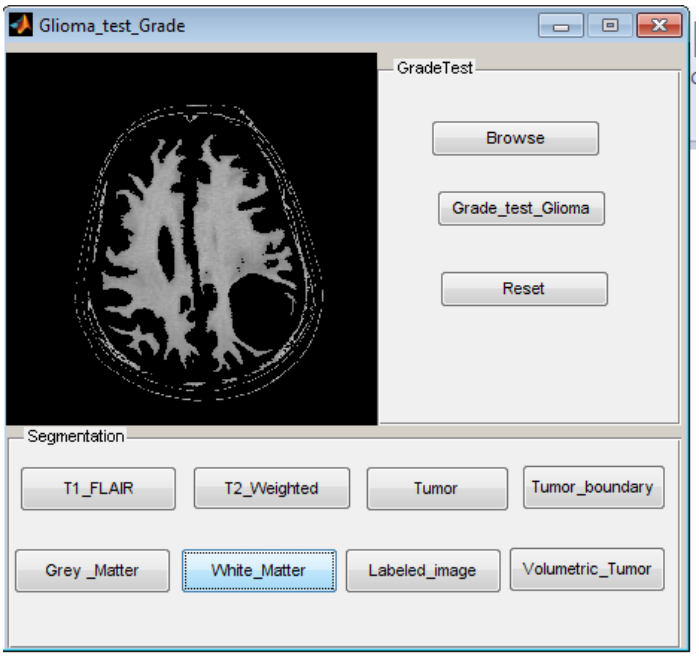

Fig.8.9 The extracted White matter, when the White_Matter button is activated

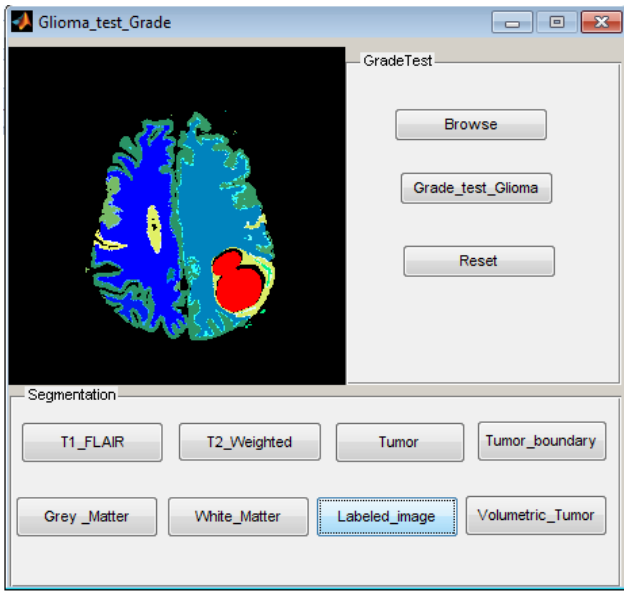

Fig.8.10 An example of extracted labelled image when the push button Labeled_Image is enabled

Labeled _image: This entry is used for displaying the segmented and color labeled regions of tumor, white matter and Grey matter with skull removed image. Fig 8.10 shows the example of labeled image when the *Labeled _image* button is activated for given set of input image.

Grade_Test_Glioma: This entry will automatically segment and display and detect the grade of glioma region if present, based on the thresholds automatically fixed for low and high grade glioma. A dialog box appears based on the detected grade of the glioma when the push button *Grade_Test_Glioma* is activated. Fig.8.11 shows an example for high grade glioma detection and correspondingly a message box appeared as "high grade glioma'. Similarly , low grade detection is shown in Fig. 8.12.

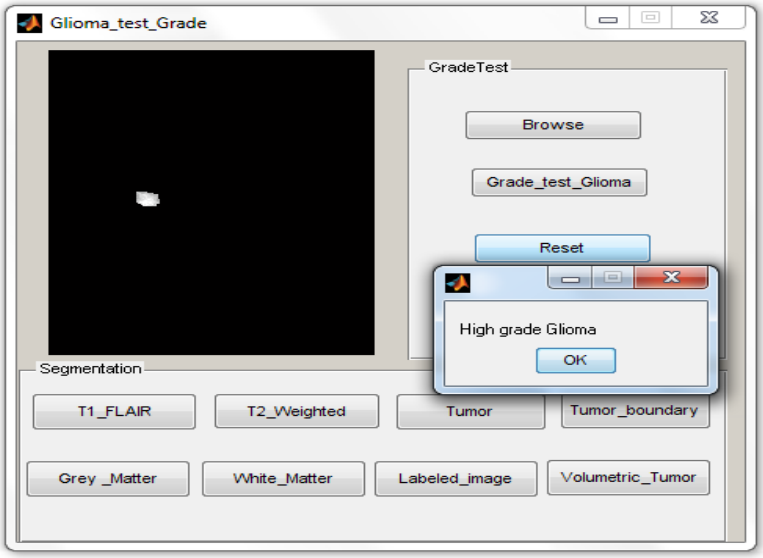

Fig.8.11 Example for grade test when push button Grade_test_ Glioma is enabled. The test result is high grade glioma

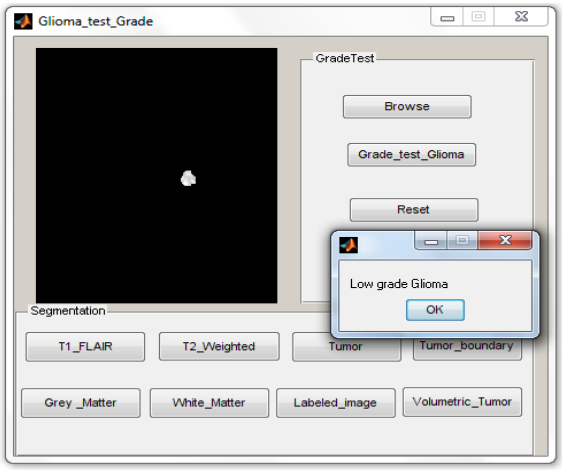

Fig.8.12 An example of Low grade glioma when activating Grade_test_Glioma push button after selecting a T2 weighted image from the database

‘

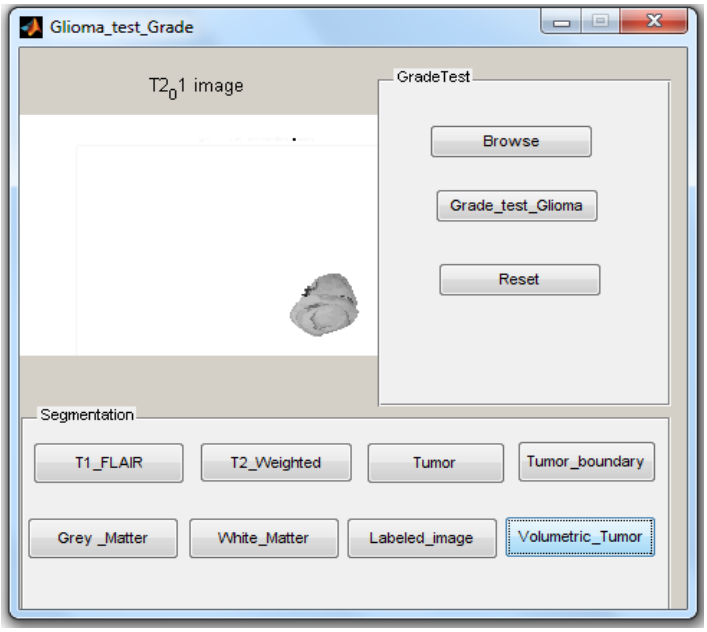

Fig 8.13 The example of volumetric modeling of tumor using segmented tumor slices in an image database when push button Volumetric Tumor is enabled.

Volumetic_Tumor: When this entry is enabled, all segmented slices in a database are stacked together to form a MAT file; based on the method discussed in Chapter7 to form the volumetric image of stacked slices when enabling volumetric_Tumor function key. Fig.8.13 shows the volumetric image model of glioma tumor when the corresponding push button is enabled. The volumetric modelling of segmented slices using the software package -3D Doctor cannot be implemented in this system because it requires some user intervention for exporting it into the 3D DOCTOR software environment.

Reset: When Reset entry is activated by the *Reset* push button then all running progams are cleared and the figure window is also cleared. That is, GUI will return to its initial state.

Conclusions

A novel and fully automatic system for automatic segmentation, Grade detection and 3D Modelling of glioma tumors, from conventional MRI is developed. A GUI with 11 entry keys for different functions was developed using MATLAB R2008a. All functions, that is, Segmentation, Glioma grade detection and 3D modelling are automated. The image database used here are clinically and experimentally tested and validated. Here we used only 20 image database which contains 20 slices each.

We used only images in DICOM formats for segmentation and grade detection. But in the case of ROI extraction using T1FLAIR and T2 weighted images, the images can be of TIFF or JPEG formats. These segmented slices were used for 3D modelling of glioma tumors. The advantage of this GUI is that human intervention is not required, after the images are selected, for segmentation and further processing. Hence this system is vey user friendly and less time consuming. It is an aid to radiologists to save time, as they need to confirm only cases where second opinion is required.

Chapter 9
Conclusions and Future Work

9.1 Thesis Highlights

This chapter brings the thesis to a close by presenting the conclusions drawn from the research. The objectives of research is introduced in chapter one. A medical perspective of Glioma and its visualization using different imaging techniques is examined in chapter two. Methods for Segmentation of various human organs including brain structures have been investigated in chapter three. The states of art methods for segmentation of brain tissues, classification or detection of different abnormalities present in human organs using statistical texture analysis from different imaging modalities are also reviewed in chapter three. A brief overview of basic image processing tools used in this research is discussed in chapter four. Chapter five discusses a novel method known as Adaptive Gray level Algebraic set Segmentation Algorithm (AGASA) developed for extraction of low and high grade glioma tumor and other brain subjects. A comparative study between the developed methods and the existing methods are also included in this chapter. Next, a novel method for grade detection of glioma tumors using statistical methods from the segmented low and high grade MR images is detailed in Chapter six. Chapter seven gives a state of art method for volumetric modeling of glioma tumors using the segmented image slices for assessing growth rate of tumor. A novel software system 'AVG glioma' is developed for the automatic extraction and grade detection of glioma tumor and its 3D visualization implementation is presented in chapter eight.

9.2Extraction of Low and High Grade Glioma and other Brain Tissues using Adaptive Gray level Algebraic set Segmentation Algorithm (AGASA)

Two methods were developed for segmentation of low and high grade glioma. First method is an, accurate and robust method for automatic extraction of low and high grade tumors from T2 weighted MRIs. The robustness of the algorithm with respect to Guassian noise and speckle noise was also discussed. Using this method, it is able to delineate back ground structures other than tumor and reduce partial volume effect other noise present in the image. The main drawback of this algorithm is that using the single modality -T2 weighted images- it is difficult to extract other brain subjects such as white matter and grey Matter. These segmented images are used for grade detection of glioma.

This difficulty was overcome by developing the novel and robust algorithm, named as Adaptive Gray level Algebraic set Segmentation Algorithm (AGASA) for the extraction of definable objects such as white matter, grey matter, tumor and tumor boundary. The method was validated with manually segmented images as ground truth images. The accuracy of the methods in terms of segmented region of interests was validated by computing True Positive, False Positive, and False Negative with respect to ground truth images. The Tanimoto Index, Percentage Match, Positive Prediction Value were calculated and its ranges show excellent performance with average score of 98.7%. The main goal of development of this automated segmentation method is to make segmentations of MR images more practical by replacing manual outlining, which reduces operator time with measurable effect and to improve reproducibility. This segmentation method is suitable for image registration for surgical planning, detection of tumor growth and for determining prognosis of patients in the case of high grade tumors. Partial volume effects were very much reduced. This method is fairly simple when compared with other frequently used methods. The segmented ROIs retained the gray level values of each pixel and hence were directly used these segmented tumors are used for statistical texture analysis and grade detection of glioma tumor. Segmented gray level tumors are also used for 3D rendering of glioma tumors which can be used for volumetric analysis.

These two methods were compared with respect to an existing method fuzzy c-means clustering technique in terms of its accuracy and computation time. It is observed that these two methods are more accurate and less time consuming than fuzzy c means clustering technique.

9.3 Grade Detection of Glioma Tumors using Statistical Texture Analysis

A novel method for grade detection of glioma tumors from segmented MRIs was developed. Entire segmented region of interest was considered for texture analysis. Statistical quantification of tumor texture was done using first order and GLCM based second order statistics. Five first order statistical features were extracted and it is found that these features are well discriminated. From these features it was observed that high grade glioma had heterogeneous tumor textures and it is an evidence for the fact that as malignancy increases tumor tissue heterogeneity is also increasing. Ten Gray level co-occurrence (GLCM) based texture descriptors were extracted and seven well discriminant descriptors were selected using box plots.

Three feature sets are formulated based on selected descriptors thresholds for each feature was fixed and based on these thresholds, a decision system was developed. The performance of the decision algorithm was evaluated for three feature sets. Area under the Curve (AUC) for feature sets1, 2, 3 are 0.8743, 0.9083 and 0.9735 respectively. The sensitivity and specificity using feature sets1, 2, 3 in detecting grade of tumors are 94.56, 97.13, 99.03 and 77.72, 83.042, 92.53 respectively. The experiments proved that using feature set 3 had better detection performance than using other two feature sets.

9.4 Volumetric modeling of glioma

A Novel method for the 3D modeling of glioma tumors using 2D segmented slices is developed. Manual segmentation of 2D slices is more time consuming and is very much prone to error. This interactive 3D modeling method is very accurate and less time consuming than any other method. These volumetric tumors can be used for volumetric analysis because it is preserving the gray level values of the original image for processing. The volumes of ten 3D modeled

tumors are calculated using the method and execution time and human intervention is reduced. Manual slice by slice segmentation in 3D Doctor Software package is replaced by automatic segmentation .Tumor growth rate is also calculated using this method.

The Volumetric tumor representations are suitable for image registration, surgical planning for assessment of tumor growth and also for determining prognosis of patients in the case of high grade tumors. It may be noted that, the use of this method is fairly simple when compared to the other frequently used methods. Since it is preserving the gray level values it will be very useful for texture quantification using statistical, structural and spectral approach.

9.5 Suggestions for Future research

Although the present research gave good results, certain proposals for future work are listed below:

- Along with the statistical features by incorporating histopathological properties, edema properties, tumor shape etc., more sophisticated and robust system could be developed for detecting all grades and sub types of glioma.
- Detection/ Classification using fractal dimensions of glioma tumor and metastatic tumors can be performed.
- Research work can be done for classification between different subtypes of tumor using Gabor transform an Gray level Run length matrices and by principal component analysis.

APPENDIX

1)Robustness of Method 1 with respect to Rician Noise

The effect of Rician noise in MR images is as follows.

Here, the image intensity in magnetic resonance magnitude images in the presence of noise is to be governed by a Rician distribution. Rician noise depends on the data itself; it is not additive.So to add Rician noise to data, we really make the data Rician distributed. The magnetic resonance signals are acquired in quadrature channels. Each signal produces an image that is degraded by a zero-mean Gaussian noise of standard deviation σ_0 (which we define as the noise level). The two images are then combined into a magnitude image and the Gaussian noise probability distribution function (PDF) is transformed into a Rician noise PDF.

A signal X is said to be corrupted by Rician noise if its PDF is given by eqn.

$$\boldsymbol{p(X|A) = \frac{X^2}{\sigma} exp\left(-\frac{X^2 + A^2}{2\sigma^2}\right) I_0(\frac{XA}{\sigma^2})}$$

Where, A is the image pixel intensity in the absence of noise. σ is the standard deviation of the noise, and I_0 is the modified zeroth-order Bessel function of the first kind. Rician distribution is far from Gaussian for small SNR ($X/\sigma \leq 1$). However, for ratios $X/\sigma \geq 3$, it starts to approximate to Gaussian distribution.

Table 1 shows TI of the segmented tumor from the Rician noise added images. The SNR of the images were computed for different noise levels. This is achieved by modelling Rician noise added image. The TI is calculated for SNR, 5dB to 70 dB. Fig.1 shows a plot of performance evaluation of the

method with respect to different levels of Rician noise affected images. From the graph it can be observed that, this method is robust enough for Rician noise also.

Table 1 shows Computed values of TI from Rician noise affected images having low and high grade tumors with different values of standard deviation and SNR

Image	Variance	SNR (Rician Noise)	TI (low grade)	TI (high grade)
1	0.0028	5	60.46	70.80
2	0.0026	7	63.17	74.78
3	0.0024	8	69.41	78.91
4	0.0022	9	80.33	83.09
5	0.002	10	83.14	90.84
6	0.0018	11	85.74	93.01
7	0.0016	12	89.16	95.58
8	0.0014	15	91.32	96.65
9	0.0012	20	93.37	97.68
10	0.001	30	95.07	98.01
11	0.0008	40	96.97	98.70
12	0.0006	50	97.17	99.03
13	0.0004	60	97.96	99.33
14	0.0002	70	98.54	99.60

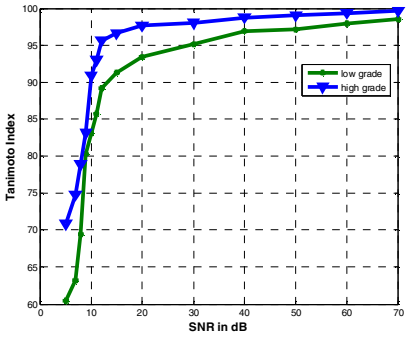

Fig.1 Tanimoto Index of the segmented of low and high grade glioma with respect to SNR at different levels of Rician noise

Table 2shows Computed values of TI from Gaussian noise affected images having low and high grade tumors with different values of standard deviation and SNR

Image	Mean	Variance	SNR (Gaussian Noise)	TI (low grade)	TI (high grade)
1	0.93	0.0028	5	68.78	73.50
2	0.84	0.0026	7	72.03	78.20
3	0.73	0.0024	8	76.54	87.42
4	0.68	0.0022	9	85.93	90.86
5	0.62	0.002	10	90.51	93.65
6	0.5	0.0018	11	92.65	96.27
7	0.4	0.0016	12	95.61	97.91
8	0.3	0.0014	15	96.93	99.16
9	0.1	0.0012	20	97.12	98.66
10	0.09	0.001	30	97.59	99.30
11	0.07	0.0008	40	98.62	99.47
12	0.05	0.0006	50	98.82	99.63
13	0.04	0.0004	60	98.86	99.67
14	0.02	0.0002	70	98.87	99.69

Table 3 shows Computed values of TI from speckle noise affected images having low and high grade tumors with different values of standard deviation and SNR

Image	Variance	SNR (Speckle Noise)	TI (low grade)	TI (high grade)
1	0.88	5	62.26	63.80
2	0.68	7	65.25	69.78
3	0.48	8	70.28	75.91
4	0.25	9	76.09	81.21
5	0.1	10	81.70	84.84
6	0.08	11	84.62	90.01
7	0.06	12	88.32	92.15
8	0.03	15	90.18	96.95
9	0.01	20	94.37	98.48
10	0.009	30	96.15	98.78
11	0.008	40	97.50	99.20
12	0.001	50	98.19	99.62
13	0.0008	60	98.88	99.74
14	0.0003	70	98.94	99.69

Table 2 and Table 3 shows TI computed from Guassian and speckle noise added image , which was not included in Section 5.2.2.3

2. Robustness of AGASA with respect to Gaussian, Speckle and Rician noise

In order to check the performance of AGASA in the presence of noise, Gaussian noise, speckle noise and Rician noise at different noise levels were added to the MR images as mentioned in Section 5.2.2.3 and segmentation was carried out without using any pre-processing filters.

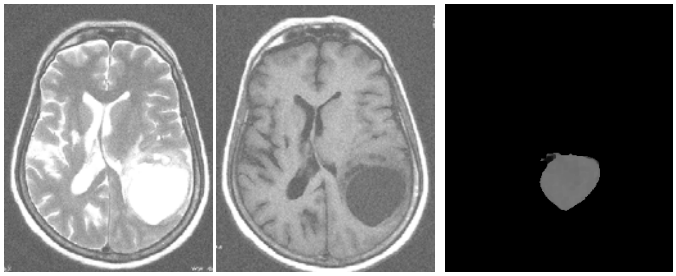

(a) (b) (c)

Fig.1 shows the example for checking performance of AGASA on Gaussian noise added images of 20dB SNR. (a) T2- weighted (b) T1-FLAIR (c) segmented tumor

Fig 1 shows an example of Gaussian noise added in T2 weighted (Fig.1a) and T1 FLAIR (Fig.1b) images of corresponding and segmented tumor (Fig.1c) using AGASA. The SNR of the images were varied by changing the mean and standard deviation of Gaussian noise and segmentation was carried out. Speckle noise added T2 weighted image and T1 FLAIR with SNR of 20dB are shown in Fig. 2a and Fig.2b respectively. The resulting extracted tumor is shown in (Fig.2c). From these figures, it can be observed that the presence of noise does not affect shape of the segmented tumor. Rician noise affected images were mathematically modelled and is shown in Fig.3 a (T2 weighted) and Fig.3 b (T1 FLAIR). The segmented tumor extracted from the Rician noise affected images is shown in Fig.3c.

From these figures, it can be observed that, the method is able to delineate the presence of noise and the segmentation can be done very efficiently.

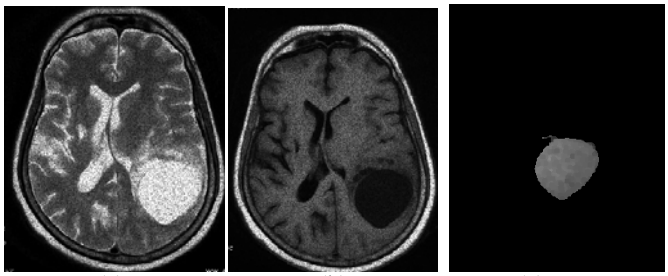

(a) (b) (c)

Fig.1 shows the example for checking performance of AGASA on speckle noise added images of 20dB SNR. (a) T2- weighted (b) T1- FLAIR (c) segmented tumor

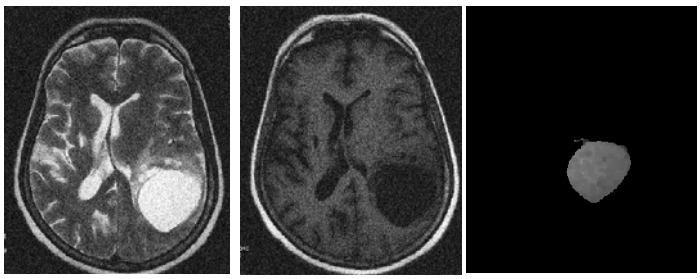

(a) (b) (c)

Fig.3 shows the example for checking performance of AGASA on Rician noise added images of 20dB SNR (a) T2- weighted (b) T1-FLAIR (c) segmented tumor

To validate the robustness of AGASA, with respect to the various noises, T1 values were calculated. Table 1 shows validation of robustness of the algorithm with respect to Gaussian noise on 14 randomly selected images.

Table 1 Computed values of TI from Gaussian noise added images having low and high grade tumors with different values of mean, standard deviation and SNR

Image	Mean	Variance	SNR (Gaussian Noise)	TI (low grade)	TI (high grade)
1	0.93	0.0028	5	69.78	75.50
2	0.84	0.0026	7	72.30	79.20
3	0.73	0.0024	8	77.54	88.42
4	0.68	0.0022	9	85.93	91.86
5	0.62	0.002	10	90.51	93.65
6	0.5	0.0018	11	92.65	96.87
7	0.4	0.0016	12	94.61	97.49
8	0.3	0.0014	15	96.93	97.69
9	0.1	0.0012	20	97.12	98.66
10	0.09	0.001	30	97.59	99.30
11	0.07	0.0008	40	98.62	99.47
12	0.05	0.0006	50	98.82	99.63
13	0.04	0.0004	60	98.86	99.74
14	0.02	0.0002	70	98.87	99.86

Table 2 Computed values of TI from speckle noise added images having low and high grade tumors with different values of standard deviation and SNR

Image	Mean	Variance	SNR (Speckle Noise)	TI (low grade)	TI (high grade)
1	0	0.88	5	62.61	63.80
2	0	0.68	7	65.50	69.78
3	0	0.48	8	70.84	75.91
4	0	0.25	9	76.93	81.21
5	0	0.1	10	81.70	84.84
6	0	0.08	11	85.62	90.01
7	0	0.06	12	88.32	92.15
8	0	0.03	15	90.18	96.95
9	0	0.01	20	94.74	97.48
10	0	0.009	30	96.15	97.78
11	0	0.008	40	97.50	98.20
12	0	0.001	50	98.19	99.62
13	0	0.0008	60	98.88	99.74
14	0	0.0003	70	98.94	99.86

Table 3 Computed values of TI from R ician noise affected images having low and high grade tumors with different values of standard deviation and SNR

Image	Variance	SNR (Rician Noise)	TI (low grade)	TI (high grade)
1	0.0028	5	63.46	72.98
2	0.0026	7	69.22	76.78
3	0.0024	8	72.54	80.42
4	0.0022	9	82.93	88.21
5	0.002	10	85.51	91.48
6	0.0018	11	88.47	94.70
7	0.0016	12	90.62	97.86
8	0.0014	15	92.93	98.69
9	0.0012	20	94.84	98.66
10	0.001	30	95.90	99.20
11	0.0008	40	96.25	99.37
12	0.0006	50	97.67	99.43
13	0.0004	60	98.06	99.56
14	0.0002	70	98.17	99.76

The mean and variance is varied for obtaining images with different noise levels or SNR and the corresponding TI values are calculated. Table 2 and 3 is gives an idea of robustness of the algorithm with respect to Speckle and Rician noise respectively for different values of SNR.

The performance of the algorithm with respect to Gaussian, Rician and speckle noise is plotted in Fig.4 (a), Fig. 4(b) and Fig.4(c). From the graph, it can be observed that the algorithm is robust enough for images having SNR of 10dB Gaussian noise, 15dB for Speckle noise and 12db for Rician noise.

When comparing the performance of the method 1 in Section 5.2.2.3 and AGASA, in terms of robustness with respect to noise, AGASA method is more

suitable than method 1, for SNR greater than 20dB. For low SNR, performance of the two methods is almost same.

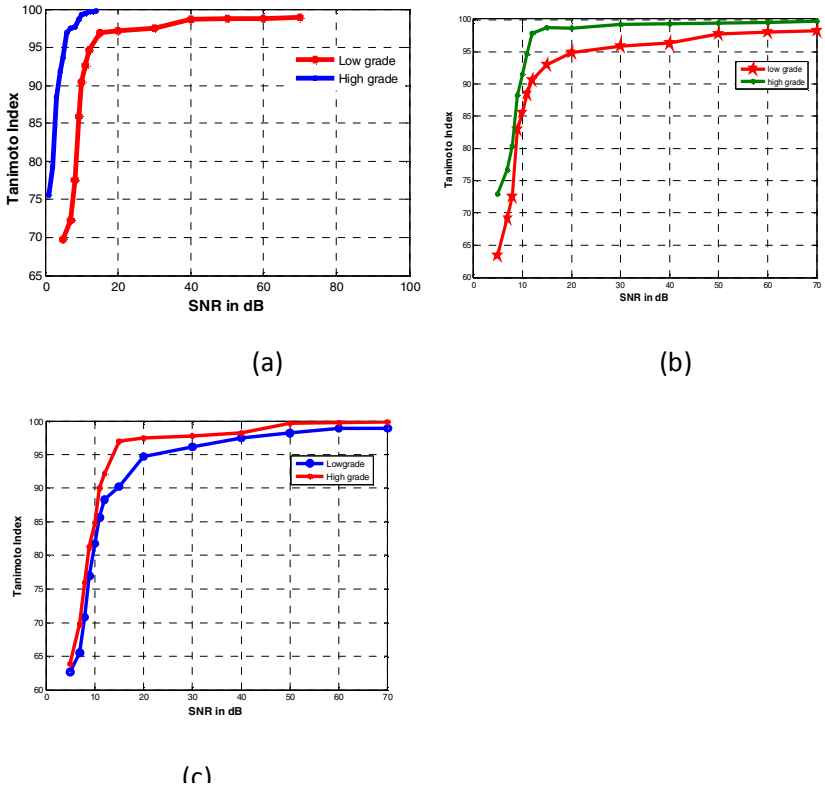

Fig.4 Tanimoto Index of the segmented of low and high grade glioma with respect to SNR at different noise levels. (a) Gaussian noise added images with different noise levels (b) Rician noise added images with different noise levels (c) Speckle noise added images with different noise levels

LIST OF PUBLICATIONS

International Journals

1. **S. Ananda Resmi,** Tessamma Thomas, A semi-automatic method for segmentation and 3D modeling of glioma tumors from brain MRI , J. Biomedical Science and Engineering, 2012, 5, 378-383
2. **S. Ananda Resmi,** Tessamma Thomas,'Texture description of low grade and high grade glioma using statistical features in brain MRIs, Int. J. of Recent Trends in Engineering and Technology, Vol. 4, No. 3, Nov 2010, pp.27-33
3. **S. Ananda Resmi,** Tessamma Thomas, IF12A05-MICR1 Segmentation and Texture Analysis of Brain MRIs using Statistical Features for low grade and high Grade Glioma detection. Special issue on Information Fusion in Medical Image Computing Systems, Information Fusion Journal Elsivier (under Revision).
4. **S. Ananda Resmi,** Tessamma Thomas, Bejoy Thomas , A Novel Automatic Method for Extraction of Glioma Tumor, White matter and Grey matter from Brain Magnetic Resonant Images, Biomedical imaging intervention Journal (Accepted for publication)
5. Dr.John P.S. ,Tessamma Thomas, **S. Ananda Resmi,** ,Dinesh Kumar 'A novel computer assisted technique for pedicle screw insertion' International Journal on Medical Robotics March 3(2007) pp:59-63

International Conferences

1. **S. Ananda Resmi,** Tessamma Thomas,' Automatic segmentation of Brain MRIs using morphological methods' InternationalConference on Modeling and Simulation (MS09) India 1-3 Dec 2009 pp:121-125
2. **S. Ananda Resmi,** Tessamma Thomas, Automatic Segmentation framework for Primary tumors from brain MRIs using Morphological filtering Techniques, proceedings of 5th International Conference on BioMedical Engineering and Informatics (BMEI'12) held from 16-18 October 2012, in Chongqing, China
3. **S. Ananda Resmi,** Dinesh Kumar V.P, Tessamma Thomas, Dr.John P.S ' A novel computer assisted technique for pedicle screw insertion' International conference on Advanced Information and Telemedicine Technologies for Health November 8-10, 2005,Minsk,Belarus